Modelling the ultraviolet-to-infrared spectral energy distributions of galaxies

Elisabete da Cunha

To cite this version:

Elisabete da Cunha. Modelling the ultraviolet-to-infrared spectral energy distributions of galaxies. Astrophysics [astro-ph]. Université Pierre et Marie Curie - Paris VI, 2008. English. NNT : . tel-00448304

HAL Id: tel-00448304
https://theses.hal.science/tel-00448304

Submitted on 18 Jan 2010

École Doctorale d'Astronomie et Astrophysique d'Île-de-France
Université Paris VI – Pierre & Marie Curie

DOCTORATE THESIS

to obtain the title of Doctor of the University of Pierre & Marie Curie
in Astrophysics

defended by
Elisabete da Cunha

Modelling the Ultraviolet-to-Infrared Spectral Energy Distributions of Galaxies

Thesis Advisor: Stéphane Charlot

prepared at Institut d'Astrophysique de Paris, CNRS (UMR 7095),
Université Pierre & Marie Curie, with financial support from the EC Marie
Curie Research Training Network MAGPOP

defended on October 9th, 2008

Reviewers	Vassilis Charmandaris	University of Crete, Greece
	Hans-Walter Rix	MPIA Heidelberg, Germany
Advisor	Stéphane Charlot	IAP, Paris, France
President	Patrick Boissé	IAP, Paris, France
Examinators	Jarle Brinchmann	Leiden Obs., The Netherlands
	David Elbaz	CEA, Saclay, France
	George Helou	NASA/IPAC, Pasadena, USA

Aos meus pais

On ne fait jamais attention à ce qui a été fait; on ne voit que ce qui reste à faire.
– Marie Curie

Acknowledgments

I would like to thank here the people who have supported and encouraged me during the time of my thesis.

Firstly, I thank my thesis supervisor Stéphane Charlot, for the guidance and encouragement he has given me since the beginning of my thesis. Thank you for all that you have taught me and for always stimulating me to do things better. This learning process was not always easy, nevertheless it has been a privilege to work with you and to learn from you.

A big 'obrigada' to Jarle Brinchmann, for your support and advice back in Porto even before I started my thesis. Also for your constant help and interest in my work throughout my thesis, and for giving me the opportunity to go back to CAUP to give a seminar.

I warmly thank David Elbaz for very inspiring discussions, good advices, insightful comments, and for always being available to answer my questions. This thesis has much benefited from your expertise on infrared observations of galaxies, your broad knowledge on galaxy evolution, and especially your good humor.

Many thanks also to David Schiminovich for giving me the opportunity to work with the SSGSS team, for having received me so well at Columbia University, and for having matched the SDSS-*IRAS* sample of Chapter 5 with the latest data from *GALEX*. I would also like to thank Antara Basu-Zych for the good times and interesting conversations we had in New York, and Ben Johnson for our discussions on the work about the SSGSS sample.

I am also extremely grateful to Celine Eminian, with whom it has been such a pleasure to work with. Thank you so much for your excellent work with our SDSS-*IRAS* sample, and for being such a good friend and an example of gentleness.

All the friends who have supported me, kept me from stressing too much at times, and who made the last three years enjoyable and full of good memories deserve a very especial place here. I thank my friends of the 'comunidade portufónica do IAP': Tatiana, thank you for all the good times we had in Paris, and for being such a good friend, even from the other side of the ocean; Jaime, for your constant good humour and example of passion for Astronomy; and Paula, thank you for your support, understanding and friendship especially in the last times of my thesis. Vocês trouxeram mais luz a Paris.

I am also grateful to my good friends at the IAP: Jakob, Oliver, Gwenael (thank you for our conversations and for being my jogging 'coach'!), Guilhem (for the countless times you have helped me with computers), Elisabetta, Jean-Christophe, Alessandro, François (for always making me laugh), Yuko (thank you for the chocolates) and Florence. I would also like to thank Chantal and Lysiane, for their constant kindness and good will, and all the researchers at the IAP who kept an interest in my work and with whom I have had interesting discussions.

I would also like to thank my MAGPOP friends Vivienne, Jérémy, Dimitri, Michael, Andrew, Dolf and Anna, with whom I have learnt so much and I also had so much fun in MAGPOP events.

I could not forget my friends from home. Thank you for all the support and encouragement you have given me, and for the great fun we always have when we get together again, especially Filipe and Bárbara (sobretudo pelas boas memórias da vossa visita a Paris), but also Cristina ‘Rasteirinha’, Paula, Ana, Rui ‘Waffles’, a Carol, João e o resto do ‘pipôle’.

I wish to thank the especial person with whom I have shared my life in the last years. Obrigada Brent, for all your love, support and understanding, for being there for me even when far away, for knowing the right times to be a boyfriend and an astronomer, for showing me wonderful Oz and your beautiful family, for making me discover so many new things. And thank you for having been the first reader of my thesis manuscript, for your help, advices and constructive criticism. You have kept me smiling even in the toughest moments.

Finally, I thank my family in Portugal. Um agradecimento especial à minha família. Obrigada pelo apoio constante, mesmo de longe, e especialmente a mamã e ao papá, pelo exemplo de coragem que me têm dado para atravessar os momentos difíceis.

I gratefully acknowledge financial support from the European Community for a Marie Curie PhD Fellowship through the MAGPOP Research and Training Network. I thank the network coordinator, Guinevere Kauffmann, as well as all the node coordinators of the network for making this possible.

Abstract

The spectral energy distributions of galaxies at ultraviolet, optical and infrared wavelengths are clues to both the radiation produced by stellar populations and the effect of gas and dust in the interstellar medium (ISM) on this radiation. Spectral interpretation studies are therefore crucial to understand how galaxies formed and evolved. Observationally, combined ultraviolet, optical and infrared data are now becoming available for large samples of galaxies. So far, these have focused mainly on the local galaxy population, but future deep surveys will provide observations of large galaxy samples at higher redshifts. To extract constraints on the stellar populations and ISM of galaxies from these multi-wavelength observations requires the consistent modelling of the emission by stars, gas and dust.

In this thesis, we present a simple, largely empirical but physically motivated model, which is designed to interpret consistently multi-wavelength observations from large samples of galaxies in terms of physical parameters, such as star formation rate, stellar mass and dust content. This model relies on an existing angle-averaged prescription to compute the absorption of starlight by dust in stellar birth clouds and in the ambient interstellar medium (ISM) in galaxies. We compute the spectral energy distribution of the power re-radiated by dust in stellar birth clouds as the sum of three components: a component of polycyclic aromatic hydrocarbons (PAHs); a mid-infrared continuum characterising the emission from hot grains at temperatures in the range 130–250 K; and a component of grains in thermal equilibrium with adjustable temperature in the range 30–60 K. In the ambient ISM, we fix for simplicity the relative proportions of these three components to reproduce the spectral shape of diffuse cirrus emission in the Milky Way, and we include a component of cold grains in thermal equilibrium with adjustable temperature in the range 15–25 K.

Our model is both simple and versatile enough to allow the derivation of statistical constraints on the star formation histories and dust contents of large samples of galaxies using a wide range of ultraviolet, optical and infrared observations. We illustrate this by deriving median-likelihood estimates of a set of physical parameters describing the stellar and dust contents of local star-forming galaxies from three different samples. The model reproduces well the observed spectral energy distributions of these galaxies across the entire wavelength range from the far-ultraviolet to the far-infrared, and the star formation histories and dust contents of the galaxies are well constrained.

A main advantage provided by this model is the ability to study the relation between different physical parameters of observed galaxies in a quantitative and statistically meaningful way. Our analysis of star-forming galaxies from the *Spitzer* Infrared Nearby Galaxy Sample (SINGS) and the *Spitzer*-SDSS-*GALEX* Spectroscopic Survey (SSGSS) reveals that the mid- and far-infrared colours of galaxies correlate strongly with the specific star formation rate, as well as with other galaxy-wide quantities connected to this parameter, such as the ratio of infrared luminosity between stellar birth clouds and the ambient ISM, the contributions by PAHs and grains in thermal equilibrium to the total infrared emission, and the ratio of dust mass to stellar mass. These correlations provide important insight into the link between star formation and ISM properties in galaxies.

We investigate further the relation between star formation activity and dust content in galaxies by assembling a large sample of 3321 galaxies with available observations at ultraviolet (*GALEX*), optical (SDSS) and infrared (*IRAS*) wavelengths. We find that the star formation rate correlates remarkably well with galaxy dust mass over four orders of magnitude in both quantities. This allows us to provide a simple empirical recipe to estimate the total dust mass of galaxies from the star formation rate. We compare our findings with the predictions from recent models of the chemical evolution of galaxies. We also compare the relations between the specific star formation rate, the ratio of dust luminosity to stellar mass and the ratio of dust luminosity to star formation rate obtained from our analysis with those predicted by state-of-the-art cosmological simulations of galaxy formation.

The model presented in this thesis can be straightforwardly applied to interpret ultraviolet, optical and infrared spectral energy distributions from any galaxy sample.

Résumé

Les distributions spectrales d'énérgie des galaxies en ultraviolet, optique et infrarouge nous donnent des pistes sur le rayonnnement produit par les populations stellaires et l'effet du gaz et de la poussière du milieu interstellaire sur ce rayonnement. Des études d'interpretation spectrale sont donc déterminantes pour comprendre la formation et l'évolution des galaxies. Observationellement, des données en ultraviolet, optique et infrarouge deviennent disponibles pour des grands échantillons de galaxies. Jusqu'à présent, ces études se sont concentrées principalement sur la population locale de galaxies, mais de futurs relevés plus profonds apporteront des observations de grands échantillons de galaxies a des plus grandes décalages spectrales vers le rouge. Pour extraire des contraintes sur les populations stellaires et le milieu interstellaire des galaxies a partir de ces observations multi-longueur d'ondes, on a besoin de modéliser d'une façon cohérente l'émission par les étoiles, le gaz et les poussières.

Cette thèse présente un modèle simple, largement empirique mais avec une motivation physique, qui est déstiné a interpreter systématiquement les observations multi-longueur d'ondes de grands échantillons de galaxies en termes de ses paramètres physiques, comme par exemple le taux de formation d'étoiles, la masse stellaire et le contenu en poussière. Ce modèle est relié a un modèle déjà existant qui permet de calculer l'absorption de la lumière des étoiles par la poussière dans les nuages moleculaires ou sont nées les étoiles et dans le milieu interstellaire environment des galaxies. On calcule la distribution spectrale de l'energie re-émise par la poussière dans les nuages de formation d'étoiles comme la somme de trois composantes: une composante de hydrocarbures aromatiques polycycliques (PAHs); un continu en infrarouge moyen qui caracterize l'émission par des grains de poussière a des températures dans la gamme 130–250 K; et une composante de grains en équilibre thérmique avec température réglable dans la gamme 30–60 K. Dans le milieu interstellaire environmental, on fixe par simplicité les proportions rélatives de ces trois composantes de façon a réproduire la forme spectrale de l'émission diffuse *cirrus* de la Voie Lactée, et on inclu une composante de grains froids en équilibre thérmique avec température réglable dans la gamme 15–25 K.

Ce modèle est au même temps assez simple et versatile pour permettre d'obtenir de contraintes statistiques sur les taux de formation d'étoiles et contenus en poussière de grands échantillons de galaxies en utilisant une vaste gamme d'observations en ultraviolet, optique et infrarouge. On illustre ce fait en tirant des estimations de 'vraisemblence mediane' d'une série de parametres physiques qui décrivent le contenu en étoiles et en poussières de galaxies à formation d'étoiles locales provennant de trois échantillons differents. Le modéle réproduit bien les distributions spectrales d'énergie observées de ces galaxies dans toute la gamme de longueur d'onde de l'ultraviolet lointain à l'infrarouge lointain, et les histoires de formation d'étoiles et contenus en poussières sont bien contraints.

Une des avantages de ce modèle est la capacité d'étudier le rapport entre des différents parametres physiques des galaxies observées d'une manière quantitative et statistiquement significative. L'analyse des galaxies à formation d'étoiles des échantillons *Spitzer* Infrared Nearby Galaxy Sample (SINGS) et *Spitzer*-SDSS-*GALEX* Spectroscopic Survey (SSGSS) révèle que les couleurs des galaxies en infrarouge moyen et lointain sont fortement corrélées avec le taux de formation d'étoiles spécifique, aussi bien que avec d'autres quantités galactiques reliées a ce parametre, comme par example le rapport entre la luminosité infrarouge des régions de formation d'étoiles et celle du milieu interstellaire environment, les contributions par des PAHs et grains de poussière en équilibre thérmique pour l'émission infrarouge totale, et le rapport entre la masse de poussière et la masse d'étoiles. Ces corrélations fournissent des informations importantes sur le lien entre la formation d'étoiles et les propriétes du millieu interstellaire dans les galaxies.

On étudie d'avantage le rapport entre l'activité de formation d'étoiles et le contenu en poussières des galaxies. Pour cela, on rassemble un grand échantillon de 3321 galaxies avec des observations disponibles en ultraviolet (*GALEX*), optique (SDSS) et infrarouge (*IRAS*). On trouve que le taux de formation d'étoiles corrèle remarquablement bien avec la masse de poussière des galaxies sur quatre ordres de grandeur en les deux quantités. Cela nous permet de fournir une recette empirique simple pour évaluer la masse totale de poussière des galaxies à partir du taux de formation d'étoiles. On compare nos résultats avec les prédictions de modèles recents de l'évolution chimique des galaxies. On compare aussi les corrélations entre le taux de formation d'étoiles spécifique, le rapport entre la luminosité de poussière et la masse d'étoiles, et le rapport entre la luminosité de poussière et le taux de formation d'étoiles obtenus dans notre analyse avec ceux qui sont prévus par des modernes simulations cosmologiques de formation des galaxies.

Le modèle présenté dans cette thèse peut être appliqué simplement pour interpreter les distributions spectrales d'énergie de n'importe quel échantillon de galaxies.

Contents

List of Figures

List of Tables

Chapter 1

Introduction

One of the greatest scientific breakthroughs of the last century was the discovery by Edwin Hubble, in 1925, that the Milky Way is not the only galaxy in the Universe. Until then, it was believed that the Universe did not extend beyond our own Galaxy, and observed external galaxies were thought to be diffuse ‘nebulae’ within the Galaxy. Hubble (1925) measured the distance to these ‘nebulae’ and realised that some of the observed nebulae were in fact too distant to be part of the Milky Way. Moreover, based on their distance and angular size on the sky, he concluded that these objects had similar sizes to our Galaxy and therefore they could be stellar systems of the same kind as the Milky Way, i.e. galaxies. This discovery marked the start of the fascinating field of Extragalactic Astronomy.

1.1 Galaxy basics

To set the framework of this thesis, we first briefly summarize some essential facts about galaxies.

The morphology of galaxies. Galaxies exhibit a wide variety of shapes. Hubble compiled observations of galaxies and elaborated a morphological classification scheme, the *Hubble sequence* (Hubble 1926), which is still widely used in modern Astrophysics (see also the revised Hubble sequence by de Vaucouleurs 1974). In this scheme, galaxies are classified as ‘ellipticals’ (E), ‘lenticulars’ (S0),‘spirals’ (S), ‘barred spirals’ (SB) and irregulars (Irr).

Fig. 1.1 summarizes this classification. Elliptical galaxies, as the name indicates, appear as ellipses, and show smooth light distributions. They are classified as En, where n is a measure of the ellipticity which varies between 0 (nearly circular) and 7 (very elongated). This quantity is computed from the observed major axis a and minor axis b as $n = 10 \times (a - b)/a$. Elliptical galaxies represent only about 20 per cent of the total number of galaxies in the local Universe, but they represent 50 per cent of the total mass. Spiral galaxies are the most numerous type in the local Universe. They present a flat disc with spiral arms and a central spherical bulge. These galaxies are divided in two types: normal spirals and barred spirals, depending on the existence of a central bar. In each of these types, galaxies are classified from ‘early-types’ (Sa and SBa) to ‘late-types’ (Sc and SBc). From early- to late-types, the relative size of the bulge relative to the disc decreases, the spirals arms become more separated, and the amount of gas and dust in the interstellar medium (ISM), as well as the number of young blue stars increases. Lenticular

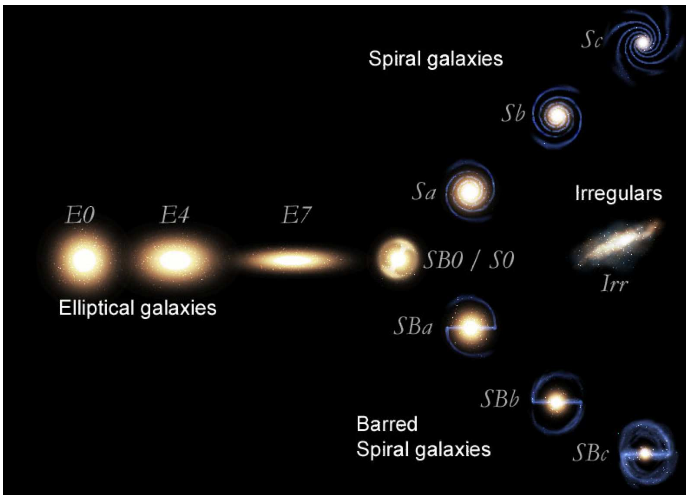

Figure 1.1: The 'tuning fork' diagram describing the morphological galaxy classification scheme by Hubble. *Figure credits:* Fahad Suleria, www.novacelestia.com (Astronomical illustrations and space art).

galaxies are an intermediate type between ellipticals and spirals. They present an important bulge, but also a disc component. The disc of a lenticular galaxy is very different from that of a spiral galaxy, with typically very little gas and almost no star formation occurring. Finally, irregular galaxies are galaxies with no regular structure, i.e. they do not exhibit a clear spherical or disc component.

An interesting property of the Hubble sequence is that galaxies are found to form not only a morphological sequence, but also a sequence in physical properties such as the integrated colour and the amount of gas in the interstellar medium (see Roberts & Haynes 1994 for a review). We will see in Section 1.3.3 that the properties of galaxies along the Hubble sequence can be explained by different histories of star formation (see also Sandage 1986; Kennicutt 1998a). However, current models of galaxy formation cannot yet fully explain how the galaxies we see today have formed and evolved.

The expanding Universe. After having established that galaxies are extragalactic objects, Hubble made an observation that revolutionised Cosmology. He observed that the light emitted by distant galaxies was shifted towards longer wavelengths, and that this 'redshift' was proportional to the distance to the galaxies. Based on the Doppler effect[1], he concluded that galaxies are moving away from the Milky Way, and that their recession velocities increase with distance (Hubble 1929; Hubble

---

[1] The Doppler effect, or Doppler shift, is the change in frequency and wavelength of a wave for an observer moving relative to the source of the wave. The received frequency is higher than the emitted frequency when the source approaches the observer and is lower than the emitted frequency when the source is moving away from the observer.

& Humason 1931). This has become known as the *Hubble law*, which can be written

$$cz = H_0\, d\,, \tag{1.1}$$

where cz is the recession velocity of the galaxy (c designates the speed of light and z the cosmological 'redshift'), H_0 is the 'Hubble constant' and d is the distance to the galaxy. The Hubble constant is a fundamental cosmological parameter. The best modern estimates place the value of this parameter between 70 and 75 km s^{-1} Mpc^{-1}. The observed cosmological redshift z quantifies the amount by which the radiation emitted by a galaxy is shifted towards longer wavelengths:

$$z = \frac{\lambda_{\rm obs} - \lambda_{\rm em}}{\lambda_{\rm em}}\,. \tag{1.2}$$

The observed cosmological redshift is a widely used tool in Extragalactic Astronomy, as it provides a way of determining distances to galaxies.

An important cosmological consequence of Hubble's law is that the Universe is expanding. Aleksander Friedmann had demonstrated that an expanding universe was one possible solution of Einstein's equations in the framework of General Relativity. However, until Hubble's discovery, cosmologists preferred the solution of a static Universe. Georges Lemaitre, based on Friedmann's equations and on Hubble's observations, has set the basis of modern cosmology theories of the 'Big Bang'. These theories aim at explaining the evolution of the Universe as it expands from a hot and dense initial state.

Galaxy formation and evolution. One of the most important challenges of modern Astrophysics is to explain the formation and evolution of galaxies in the framework of current cosmological theories.

Observations of the cosmic microwave background radiation and of the large scale distribution of galaxies show that the Universe is homogeneous and isotropic on large scales. However, detailed studies of the cosmic microwave background radiation using observations from the *Cosmic Background Explorer* (COBE; Smoot et al. 1992) have shown that very small density fluctuations existed in the early universe. Theories of structure growth explain that the structures we observe in the present-day Universe, such as galaxies and clusters of galaxies, have evolved from these primordial density fluctuations. In the current picture, as the Universe expanded and cooled down, over-dense clumps of matter condensed and grew by attracting gravitationally more dark matter and baryonic matter. These structures formed the first galaxies.

While modern cosmological simulations can successfully explain the gravitational evolution of dark matter in the Universe and reproduce the large-scale distribution of dark matter, the detailed evolution of baryonic matter is still unclear. Much remains to be explained on how galaxies have formed stars and metals inside dark matter haloes throughout the history if the Universe. To investigate this, the physical processes governing the evolution of baryonic matter in galaxies (i.e. stars,

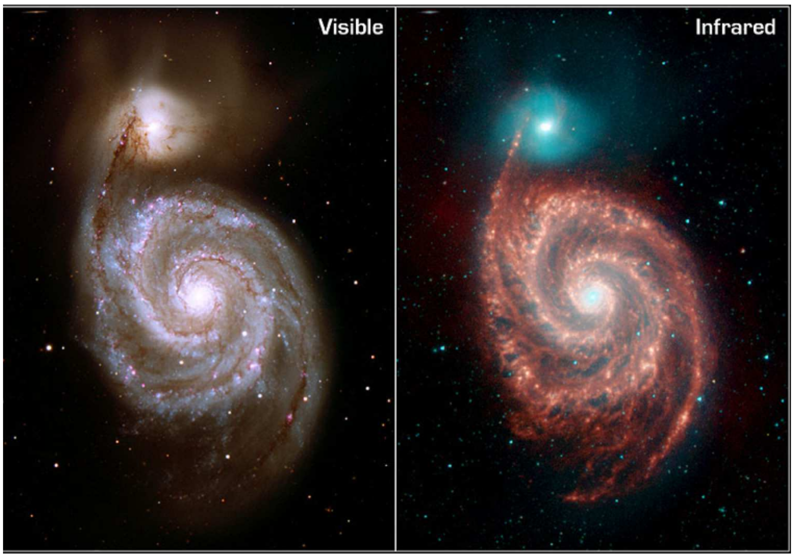

Figure 1.2: The nearby spiral galaxy M 51 imaged at optical (left) and infrared wavelengths (right). *Image credits:* Visible image: Digitized Sky Survey; Infrared image: NASA/JPL-Caltech/R. Kennicutt (University of Arizona).

gas and dust) need to be understood in detail. This requires observations of large samples of galaxies at different evolutionary stages of the Universe (i.e. different redshifts). In addition, to relate these observations to theories of galaxy formation, we need models to interpret the light emitted by galaxies in terms of physical parameters such as star formation rate, metallicity and dust content.

1.2 The spectral energy distributions of galaxies

Galaxies emit radiation across the full electromagnetic spectrum. Most of the energy is emitted in the ultraviolet, optical and infrared spectral ranges. This emission originates primarily from stellar radiation, either direct or reprocessed by gas and dust in the ISM. Observations at different wavelengths probe these different components in different ways. As an example, in Fig. 1.2, we compare the optical image of a well-known nearby spiral galaxy, M 51, with an image taken at infrared wavelengths. The optical image (on the left) reveals the direct radiation from stars. This image also evidences large dusty clouds in the galaxy spiral arms, which absorb the light radiated by stars. These dust clouds shine in the infrared image (right-hand side of Fig. 1.2), because they reradiate ultraviolet and optical light absorbed from stars at these longer wavelengths. Hence, the relative distribution of spectral energy at ultraviolet, optical and infrared wavelengths contains valuable information about the production of starlight in a galaxy and its absorption by dust. In Fig. 1.3, we show an example of spectral energy distribution of a galaxy forming stars at a rate of 1 $M_\odot/yr^{-1}$. The shape of the spectral energy distribution depends on both the radiation emitted by the stellar population of the galaxy and the interaction of this

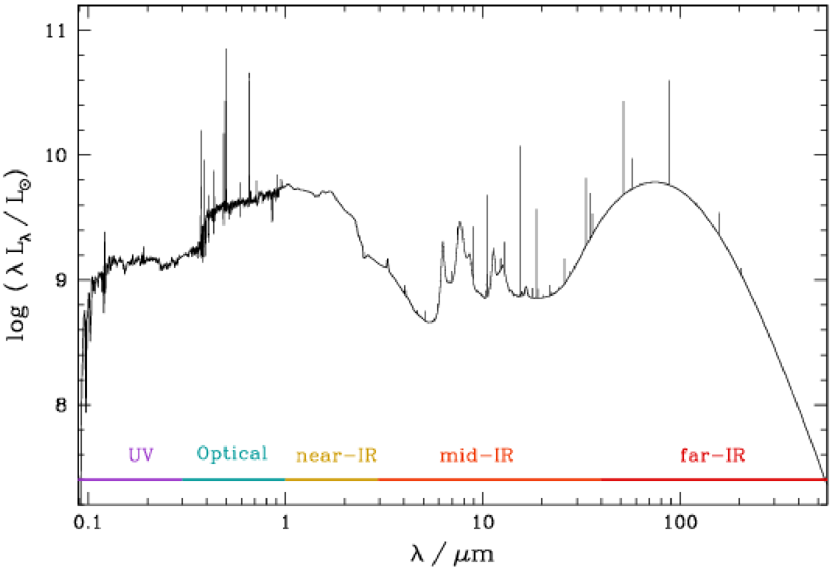

Figure 1.3: Example of the ultraviolet-to-infrared spectral energy distribution of a typical galaxy forming stars at a rate of 1 $M_\odot$ yr^{-1}. The continuum emission was computed using the models described in Chapter 2 of this thesis. The nebular emission lines were computed consistently using the prescription of Charlot & Longhetti (2001).

radiation with the gas and dust in the ISM of the galaxy.

In the past, when only ground-based telescopes were available, observations of galaxies were limited to optical and near-infrared wavelengths. Only in the past few decades have ultraviolet and infrared observations become available thanks to improvements of observational technology and the launch of stratospheric and space telescopes. These observatories have brought new insights into the physical processes occurring in galaxies. Nowadays, observations at ultraviolet, optical and infrared wavelengths are becoming available for large samples of galaxies. These include:

- ultraviolet observations from space by the *Galaxy Evolution Explorer* (*GALEX*, Martin et al. 2005);
- optical ground-based observations by the Two-degree Field Galaxy Redshift Survey (Colless et al. 2001) and the Sloan Digital Sky Survey (SDSS, Stoughton et al. 2002);
- near-infrared ground-based observations by the Two Micron All Sky Survey (2MASS, Skrutskie et al. 1997);
- space-based observations in the mid- and far-infrared by the *Infrared Astronomical Satellite* (*IRAS*, Beichman et al. 1988), the *Infrared Space Observa-*

tory (*ISO*, Kessler et al. 1996) and the *Spitzer Space Telescope* (Werner et al. 2004);

Extracting constraints on the stellar populations and ISM of galaxies from these multi-wavelength observations requires the consistent modelling of the emission by stars, gas and dust.

A standard approach to model consistently the emission from stars and dust in galaxies has been to solve the radiative transfer equation for idealised (bulge + disc) spatial distributions of stars and dust (e.g. Rowan-Robinson 1980; Efstathiou & Rowan-Robinson 1990; Gordon et al. 2001; Misselt et al. 2001; Popescu et al. 2000; Misiriotis et al. 2001). More sophisticated models couple the radiative transfer through a dusty ISM and the spectral evolution of stellar populations (Silva et al. 1998; Dopita et al. 2005). This type of model is useful in interpreting in detail the emission from individual galaxies in terms of constraints on stellar populations and the spatial distribution and physical properties of the dust. However, because of the complexity of radiative transfer computations, these models are not optimised to derive statistical constraints from observations of large samples of galaxies.

A model optimised to constrain the physical properties of large samples of galaxies is a necessity in the era when deeper and wider surveys are gathering multi-wavelength observations of large numbers of galaxies at different redshifts. Example of such surveys are the *Great Observatories Origins Deep Survey* (GOODS; Dickinson & GOODS Legacy Team 2001), the *Cosmic Evolution Survey* (COSMOS; Scoville et al. 2007) and the *The All-Wavelength Extended Groth Strip International Survey* (AEGIS; Davis et al. 2007), and planned surveys including far-infrared observations with the future *Herschel Space Telescope* (e.g Latter, NHSC & HSC Teams 2007), such as the ATLAS wide-field survey (P.I. Stephen Eales) or the *The Herschel Multi-tiered Extragalactic Survey* (HerMES; P.I. Seb Oliver). To take full advantage of the richness of these data sets, we need to be able to make the link between the observations and the physical parameters of the galaxies. More specifically, we need a model to interpret consistently the multi-wavelength emission from galaxies in terms of physical parameters, such as star formation rate, stellar mass and dust content. This will enable us to exploit the new observational surveys to set the best constraints on galaxy formation and evolution scenarios.

Our primary goal in this thesis is to build such a model. We present a simple and versatile prescription to interpret the mid- and far-infrared spectral energy distributions of galaxies consistently with the emission at ultraviolet, optical and near-infrared wavelengths. This model is easily applicable to large samples of observed galaxies and allows us to derive statistical estimates of physical parameters such a star formation rate, stellar mass, dust content and dust properties from combined ultraviolet, optical and infrared galaxy spectra. We exemplify this by deriving median-likelihood estimations of the physical parameters of local samples. We find important correlations between galaxy properties which can provide insight into the relation between the star formation and dust content of galaxies.

In the remainder of this chapter, we briefly review the production of starlight in galaxies and its transfer in the interstellar medium. We provide the basic elements to interpret the spectra energy distributions of galaxies, from which we build the model presented in the next chapter.

1.3 The production of starlight in galaxies

In this section, we review the stellar emission of galaxies. This emission dominates the galactic spectral energy distributions at ultraviolet, optical and near-infrared wavelengths. The total stellar spectrum of a galaxy is a result of the contribution by all the individual stars it comprises. Therefore, to interpret observed galactic spectra, we need to understand the *stellar population* of a galaxy (composed of stars of different masses, chemical compositions and ages) and follow the evolution of the different stars with time.

1.3.1 Stellar populations in galaxies

The first classification of stellar populations in galaxies was made in the 1940's by Walter Baade when analysing photographs of unprecedented quality of Andromeda and other nearby galaxies. These observations allowed, for the first time, to resolve individual stars of external galaxies (Baade 1944). Baade distinguished two types of stars:

- Population I stars, which have solar-like metallicities and are distributed in the discs of galaxies, with low velocity dispersions; the brightest stars of this population are blue, young, hot and massive;

- Population II stars, which tend to be red, old and cool, have low metallicities and are distributed in the bulges and halos of galaxies, with high velocity dispersions.

Baade also noticed that Population I stars tend to populate the same region of the Hertzprung-Russel (H-R) diagram[2] as open clusters, whereas Population II stars occupy the same region as globular clusters in this diagram. Moreover, he remarked that early-type galaxies (ellipticals and lenticulars) are dominated by Population II stars, while in late-type galaxies (spiral and irregulars), the two populations of stars are found.

Since the pioneer work of Baade, the improvement in observational techniques has revealed that, in reality, stellar populations in galaxies are not optimally classified using discrete classes. Instead, stars in a galaxy present a continuous distribution of properties, which result from the history of star formation and chemical enrichment of the galaxy. Therefore, we can use the emission from the stellar populations to trace star formation history and the chemical evolution of galaxies.

---

[2] The Hertzprung-Russal diagram shows the relation between the bolometric luminosity and the effective temperature of stars.

We can perform studies of this type to interpret the emission from stellar populations of galaxy samples at different redshifts. The results of such studies provide constraints on galaxy formation and evolution scenarios. However, when studying distant galaxies, the individual stars cannot be resolved. Therefore, we need tools that allow us to extract the stellar population properties of distant galaxies from the integrated light we observe. In the next section, we describe such models in more detail.

1.3.2 Stellar population synthesis models

The first attempts to interpret integrated galaxy spectra in terms of the stellar content of galaxies reproduced the observed spectra using linear combinations of individual stellar spectra of various types (e.g. Spinrad & Taylor 1971; Faber 1972; O'Connell 1976; Turnrose 1976). This approach was soon abandoned because the number of free parameters was too large to be constrained by typical observed galaxy spectra. More recent, widely-used models are based on the evolutionary population synthesis technique (e.g. Tinsley 1978; Bruzual 1983; Arimoto & Yoshii 1987; Guiderdoni & Rocca-Volmerange 1987; Buzzoni 1989; Bruzual & Charlot 1993; Bressan, Chiosi & Fagotto 1994; Worthey 1994; Leitherer & Heckman 1995; Fioc & Rocca-Volmerange 1997; Maraston 1998; Vazdekis 1999; Bruzual & Charlot 2003). The main adjustable parameters in these 'stellar population synthesis models' are the initial mass function (IMF), the star formation rate (ψ) and, in some cases, the chemical enrichment rate.

Throughout this thesis, we use the evolutionary synthesis models by Bruzual & Charlot (Charlot & Bruzual 1991; Bruzual & Charlot 1993, 2003, Charlot & Bruzual, in preparation) to compute the spectral evolution of stellar populations in galaxies. These models are based on the *isochrone synthesis technique*, which builds on the property that stellar populations with any star formation history can be expanded in series of instantaneous bursts, named 'simple stellar populations' (SSPs). In this approach, the spectral energy distribution at time t of a stellar population characterized by a star formation rate $\psi(t)$ and a metal-enrichment law $\zeta(t)$ can be written as

$$L_\lambda(t) = \int_0^t dt'\, \psi(t-t')\, S_\lambda[t', \zeta(t-t')]\,, \tag{1.3}$$

where $S_\lambda[t', \zeta(t-t')]$ is the power radiated per unit wavelength per unit initial stellar mass by a SSP of age t' and metallicity $\zeta(t-t')$, assuming that the initial mass function (IMF) remains constant with time.

The emission from the simple stellar population $S_\lambda[t', \zeta(t-t')]$ is computed as the sum of the spectra of the stars defining its isochrone (which defines the position of stars of different masses in the H-R diagram at a time t'), at metallicity $\zeta(t-t')$ and at age t'.

1.3.2.1 Stellar evolution

It is worth giving a very brief summary of the main features of stellar evolution to appreciate the spectral analysis technique presented later in this thesis. The shape of the spectrum of a SSP, $S_\lambda[t', \zeta(t-t')]$, depends mainly on the total luminosity and effective temperature of the stars which compose the SSP at a given age. The higher the bolometric luminosity of a star, the more the emission of the star contributes to the total spectrum. Moreover, the effective temperature of a star determines the wavelength at which the star radiates most of the energy. Therefore, it is crucial to understand the evolution of stars in the H-R diagram to interpret the total emission from galaxies.

The evolution of a star depends mainly on its initial mass: this determines the rate at which the star has to produce energy in order to balance the gravitational force and remain in hydrostatic equilibrium. The higher the initial mass of star, the higher the energy production rate it requires to remain in equilibrium. Therefore, higher-mass stars have higher luminosities. These stars run out of fuel for the production of energy quicker than lower-mass stars. As a consequence, the lifetimes of high-mass stars are shorter than those of lower-mass stars. In Fig. 1.4, we show three examples of evolutionary tracks in the H-R diagram of stars with different initial masses: a low-mass star (1 $M_\odot$), an intermediate-mass star (5 $M_\odot$) and a high-mass star (25 $M_\odot$), from Iben (1991). We now summarize the main stages of the evolution of stars of different initial masses after the zero-age main sequence.[3]

Very low-mass stars ($\lesssim 0.25$ $M_\odot$). Stars with masses between 0.08 and 0.25 $M_\odot$ have a very slow evolution; they can reach lifetimes of more than 13 Gyr. These stars have convective interiors. Therefore, the core is continuously being recycled with hydrogen coming from the outer layers, and they can convert all the initial hydrogen in helium. When H is exhausted in the stars, they start contracting. Because of the low stellar mass, the gravitational energy released during the contraction is not enough to make the central temperature reach sufficiently high values to start He-burning reactions. With no other source of energy available, these stars cool down and become white dwarves.

Low-mass stars ($\lesssim 2$ $M_\odot$). A star with initial mass around 1 $M_\odot$ spends about 10 Gyr on the main sequence, radiating most of the energy at optical wavelengths. During this time, the temperature in the core increases gradually and the stars expands slightly.

When H in the nucleus runs out, the star starts burning H in a shell around the He core. The core contracts, heating up the surrounding H-burning layer. This causes an increase in the production of energy which heats up the outer envelope of the star and makes it expand. Consequently, the radius of the star increases, and

---

[3] The main sequence is, by definition, the period during which a star produces energy by burning hydrogen in the core. The zero-age main sequence marks the beginning of the main sequence phase: it is the time when H-burning reactions start in the core.

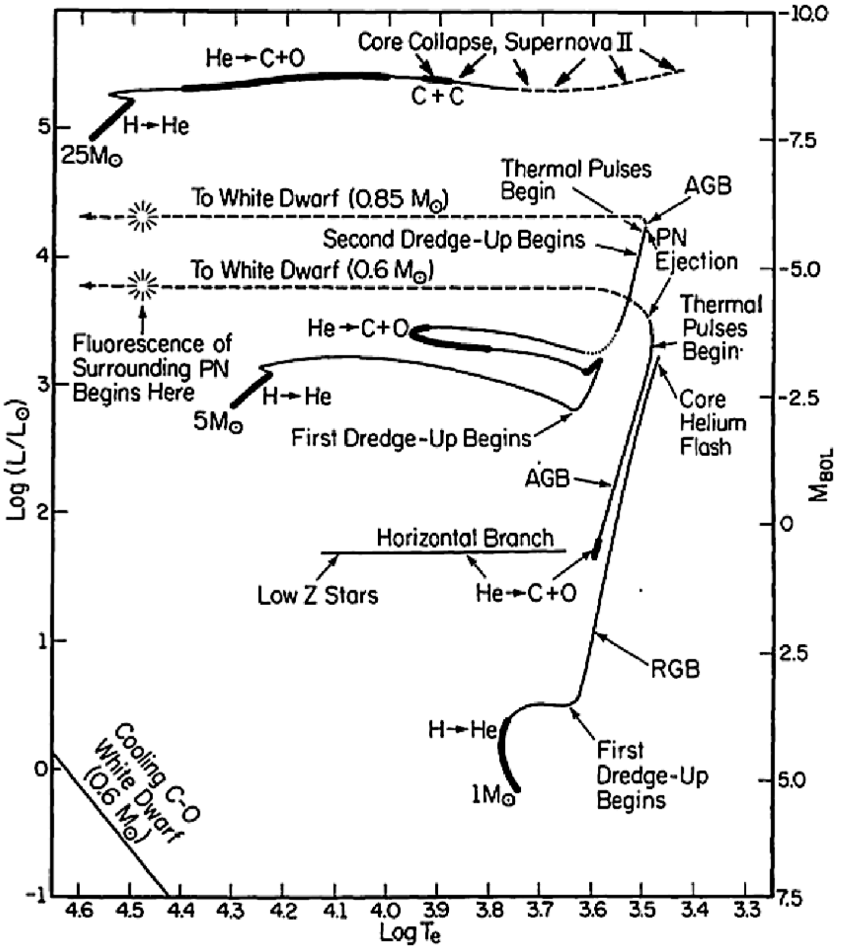

Figure 1.4: Evolutionary tracks in the Hertzprung-Russel diagram for three model stars with low (1 M$_\odot$), intermediate (5 M$_\odot$) and high (25 M$_\odot$) initial masses. The effective temperature T_e is given in K, and the bolometric luminosity, L, is in solar luminosity units. The tracks stars at the zero-age main sequence and end at remnant stage. The heavy portions of each curve define locations where major nuclear burning phases occur. Figure taken from Iben (1991).

the effective temperature decreases, shifting the peak of the stellar emission towards longer wavelengths. The temperature drop increases the opacity, and convection starts to provide an effective transport of energy from the stellar interior (first dredge-up). At this point, the star cannot expand any further, and therefore the luminosity starts increasing – the star moves up the ‘red giant branch’ (RGB). RGB stars have high luminosities and they radiate mainly at near-infrared wavelengths due to their cool temperatures. We will see in Section 1.3.2.3 that these stars dominate the spectral energy distributions of SSPs at old ages.

During the red giant phase, the He core keeps contracting and increasing in mass due to infall of He being produced in the circumnuclear shell. The core is so dense that the electrons become a degenerate gas; the pressure of degenerate gas depends only on the density (not the temperature) and counterbalances the gravitational force. As the core contracts, the temperature rises, reaching eventually the minimum temperature to start burning He (i.e. about 10^8 K). Once He starts burning in a part of the core, the resulting heat propagates quickly by conduction through the whole core. The increase in temperature does not make the core expand, since the core is made of degenerate gas; instead, the rate of He-burning reactions increases, producing an 'helium flash'. These quick reactions increase the core temperature until the gas becomes non-degenerate, allowing for the core to expand and cool down. After the helium flash, the outer layers of the star contract, causing the radius and luminosity to decrease, and the effective temperature to increase gradually. The star moves downward and to the left in the H-R diagram (Fig. 1.4). At this stage, the star burns He steadily in the core and H in a shell surrounding the core.

When He is exhausted in the core, the fusion continues in a shell around a core of carbon and oxygen which has contracted and increased in density until the gas has become degenerate. The star moves up the 'asymptotic giant branch' (AGB) in the H-R diagram, which is parallel to the RGB, but with even faster energy generation (therefore this phase lasts for a shorter time). Although the AGB phase is relatively short, it is crucial to understand this stage of stellar evolution in order to interpret the spectral energy distributions of star-forming galaxies, since AGB stars contribute significantly to the near-infrared emission of galaxies.

The 'thermally-pulsating AGB' (TP-AGB) phase begins when the He shell around the core runs out of fuel. When that happens, the main energy source of the star becomes the H-burning shell around it. The He-burning reactions are very sensitive to changes in temperature, and therefore the He shell switches on periodically in violent pulses in which huge amounts of energy are generated, alternated with more quiet phases of energy production in the H-burning shell. During this phase, the star pulsates and the luminosity varies. In each pulse, huge amounts of energy are produced and transported outward through convection. Strong stellar winds triggered by the pulsations expel gas rich in heavy elements from the star, causing an enrichment of the ISM. The gas in the outer layers of the star forms an expanding shell which cools down as it moves away from the star, allowing for dust particles and molecules to form. The strong stellar winds eventually provide enough kinetic energy for the outer layers to be ejected, forming a planetary nebula. At the center of this nebula remains the core of the star which, for a star of 1 $M_\odot$ initial mass, never reaches high enough temperature to start burning carbon, and cools down to become a white dwarf. The nebula keeps expanding until it dissipates in the interstellar medium.

Intermediate-mass stars ($\sim 2-7\ M_\odot$). A star with initial mass around 5 $M_\odot$ needs to produce more energy than a solar-mass star while on the main sequence to remain in hydrostatic equilibrium. Therefore, it burns H in the center at a faster rate and the effective temperature and luminosity are higher. The H in the core is rapidly exhausted, and the star leaves the main sequence at a much younger age than a solar-mass star.

When the star leaves the main sequence, the core contracts and H-burning reactions start in a shell around the He core, which supports the weight of the material above it for some time. When this equilibrium ends, the core contracts more rapidly and its temperature increases, causing the energy production in the H-burning shell to increase and the outer layers of the star to expand. The surface temperature decreases, and the star moves to the right in the H-R diagram (Fig. 1.4). Then, convection starts being effective in transporting energy from the deepest layers (first dredge-up), and the luminosity of the star increases, making the star ascend the RGB. During this phase, the central temperature of the star continues to rise due to the core contraction, until the ignition of He-burning reactions in the non-degenerate core.

When He is exhausted in the center, the carbon core contracts, and He keeps burning in a shell around the core (which is also surrounded by the H-burning shell). The core contracts and heats, the outer layers expand and the effective temperature decreases, until the star reaches the AGB stage. We will see in Section 1.3.2.3 that these luminous AGB stars dominate the near-infrared light of a SSP at intermediate ages (i.e. around 100 Myr). As in the case of solar-mass stars, thermal pulses cause strong stellar winds and the star loses a large part of its mass. During this time, the carbon core keeps contracting and heating until the gas becomes degenerate. If the temperature reaches high enough values to ignite carbon, the star will undergo a 'carbon flash', leading to a supernova explosion. If the temperature of the degenerate core is too low, the star loses its outer layers as a planetary nebula and the core cools down as a white dwarf. The initial mass and chemical composition of the star, and the total mass lost during its evolution, determine which of the two scenarios occurs. In either case, the star returns material to the interstellar medium at the end of its life.

High-mass stars ($\gtrsim 7$ M$_\odot$). The evolution of the most massive stars is extremely rapid. These very hot stars radiate huge amounts of energy during their short lifetimes of typically a few Myr. The ultraviolet radiation originating from these stars has important effects on the spectra of galaxies. The radiation from massive stars dominates the emission of a SSP at young ages (Section 1.3.2.3) and ionizes the gas in the surrounding ISM (Section 1.4). High-mass stars lose a large part of their initial mass due to strong stellar winds during the main sequence evolution. Such important mass losses make the evolution of these stars very complex to model.

In a star of initial mass around 25 M$_\odot$, after central H is consumed, the core starts contracting and the outer envelope expands – the star becomes a 'red supergiant'. The central temperature rapidly reaches high enough values to start burning He in a non-degenerate core surrounded by a H-burning shell. At this stage, the effective temperature of the star increases and the star becomes a 'blue supergiant'.

After all the central He has been converted into C, the core contracts again until it reaches high enough central temperatures to start burning carbon: the star becomes a red supergiant again. Because of its high mass, the star can reach high enough temperatures for the C-burning reactions to begin before the core becomes degenerate. When the central C gets exhausted, the core contracts again and the next reactions, burning O, Mg and Ne all the way to Fe, occur very quickly until the star consists of a compact core of iron with surrounding shells burning successively lighter elements. The nucleus of the Fe atom has a much higher binding energy than lighter elements, and the star cannot produce energy through its fusion (in fact, the Fe fusion reactions require an input of energy). Therefore, the star is incapable of continuing to produce energy in the core, and the core collapses gravitationally to extremely high density and explodes violently as a supernova. The outer layers of the star are returned to the interstellar medium, and the core remains as a neutron star.

1.3.2.2 The stellar initial mass function

As we have seen in the previous section, the initial mass of a star determines the way it produces and radiates energy. This has a crucial impact on the study of the integrated emission from galaxies. Stars of different initial masses dominate the energy output at different wavelengths and at different ages. When adding up the spectra of all stars of a SSP, it is important to get the right proportions of stars of different masses. Therefore, the initial mass function is a fundamental ingredient in stellar population synthesis models.

The initial mass function has been investigated by many since the Salpeter's (Salpeter 1955) pioneering study (e.g. Scalo 1986; Kroupa 2001; Chabrier 2003). Such studies aim at determining the proportions of stars of different masses in nearby environments, such as stellar clusters and the solar neighbourhood, to get the present-day mass function of stars, and then correcting for the number of stars that have already evolved out of the main sequence for a given formation time. However, the accurate determination of the IMF is complex due to factors such as the evolution of stars, the mixing of different stellar populations (with different ages) and the conversion from observed stellar luminosities to stellar masses.

In all applications in this thesis, we assume the Chabrier (2003) single-star IMF of the Galactic disc, described by:

$$\phi[\log(m)] \propto \begin{cases} \exp\left[-\frac{(\log m - \log m_c)^2}{2\sigma^2}\right], & \text{for } m \leq 1 \text{ M}_\odot, \\ m^{-1.3}, & \text{for } m > 1 \text{ M}_\odot, \end{cases} \tag{1.4}$$

with $m_c = 0.08$ M$_\odot$ and adopt lower and upper mass cut-offs 0.1 M$_\odot$ and 100 M$_\odot$, respectively. This IMF is physically motivated and fits well the counts of low-mass stars and brown dwarfs in the Galactic disc, providing more accurate mass-to-light ratio determinations (Chabrier 2003).

In Figure 1.5, for reference, we compare the Chabrier (2003) IMF with the

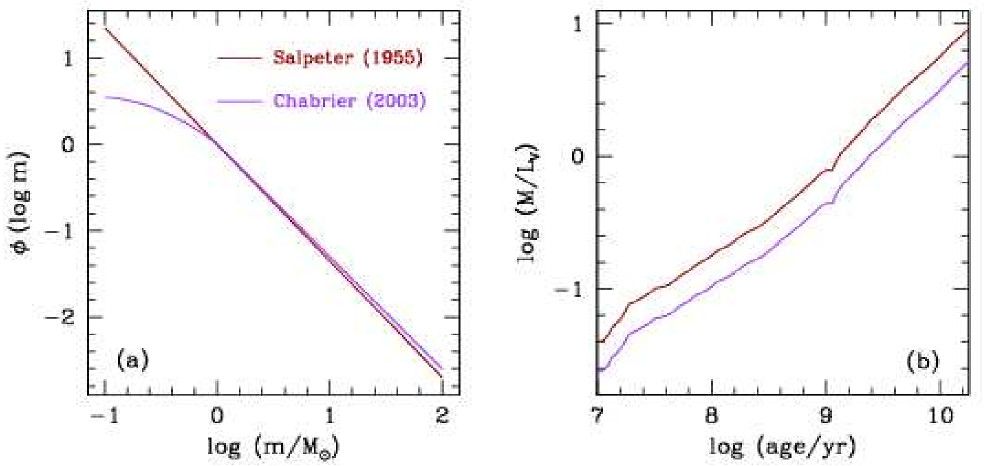

Figure 1.5: Comparison between the Salpeter 1955 (in red) and Chabrier 2003 (in purple) initial mass functions. (a) Comparison between the two IMFs (both are normalised to $\phi[\log(m = 1\ \mathrm{M}_\odot)] = 0$; (b) Comparison between the mass-to-light ratios (i.e. total stellar mass divided by the total V-band luminosity) given by the two IMFs.

Salpeter (1955) IMF, which is described by $\phi[\log(m)] \propto m^{-1.35}$. In panel (a), it is clear that the Salpeter IMF produces a higher number of low-mass stars than the Chabrier IMF. This causes the systematically higher mass-to-light ratio for the Salpeter IMF, plotted in panel (b), since the bulk of stellar mass in galaxies is contributed by low-mass stars. In fact, the Salpter IMF produces stellar masses of model galaxies which are about 1.6 times higher than the Chabrier IMF.

1.3.2.3 Spectral evolution of a simple stellar population

We now describe the spectral evolution of a simple stellar population. This corresponds to computing the term $S_\lambda[t', \zeta(t-t')]$ in equation (2.1). The basics ingredients necessary to compute the spectral evolution of a SSP are:

- evolutionary tracks of stars of different initial masses and chemical compositions in the H-R diagram, provided by stellar evolution theory – these tracks allow us to compute isochrones, which define the positions of stars of different masses and metallicities in the H-R diagram at a given time;
- the initial mass function, which determines the proportions of stars of different masses in the SSP;
- libraries of stellar spectra, used to assign an ultraviolet-to-infrared spectrum to stars along the isochrone.

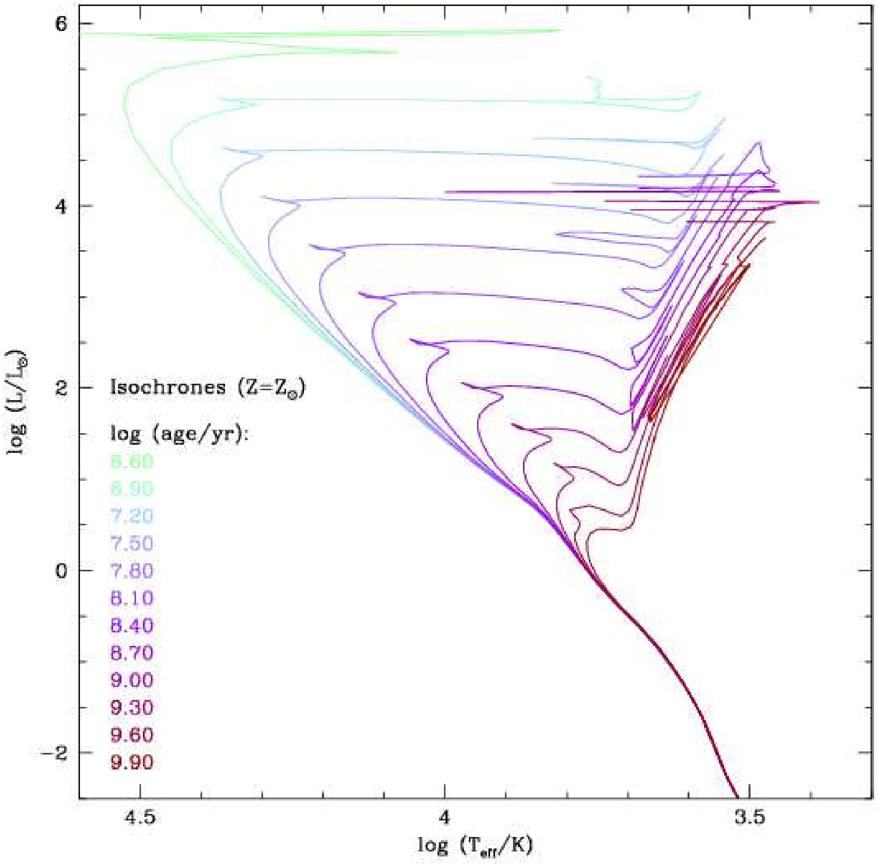

Figure 1.6: Example of isochrones with solar metallicity computed using the latest version of the 'Padova 1994' stellar evolution prescription (Marigo et al. 2008). The isochrones show the location on the H-R diagram of the stars of a SSP at a given age. Here we plot 12 ages from 4×10^6 (green) to 8×10^9 yr (red). At the youngest age, most of the stars are in the main sequence, except the very massive ones; as the age of the SSP increases (towards red isochrones), less massive stars evolve out of the main sequence. The effective temperature of a star determines at which wavelengths it radiates most of its emission. The higher the bolometric luminosity of a star, the more it contributes to the integrated stellar spectral energy distribution of the galaxy.

To model the stellar emission from galaxies, we must include the evolution of the full range of possible initial stellar masses. In stellar population synthesis models, a detailed stellar evolution prescription defines how stars of different masses and chemical compositions evolve. In practice, this is done by providing stellar evolutionary tracks which describe the evolution of stars of different masses in the H-R diagram.

In all applications of the Bruzual & Charlot (2003) models in this thesis, we use the 'Padova 1994' stellar evolutionary tracks computed by Alongi et al. (1993), Bressan et al. (1993), Fagotto et al. (1994a) and Fagotto et al. (1994b). These tracks provide the evolution from the zero-age main sequence to the beginning of the thermally-pulsating regime of asymptotic giant branch (TP-AGB) for low- and intermediate-mass stars and core-carbon ignition for massive stars, for a wide range of initial metallicities and stellar masses (see more details in Bruzual & Charlot 2003). The most recent version of the code also incorporates a new prescription by Marigo & Girardi (2007) for the TP-AGB evolution of low- and intermediate-mass stars (Marigo et al. 2008). These tracks are complemented with additional stellar evolution prescriptions to account for the post-AGB evolution until the remnant stage (Vassiliadis & Wood 1994, more detail in Bruzual & Charlot 2003). In Fig. 1.6, we plot examples of isochrones (for solar metallicity) computed using the latest version of the 'Padova 1994' stellar evolution prescription (Marigo et al. 2008).

The different evolutionary stages along the isochrone are populated by stars of different initial masses in proportions given by the IMF weight $\phi(m)$, defined such that $\phi(m)dm$ is the number of stars born with masses between m and $m + dm$ (see Section 1.3.2.2). Following this, each star in the isochrone is assigned a spectrum from a library of stellar spectra. This spectrum corresponds to the specific characteristics and evolutionary stage of that particular star. The spectral libraries used to perform this can consist of observed spectra, theoretical spectra computed from stellar atmosphere models, or a mix of both. Ideally, spectral libraries must cover the whole the spectral energy distributions of stars for all masses and at all evolutionary stages, but this is not trivial because of both observational and modelling limitations (Gustafsson, Heiter & Edvardsson 2007; Martins & Coelho 2007; Coelho 2008). We use one of the stellar libraries available with the Bruzual & Charlot (2003) code which uses the empirical library 'STELIB' (Le Borgne et al. 2003) in the optical range, extended to the ultraviolet and infrared using the 'BaSeL 3.1' theoretical library (Westera et al. 2002). Finally, the spectral energy distribution of the SSP S_λ at age t' is obtained by simply summing the spectra of individual stars along the isochrone.

In Figure 1.7, we plot the spectral energy distribution of a SSP of solar metallicity at several ages between 1 Myr and 13 Gyr. The spectral evolution shown in this figure can be interpreted as the evolution of the stellar content of the SSP with time. The young, massive stars, radiating predominantly at ultraviolet wavelengths, dominate the luminosity of the SSP at young ages (i.e. between 10^6 and 10^7 yr). The most massive stars evolve very rapidly and, at around 10^7 yr, they leave the main sequence and become red supergiants, causing a drop in the ultraviolet light and an increase in the near-infrared light. The ultraviolet light continues to decrease until 10^9 yr as massive stars gradually leave the main sequence, while the near-infrared continues to be high during this time due to the presence of AGB stars. After 1 Gyr, RGB stars account for most of the near-infrared luminosity, and the accumulation of low-mass, post-AGB stars causes the far-ultraviolet emission to rise again until 13 Gyr.

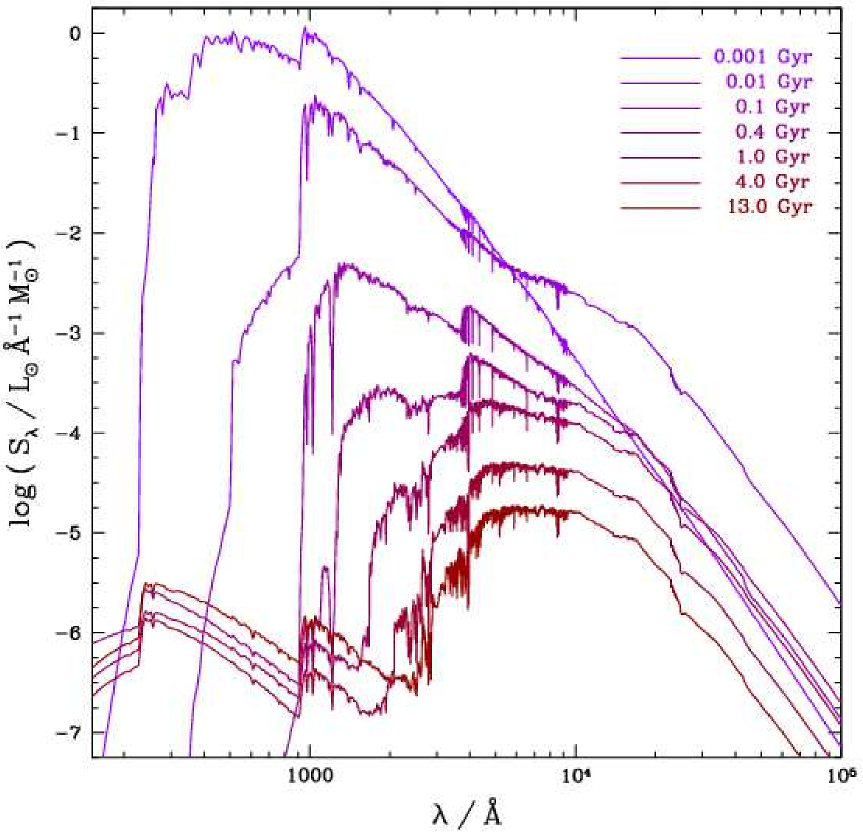

Figure 1.7: Spectral evolution of a simple stellar population with solar metallicity and with the distribution of stellar masses following a Chabrier (2003) IMF, computed using the latest version of Bruzual & Charlot (2003) models, with ages indicated on the top right corner. Figure adapted from Bruzual & Charlot (2003).

1.3.3 The star formation history

The star formation history describes the rate at which the galaxy forms stars as a function of time. This can be regarded as the term $\psi(t-t')$ in equation (2.1). The star formation history of a galaxy determines the age distribution of the stars contributing to the total spectrum.

The evolution of the star formation rate with time in galaxies depends mainly on the amount of gas available in the ISM to form new stars. In the local universe, it is observed that the present-day star formation rate of elliptical galaxies is low and that in late-type spirals the star formation rate high. This is mainly due to the fact that there is much more gas available to form new stars in the ISM of late-type galaxies than in the ISM of early-type galaxies. This change in star formation rate along the Hubble sequence is of great interest for galaxy evolution studies.

Several studies suggest that the observed Hubble sequence is mainly driven by a

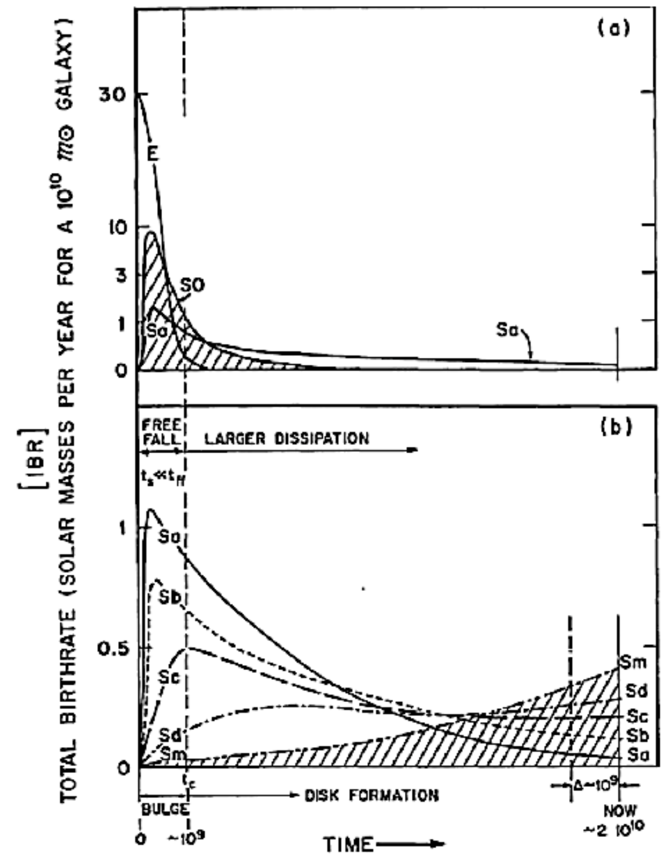

Figure 1.8: Schematic representation of the evolution of star formation rate (*integrated birth rate*) of galaxies according to Hubble type: (a) from ellipticals, E, to early-type spirals, Sa; (b) from early-type spirals, Sa, to late-type irregulars, Sm. The ratio between the dissipative collapse timescale t_c and the time to complete star formation determines if a disk forms – this markes the separation between elliptical and disk galaxies; for disk galaxies, the higher this ratio is, the higher becomes the bulge-to-disk ratio – this explains the different Hubble types of disk galaxies. Figure from Sandage (1986).

sequence in timescale of star formation in galaxies (Sandage 1986; Kennicutt 1998a, and references therein). Based on previous studies from Gallagher, Hunter & Tutukov (1984), Sandage (1986) proposed that the different properties observed in galaxies of different Hubble types (such as bulge-to-disc ratio, disc surface brightness, integrated colour, mean disk age, and present star formation rate per unit stellar mass, i.e, specific star formation rate) can be simply explained by different time variations of the star formation rate. In Fig. 1.8, we plot the schematic representation of the star formation histories of galaxies of different Hubble types proposed by Sandage (1986). The ratio between the dissipative collapse timescale t_c and the time to complete star formation determines if a disk forms. This ratio markes the separation between elliptical and disk galaxies. For disk galaxies, the higher this ratio is, the higher becomes the bulge-to-disk ratio of the galaxy; this explaines the different Hubble types of disk galaxies from early-type, Sa, to late-type, Sm.

In this framework, the star formation rate of galaxies can be described with exponentially declining functions of the form $\psi(t-t') \propto \exp(-\gamma t)$, where γ is the inverse of the star formation timescale. In elliptical galaxies, the timescale of star formation is very short, corresponding to high values of γ. This is equivalent to a single burst at the time of their formation that consumes all the gas available in the beginning. Late-type spirals have a longer timescale of star formation (i.e. γ value close to zero), as such the star formation is practically constant with time. However, this parametrization of the star formation rate is not enough to reproduce the integrated colours of all types of galaxies. For example, these purely exponential star formation histories fail to reproduce the emission from irregular galaxies with very blue colours. To account for the full range of observed galaxy properties, we need to include random bursts of star formation superimposed to the exponential star formation history law. This is because, in the bluest galaxies, star formation has a stochastic nature which can be induced by interactions. This simple way of describing galactic star formation histories, even though it does not explicitly include the physics of galaxy formation and gas consumption in galaxies, provides a robust way of reproducing the observed spectral energy distributions of different types of galaxies.

In Fig. 1.9, we plot four examples of the typical star formation histories of galaxies along the Hubble sequence, corresponding to an elliptical galaxy, an early-type spiral, a late-type spiral, and an irregular starburst galaxy, following Sandage (1986). For each galaxy, we plot the evolution of the star formation rate with time in the left panel and the Bruzual & Charlot (2003) spectral energy distribution L_λ at an age of 10 Gyr, computed using equation (2.1), in the right panel. We assume solar metallicity and a Chabrier (2003) IMF in all cases. The star formation history of the elliptical galaxy corresponds to a star formation timescale of 0.5 Gyr (i.e. $\gamma = 2$ Gyr^{-1}); for the early-type spiral, $\gamma = 0.25$ Gyr^{-1}, and for the late-type spiral, $\gamma \approx 0$, i.e. the star formation rate is nearly constant with time. For the irregular galaxy, we superimpose two bursts of star formation (one at about 4.5 Gyr, and the other just before 10 Gyr) to the previous constant star formation rate.

Since the spectral energy distributions plotted in Fig. 1.9 correspond to model galaxies with the same metallicity, IMF and age, the differences between these spectra are caused only by the different star formation histories. In elliptical galaxies, practically all the stars are formed in a single, initial burst of star formation. Therefore, after 10 Gyr, the stellar emission from elliptical galaxies is very similar to the emission by an old simple stellar population (see, for example, the emission by the SSP plotted in Fig. 1.7 at 4 and 13 Gyr). In spiral galaxies, the star formation also decreases with time because the amount of gas available to form new stars also decreases with time. However, the timescale of star formation is longer than in elliptical galaxies, and stars are continuously formed in the discs. Therefore the spectral

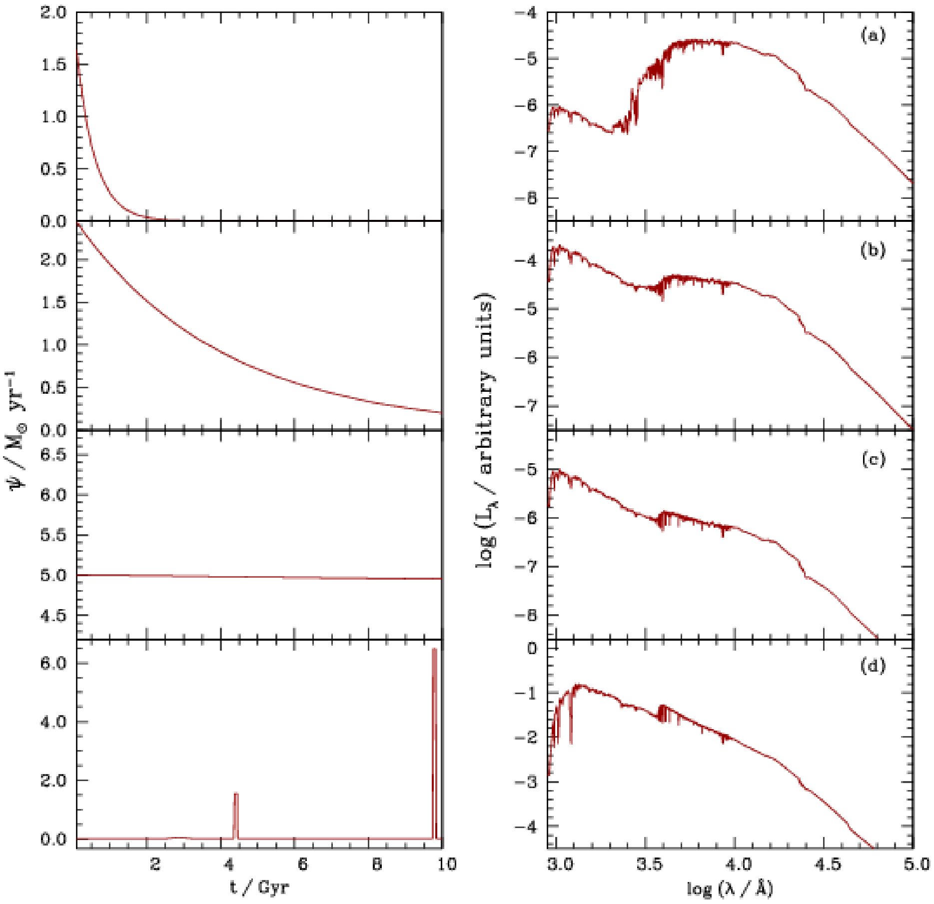

Figure 1.9: *Left-hand panels:* Schematic representation of the star formation histories of (a) an elliptical galaxy, (b) an early-type spiral, (c) a late-type spiral, and (d) an irregular galaxy, following Sandage (1986). *Right-hand panels:* Bruzual & Charlot (2003) spectral energy distributions computed using equation 2.1 for each star formation history ψ at age 10 Gyr, assuming solar metallicity and Chabrier (2003) IMF.

energy distributions of these galaxies show contributions by both an old stellar component (dominating the emission at optical and near-infrared wavelengths) and a young stellar component (dominating the emission in the ultraviolet) to the total emission. In late-type, irregular galaxies, interaction-induced bursts may occur as illustrated in Fig. 1.9. This causes the spectral energy distributions of these galaxies to appear very blue, as their integrated light becomes dominated by the young stellar population formed in the burst (appearing similar to the spectrum of a young SSP in Fig. 1.7).

In should be noted that, in hierarchical scenarios of galaxy formation, not only late-type irregular galaxies merge or interact gravitationally with other galaxies, rather all types can experience this. However, interactions produce significant bursts of star formation mainly in galaxies which still contain large amounts of gas available to form new stars.

In this section, we have reviewed the basic elements of the production of starlight in galaxies and the main ingredients of stellar population synthesis models. We will show in this thesis that these models are a valuable tool to compute the emission by stars in galaxies from ultraviolet to infrared wavelengths. However, the total emission from galaxies is not purely stellar. The light produced by stars in galaxies interacts with gas and dust in the interstellar medium before escaping the galaxies. Therefore, to fully understand the multi-wavelength emission from galaxies, we need to include the transfer of starlight in the ISM. In the next section, briefly review the main effects of the ISM on the ultraviolet-to-infrared spectral energy distributions of galaxies.

1.4 The transfer of starlight in the interstellar medium

By definition, the interstellar medium of galaxies consists in the matter occupying the large space between stars. The first direct evidence of the existence of interstellar matter was provided by Johannes Hartmann in 1904, when studying the spectrum of the star δ Orionis (Hartmann 1904). In this study, this author observed that the calcium line at 3934 Å was not shifted (by Doppler effect) by the motion of the star in the same way as the other stellar absorption lines. To explain this, he advanced the hypothesis that this particular line was caused by a cloud consisting of calcium vapour in the line of sight.

Our understanding of the interstellar medium of galaxies has much advanced since the pioneer work of Hartmann. The current view is that the ISM consists mainly of gas, dust grains, and relativistic charged particles (cosmic rays). About 99 per cent of the mass of the ISM is in the form of gas, of which 75 per cent is in the form of H, and the remaining is mostly in the form of He, with heavier elements present only in trace amounts.

The ISM is a crucial component of galaxies since galactic evolution is affected by the interactions between the radiation produced by stars and the interstellar matter. In this chapter, we elaborate on several processes by which the stellar light interacts with gas and dust in the interstellar medium of galaxies. In this thesis, we will focus mainly on the effects of the ISM on the observed ultraviolet-to-infrared spectral energy distributions of galaxies.

In Fig. 1.10, we show a schematic representation of the main interactions between the stars and the interstellar medium of galaxies. The gravitational collapse of dense molecular clouds (in which hydrogen is in molecular form, H_2) leads to the formation of stars. The radiation produced by hot massive stars (OB stars), which

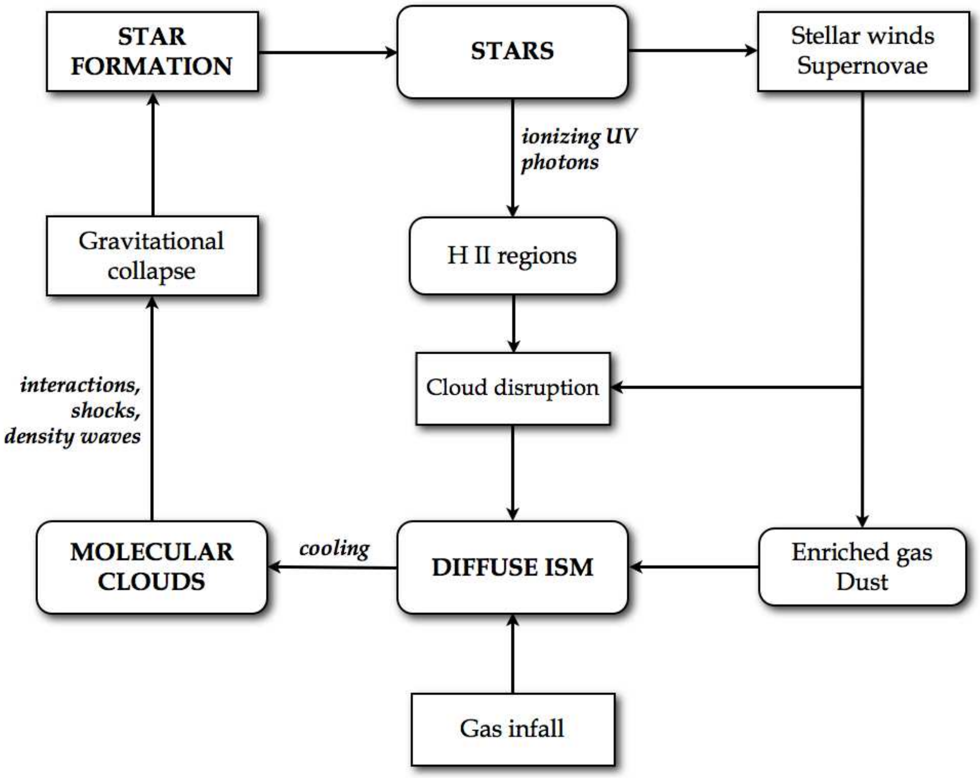

Figure 1.10: Schematic representation of the main interactions that occur between the stars and the interstellar medium of galaxies.

emit mostly at ultraviolet wavelengths (see Section 1.3), ionizes the surrounding gas, creating H II regions (i.e. regions where hydrogen is ionized, H^+) around these young stars. The diffuse ISM around older stars is mostly in neutral form (H I), because older stars do not produce enough ionizing photons. During their lifetimes, stars of all masses produce heavy elements by nucleosynthesis and may eject gas back into the ISM, either by mass loss via stellar winds or by supernova explosions (for stars with sufficiently high masses; see Section 1.3). These processes enrich the interstellar medium with metals. Also, in the cold atmospheres of evolved stars (red giants and AGB stars) or in the ejecta of supernovae explosions (Dwek 1998), the metals may condense and form dust grains, which are then returned to the ISM. The diffuse ISM, enriched in metals (in gas form or in dust grains), may then cool down and form molecular clouds, which collapse gravitationally and produce new generations of stars with higher initial metallicities.

The interaction of stellar light with the various components of the ISM in galaxies can be studied through the galactic spectral energy distributions, which contain important information about the amount of gas and dust in galaxies, and also about the physical conditions of the ISM (such as temperature, density, ionization state).

1.4.1 Generalities

The interstellar medium in galaxies presents a variety of phases. These phases are usually characterized by the state of hydrogen, which is by far the most abundant gas. Dust is mixed with the gas in all these different phases and affects differently the light produced by stars. We now briefly review the different gas components of the ISM of galaxies. In Sections 1.4.3, we will describe the properties of interstellar dust and how it affects the observed emission from galaxies.

(i) *Molecular gas.* In the ISM of galaxies, molecular clouds are composed mainly of H_2, with other molecules present in very small amounts. Molecular hydrogen forms in dense ($n \gtrsim 10^3$ cm^{-3}) and cold ($T = 10 - 20$ K) environments, predominately via collisions between hydrogen atoms on the surface of dust grains (e.g. Hollenbach & Salpeter 1971). Besides providing a site for H_2 formation, dust grains also absorb the binding energy liberated when a stable molecule forms. They provide shielding against ultraviolet photons, preventing the photo-dissociation of H_2 molecules.

Interstellar molecules can be observed through the absorption lines they produce in stellar spectra (when the interstellar matter containing these molecules is in the line of sight to the observed star) or through their emission at infrared and radio wavelengths (through electronic, rotational and vibrational transitions).

The first interstellar molecules (CH, CH^+ and CN) were discovered in the 1930's through the detection of absorption lines in stellar spectra. The most abundant interstellar molecule, H_2, has a strong absorption feature in the far-ultraviolet (at 1050 Å). Therefore, it is much more challenging to detect observationally from ground observations. Molecular hydrogen can also be identified by its rotational emission lines in the mid-infrared.

The second most abundant interstellar molecule, CO, is more easy to identify than H_2. In particular, this molecule is easily detectable by the 2.6 mm $J = 1 - 0$ rotational transition (Wilson, Jefferts & Penzias 1970). Many other interstellar molecules (such as OH, CS, SiO, SO, H_2O, HCN or NH_3) have been detected in the radio. The advantage of observing at radio wavelengths is that we can detect molecules inside very dense, optically thick interstellar clouds. For molecules to be detected through absorption in stellar spectra, they must reside in the diffuse (optically thin) ISM. We note that the H_2 molecule cannot be detected using radio observations, since it is symmetric and therefore has no electric dipole. Since CO molecules are excited by collisions with the H_2 molecules, radio observations of CO are generally used to trace H_2.

Another type of molecules, the polycyclic aromatic hydrocarbons (PAHs) are found in the interstellar medium. These are large aromatic molecules (some can include more than a hundred carbon atoms), which can be detected by their emission at mid-infrared wavelengths. These molecules are so big that they are traditionally treated as a dust component (see Section 1.4.3.4).

(ii) *Neutral atomic gas.* Most of the mass in the ISM is in the form of neutral hydrogen, H I. Neutral hydrogen cannot be easily detected through the Lyman series transitions between excited states and the ground level. These transitions (including the well-known Lyα line at 1216 Å) arise in the far-ultraviolet and therefore are not detectable from ground-based observations.

The most efficient way to detect neutral hydrogen in the ISM of the Milky Way and external galaxies even from the ground is by observing the 21-cm line. This line corresponds to the transition between the two hyperfine levels of the fundamental state of the H atom. The hyperfine structure results from the interaction between the spins of the electron and the proton. The existence of detectable 21-cm H line in the interstellar medium was predicted in the 1940's by Hendrik van de Hulst and observed for the first time by Ewen & Purcell (1951). This technique quickly became of standard use to study atomic H and its distribution.

Observations of the 21-cm line in emission and in absorption highlight two neutral, thermally stable phases (e.g. Field, Goldsmith & Habing 1969) which coexist in the ISM:

- Cold H I, observed in emission and absorption. This medium is composed of dense clouds with densities of the order of 10 cm^{-3} and temperatures of about 100 K. This component is also found in the envelopes of molecular clouds.
- Warm H I, observed mainly in emission. This is a more diffuse ($n \approx 0.15$ cm^{-3}) and warmer medium ($T \approx 10^4$ K) gas which exists between the denser clouds.

Besides H I, the neutral ISM also contains atoms and ions of heavier elements. These can be identified by fine-structure lines in the far-infrared, which correspond to forbidden transitions. Some of these elements (such as C, Mg, Si and S) have ionization potentials lower than 13.6 eV, and therefore they can be ionized in H I regions. In fact, the main coolant of the cold neutral medium is the [C II]λ157.7 μm forbidden line. In the warm neutral medium the [O I]λ6300 Å line provides a cooling source in addition to the Lyα line. Other abundant species whose lines also contribute to the cooling of the neutral ISM are C I, Si II, S II and Fe II (e.g. Spitzer & Fitzpatrick 1993).

(iii) *Ionized gas.* The interstellar gas can be ionized by far-ultraviolet radiation produced by young OB stars or other processes, such as collisional ionization in shocks, X-ray ionization and ionization by charged particles of high energy.

A large fraction of the energy output of OB stars in galaxies consists in ionizing ultraviolet radiation (with $\lambda \leq 912$ Å, see Section 1.3). The radiation with energy higher than 13.6 eV ionizes the neutral hydrogen around the stars, forming H II regions. Photons of energies much higher than the H ionization potential can also ionize He and other heavier elements.

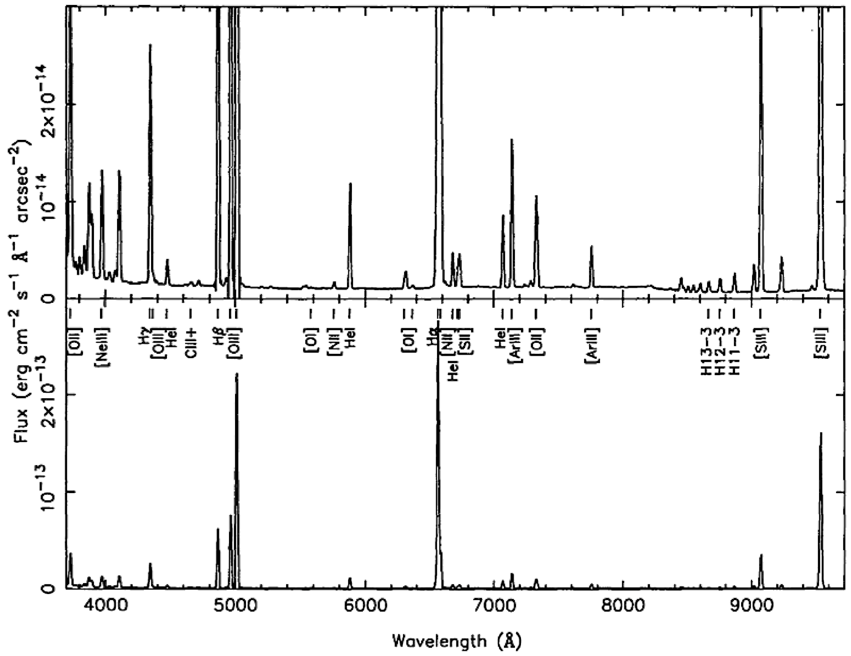

Figure 1.11: Typical optical emission spectrum of a H II region, with the strongest lines labelled on the bottom panel. The flux scale on the top panel highlights the less luminous lines. Spectrum from the Orion nebula taken from Baldwin et al. (1991).

The observed spectra of galactic H II regions is dominated by strong emission lines in the ultraviolet, optical (see Fig. 1.11, Baldwin et al. 1991), infrared Peeters et al. (2002) and radio. These emission lines are in general collisionally excited 'forbidden' lines from heavy ions and hydrogen (and helium) 'recombination' lines.

The recombination lines are emitted when a free electron recombines with an ion (mainly H II) to an excited level, $n > 1$, and undergoes radiative transitions in cascading down to the ground level, $n = 1$. This recombination process is theoretically described by two cases: 'case A' and 'case B' (Baker & Menzel 1938; Osterbrock 1989). What distinguishes case A from case B is the optical thickness of the ionized gas in the Lyman lines. The Lyman lines are produced by electronic transitions from an excited state, with $n > 1$, to the ground state, $n = 1$, with the excited state reached through the radiative cascade (or directly) of a recombined electron. Ionized nebulae in which the gas is optically thin in the H I Lyman lines are described by case A recombination. In this case, the Lyman-line photons escape the nebula without further absorption. In case B, the optical depth in the Lyman lines is high. As a consequence, Lyman-line photons do not escape the nebula: they are readily absorbed by nearby neutral H atoms in the ground state.

Therefore, any Lyman photon other than Lyα will be converted into a lower series photon plus a Lyα photon or two-photon emission. Case A and case B result in different ratios of the higher order lines such as the Balmer lines[4] . The ratios of the Balmer lines, called the 'Balmer decrement', are fixed for a given electron temperature T_e and density n_e. The conditions for case B recombination generally apply in normal (i.e. galactic-type) H II regions. In this case, the observed Balmer decrement can be taken as fixed, with the ratio of Hα/H$\beta \sim 2.85$ (Osterbrock 1989) for the typical electron temperature and density of H II regions ($T_e = 10^4$ K and $n_e \lesssim 10^4$ cm^{-3}).

Emission lines allow us to study the physical conditions in H II regions. The line emission spectrum depends on the chemical abundances of the various elements, the local ionization, density and temperature. Therefore, emission line diagnostics can be used to study the ionized gas: for example, the observed Balmer decrement Hα/Hβ gives an indication on the extinction when compared with the fixed ratio predicted for case B recombination. The temperature and density of the gas in H II regions can be derived using line intensity ratios of the same ion. This can be achieved by combining a temperature-dependent ratio with one dependent on intensity, as it is the case, for example, when comparing optical and infrared forbidden lines of [O III] (e.g. Menzel, Aller & Hebb 1941; Dinerstein, Lester & Werner 1985).

The emission lines produced by H II regions in actively star-forming galaxies can be observed in their integrated emission (e.g. Kennicutt 1992, see Fig. 1.12). Studies of these emission lines provide constraints on the amount of ionized gas in external galaxies, on the properties of this gas and provide a star formation rate indicator (e.g. Kennicutt 1998a; Charlot & Longhetti 2001; Charlot et al. 2002).

In addition to emission lines, the H II regions present a radio continuum which is caused by free-free emission (or thermal Bremsstrahlung): electrons in the interstellar plasma are accelerated by electric interaction with ions, and radiate energy due to this acceleration. This emission can be used as a star formation tracer in galaxies (e.g. Yun, Reddy & Condon 2001; Bell 2003). However, there are difficulties associated with this approach, because the radio emission from galaxies shows an additional contribution from non-thermal emission from cosmic-ray electrons spiralling in the magnetic field of the galaxy (e.g. Condon 1992). Since the thermal and the non-thermal emission have different spectral shapes, the distinction between these two contributions to the radio emission can be done by associating observations at different radio frequencies.

Besides H II regions, the ISM contains a colder *diffuse ionized gas* component, of typical temperature around 8 000 K and very low density ($n \approx 0.10$ cm^{-3}).

---

[4] The Balmer lines are produced by electronic transitions from an excited state, with $n > 2$, to the first excited state, $n = 2$.

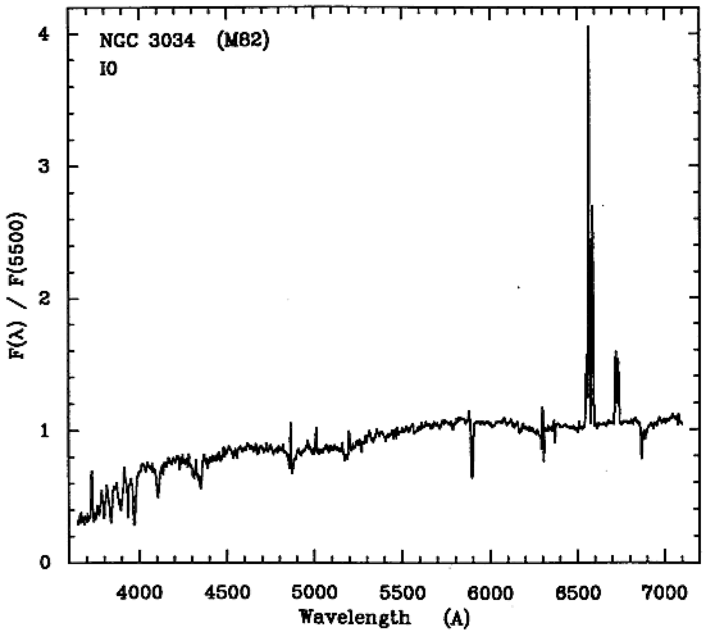

Figure 1.12: Optical spectrum of the starburst galaxy M 82. The dominant feature is the Hα emission line, coming from the H II regions of the galaxy, which are powered by newly-formed OB stars. Figure taken from Kennicutt (1992).

> This component contributes with most of the mass in the form of ionized gas in galaxies. The diffuse ionized gas originates mainly from ionizing radiation from OB stars that leaks from the H II regions and from ultraviolet radiation produced by massive stars in the diffuse medium. Other sources of ionization of this gas include shocks caused by supernova explosions and stellar winds, and ionizing radiation from planetary nebula nuclei. This component, as H II regions, is traced by recombination lines, forbidden lines and radio continuum
>
> Another important ionized ISM component in galaxies is the *coronal gas* (Spitzer 1956). This gas has higher temperature than ionized gas in H II regions (typically between 10^5 and 10^6 K) and very low densities (of about 10^{-3} cm^{-3}). The heating and ionizing sources of this medium are likely to be shocks driven by stellar winds or supernova explosions. Coronal gas can be traced through ultraviolet absorption lines of highly ionized species such as C IV, S VI, N V or O VI (e.g. York 1974). This gas is also detected by emission in X-rays, extreme ultraviolet and radio.

The different phases of the ISM described above contribute in different proportions to the total mass of gas of galaxies. Typically, in the Milky Way, neutral gas contributes with most of the mass of the ISM (about 68 per cent of the total mass of gas), followed by molecular clouds and diffuse ionized gas. H II regions and coronal gas contribute at most to a few per cent of the total mass of gas. In Table 1.1, we summarize the typical values of physical parameters estimated for the different

Table 1.1: Summary of the physical properties of the main ISM phases of the Milky Way. The estimated mass of each component is highly uncertain. We adopt the values quoted by Tielens (2005).

Phase	Density n/cm^{-3}	Temperature T/K	Mass $M/10^9\ \mathrm{M}_\odot$	Fraction of total mass %
Molecular	$\gtrsim 10^3$	10 – 20	1.30	17
Neutral				
Cold	10 – 50	10^2	2.20	30
Warm	0.15 – 0.50	10^4	2.80	38
Ionized				
Diffuse	0.10	8×10^3	1.00	13
H II regions	10^2 – 10^6	10^4	0.05	0.7
Coronal	10^{-3}	10^5 – 10^6	1.00	1.3

ISM phases of the Milky Way.

1.4.2 Description of the ISM in this thesis

In this thesis, we are interested in the modelling the ultraviolet, optical and infrared spectral energy distributions of star-forming galaxies. For this purpose, we describe the main properties of the ISM outlined in Section 1.4.1 by considering two main components: the diffuse interstellar medium and the star-forming regions (Fig. 1.13, Charlot & Fall 2000).

- *Diffuse interstellar medium.* The diffuse ISM (or cirrus) is composed mainly of neutral hydrogen, but also contains small amounts of molecular and ionized gas.

  This component constitutes the bulk of the ISM in galaxies, and it is renewed by infall of extragalactic material into the galaxy and by mass loss from stellar winds and supernova explosions. A fraction of the gas mass initially converted into stars remains locked in stellar remnants (white dwarves, neutron stars and black holes; see Section 1.3). Therefore, as the galaxy evolves and forms successive generations of stars, the gas in the ISM is consumed. With time, the amount of gas available to form new stars decreases (unless the galaxy is enriched by lots of gas infall).

- *Star-forming regions (stellar birth clouds).* In galaxies, stars form through the gravitational collapse of dense molecular clouds. These molecular clouds originate from material in the diffuse ISM when the diffuse gas becomes gravitationally unstable and collapses, becoming denser and cooler. Several factors

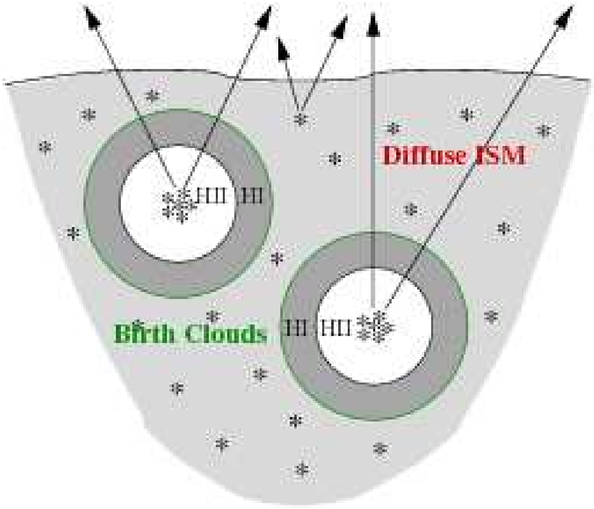

Figure 1.13: Schematic representation of the birth clouds and ambient ISM surrounding each generation of stars in a model galaxy. Light rays leaving the galaxy in different directions are also shown. Figure adapted from Charlot & Fall (2000).

may cause instabilities in the diffuse gas: shocks induced by supernova explosions or strong stellar winds, density waves or interactions with other galaxies. The largest molecular clouds, the 'giant molecular clouds', can reach masses of $10^4 - 10^6$ $M_\odot$, and densities of the order of 10^2 cm^{-3}.

The most massive stars formed in molecular clouds are the OB stars. These stars have very high effective temperatures and release most of their energy at ultraviolet wavelengths (Section 1.3). The ultraviolet radiation produced by these massive stars ionizes the surrounding gas left over from the molecular cloud from which the stars have formed, creating an H II region. This ionized gas is surrounded by a layer of H I (Fig. 1.13). The interface between the ionized gas and the neutral and molecular gas is a photo-dissociation region (PDR, see Fig. 1.14). In PDRs, the non-ionizing far-ultraviolet photons coming from stars penetrate the neutral hydrogen and can dissociate and ionize molecular species such as H_2, CO, OH, O_2 and H_2O (e.g. Hollenbach & Tielens 1997; Tielens 2005). These regions present very strong [C II]λ158 μm and [O I]λ63 μm lines (which are the main coolants), as well as rotational and vibrational H_2 lines, and strong aromatic emission features in the mid-infrared (see Fig. 1.14).

Stellar birth clouds have finite lifetimes of typically 10^7 yr (Blitz & Shu 1980). After that time, they are eventually disrupted by the energy input from newly-formed stars, via strong stellar winds, expanding H II regions and supernova explosions. We will see in the next chapter that the finite lifetimes of stellar birth clouds is a key ingredient to interpret consistently the line and continuum emission from galaxies.

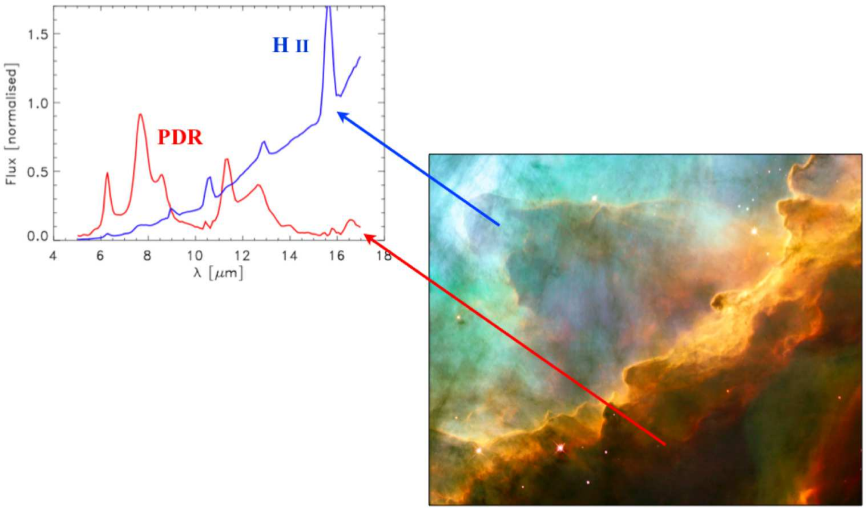

Figure 1.14: *Right:* Optical image of the SW part of the star-forming region M17 taken with the WFPC2 instrument on the *Hubble* Space Telescope. The newly-formed, ionizing stars are located in the direction of the upper left corner of the picture. The image is a composite of three filters that capture three strong emission lines observed in H II regions: red – N II; green – Hα; blue – O III. Image credit: ESA, NASA, and J. Hester (Arizona State University). *Left:* Mid-infrared spectrum of the H II region (in blue) and of the photo-dissociation region (in red) extracted from the *ISO*/ISOCAM observations of Cesarsky et al. (1996) by Madden et al. (2006). These spectra highlight the difference in physical conditions inside H II regions and PDRs, which translate in different dust emission properties. The spectrum of the H II region is dominated by a rising continuum from very hot small grains, strong emission lines from ionized gas (e.g., the strong [Ne III] line at 15.8 μm), and no emission by PAHs molecules, which are destroyed by the intense ultraviolet radiation field from hot stars; the spectrum from the PDR is dominated by the emission features from PAHs molecules, which are shielded from the extreme ultraviolet radiation and can survive (more details about the emission by dust will be presented in Section 1.4.3.4).

1.4.3 Influence of interstellar dust on galactic emission

Metals in the interstellar medium can be condensed in dust grains. Interstellar dust is an important component of the interstellar medium which plays a fundamental role in the star formation and the chemical evolution of galaxies. Dust grains are small solid particles, with diameters typically less than 1 μm, composed of dielectric and refractory materials (mainly graphite and silicates). They are found in a wide variety of astrophysical environments, such as molecular clouds (where they play a fundamental role in star formation by accelerating the gas cooling, and thus, the collapse of these clouds), diffuse nebulae, reflection nebulae, H II regions, photodissociation regions, the envelopes of evolved stars (such as red giants or

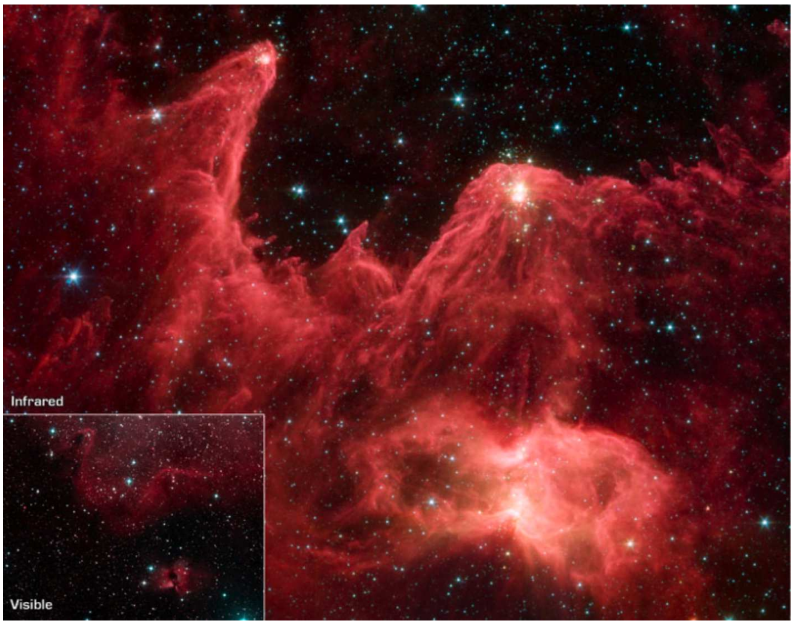

Figure 1.15: W5 star-forming region in the constellation of Cassiopeia. The main image shows a composite of the infrared emission in the four *Spitzer*/IRAC bands from wavelengths of 3.6 μm (blue), 4.5 μm (green), 5.8 μm (orange), and 8.0 μm (red). The inset image shows the same region in optical (visible) wavelengths, from the California Institute of Technology Digitized Sky Survey. *Figure credits:* NASA/JPL – Caltech/L. Allen (Harvard-Smithsonian CfA).

AGB stars), and supernova remnants. As an example, in Fig. 1.15, we show a star-forming region observed in the infrared, and in the optical. The presence of dust can be inferred from the dark, highly obscured regions in the optical image (the dust absorbs the hot radiation from the newly-formed stars), as well as in reflection (some of the stellar light is scattered by dust). At 3.6 and 4.5 μm, the dust is more ‘transparent’, and it becomes possible to observe the near-infrared continuum emission from stars through the dust. The obscured regions in the optical image shine in the infrared image: the dust reemits the absorbed stellar light at infrared wavelengths. This is seen in the longer-wavelength bands, at 5.8 and 8.0 μm.

Interstellar dust grains can form where the kinetic temperature of the gas is low enough and the pressure is high enough to allow the condensation of heavy elements into solid state. These conditions may occur in the cold interior of dense molecular clouds, in the cold envelopes of evolved stars (such as red giants or AGB stars) and in cold supernova ejecta (e.g. Dwek 1998).

Dust grains interact with stellar radiation, regulate the temperature of the ISM and chemical reactions to occur in their surfaces, allowing for the formation of molecules such as H_2. Dust grains also harbour a big fraction of the heavy elements outside of stars in galaxies.

Several observational effects probe the interaction of starlight with interstellar dust grains:

- Starlight passing through dusty regions in the interstellar medium, it suffers a wavelength-dependent *extinction* caused by a combination of absorption and scattering by dust grains;
- Starlight emitted towards dusty clouds can also be scattered by dust grains into the line of sight;
- *Polarization* of starlight may occur either by scattering, or when it passes through regions with (non-spherical) dust grains macroscopically aligned by interaction with a magnetic field.

Interstellar dust grains do not only absorb and scatter starlight. They also reemit the radiation they have absorbed from stars, mostly at infrared wavelengths. Most of this radiation is not detectable from ground-based observatories. With modern infrared space telescopes, we are now able to detect the emission from dust grains, which can have different origins:

- Mid- and far-infrared thermal continuum emission from large dust grains in thermal equilibrium with the radiation field;
- Near- and mid-infrared thermal emission from small grains which are not in thermal equilibrium with the radiation field, and are stochastically heated through the absorption of single photons, reaching high temperatures;
- Emission features from grains and large molecules, primarily the mid-infrared emission features from polycyclic aromatic hydrocarbons (PAHs).

In this section, we focus on the general properties of interstellar dust and on the main implications it has on the study of the spectral energy distributions of galaxies in this thesis.

1.4.3.1 Interstellar extinction

Interstellar extinction can be defined as the process by which photons coming from a distant, point-like source (such as a star) in a given line of sight is removed from the line of sight when they pass through a column density of interstellar dust. Photons can be removed in two ways: by absorption onto the surface of dust grains, and by scattering out of the line of sight.

The importance of this effect was first demonstrated and quantified by Trumpler (1930). Trumpler observed a sample of a hundred open stellar clusters in the Milky Way for which the 'photometric distances' (based on the inverse square law) were computed using the *distance modulus*,

$$m_\lambda - M_\lambda = 5\,\log\left(\frac{d}{10\,\mathrm{pc}}\right) - 5\,, \tag{1.5}$$

where m_λ is the apparent magnitude at wavelength λ, M_λ is the absolute magnitude[5] at wavelength λ, and d is the distance in parsec. Trumpler also computed 'diameter distances' to these clusters by comparing their angular diameter in the sky with their intrinsic linear diameter (computed by assuming that clusters with the same constitution, i.e., same number of stars and radial stellar concentration, have on average the same intrinsic sizes). The comparison between the distances derived in this way and the photometric distances showed that, for the most distant clusters, the photometry-based estimates of distance were lower than the diameter-based estimates, i.e., the intrinsic brightness of the distant clusters was lower than expected. Trumpler concluded that the interstellar space between these clusters and us must contain small cosmic particles of various sizes – interstellar dust grains – which cause the absorption of the stellar light, and that this absorption is selective, decreasing with increasing wavelength.

In fact, to accurately compute the distance to a star (or other astronomical object) from its observed magnitude, the extinction of light by dust in the interstellar medium must be included in equation (1.5); then, the distance modulus becomes

$$m_\lambda - M_\lambda = 5\,\log\left(\frac{d}{10\,\mathrm{pc}}\right) - 5 + A_\lambda\,, \tag{1.6}$$

where A_λ measures the extinction, in units of magnitude, at wavelength λ. This extinction is defined as the difference between the observed magnitude of the source and the magnitude that would be observed in the dust-free case (with no extinction). The interstellar extinction can be computed as

$$A_\lambda = -2.5\log\frac{F_\lambda}{F_\lambda(0)} = 2.5\log(e)\,\tau_\lambda = 1.086\,\tau_\lambda\,, \tag{1.7}$$

where F_λ is the observed flux, $F_\lambda(0)$ is the intrinsic flux of the source, and τ_λ is the optical depth along the line of sight. τ_λ the product of the number of dust grains per cm^2 along the line of sight (i.e. the column density) and the optical cross section of the grains.

The consequences of Trumpler's work are of great importance. For example, the accurate (extinction-corrected) measure of distances within the Galaxy allowed the first accurate estimates of the size of the Milky Way and the position of the Sun within it (e.g. Shapley 1933).

Since this work, it became well-known that interstellar dust extinction affects greatly observations of galactic and extragalactic objects, specially at ultraviolet and optical wavelengths, and therefore needs to be taken into account when interpreting observed fluxes and computing distances.

The interstellar extinction law. The light from stars and galaxies is most affected by dust extinction at ultraviolet and optical wavelengths. Therefore, to interpret

---

[5] The absolute magnitude of an object is defined as the magnitude that would be observed if the object was located at a distance of 10 pc.

observations of stars and galaxies, it is crucial to know the shape of the interstellar extinction law, i.e. the wavelength dependence of extinction. The detailed knowledge of the extinction allows us to make the necessary corrections in order to recover the intrinsic luminosity of the observed sources. Moreover, the study of the shape of the extinction curve itself is of great interest. The extinction by the ISM in galaxies depends on the physical properties of interstellar dust grains such as their sizes, shapes, chemical compositions and optical properties. Therefore, the comparison between the observed extinction curve and the extinction curve produced by physical dust models allows us to constrain the properties of dust grains (e.g. Mathis, Rumpl & Nordsieck 1977; Désert, Boulanger & Puget 1990; Pei 1992).

The 'extinction law' describes the dependence of extinction on wavelength and is generally given by the ratio A_λ/A_V, where A_V is the 'visual extinction'. The reddening of starlight in a given line of sight can be measured using the difference between the observed colour index $(B-V)$, and the intrinsic colour index $(B-V)_0$ (which is due to the intrinsic shape of its spectrum), usually expressed in terms of the 'colour excess'[6]:

$$E_{B-V} = A_B - A_V = (B-V) - (B-V)_0 \,. \tag{1.8}$$

The visual extinction and the colour excess are related by the ratio of total to selective extinction:

$$R_V = \frac{A_V}{E_{B-V}} = -\left[\frac{E_{\lambda-V}}{E_{B-V}}\right]_{\lambda\to\infty} . \tag{1.9}$$

The ratio of total to selective extinction depends on the chemical composition, physical properties and size distribution of the dust grains. Therefore, it may vary along different lines of sight. On average, $R_V \approx 3.1$ for the diffuse ISM of the Milky Way, but it can reach much higher values (between 4 and 6) in dense molecular clouds (e.g. Mathis 1990). In general, the value of R_V provides a measure of the slope of the extinction curve – larger values of R_V correspond to flatter extinction curves.

The only galaxies for which we can accurately derive the extinction along different lines of sight and obtain empirical extinction laws are the Milky Way (e.g. Savage and Mathis 1979) and the Magellanic Clouds (e.g. Fitzpatrick 1989). This is done by comparing reddened and unreddened stars and using the simple framework described above – the stars are point sources and the interstellar dust between the stars and the observer can be assimilated to a screen absorbing the light.

The average observed extinction curves of the Milky Way and the Magellanic Clouds are plotted as points in Fig. 1.16. The three curves are similar in the optical and the infrared, but they differ substantially at ultraviolet wavelengths. There is an increase in far-ultraviolet extinction from the Milky Way to the Large Magellanic Cloud (LMC) to the Small Magellanic Cloud (SMC). Furthermore, the bump at

---

[6] The V (visual) and B (blue) photometric bands of the Cousins system correspond to effective wavelengths of 5470 and 4340 Å, respectively.

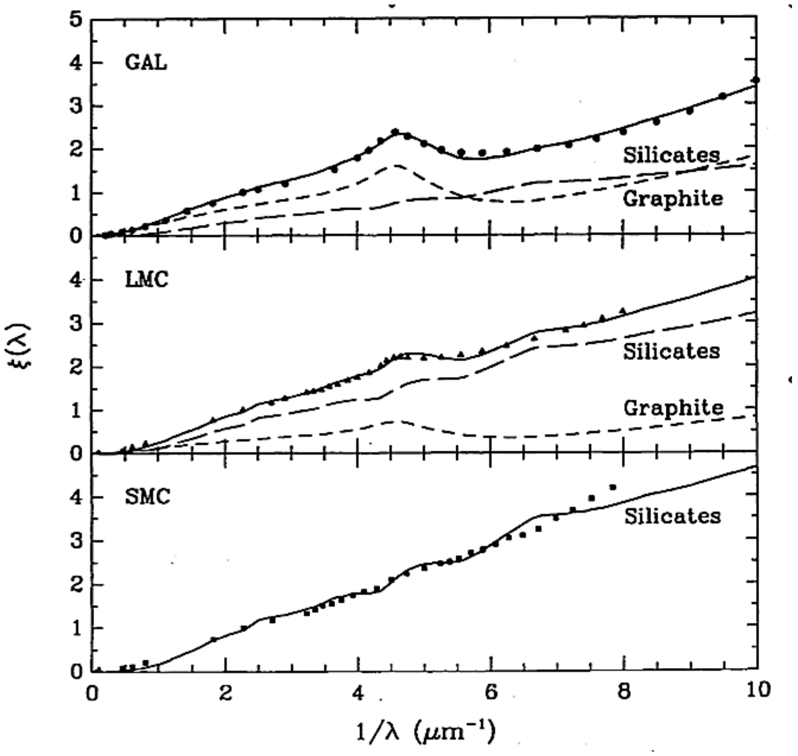

Figure 1.16: Comparison between the extinction curves of the Milky Way (GAL, top panel), Large Magellanic Cloud (LMC, middle panel), and Small Magellanic Cloud (SMC, bottom panel). The extinction curves are defined as $\xi(\lambda) \equiv A_\lambda/A_B$. The points correspond to the mean observed extinction curves. The solid lines show the total model extinction curves, composed of a sum of graphite (short-dashed line) and silicates (long-dashed line). Figure from Pei (1992).

2175 Å in the Milky Way extinction curve is much weaker in the curve from the LMC, and practically absent in the curve from the SMC. This suggests that dust grains responsible from the 2175 Å feature in the extinction curve (which may be small graphite particles with sizes less than 0.005 μm) must be less abundant in the LMC and in the SMC than in the Milky Way. These variations in the extinction curves are evidences that there might be variations in the physical properties of the dust in these galaxies, such as their chemical composition or the size distribution of the grains.

Constraints on dust models using the observed extinction law. Several dust models have been proposed to interpret the observed extinction curve of the Milky Way based on the physical properties of interstellar dust grains. One of the first and most widely used models is the 'graphite-silicate model' for which the size distribution of dust grains was computed by Mathis, Rumpl & Nordsieck (1977) and the optical properties were computed by Draine & Lee (1984).

Mathis, Rumpl & Nordsieck (1977) have proposed that the observed extinction law can be explained using a mixture of graphite and silicate grains with a power-law distribution of sizes

$$dn \propto a^{-3.5}\, da\,, \tag{1.10}$$

where dn is the number density of grains of type with radii between a and $a + da$. The optical properties of graphite and silicate grains were then computed by Draine & Lee (1984). These properties determine how the dust grains absorb, scatter, polarize and emit radiation. In this model, graphite grains account for the bump in the Galactic extinction curve at 2175 Å, whereas silicates are responsible for the mid-infrared absorption features at 9.7 and 18 μm (Draine & Lee 1984).

Based on these models, Désert, Boulanger & Puget (1990) proposed that the interstellar extinction curve and the emission from interstellar dust could be both interpreted consistently by considering three components: 'big grains' mainly composed of silicates, 'very small grains' composed mainly of graphite, and 'polycyclic aromatic hydrocarbon' molecules.

1.4.3.2 Attenuation by dust in external galaxies

We have seen that the study of the interstellar extinction provides important clues on the chemical composition, size distribution and optical properties of dust grains in the ISM. In this thesis, we are interested in modelling the spectral energy distributions of galaxies by taking into account the emission from stellar populations and the effects of the ISM on starlight (we will treat this in detail in Chapter 2). In particular, it is important to determine the internal attenuation of stellar light caused by dust in the ISM of external galaxies. This allows will allow us to make the appropriate corrections in order to recover the intrinsic properties of the stellar component of galaxies. This is crucial to accurately determine galactic properties such as the star formation rate, the mean age of the stellar population and the total amount of dust.

The geometry of the problem of internal 'attenuation'[7] in extended sources such as galaxies is more complex than simply considering point sources behind a screen of dust, as we did for the extinction of stars in the Milky Way in Section 1.4.3.1. The *attenuation curve* for the external galaxies, which describes the wavelength dependence of the attenuation, depends on both the physical properties of dust grains and the spatial distribution of the dust (e.g. Natta & Panagia 1984; Witt, Thronson & Capuano 1992; Calzetti, Kinney & Storchi-Bergmann 1994). For example, if stars and dust are homogeneously mixed in the ISM of galaxies, the shorter the wavelength of radiation, the smaller the optical depth of the dust layer from which the

---

[7] Attenuation is defined as the process by which the light emitted by stars in a galaxy is dimmed due to the presence of dust in the ISM. We will also use the term 'effective absorption' employed by Charlot & Fall (2000). This has also been referred to as 'effective extinction', 'apparent extinction', 'obscuration' or 'absorption' in several other studies (e.g. Calzetti, Kinney & Storchi-Bergmann 1994; Meurer, Heckman & Calzetti 1999).

radiation can emerge. Therefore an observer will only detect short-wavelength light from the closest, outer layer of the distribution, while longer-wavelength light will also come from deeper layers. Moreover, before escaping the galaxy, the photons travelling in the ISM have non-negligible probabilities of being scattered into and out of the line of sight. The result of these effects is that the effective attenuation curve of external galaxies is 'greyer' (i.e. shallower) than the extinction curve of the Milky Way (e.g. Bruzual, Magris & Calvet 1988; Calzetti 2001).

1.4.3.3 The model of Charlot & Fall (2000)

In this thesis, we will use the model of Charlot & Fall (2000) to describe the transfer of starlight through dust in galaxies. Charlot & Fall (2000) propose a simple, physically-motivated model to account for the effects of dust in the spectral energy distributions of galaxies. The transfer of radiation is treated in a simplified way (especially for scattering), which is appropriate to deal with angle-averaged quantities such as luminosities. In this model, the ISM is described in using the two main components of Section 1.4.2. The main features of the model of Charlot & Fall (2000) are:

- *Finite lifetime of stellar birth clouds.* Stars are formed in dense molecular clouds. The young, hot OB stars born in these regions ionize the inner parts, so that the birth clouds consist of a central H II region surrounded by neutral hydrogen (H I region). These birth clouds have finite lifetimes of typically 10^7 yr, after which they are disrupted due to the energy input from massive stars (Blitz & Shu 1980). The main consequence of this for the emission from galaxies is that photons originating from stars that live longer than the birth clouds propagate only through the ambient (diffuse) ISM, where they are treated in the same way as photons emerging from the birth clouds before they escape the galaxy (see Fig. 1.13). The birth clouds are more optically thick than the surrounding ISM, and therefore the amount of attenuation in the ambient ISM is only a fraction of the attenuation in the birth clouds.

- *Effective absorption curve.* The attenuation by dust in galaxies is described in terms of an 'effective absorption curve', $\hat{\tau}_\lambda \propto \lambda^{-n}$. The slope of this curve is empirically determined and depends both on the optical properties of the dust and its spatial distribution. The normalization of this curve depends mainly the amount of dust in the galaxy.

Charlot & Fall (2000) show that an exponent of the effective absorption curve $n = 0.7$ is favoured by observations of the ultraviolet and infrared properties of starburst galaxies. The use of two components (birth clouds and ambient ISM) with different normalizations of $\hat{\tau}_\lambda$ solves the apparent discrepancy between line and continuum attenuation starburst galaxies.

The effective absorption curve is less steep than the typical extinction curves of the Milky Way and the Magellanic Clouds, which can be approximated by $\tau_\lambda \propto$

λ^{-m}, with m=1.3 (Pei 1992). As discussed in the beginning of this section, this is because the exponent n of the effective absorption curve includes the optical properties and the spatial distribution of dust. Charlot & Fall (2000) show that an effective absorption curve $\hat{\tau}_\lambda \propto \lambda^{-0.7}$ is equivalent to considering a typical extinction curve $\tau_\lambda \propto m^{-1.3}$ combined with a realistic spatial distribution of dust consisting of a random distribution of discrete clouds.

Recombination lines from dusty H II regions. As described in Section 1.4.1, the H II regions around hot OB stars are characterized by an emission-line spectrum. Dust grains are present in H II regions and they absorb a fraction of the ionizing photons produced by young stars. In addition, line photons emerging from the H II regions are attenuated by dust in the surrounding H I regions and in the ambient ISM in the same way as continuum photons. Therefore, to predict the emergent emission line fluxes from galaxies Charlot & Fall (2000) include the absorption of ionizing radiation by dust in the H II regions and the absorption of line photons by dust in the surrounding H I and diffuse ISM.

The number of Lyman continuum photons (i.e. ionizing photons) produced by a simple stellar population (Section 1.3 can be simply computed from its spectral energy distribution, S_λ, as

$$N_{\rm Lyc} = \frac{1}{hc} \int_0^{\lambda_{\rm L}} d\lambda \; \lambda S_\lambda \,. \tag{1.11}$$

The fraction $T_{\rm ion}$ of Lyman continuum photons absorbed by gas rather than by dust in the H II regions is computed using the analytic formula derived by Petrosian, Silk & Field (1972):

$$T_{\rm ion} = \frac{(\hat{\tau}_{\lambda_{\rm L}}^{\rm H\,II})^3 \exp(-\hat{\tau}_{\lambda_{\rm L}}^{\rm H\,II})}{3\{(\hat{\tau}_{\lambda_{\rm L}}^{\rm HII})^2 - 2\tau_{\lambda_{\rm L}}^{\rm H\,II} + 2[1 - \exp(-\hat{\tau}_{\lambda_{\rm L}}^{\rm H\,II})]\}} \,, \tag{1.12}$$

where $\hat{\tau}_{\lambda_{\rm L}}^{\rm H\,II}$ is the dust effective optical depth at the Lyman limit, computed using the Charlot & Fall (2000) attenuation law. The ionization rate $\dot{N}$ can then be computed by multiplying the fraction of Lyman continuum photons transmitted to the gas by the number of Lyman continuum photons produced by the stars:

$$\dot{N} = \frac{T_{\rm ion}}{hc} \int_0^{\lambda_{\rm L}} d\lambda \; \lambda S_\lambda \,. \tag{1.13}$$

Charlot & Fall (2000) compute the emergent luminosities of the Hα and Hβ Balmer recombination lines, $S_{{\rm H}\alpha}$ and $S_{{\rm H}\beta}$, by assuming that, given an ionization rate $\dot{N}$, the production of all H recombination photons are the same as for the dust-free case B recombination (see Section 1.4.1 for a description of case B recombination). This assumption is validated by detailed photoionization models of H II regions which include the effects of dust (e.g. Ferland 1996). For realistic values of electron density and temperature, $n_e \lesssim 10^4$ cm^{-3} and $T_e \sim 10^4$ K, the luminosities of the Hα and Hβ Balmer lines are given by Osterbrock (1989):

$$S_{\mathrm{H}\alpha} = 0.450\ (hc/\lambda_{\mathrm{H}\alpha})\dot{N}\,, \tag{1.14}$$

$$S_{\mathrm{H}\beta} = 0.117\ (hc/\lambda_{\mathrm{H}\beta})\dot{N}\,. \tag{1.15}$$

It is assumed that the power radiated in the form of Lyα photons, $\tilde{S}_{\mathrm{Ly}\alpha} = 0.676\ (hc/\lambda_{\mathrm{Ly}\alpha})\dot{N}$ is eventually absorbed by dust as a consequence of resonant scattering.

The total power from ionizing radiation that neither is absorbed by dust nor emerges in the Hα and Hβ lines is computed and distributed uniformly between 3000 and 6000 Å, which is a range that includes most of the relevant emission lines. A more recent model by Charlot & Longhetti (2001) combines population synthesis models (Bruzual & Charlot 2003), the Charlot & Fall (2000) simple model for the attenuation by dust and photoionization models by Ferland (1996) to compute the nebular emission from H II regions including all the relevant lines from optical to infrared wavelengths (see Charlot & Longhetti 2001; Charlot et al. 2002).

In Chapter 2 of this thesis, we use the model of Charlot & Fall (2000) to account for the attenuation of galaxy spectral energy distributions by dust, and to compute the total energy (including line + continuum) absorbed and reradiated by dust in galaxies. The novelty of this thesis is to provide a simple prescription to compute the distribution in wavelength of the luminosity radiated by dust in the infrared. In the next section, we briefly review the most important elements of the emission by interstellar dust that are used as the physical motivation of the model presented in Chapter 2.

1.4.3.4 Emission by interstellar dust

Dust grains are heated mainly by the absorption of ultraviolet and optical photons and they cool down by reemitting the absorbed energy in the infrared[8]. This emission depends mainly on the the optical properties and the sizes of the grains.

The observed emission of the diffuse ISM of the Milky Way from 3 to 1000 μm is shown in Fig. 1.17. The total energy output from interstellar dust is dominated by the far-infrared emission of cold dust grains in thermal equilibrium. These grains radiate as modified black bodies[9] with this emission peaking at around 100 μm, which implies an equilibrium temperature of the grains of about 20 K. Dust grains of small sizes are not in thermal equilibrium with the radiation field, and they have strongly fluctuating temperatures (see Fig. 1.18), which can reach high values (of hundreds of degrees) by the absorption of single photons. Therefore these grains

---

[8] Collisions with interstellar gas also contribute to a small fraction of dust heating. We do not include this for simplicity.

[9] A ‘modified black body’ is a function of the form $\lambda^{-\beta}\ B_\lambda(T)$, where $B_\lambda(T)$ is the Planck function of temperature T.

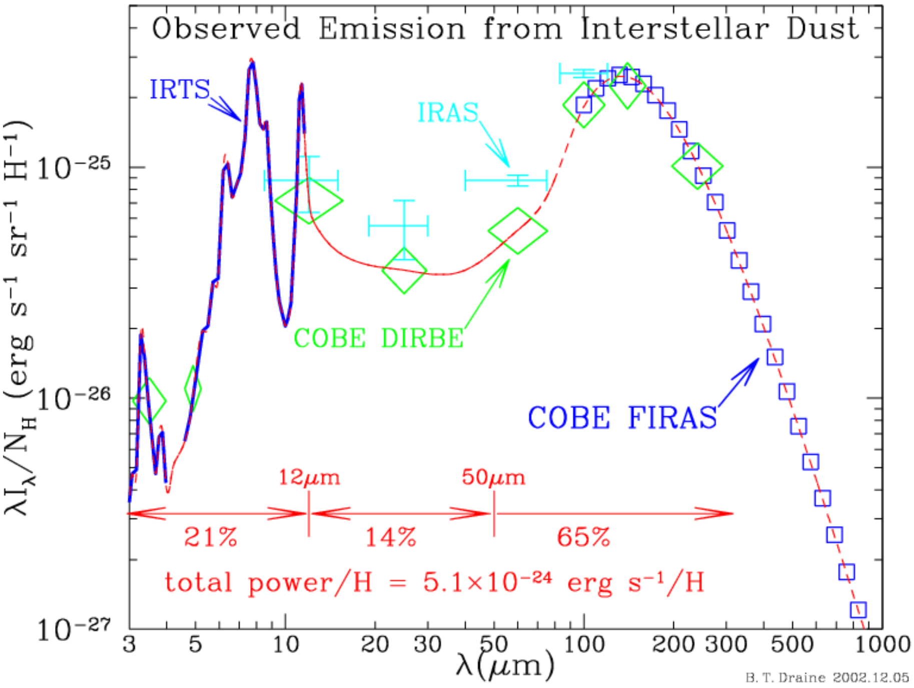

Figure 1.17: Emission from the diffuse interstellar dust of the Milky Way between 3 and 1000 μm, observed using various instruments: *crosses* – IRAS (Boulanger & Perault 1988); *squares* – *COBE*/FIRAS (Finkbeiner, Davis & Schlegel 1999); *diamonds* – *COBE*/DIRBE (Arendt et al. 1998); *blue line* – IRST (Onaka et al. 1996; Tanaka et al. 1996). Figure taken from Draine (2003).

emit at shorter wavelengths. The shape of the emission from these very small grains is different from a modified black body characteristic of thermal equilibrium emission. Finally, at wavelengths between 3 and 20 μm, emission features are observed, which are commonly attributed to large organic molecules in the ISM, the PAHs. These molecules are excited by optical and ultraviolet photons and their emission peaks in PDRs (Section 1.4.2).

Stochastic heating of dust grains. Interstellar dust grains embedded in a radiation field are heated through a stochastic process, the absorption of individual photons. Since the absorption efficiency increases with energy (until extreme ultraviolet wavelengths), the dust grains absorb mostly ultraviolet and optical photons.

The stochastic heating of dust grains by the absorption of individual photons is illustrated in Fig. 1.18. Also shown is the time variation of the temperatures of dust grains of four different sizes being heated by the average galactic radiation field. Small grains, with sizes $a \lesssim 100$ Å, have strongly fluctuating temperatures. The smaller the grains, the bigger is the amplitude of these fluctuations. Very small grains have very low heat capacities, thus the temperature of these grains will greatly increase when they absorb a single photon. The temperature can reach several hundred degrees if they absorb very energetic photons like UV. Further-

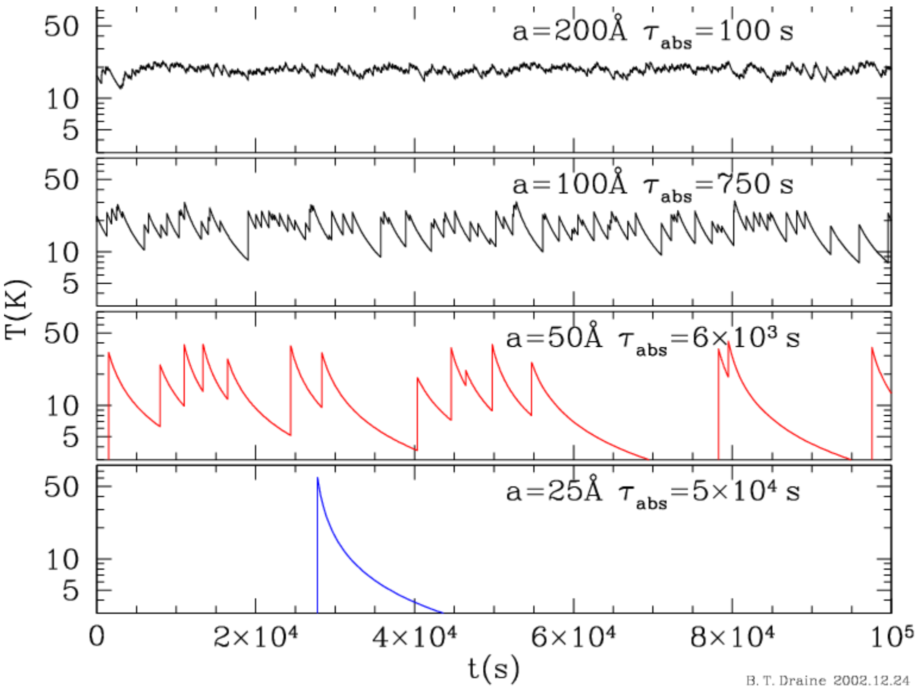

Figure 1.18: Interstellar dust grain temperature as a function of time for four grains of different radius a heated by the average galactic interstellar radiation field. Large grains (with $a \gtrsim 200$ Å) have nearly constant temperature. Smaller grains (with $a \lesssim 100$ Å) show a high increase in temperature after the absorption of an individual photon followed by a gradual decrease until the next photon absorption (the larger the radius, the larger the cross section of the grain, and therefore the time between two absorptions $\tau_{\rm abs}$ is smaller). Figure taken from Draine (2003).

more, these grains have very small effective cross sections. Hence, the time interval separating the absorption of photons absorptions is very long – it is longer than the cooling time.

The shape of the emitted spectrum does not depend upon the intensity of the incident radiation, as long as the interval between successive photon absorptions remains longer than the cooling time. However, the shape of the spectrum depends on the maximum temperature, which depends on the energy of the absorbed photon and on the size of the grain (which determines its heat capacity).

The rate at which spherical grains of radius a reemit the energy they have absorbed is

$$\frac{dE_{\rm em}}{dt} = \int_0^\infty \int_0^\infty d\lambda \, 4\pi a^2 \, Q_\lambda^{\rm abs} \, \pi B_\lambda(T) \, p(T) \, dT \, , \tag{1.16}$$

where Q_λ^{abs} is the emission efficiency and $p(T)$ is the probability that the grains have a temperature between T and $T + dT$.

Dust grains of different sizes will undergo different temperature fluctuations, as previously discussed (see Fig. 1.18). Therefore, the temperature distribution

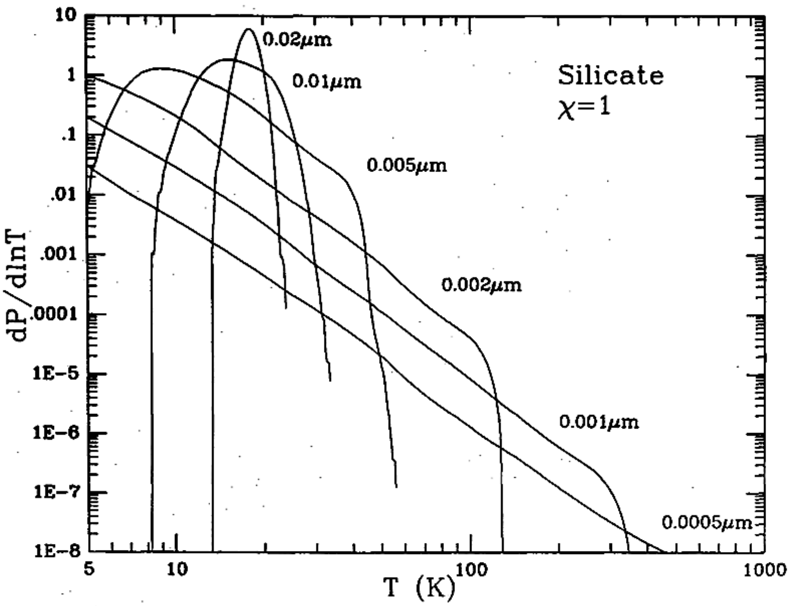

Figure 1.19: Temperature distributions for silicate grains of various sizes exposed to the interstellar radiation field. $P(T)$ is the probability of finding a grain with temperature higher than T. Each curve is labelled by the grain radius a. Figure taken from Draine & Anderson (1985).

$p(T)$ is driven primarily by the size of the grains. Draine & Anderson (1985) computed $p(T)$ using the optical properties of graphite and silicate grains from Draine & Lee (1984) for different size distributions (see also, e.g. Purcell 1976; Aannestad & Kenyon 1979; Guhathakurta & Draine 1989; Draine & Li 2001). In Fig. 1.19, we show the Draine & Anderson (1985) temperature distributions for silicate grains of various radii from 5 to 200 Å, exposed to the typical interstellar radiation field of the Milky Way. The smallest grains correspond to very broad probability distributions, because their temperatures fluctuate the most. As the size of the grains increases, the maximum temperature reached by the absorption of a single photon decreases. The temperature distribution also becomes less broad as the size of the grains increases, because the time between photon absorptions decreases, making the temperature fluctuate less.

Thermal equilibrium. Figs. 1.18 and 1.19 show that big grains, with sizes greater than about 200 Å, have nearly constant temperatures – these grains are in thermal equilibrium with the radiation field. In fact, the temperature distribution of big grains (plotted in Fig. 1.19) can be approximated by a delta function $\delta(T - T_{\rm eq})$, where $T_{\rm eq}$ is the equilibrium (or steady-state) temperature, in equation 1.16. The equilibrium temperature is determined by computing the balance between the total energy absorbed $E_{\rm abs}$ and the total energy emitted $E_{\rm em}$ by the grain,

$$E_{\rm abs} = E_{\rm em} \implies c \int_0^\infty d\lambda \, Q_\lambda^{\rm abs} \, u_\lambda = 4\pi \int_0^\infty d\lambda \, Q_\lambda^{\rm abs} \, B_\lambda(T_{\rm eq}) \, , \tag{1.17}$$

where u_λ is the energy density of the radiation field heating the grains. For reference, Mathis, Mezger & Panagia (1983) propose an interstellar radiation field for the solar neighbourhood consisting of three black bodies at temperatures 3000, 4000 and 7500 K (to account for the emission from stars at optical and near-infrared wavelengths), plus an ultraviolet component from young, hot stars which dominates the emission between 912 and 2500 Å. As we have seen before, most of the absorption of energy occurs in the ultraviolet and optical, because of the wavelength dependence of the absorption efficiency. Since dust grains in equilibrium reach low temperatures (typically between 15 and 25 K), most of the thermal emission is radiated at far-nfrared wavelengths.

The emission efficiency of the dust is often approximated by a power-law: $Q_\lambda^{\rm abs} \propto \lambda^{-\beta}$, where the exponent β varies typically between 1 and 2. The exact value of β depends on the physical properties of the grains. The emission from grains in thermal equilibrium at temperature $T_{\rm eq}$ is equivalent to a modified black body, described as $\lambda^{-\beta} B_\lambda(T_{\rm eq})$, which peaks at wavelength $\lambda_{\rm max} = 2900[(5+\beta)/5]/T_{\rm eq}$, where $\lambda_{\rm max}$ is in μm and $T_{\rm eq}$ in K (e.g., Mezger, Mathis & Panagia 1982).

Total emission from graphite and silicate grains. In Fig. 1.20, we show the emission spectra of mixtures of graphite and silicate grains heated by the average interstellar radiation field. This was computed by Draine & Anderson (1985) by integrating the emission from a mixture of graphite and silicate dust grains, each type following a distribution of sizes $n_i(a)$ and a distribution of temperatures $P_i(a,T)$:

$$\frac{I_\lambda}{N_{\rm H}} = \sum_{i=1}^{2} \int_{a_{\rm min}}^{a_{\rm max}} da \frac{dn_i}{da} \, Q_\lambda^{\rm abs} \, \pi a^2 \int_0^\infty \frac{dT}{T} \frac{dP_i(a,T)}{d\ln T} \, B_\lambda(T) \, , \tag{1.18}$$

where $I_\lambda/N_{\rm H}$ is the flux density per unit solid angle, per column density of H atoms, and the sum is performed for two types of dust grains i, graphite and silicates. The emission at mid-infrared wavelengths ($\lambda \lesssim 40$ μm) is dominated by the emission from very small grains heated stochastically to high temperatures – this emission depends strongly on the size distribution of the grains. At far-infrared wavelengths ($\lambda \gtrsim 40$ μm), the emission resembles a modified black body, since big grains in thermal equilibrium dominate the emission at these wavelengths.

Mid-infrared emission features. In addition to the continuum emission described above, the infrared spectrum of the ISM of the Milky Way (e.g. Fig. 1.17) and external galaxies presents strong emission features in the mid-infrared (between 3 and 20 μm). These features were first observed in the spectrum of reflection nebulae by Sellgren (1984) and are commonly attributed to polycyclic aromatic

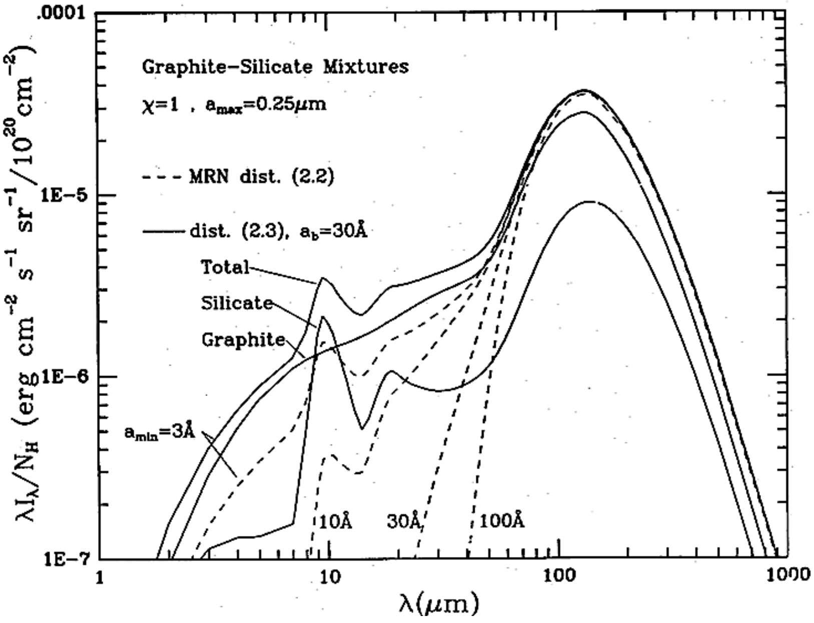

Figure 1.20: Emission spectra of mixtures of graphite and silicate grains with various size distributions, heated by the average interstellar radiation field. Curves are labelled by $a_{\rm min}$, the lower cutoff on the size distribution; an upper cutoff $a_{\rm max} = 0.25$ μm is taken in all cases. The dashed lines are for a classical Mathis, Rumpl & Nordsieck (1977) size distribution, whereas the plain lines show a size distribution with a higher relative quantity of small particles. Figure taken from Draine & Anderson (1985).

Table 1.2: Processes which cause the main infrared aromatic features observed in astrophysical media (Tielens 2005).

3.3 μm	Stretching mode of C–H attached to an aromatic ring
6.2 μm	C–C stretch in aromatic solid or molecule
7.7 μm	C–C stretch in aromatic solid or molecule
8.6 μm	C–H in-plane bending modes
11.3 μm	C–H out-of plane bending modes
12.7 μm	C–H out-of plane bending modes
16.4 μm	C–C–C bending modes in pendant ring

hydrocarbons. PAH emission contributes with an important fraction of the total interstellar dust emission. PAHs features are observed mostly in photodissociation regions (PDRs) at the interface between H II regions and molecular clouds (see Fig. 1.14), but also in the diffuse ISM, in reflection nebulae or in planetary nebulae. The strongest features are located at 3.3, 6.2, 7.7, 8.6, 11.3, 12.7 and 16.4 μm (see Fig. 1.21). These features correspond to vibrational, stretching and bending modes of PAH molecules (see Table 1.2) excited to high energy levels by the absorption of

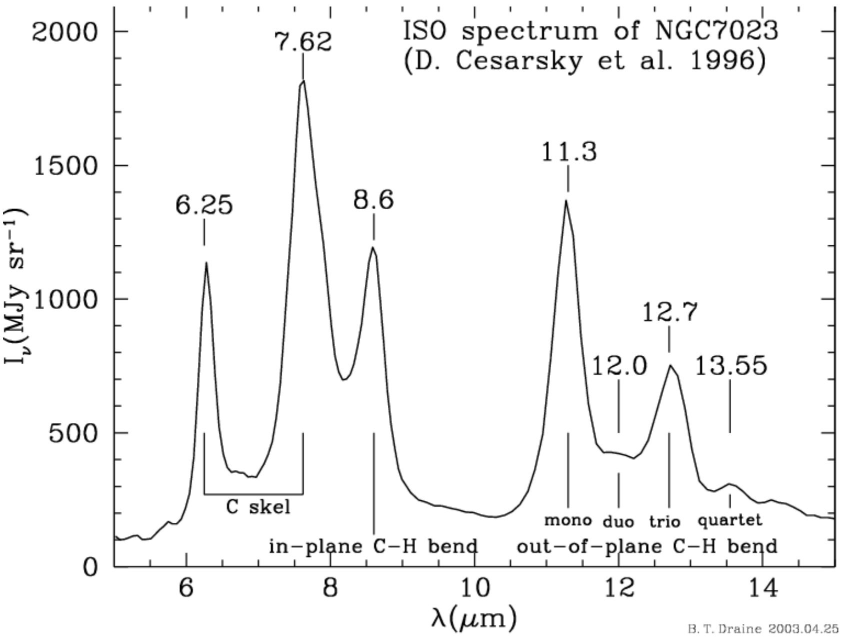

Figure 1.21: Emission spectrum of the reflection nebula NGC 7023 measured by *ISO*/ISOCAM (Cesarsky et al. 1996). Some of the most important aromatic features are shown. Figure taken from Draine (2003).

single ultraviolet and optical photons (Leger & Puget 1984; Allamandola, Tielens & Barker 1985).

The emission from PAH molecules depends upon their number of carbon atoms, their hydrogenation (number of H atoms per C atoms), and their ionization state. In detailed studies of the PAH emission in different interstellar environments, it is observed that extreme physical conditions (such as intense and hard radiation fields, for example, in H II regions or in the proximity of AGN) may cause large variations of the PAH emission, since the PAH molecules in these sites can be ionized or even destroyed (e.g. Omont 1986).

PAHs emission from galaxies. Observations with ISOCAM in the 1990's provided mid-infrared spectra of large numbers of objects, including nearby galaxies. More recently, further observations with higher resolution have become available from the IRS spectrograph on board of the *Spitzer* Space Telescope. We will analyse in more detail such spectra in Chapter 4.

PAH features similar to the ones observed in Galactic PDRs (e.g. Fig. 1.21) are common in the mid-infrared spectra of starforming galaxies, overlayed on a continuum from hot, stochastically-heated small grains. This is illustrated in Fig. 1.22, which shows the typical mid-infrared spectrum of a starburst galaxy obtained by Brandl et al. (2006).

One of the most important results of the first *ISO* observations of the mid-infrared spectra of normal galaxies was the observation that the relative strengths of

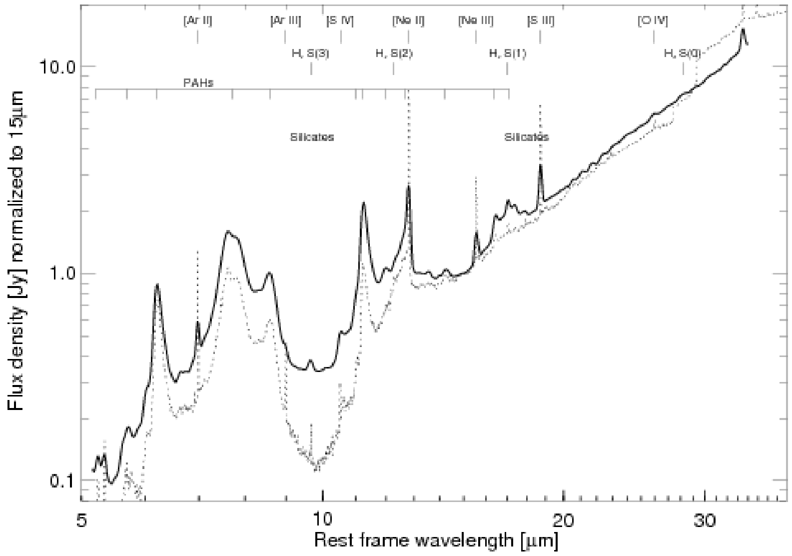

Figure 1.22: Average *Spitzer*/IRS spectrum of 13 starburst galaxies (solid line), compared with the *ISO*/SWS spectrum of the galaxy M 82 (dotted line) observed by Sturm et al. (2000). Figure taken from Brandl et al. (2006).

the different PAH features does not vary substantially with galaxy properties such as their infrared colours (Helou et al. 2000). This result suggested that PAH particles are not in thermal equilibrium, otherwise their emission would vary with infrared colours that are sensitive to the strength of the radiation field, such as the ratio between the 60-μm and 100-μm *IRAS* fluxes. In general, this can be explained by the fact that variations in the PAH emission found locally in galactic environments are all smoothed out when observing the large-scale, integrated emission from entire galaxies (e.g. Brandl et al. 2006).

We note, however, that recent studies with the *Spitzer Space Telescope* (e.g. Smith et al. 2007) show that there can be significant variations between the line strengths of PAH features in the integrated emission from galaxies. This occurs mainly in galaxies which harbour an AGN. The AGN provides a hard radiation field which may ionize or even destroy PAH molecules in the ISM(Allamandola, Hudgins & Sandford 1999; Li & Draine 2001; Draine & Li 2007; Smith et al. 2007). As a consequence, for some galaxies harbouring AGN, no PAH emission (or very little) is detected in the mid-infrared spectra. This can be caused by two effects: (i) the radiation from the AGN may completely destroy the PAH molecules; (ii) the PAH features are diluted in the strong mid-infrared continuum from very hot small grains heated by the AGN. These emission characteristics may provide useful a way to identify AGN using mid-infrared spectra (e.g. Sturm et al. 2000; Laurent et al. 2000; Smith et al. 2007; see Fig. 1.23 for a comparison between the mid-infrared spectrum of star-forming regions and AGN).

Another important factor driving PAH emission in galaxies is metallicity. In

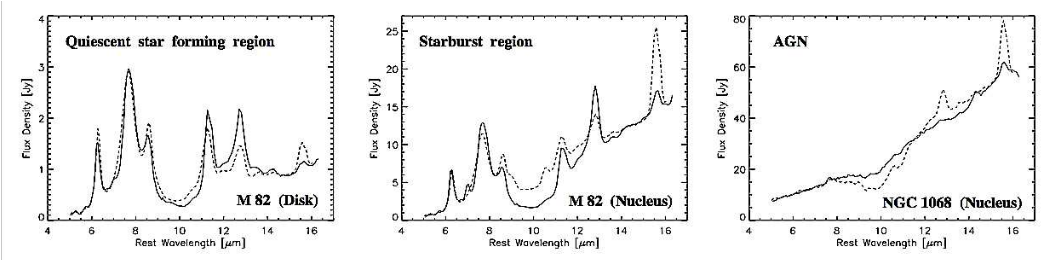

Figure 1.23: Examples of observed mid-infrared spectra (solid lines) of a quiescent starforming region (M 82 disk), a starburst region (M 82 nucleus) and an AGN (NGC 1068 nucleus). Both starforming regions show strong PAH emission, and the main difference between the two is a stronger continuum from stochastically heated small grains in the starburst region. In the AGN, there is practically no PAH emission due to destruction by the hard AGN radiation field, or dilution in the strong continuum from small grains. Figure taken from Laurent et al. (2000).

low-metallicity galaxies (with metallicities lower than 0.25 $Z_\odot$), observations show that PAH emission is suppressed (e.g. Engelbracht et al. 2005; Madden et al. 2006; Smith et al. 2007; Draine et al. 2007). This result is a combination of several effects: (i) at low metallicities, there are less carbon atoms available to produce PAH molecules; (ii) low-metallicity environments such as blue dwarf galaxies tend to form massive stars which generate harder radiation fields; (iii) at low metallicities, there is less dust production, and therefore PAH molecules are less shielded from intense radiation fields.

In the following chapters of this thesis, we will assume, for simplicity, that the shape of the integrated PAHs emission from galaxies is nearly constant. In Chapter 4 we will analyse the detailed mid-infrared spectroscopy of a sample of local galaxies. This analysis will enable us to validate our approach and discuss possible limitations.

1.5 Summary

In this chapter, we outlined the motivation of this thesis and we have provided the basic elements which allow us to compute the integrated emission of galaxies by taking into account the production of starlight in galaxies and its transfer through the ISM.

In Section 1.3, we have reviewed the basic elements of evolutionary synthesis models, with special focus on the models of Bruzual & Charlot (2003), which we will use to compute the integrated emission from stellar populations in galaxies in the next chapters of this thesis. The main ingredients of these models are:

- evolutionary tracks of stars of different initial masses and chemical compositions in the H-R diagram, which allow us to compute isochrones, i.e. define the positions of all the different stars in the H-R diagram at a given time;

- the initial mass function, which determines the proportions of stars of different masses in formed in a generation of stars;
- libraries of stellar spectra, which are used to assign ultraviolet-to-infrared spectra to each star along the isochrone.

Some models may include a chemical evolution prescription, which allows to compute the time-dependence of the overall metallicity of galaxies [$\zeta(t-t')$ in equation (2.1)], as stars produce and eject heavy elements in the ISM throughout their lives. In this thesis, we assume constant metallicities for galaxies.

The evolution of star formation rate with time is the other fundamental ingredient to compute the total spectrum from a galaxy. The integrated light from a galaxy is computed as the sum of the spectra of the different generations of stars (SSPs) it contains, weighted by the star formation rate (equation 2.1). We have seen in Section 1.3.3 that the different spectral energy distributions of galaxies along the Hubble sequence can be attributed to different histories of star formation in these galaxies.

The light produced by stars in galaxies interacts with gas and dust in the interstellar medium of galaxies before reaching us. Therefore, to fully understand and model the integrated, multi-wavelength emission from galaxies, we need to take into account the physical processes that take place in the ISM of galaxies.

In Section 1.4, we have presented an overview of the different components of the interstellar medium in galaxies, concentrating on the main interactions that occur between interstellar matter and the radiation produced by stars which originate strong signatures in the ultraviolet-to-infrared spectral energy distributions of galaxies.

The interstellar medium of star-forming galaxies is mainly organized in two components:

- Star-forming regions: these are dense molecular clouds which collapse gravitationally and form new stars. The radiation produced by newly-born OB stars ionizes the surrounding gas, producing an H II region, which is surrounded by a layer of H I. The typical lifetime of these clouds is 10^7 yr.
- Diffuse ISM: this is the intercloud medium, which is less dense and composed mainly of H I, although some H II and H_2 may also exist, as well as other molecules, atoms and ions of heavier elements. This component constitutes the bulk of the mass of the ISM in galaxies and it is heated mainly by stars older than 10^7 yr, which have already left their birth clouds.

When studying the integrated spectral energy distributions of star-forming galaxies, the main observable effects from the interaction between starlight and dust are:

- The emission lines (recombination and forbidden lines) from ionized regions (H II regions).

- The attenuation of lines and continuum due to dust absorption.
- The emission from different dust components at mid- and far-infrared wavelengths.

In Chapter 2, we build a simple model for the emission by dust in galaxies based on the theoretical and observational results presented in Section 1.4.3.4. This prescription is associated with the Bruzual & Charlot (2003) stellar population synthesis model (discussed in Section 1.3.2) and the simple, angle-averaged dust attenuation model by Charlot & Fall (2000), presented in Section 1.4.2.

Chapter 2

A simple model to interpret the ultraviolet, optical and infrared emission from galaxies

This chapter is extracted from the paper *A simple model to interpret the ultraviolet, optical and infrared emission from galaxies*, by Elisabete da Cunha, Stéphane Charlot and David Elbaz, published in the Monthly Notices of the Royal Astronomical Society (da Cunha, Charlot & Elbaz 2008).

2.1 Introduction

The spectral energy distributions of galaxies contain valuable information about their contents in stars, gas and dust. Direct ultraviolet, optical and near-infrared radiation from stars provides clues on the past star formation history, chemical enrichment and attenuation by dust. Nebular emission lines produced by the gas heated by young stars provide further clues on the current star formation activity and the physical conditions of the star-forming gas. At wavelengths $\lambda \gtrsim 3\ \mu$m, the mid- and far-infrared emission reflects the heating of dust in different components of the interstellar medium (ISM) by stars of all ages. Observations at ultraviolet, optical and infrared wavelengths are now becoming available for large samples of galaxies. These include data collected in the ultraviolet by the *Galaxy Evolution Explorer* (*GALEX*, Martin et al. 2005), in the optical by the Two-degree Field Galaxy Redshift Survey (Colless et al. 2001) and the Sloan Digital Sky Survey (SDSS, Stoughton et al. 2002), in the near-infrared by the Two Micron All Sky Survey (2MASS, Skrutskie et al. 1997), in the mid- and far-infrared by the *Infrared Astronomical Satellite* (*IRAS*, Beichman et al. 1988), the *Infrared Space Observatory* (*ISO*, Kessler et al. 1996) and the *Spitzer Space Telescope* (Werner et al. 2004), and in the sub-millimetre by the Sub-millimeter Common User Bolometer Array (SCUBA) on the James Clerk Maxwell Telescope (Holland et al. 1999). Extracting constraints on the stellar populations and ISM of galaxies from these multi-wavelength observations requires the consistent modelling of the emission by stars, gas and dust.

A standard approach to model consistently the emission from stars and dust in galaxies has been to solve the radiative transfer equation for idealised (bulge + disc) spatial distributions of stars and dust (e.g. Rowan-Robinson 1980; Efstathiou & Rowan-Robinson 1990; Gordon et al. 2001; Misselt et al. 2001; Popescu et al.

2000; Misiriotis et al. 2001). Early models of this type did not include the evolution of stellar populations. Silva et al. (1998) were the first to couple radiative transfer through a dusty ISM and the spectral (and even chemical) evolution of stellar populations. Their model also accounts for the fact that stars are born in dense molecular clouds, which dissipate after some time, and hence, that newly born stars are more attenuated than older stars (see also, e.g., Charlot & Fall 2000; Tuffs et al. 2004). This type of sophisticated model is useful to interpret in detail the emission from individual galaxies in terms of constraints on stellar populations and the spatial distribution and physical properties of the dust. However, because of the complexity of radiative transfer computations, it is not optimised to derive statistical constraints from observations of large samples of galaxies.

A more recent model of starburst galaxies by Dopita et al. (2005 see also Groves et al. 2007) incorporates the consistent treatment of the spectral evolution of stellar populations, the dynamic expansion of H II regions and radiative transfer of starlight through gas and dust. The authors of this model provide a simple parameterization of the ultraviolet, optical and infrared spectra of starburst galaxies by adding the spectra of different types of compact H II regions and their surrounding photo-dissociation regions. This model provides a fast and flexible tool to interpret starburst galaxy spectra in terms of the physical parameters of star-forming regions. However, it is not designed to be applicable to more quiescent galaxies, in which older stellar populations dominate the emission.

In parallel to these theoretical studies, observations by *IRAS* and *ISO* have motivated the development of simple, empirically calibrated spectral libraries to interpret the infrared emission from galaxies at wavelengths between 3 and 1000 μm. For example, Chary & Elbaz (2001) and Dale & Helou (2002) both present single-parameter families of infrared spectra to relate an observed spectral energy distribution to either the total infrared luminosity of a galaxy or the intensity of the interstellar radiation field heating the dust. These libraries can be applied easily to the interpretation of large galaxy samples. They have proved useful to characterise the infrared emission from observed galaxies and to investigate the origin of the cosmic infrared background (e.g. Franceschini et al. 2001; Chary & Elbaz 2001; Elbaz et al. 2002; Lagache, Dole & Puget 2003; Lagache et al. 2004; Dale et al. 2005; Marcillac et al. 2006). A disadvantage of this approach is that it does not relate consistently the infrared emission of the dust to the emission from stellar populations. Another potential limitation is that most existing spectral libraries were calibrated using local galaxy samples, and hence, they may not be applicable to studies of the infrared emission from galaxies at all redshifts (e.g. Pope et al. 2006; Zheng et al. 2007).

In this Chapter, we present a simple, largely empirical but physically motivated model to interpret the mid- and far-infrared spectral energy distributions of galaxies consistently with the emission at ultraviolet, optical and near-infrared wavelengths. We compute the spectral evolution of stellar populations using the Bruzual & Charlot (2003) population synthesis code. To describe the attenuation of starlight by dust, we appeal to the two-component model of Charlot & Fall (2000). This has been shown to account for the observed relations between the ultraviolet and optical (line and continuum) spectra and the *total* infrared luminosities of galaxies in wide ranges of star-formation activity and dust content (Brinchmann et al. 2004; Kong et al. 2004). We use this model to compute the luminosity absorbed and re-emitted by dust in stellar birth clouds (i.e. giant molecular clouds) and in the ambient (i.e. diffuse) ISM in galaxies. We then distribute this luminosity in wavelength to compute infrared *spectral energy distributions*. We describe the infrared emission from stellar birth clouds as the sum of three components: a component of polycyclic aromatic hydrocarbons (PAHs); a mid-infrared continuum characterising the emission from hot grains at temperatures in the range 130–250 K; and a component of grains in thermal equilibrium with adjustable temperature in the range 30–60 K. In the ambient ISM, we fix for simplicity the relative proportions of these three components to reproduce the spectral shape of diffuse cirrus emission in the Milky Way, and we include a component of cold grains in thermal equilibrium with adjustable temperature in the range 15–25 K.

2.2 The model

In this section, we describe our model to compute the mid- and far-infrared spectral energy distributions of galaxies consistently with the emission at ultraviolet, optical and near-infrared wavelengths. In Section 2.2.1, we first briefly review the stellar population synthesis code and the two-component dust model used to compute the emission of starlight and its transfer through the ISM in galaxies. Then, in Section 2.2.2, we present our model to compute the spectral energy distribution of the infrared emission from dust. We calibrate this model using a sample of 107 nearby star-forming galaxies observed by *IRAS* and *ISO*. In Section 2.2.3, we show examples of combined ultraviolet, optical and infrared spectral energy distributions of different types of star-forming galaxies.

2.2.1 Stellar emission and attenuation by dust

We use the latest version of the Bruzual & Charlot (2003) stellar population synthesis code to compute the light produced by stars in galaxies. This code predicts the spectral evolution of stellar populations at wavelengths from 91 Å to 160 μm and at ages between 1×10^5 and 2×10^{10} years, for different metallicities, initial mass functions (IMFs) and star formation histories. We use the most recent version of the code, which incorporates a new prescription by Marigo & Girardi (2007) for the TP-AGB evolution of low- and intermediate-mass stars. The main effect of this prescription is to improve the predicted near-infrared colours of intermediate-age stellar populations (Bruzual 2007; see also Charlot & Bruzual, in preparation). In all applications throughout this thesis, we adopt the Galactic-disc IMF of Chabrier (2003). More details about these models can be found in Section 1.3.

We compute the attenuation of starlight by dust using the simple, angle-averaged model of Charlot & Fall (2000). This accounts for the fact that stars are born in dense molecular clouds, which dissipate typically on a timescale $t_0 \sim 10^7$ yr. Thus the emission from stars younger than t_0 is more attenuated than that from older stars (see Fig. 1.13 for a schematic representation of the two components of this model and Section 1.4.2 for a detailed description of the ISM in this thesis). Following Charlot & Fall (2000), we express the luminosity per unit wavelength emerging at time t from a galaxy as

$$L_\lambda(t) = \int_0^t dt' \psi(t-t')\, S_\lambda(t')\, e^{-\hat{\tau}_\lambda(t')} \,, \tag{2.1}$$

where $\psi(t-t')$ is the star formation rate at time $t-t'$, $S_\lambda(t')$ is the luminosity per unit wavelength per unit mass emitted by a stellar generation of age t', and $\hat{\tau}_\lambda(t')$ is the 'effective' absorption optical depth of the dust seen by stars of age t' (i.e. averaged over photons emitted in all directions by stars in all locations within the galaxy). The time dependence of $\hat{\tau}_\lambda$ reflects the different attenuation affecting young and old stars in galaxies,

$$\hat{\tau}_\lambda(t') = \begin{cases} \hat{\tau}_\lambda^{\mathrm{BC}} + \hat{\tau}_\lambda^{\mathrm{ISM}} & \text{for } t' \leq t_0, \\ \hat{\tau}_\lambda^{\mathrm{ISM}} & \text{for } t' > t_0. \end{cases} \tag{2.2}$$

Here $\hat{\tau}_\lambda^{\mathrm{BC}}$ is the effective absorption optical depth of the dust in stellar birth clouds and $\hat{\tau}_\lambda^{\mathrm{ISM}}$ that in the ambient ISM. We also adopt the prescription of Charlot & Fall (2000) to compute the emergent luminosities $L_{\mathrm{H}\alpha}(t)$ and $L_{\mathrm{H}\beta}(t)$ of the Hα ($\lambda = 6563$ Å) and Hβ ($\lambda = 4861$ Å) Balmer lines of hydrogen produced by stars in the birth clouds. This assumes case B recombination and includes the possible absorption of ionising photons by dust before they ionise hydrogen.

The shape of the effective absorption curve depends on the combination of the optical properties and spatial distribution of the dust. We adopt the following dependence of $\hat{\tau}_\lambda^{\mathrm{BC}}$ and $\hat{\tau}_\lambda^{\mathrm{ISM}}$ on wavelength:

$$\hat{\tau}_\lambda^{\mathrm{BC}} = (1-\mu)\hat{\tau}_V \left(\lambda/5500\,\text{Å}\right)^{-1.3} \,, \tag{2.3}$$

$$\hat{\tau}_\lambda^{\mathrm{ISM}} = \mu\hat{\tau}_V \left(\lambda/5500\,\text{Å}\right)^{-0.7} \,, \tag{2.4}$$

where $\hat{\tau}_V$ is the total effective V-band absorption optical depth of the dust seen by young stars inside birth clouds, and $\mu = \hat{\tau}_V^{\mathrm{ISM}}/(\hat{\tau}_V^{\mathrm{BC}} + \hat{\tau}_V^{\mathrm{ISM}})$ is the fraction of this contributed by dust in the ambient ISM. The dependence of $\hat{\tau}_\lambda^{\mathrm{ISM}}$ on $\lambda^{-0.7}$ is well constrained by the observed relation between ratio of far-infrared to ultraviolet luminosity and ultraviolet spectral slope for nearby starburst galaxies (see Charlot & Fall 2000). The dependence of $\hat{\tau}_\lambda^{\mathrm{BC}}$ on wavelength is less constrained by these observations, because stellar birth clouds tend to be optically thick, and hence, stars in these clouds contribute very little to the emergent radiation (except in the emission lines). For simplicity, Charlot & Fall (2000) adopt $\hat{\tau}_\lambda^{\mathrm{BC}} \propto \lambda^{-0.7}$ by analogy with $\hat{\tau}_\lambda^{\mathrm{ISM}}$. We adopt here a slightly steeper dependence, $\hat{\tau}_\lambda^{\mathrm{BC}} \propto \lambda^{-1.3}$ (equation 5.4), which corresponds to the middle range of the optical properties of dust grains between the Milky Way, the Large and the Small Magellanic Clouds (see section 4 of Charlot & Fall 2000). This choice is motivated by the fact that giant molecular clouds can be assimilated to foreground shells when attenuating the light from newly born stars. In this case, the effective absorption curve should reflect the actual optical properties of dust grains. We emphasise that the dependence of $\hat{\tau}_\lambda^{\rm BC}$ on wavelength has a negligible influence on the emergent ultraviolet and optical continuum radiation. It affects mainly the attenuation of emission lines in galaxies with large $\hat{\tau}_V^{\rm BC}/\hat{\tau}_V^{\rm ISM}$ and hence small μ (Section 3.5.2 below; see also Wild et al. 2007).

The fraction of stellar radiation absorbed by dust in the stellar birth clouds and in the ambient ISM is reradiated in the infrared. We write the total luminosity absorbed and reradiated by dust as the sum

$$L_{\rm d}^{\rm tot}(t) = L_{\rm d}^{\rm BC}(t) + L_{\rm d}^{\rm ISM}(t)\,, \tag{2.5}$$

where

$$L_{\rm d}^{\rm BC}(t) = \int_0^\infty d\lambda \left(1 - e^{-\hat{\tau}_\lambda^{\rm BC}}\right) \int_0^{t_0} dt'\psi(t-t')S_\lambda(t') \tag{2.6}$$

is the total infrared luminosity contributed by dust in the birth clouds, and

$$L_{\rm d}^{\rm ISM}(t) = \int_0^\infty d\lambda \left(1 - e^{-\hat{\tau}_\lambda^{\rm ISM}}\right) \int_{t_0}^{t} dt'\psi(t-t')S_\lambda(t') \tag{2.7}$$

is the total infrared luminosity contributed by dust in the ambient ISM. For some purposes, it is also convenient to define the fraction of the total infrared luminosity contributed by the dust in the ambient ISM:

$$f_\mu(t) \equiv L_{\rm d}^{\rm ISM}(t)/L_{\rm d}^{\rm tot}(t)\,. \tag{2.8}$$

This depends on the total effective V-band absorption optical depth of the dust, $\hat{\tau}_V$, the fraction μ of this contributed by dust in the ambient ISM, and the star formation history (and IMF) determining the relative proportion of young and old stars in the galaxy.

2.2.2 Infrared emission of the dust

We now present a simple but physically motivated prescription to compute the spectral distribution of the energy reradiated by dust in the infrared (i.e. , the distribution in wavelength of $L_{\rm d}^{\rm BC}$ and $L_{\rm d}^{\rm ISM}$). By construction, the infrared emission computed in this way can be related to the emission at shorter wavelengths using equations (2.1)–(2.7) above.

2.2.2.1 Components of infrared emission

We have seen in Section 1.4.3 that the infrared emission from galaxies is generally attributed to three main constituents of interstellar dust: polycyclic aromatic hydrocarbons (PAHs), which produce strong emission features at wavelengths between 3 and 20 μm; ‘very small grains’ (with sizes typically less than 0.01 μm), which are stochastically heated to high temperatures by the absorption of single ultraviolet photons; and ‘big grains’ (with sizes typically between 0.01 and 0.25 μm), which are in thermal equilibrium with the radiation field. This picture arises from detailed models of the sizes and optical properties of dust grains and PAH molecules in the ISM of the Milky Way and other nearby galaxies (e.g., Mathis, Rumpl & Nordsieck 1977; Draine & Lee 1984; Leger & Puget 1984). Here, we build on the results from these studies to describe the different components of infrared emission in galaxies, without modelling in detail the physical properties of dust grains. As mentioned in Section 2.1, the motivation for this approach is to build a model simple enough to derive statistical constraints on the star formation and dust properties of large samples of observed galaxies, based on consistent fits of the ultraviolet, optical and infrared emission. We describe the different components of infrared emission in our model as follows:

(i) *PAH and near-infrared continuum emission.* The mid-infrared spectra of most normal star-forming galaxies are dominated by strong emission features at 3.3, 6.2, 7.7, 8.6, 11.3 and 12.7 μm. Although still uncertain, the carriers of these features are generally accepted to be PAH molecules transiently excited to high internal energy levels after the absorption of single ultraviolet photons (Leger & Puget 1984; Allamandola, Tielens & Barker 1985; Leger, D’Hendecourt & Defourneau 1989; Allamandola, Hudgins & Sandford 1999). PAH emission tends to peak in the ‘photo-dissociation regions’ (PDRs) at the interface between ionised and molecular gas in the outskirts of H II regions, where PAH molecules can survive and transient heating is most efficient (e.g., Cesarsky et al. 1996; Verstraete et al. 1996; Rapacioli, Joblin & Boissel 2005). In these environments, the non-ionising ultraviolet radiation from young stars dominates the energy balance and can dissociate molecules such as H_2 and CO (see Hollenbach & Tielens 1997 for a review).

Observations with *ISO*/ISOPHOT of the mid-infrared spectra of 45 nearby, normal star-forming galaxies do not reveal any strong variation of the PAH emission spectrum with galaxy properties such as infrared colours and infrared-to-blue luminosity ratio (Helou et al. 2000). For simplicity, we adopt a fixed template spectrum to describe PAH emission in our model.[1] We use the mid-infrared spectrum of the photo-dissociation region in the prototypical Galactic star-forming region M17 SW extracted from the *ISO*/ISOCAM

---

[1] In reality, changes in PAH molecule size and ionisation state, variations in metallicity and contamination by an AGN could cause variations of up to 40 per cent in the relative strengths of some PAH emission features (Helou et al. 2000; Brandl et al. 2006; Smith et al. 2007; Galliano, Dwek & Chanial 2007). We ignore this refinement here.

observations of Cesarsky et al. (1996) by Madden et al. (2006), shown in Fig. 1.14.The observed spectrum does not extend blueward of 5 μm. We extend it to include the 3.3 μm PAH emission feature using the Lorentzian profile parametrised by Verstraete et al. (2001), $F_\nu^{\rm Lorentz} = f_0[1 + (x - x_0)^2/\sigma^2]^{-1}$, where $x = 1/\lambda$ is the wavenumber, $x_0 = 3039.1$ cm^{-1} the central wavenumber of the feature and $\sigma = 19.4$ cm^{-1} half the FWHM. We set the amplitude f_0 so that the luminosity of the 3.3 μm emission feature is 10 per cent of that of the 11.3 μm feature (the relative ratio found by Li & Draine 2001 for neutral PAHs). We write the spectral energy distribution of PAHs in our model

$$l_\lambda^{\rm PAH} = L_\lambda^{\rm M17} \left(\int_0^\infty d\lambda \, L_\lambda^{\rm M17} \right)^{-1} , \tag{2.9}$$

where $L_\lambda^{\rm M17}$ is the adopted M17 spectral template, and $l_\lambda^{\rm PAH}$ is normalised to unit total energy.

The above *ISO*/ISOPHOT observations of a sample of 45 normal star-forming galaxies also reveal a component of near-infrared continuum emission characterised by a very high colour temperature ($\sim$ 1000 K) at wavelengths between 3 and 5 μm (Lu et al. 2003). This component accounts typically for at most a few percent of the total infrared luminosity, but it contributes significantly to the observed *Spitzer*/IRAC band fluxes at 3.6 and 4.5 μm. It is also present in the spectra of reflection nebulae (Sellgren, Werner & Dinerstein 1983) and in the diffuse cirrus emission of the Milky Way (Dwek et al. 1997; Flagey et al. 2006). The origin of this emission is still uncertain, and it could be related to the stochastic heating of PAH molecules or carbon grains (e.g. Flagey et al. 2006). Lu et al. (2003) find that the strength of this emission correlates well with that of PAH features in the spectra of the galaxies in their sample. In particular, the ratio of the continuum flux density at 4 μm to the mean flux density of the 7.7 μm PAH feature has a roughly constant value of 0.11.

To implement this component of near-infrared continuum emission associated to PAH emission in our model, we use a greybody (i.e. modified blackbody) function of the form (e.g., Hildebrand 1983)

$$l_\lambda^{T_{\rm d}} = \kappa_\lambda \, B_\lambda(T_{\rm d}) \left[\int_0^\infty d\lambda \, \kappa_\lambda \, B_\lambda(T_{\rm d}) \right]^{-1} , \tag{2.10}$$

where $B_\lambda(T_{\rm d})$ is the Planck function of temperature $T_{\rm d}$, κ_λ is the dust mass absorption coefficient, and $l_\lambda^{T_{\rm d}}$ is normalised to unit total energy. The dust mass absorption coefficient is usually approximated by a single power law of the form

$$\kappa_\lambda \propto \lambda^{-\beta} , \tag{2.11}$$

where β is the dust emissivity index. Models and observations of infrared to sub-millimetre dust emission and laboratory studies of carbonaceous and amorphous silicate grains suggest values of β in the range $1 \lesssim \beta \lesssim 2$, with some dependence on grain size and temperature (Andriesse 1974; Hildebrand 1983; Draine & Lee 1984; Reach et al. 1995; Agladze et al. 1996; Boulanger et al. 1996; Mennella et al. 1998; see also section 3.4 of Dunne & Eales 2001 and section 4 of Dale & Helou 2002 for discussions on the constraints on β). Typically, these studies favour $\beta \approx 1$ for small carbonaceous grains, which radiate most of their energy at mid-infrared wavelengths, and $\beta \approx 1.5 - 2$ for big silicate grains, which reach lower temperatures and radiate most of their energy at far-infrared and sub-millimeter wavelengths. We therefore adopt $\beta = 1$ in equation (2.11) to compute the near-infrared continuum emission in our model. We scale this emission so that the continuum flux density at 4 μm be 0.11 times the mean flux density of the 7.7 μm PAH feature (see above). We find that a temperature $T_{\rm d} = 850$ K provides optimal fits to the observed spectral energy distributions of galaxies at wavelengths between 3 and 5 μm (see, e.g., Fig. 2.1).

(ii) *Mid-infrared continuum emission from hot dust.* In addition to PAH features, the mid-infrared spectra of star-forming galaxies (out to wavelengths $\lambda \sim 40\,\mu$m) also include a component of smooth continuum emission. This component is generally attributed to a continuous distribution of small grains with very low heat capacity, which are stochastically heated to high temperatures by the absorption of single ultraviolet photons (e.g., Sellgren 1984). The accurate modelling of this emission would require the computation of temperature fluctuations of grains of different sizes and optical properties caused by the absorption of ultraviolet photons in different interstellar radiation fields (e.g. Purcell 1976; Aannestad & Kenyon 1979). For simplicity, in our model, we describe the 'hot' mid-infrared continuum emission as the sum of two greybodies (equation 2.10) of temperatures $T_{\rm d} = 130$ and 250 K, with equal contributions to the total infrared luminosity,

$$l_\lambda^{\rm MIR} = (l_\lambda^{250} + l_\lambda^{130}) \left[\int_0^\infty d\lambda \, (l_\lambda^{250} + l_\lambda^{130}) \right]^{-1} . \tag{2.12}$$

We find that these two temperatures reproduce in an optimal way the range of infrared colours of star-forming galaxies (see Section 2.2.2.2 below).

(iii) *Emission from grains in thermal equilibrium.* At far-infrared wavelengths, the emission from galaxies is generally dominated by dust grains in thermal equilibrium at low temperatures. The grain temperatures depend sensitively on the intensity of the interstellar radiation field. This is why the peak of the far-infrared spectral energy distribution of a galaxy is a good indicator of dust heating in the ISM.

We consider two types of grains in thermal equilibrium in our model: warm grains, which can reside both in stellar birth clouds and in the ambient ISM, with characteristic temperatures $T_{\mathrm{W}}^{\mathrm{BC}}$ and $T_{\mathrm{W}}^{\mathrm{ISM}}$, respectively; and cold grains, which can reside only in the ambient ISM, with characteristic temperature $T_{\mathrm{C}}^{\mathrm{ISM}}$. To account for the observed dispersion in the peak of the far-infrared emission of galaxies with different star formation activities, we allow the warm-grain temperature to vary between 30 and 60 K and the cold-grain temperature to vary between 15 and 25 K. We describe the emission from grains in thermal equilibrium using greybody spectra (equation 2.10) with emissivity index $\beta = 1.5$ for warm dust and $\beta = 2.0$ for cold dust (equation 2.11).

In summary, the infrared spectral energy distribution of stellar birth clouds in our model can be written

$$L_{\lambda,\mathrm{d}}^{\mathrm{BC}} = \left(\xi_{\mathrm{PAH}}^{\mathrm{BC}}\, l_{\lambda}^{\mathrm{PAH}} + \xi_{\mathrm{MIR}}^{\mathrm{BC}}\, l_{\lambda}^{\mathrm{MIR}} + \xi_{\mathrm{W}}^{\mathrm{BC}}\, l_{\lambda}^{T_{\mathrm{W}}^{\mathrm{BC}}}\right) (1 - f_{\mu})\, L_{\mathrm{d}}^{\mathrm{tot}}\,, \tag{2.13}$$

where $L_{\mathrm{d}}^{\mathrm{tot}}$ is the total infrared luminosity reradiated by dust (equation 5.5), f_{μ} is the fraction of this contributed by the ambient ISM (equation 2.8), $l_{\lambda}^{\mathrm{PAH}}$, $l_{\lambda}^{\mathrm{MIR}}$ and $l_{\lambda}^{T_{\mathrm{W}}^{\mathrm{BC}}}$ are computed using equations (2.9), (2.12) and (2.10), and $\xi_{\mathrm{PAH}}^{\mathrm{BC}}$, $\xi_{\mathrm{MIR}}^{\mathrm{BC}}$ and $\xi_{\mathrm{W}}^{\mathrm{BC}}$ are the relative contributions by PAHs, the hot mid-infrared continuum and grains in thermal equilibrium to the total infrared luminosity of the birth clouds. These satisfy the condition

$$\xi_{\mathrm{PAH}}^{\mathrm{BC}} + \xi_{\mathrm{MIR}}^{\mathrm{BC}} + \xi_{\mathrm{W}}^{\mathrm{BC}} = 1\,. \tag{2.14}$$

Similarly, the infrared spectral energy distribution of the ambient ISM can be written

$$L_{\lambda,\mathrm{d}}^{\mathrm{ISM}} = \left(\xi_{\mathrm{PAH}}^{\mathrm{ISM}}\, l_{\lambda}^{\mathrm{PAH}} + \xi_{\mathrm{MIR}}^{\mathrm{ISM}}\, l_{\lambda}^{\mathrm{MIR}} + \xi_{\mathrm{W}}^{\mathrm{ISM}}\, l_{\lambda}^{T_{\mathrm{W}}^{\mathrm{ISM}}} + \xi_{\mathrm{C}}^{\mathrm{ISM}}\, l_{\lambda}^{T_{\mathrm{C}}^{\mathrm{ISM}}}\right) f_{\mu} L_{\mathrm{d}}^{\mathrm{tot}}\,, \tag{2.15}$$

where $l_{\lambda}^{\mathrm{PAH}}$, $l_{\lambda}^{\mathrm{MIR}}$, $l_{\lambda}^{T_{\mathrm{W}}^{\mathrm{ISM}}}$ and $l_{\lambda}^{T_{\mathrm{C}}^{\mathrm{ISM}}}$ are computed using equations (2.9), (2.12) and (2.10), and $\xi_{\mathrm{PAH}}^{\mathrm{ISM}}$, $\xi_{\mathrm{MIR}}^{\mathrm{ISM}}$, $\xi_{\mathrm{W}}^{\mathrm{ISM}}$ and $\xi_{\mathrm{C}}^{\mathrm{ISM}}$ are the relative contributions by PAHs, the hot mid-infrared continuum and warm and cold grains in thermal equilibrium to the total infrared luminosity of the ISM. These satisfy the condition

$$\xi_{\mathrm{PAH}}^{\mathrm{ISM}} + \xi_{\mathrm{MIR}}^{\mathrm{ISM}} + \xi_{\mathrm{W}}^{\mathrm{ISM}} + \xi_{\mathrm{C}}^{\mathrm{ISM}} = 1\,. \tag{2.16}$$

In practice, we can fix the shape of the mid-infrared spectral energy distribution of the ambient ISM in our model to keep the number of adjustable parameters as small as possible. This is justified by the fact that the intensity of the average radiation field heating dust in the diffuse ISM of normal galaxies is roughly constant (e.g., Helou 1986). Moreover, sophisticated models of dust emission by Li & Draine (2001) and Draine & Li (2007) suggest that even large variations of the intensity of the interstellar radiation field have only a small influence on the overall shape of the diffuse mid-infrared spectral energy distribution. In these conditions, we can appeal for example to observations of high-Galactic-latitude (cirrus) dust emission in the Milky Way to constrain the mid-infrared spectral energy distribution of the ambient

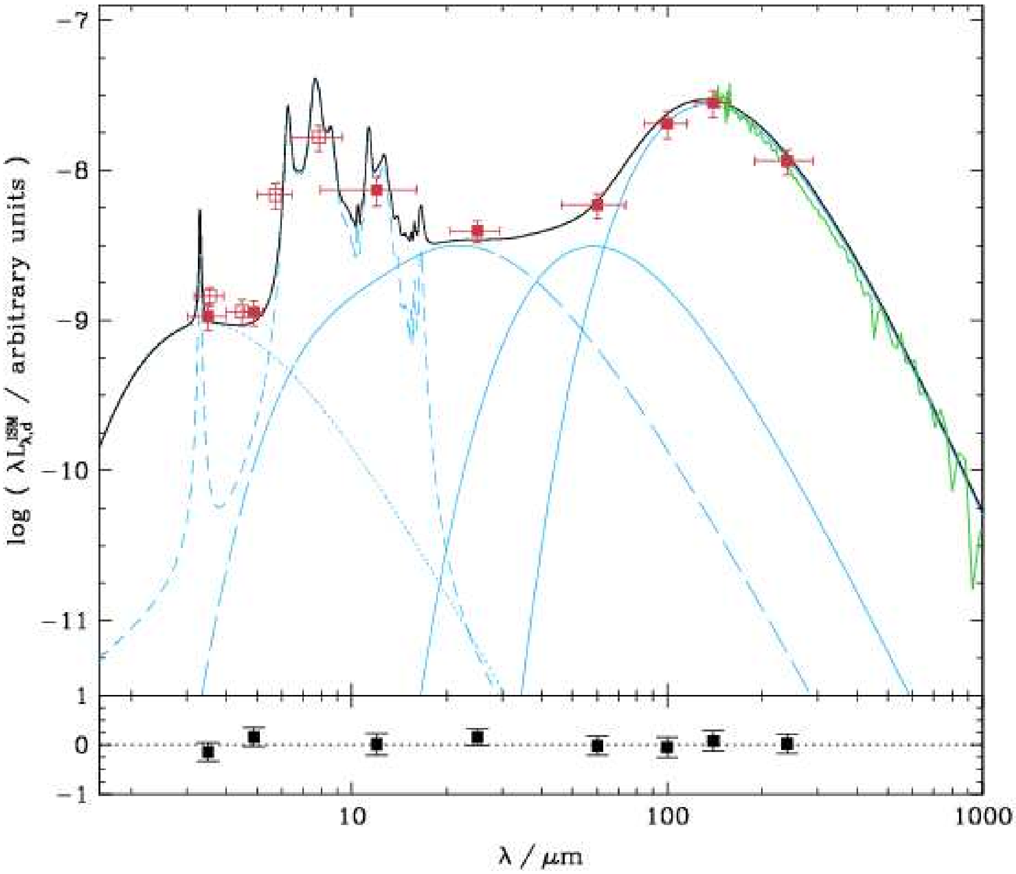

Figure 2.1: Best model fit (in black) to the observed mean spectral energy distribution of the Galactic cirrus emission. The model was computed using equation (2.15) and the parameters listed in equation (2.17). The red filled squares are the *COBE*/DIRBE observations of Dwek et al. (1997). Also shown for reference are the *Spitzer*/IRAC observations of Flagey et al. (2006,red open squares) and the *COBE*/FIRAS observations of Dwek et al. (1997,green line). The blue lines show the decomposition of the model in its different components (see Section 2.2.2): near-infrared continuum (*dotted*); PAHs (*short-dashed*); hot mid-infrared continuum (*long-dashed*) and warm and cold grains in thermal equilibrium (*solid*). The fit residuals $(L_\lambda^{\rm obs} - L_\lambda^{\rm mod})/L_\lambda^{\rm obs}$, where $L_\lambda^{\rm obs}$ and $L_\lambda^{\rm mod}$ are the observed and model fluxes in a given photometric band, are shown at the bottom.

ISM in our model. In Fig. 2.1, we show the model spectral energy distribution $L_{\lambda,{\rm d}}^{\rm ISM}$ (in black) computed using equation (2.15) that best fits the mean Galactic cirrus emission observed by the *Cosmic Background Explorer*/Diffuse Infrared Background Experiment (*COBE*/DIRBE) at wavelengths between 3.5 and 240 μm (Dwek et al. 1997). The blue lines show the different components of the best-fit model, with parameters

$$\begin{aligned} \xi_{\rm PAH}^{\rm ISM} &= 0.22 \\ \xi_{\rm MIR}^{\rm ISM} &= 0.11 \\ \xi_{\rm W}^{\rm ISM} &= 0.07 \\ \xi_{\rm C}^{\rm ISM} &= 0.60 \\ T_{\rm W}^{\rm ISM} &= 45\,{\rm K} \\ T_{\rm C}^{\rm ISM} &= 18\,{\rm K}\,. \end{aligned} \tag{2.17}$$

For reference, we include in Fig. 2.1 additional observations of the mean Galactic cirrus emission obtained with *Spitzer*/IRAC at wavelengths 3.6, 4.5, 5.8 and 8.0 μm (Flagey et al. 2006) and with the *COBE*/Far-Infrared Absolute Spectrophotometer (FIRAS) at wavelengths between 140 and 1000 μm (Dwek et al. 1997). The model reproduces these observations remarkably well, even though they were not included in the fit.

We use the constraints of Fig. 2.1 to fix the mid-infrared spectral energy distribution of the ambient ISM and reduce the number of adjustable parameters in our model. Specifically, we fix the relative contributions by PAHs, the hot mid-infrared continuum and warm grains in thermal equilibrium to the total infrared luminosity of the ambient ISM (i.e. the relative ratios of $\xi_{\rm PAH}^{\rm ISM}$, $\xi_{\rm MIR}^{\rm ISM}$ and $\xi_{\rm W}^{\rm ISM}$) to their values of equation (2.17), and we keep $\xi_{\rm C}^{\rm ISM}$ and $T_{\rm C}^{\rm ISM}$ as adjustable parameters. Thus, for a given contribution $\xi_{\rm C}^{\rm ISM}$ by cold grains in thermal equilibrium to the total infrared luminosity of the ambient ISM, the contributions by PAHs, the hot mid-infrared continuum and warm grains in thermal equilibrium are $\xi_{\rm PAH}^{\rm ISM} = 0.550(1-\xi_{\rm C}^{\rm ISM})$, $\xi_{\rm MIR}^{\rm ISM} = 0.275(1-\xi_{\rm C}^{\rm ISM})$ and $\xi_{\rm W}^{\rm ISM} = 0.175(1-\xi_{\rm C}^{\rm ISM})$, respectively.

The total spectral energy distribution of a galaxy in our model is computed as the sum

$$L_{\lambda,{\rm d}}^{\rm tot} = L_{\lambda,{\rm d}}^{\rm BC} + L_{\lambda,{\rm d}}^{\rm ISM}\,, \tag{2.18}$$

where $L_{\lambda,{\rm d}}^{\rm BC}$ and $L_{\lambda,{\rm d}}^{\rm ISM}$ are given by equations (2.13) and (2.15). For some purposes, it is also convenient to define the global contribution by a specific dust component, including stellar birth clouds and the ambient ISM, to the total infrared luminosity of a galaxy. This can be written

$$\xi_{\rm PAH}^{\rm tot} = \xi_{\rm PAH}^{\rm BC}\,(1-f_\mu) + 0.550\,(1-\xi_{\rm C}^{\rm ISM})\,f_\mu\,, \tag{2.19}$$

$$\xi_{\rm MIR}^{\rm tot} = \xi_{\rm MIR}^{\rm BC}\,(1-f_\mu) + 0.275\,(1-\xi_{\rm C}^{\rm ISM})\,f_\mu\,, \tag{2.20}$$

$$\xi_{\rm W}^{\rm tot} = \xi_{\rm W}^{\rm BC}\,(1-f_\mu) + 0.175\,(1-\xi_{\rm C}^{\rm ISM})\,f_\mu\,, \tag{2.21}$$

$$\xi_{\rm C}^{\rm tot} = \xi_{\rm C}^{\rm ISM}\,f_\mu\,, \tag{2.22}$$

for PAHs, the hot mid-infrared continuum and warm and cold dust in thermal equilibrium, respectively.

We compute luminosity densities in any filter from $L_{\lambda,\mathrm{d}}^{\mathrm{tot}}$ using the general formula

$$L_\nu^{\lambda_0} = C_{\nu_0} \frac{\int d\nu\, \nu^{-1}\, L_\nu\, R_\nu}{\int d\nu\, \nu^{-1}\, C_\nu\, R_\nu} = \frac{\lambda_0^2}{c}\, C_{\lambda_0} \frac{\int d\lambda\, L_\lambda\, \lambda\, R_\lambda}{\int d\lambda\, C_\lambda\, \lambda\, R_\lambda}\,, \tag{2.23}$$

where

$$\lambda_0 = \frac{\int d\lambda\, \lambda\, R_\lambda}{\int d\lambda\, R_\lambda} \tag{2.24}$$

is the effective wavelength of the filter of response R_λ (R_ν), and the calibration spectrum C_λ (C_ν) depends on the photometric system. For the AB system, C_ν is fixed at 3631 Jy, implying $C_\lambda \propto \lambda^{-2}$ (Oke & Gunn 1983). For the *IRAS*, *ISO*/ISOCAM and *Spitzer*/IRAC photometric systems, the convention is to use $\nu C_\nu = \lambda C_\lambda = \text{constant}$, and hence, $C_\lambda \propto \lambda^{-1}$ (see Beichman et al. 1988; Blommaert et al. 2003; Reach et al. 2005, and also the IRAC Data Handbook[2]). The *Spitzer*/MIPS system was calibrated using a blackbody spectrum of temperature 10,000 K, such that $C_\lambda = B_\lambda(10,000\,\mathrm{K})$ (MIPS Data Handbook[3]). In Fig. 2.2, we show an example of infrared spectral energy distribution $L_{\lambda,\mathrm{d}}^{\mathrm{tot}}$ computed using our model, for parameter values typical of normal star-forming galaxies (equation 2.25 below). As we shall see in Section 2.2.2.2, this parameterisation of infrared galaxy spectra allows us to account for the full range of observed colours of star-forming galaxies.

2.2.2.2 Comparison with observed infrared colours

To test how well our model can reproduce the observed infrared colours of galaxies in a wide range of star formation histories, we appeal to a sample of 157 nearby galaxies compiled by Elbaz et al. (2002), for which *IRAS* and *ISO*/ISOCAM observations are available from Boselli et al. (1998), Roussel et al. (2001), Laurent et al. (2000) and Dale et al. (2000). The galaxies in this sample span wide ranges of morphologies, absolute infrared luminosities, infrared-to-blue luminosity ratios and infrared colours (see Elbaz et al. 2002 for more detail). For nearby galaxies, the flux density collected by the ISOCAM *LW2* (6.75 μm) filter, $F_\nu^{6.75}$, tends to be dominated by the PAH emission features at 6.2, 7.7 and 8.6 μm. The *IRAS* 12-μm flux density F_ν^{12} captures the PAH emission at 11.3 and 12.7 μm and the mid-infrared continuum emission from hot dust. The ISOCAM *LW3* (15 μm) and the *IRAS* 25-μm flux densities, F_ν^{15} and F_ν^{25}, reflect primarily the mid-infrared continuum emission from hot dust. At longer wavelengths, the *IRAS* 60-μm flux density F_ν^{60} samples the emission from warm grains in thermal equilibrium in star-forming clouds, and the *IRAS* 100-μm flux density F_ν^{100} that from colder grains in thermal equilibrium in the ambient interstellar medium. To test our model, we require photometric observations in all these filters. This reduces the sample to 107 galaxies.

---

[2] http://ssc.spitzer.caltech.edu/irac/dh/

[3] http://ssc.spitzer.caltech.edu/mips/dh/

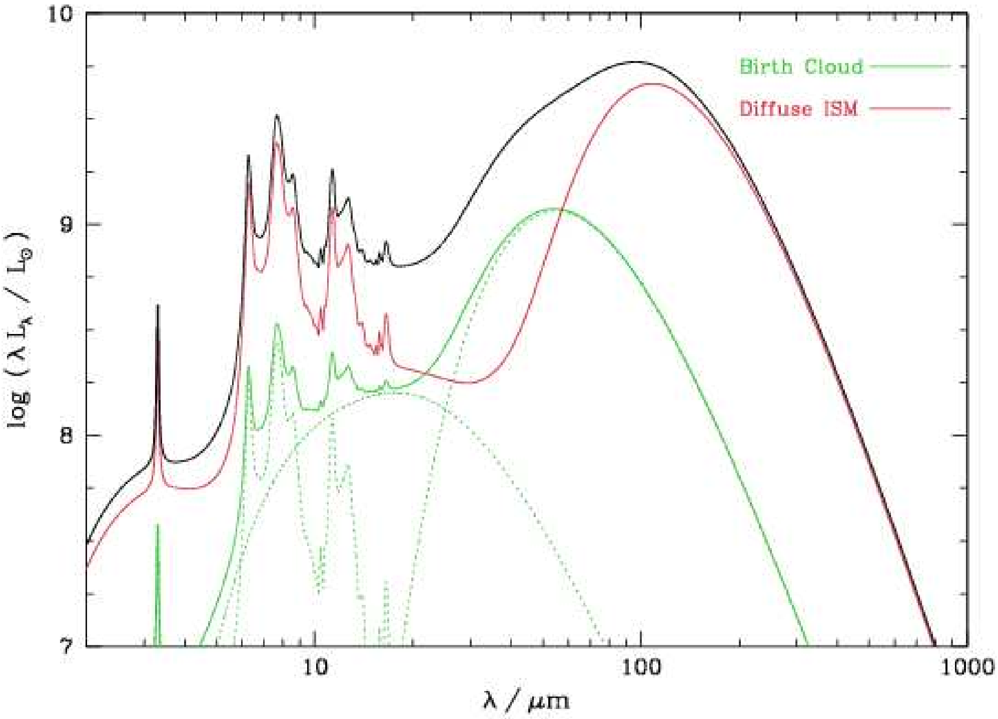

Figure 2.2: Example of infrared spectral energy distribution computed using the model presented in Section 2.2.2.1, for 'standard' values of the parameters (equation 2.25): $f_\mu = 0.6$, $\xi^{\rm BC}_{\rm PAH} = 0.05$, $\xi^{\rm BC}_{\rm MIR} = 0.15$, $\xi^{\rm BC}_{\rm W} = 0.80$, $T^{\rm BC}_{\rm W} = 48\,{\rm K}$, $\xi^{\rm ISM}_{\rm C} = 0.8$ and $T^{\rm ISM}_{\rm C} = 22\,{\rm K}$. The black curve shows the total infrared spectrum. The green solid curve shows the contribution by dust in the stellar birth clouds, and the green dashed curves the breakdown of this contribution in different components: PAHs, mid-infrared continuum and warm dust in thermal equilibrium. The red curve shows the contribution by dust in the ambient ISM. The total luminosity is $L^{\rm tot}_{\rm d} = 10^{10} L_\odot$ (equations 2.13, 2.15 and 2.18).

For the purpose of comparisons between our (angle-averaged) model and observations, we neglect possible anisotropies and equate flux ratios at all wavelengths to the corresponding luminosity ratios.

In Figs. 2.3 and 2.4, we show the locations of these galaxies in various infrared colour-colour diagrams (black crosses). Fig. 2.3 shows L^{60}_ν/L^{100}_ν as a function of L^{12}_ν/L^{25}_ν (*IRAS* colours), while Fig. 2.4 shows L^{15}_ν/L^{60}_ν as a function of $L^{6.75}_\nu/L^{15}_\nu$ (*ISO* colours). The well-known correlations between the different infrared colours of galaxies illustrated by Figs. 2.3 and 2.4 suggest that the different contributors to the total infrared emission are related to one another. These relations are generally interpreted as sequences in the overall star formation activity and dust heating (e.g. Helou 1986; Dale et al. 2001). Quiescent star-forming galaxies with strong PAH emission and cool ambient-ISM dust tend to have high L^{12}_ν/L^{25}_ν, $L^{6.75}_\nu/L^{15}_\nu$ and

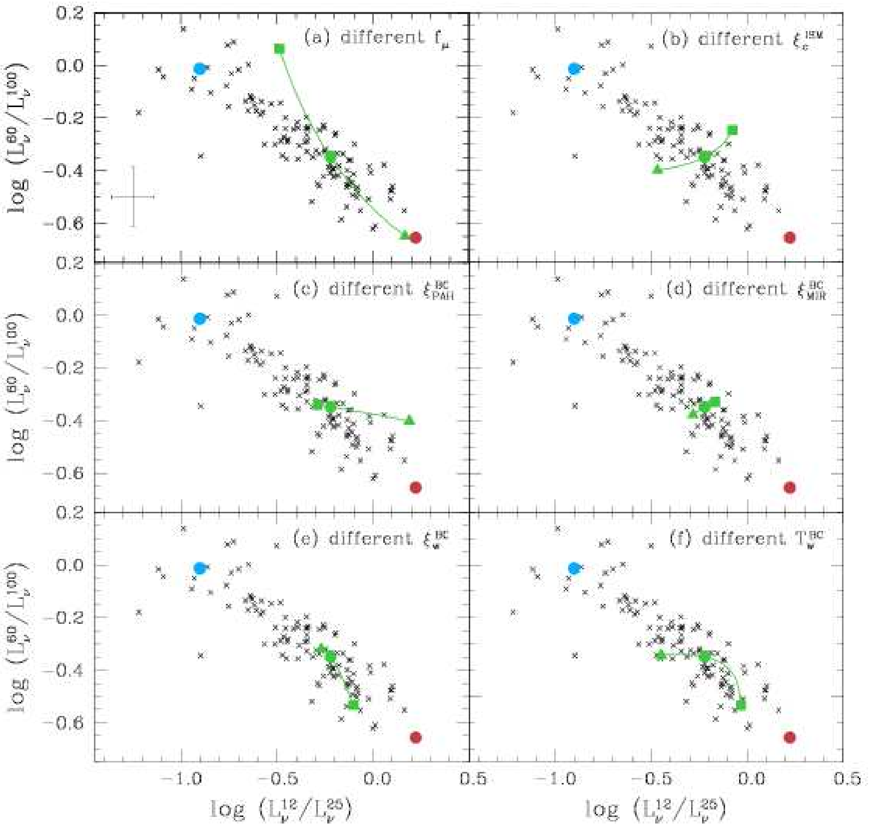

Figure 2.3: Ratio of 60-μm to 100-μm *IRAS* luminosity density plotted against ratio of 12-μm to 25-μm *IRAS* luminosity density. The data points in all panels (black crosses) are from the Elbaz et al. (2002) sample discussed in Section 2.2.2 (typical measurement errors are indicated in the upper left panel). In each panel, the green line shows the effect of varying one parameter of the model from the lower end of the range (square) to the standard value (green circle) to the upper end of the range (triangle), with all other parameters fixed at their standard values: (a) fraction of total infrared luminosity contributed by dust in the ambient ISM, $f_\mu =$ 0.05, 0.50 and 0.95; (b) contribution by cold dust in thermal equilibrium to the infrared luminosity of the ambient ISM, ξ_C^{ISM}= 0.50, 0.80, 1.0; (c) contribution by PAHs to the infrared luminosity of stellar birth clouds, ξ_{PAH}^{BC} = 0.00, 0.05 and 0.50; (d) contribution by the hot mid-infrared continuum to the infrared luminosity of stellar birth clouds, ξ_{MIR}^{BC}= 0.00, 0.15 and 0.50; (e) contribution by warm dust in thermal equilibrium to the infrared luminosity of stellar birth clouds, ξ_W^{BC} = 0.15, 0.80 and 0.95; (f) equilibrium temperature of warm dust in stellar birth clouds, T_W^{BC} = 30, 48 and 60 K. In all panels, the red circle corresponds to the same quiescent model galaxy dominated by cold dust emission, while the blue circle corresponds to an actively star-forming galaxy dominated hot dust emission (see Table 2.1 and Section 2.2.2 for a description of these models).

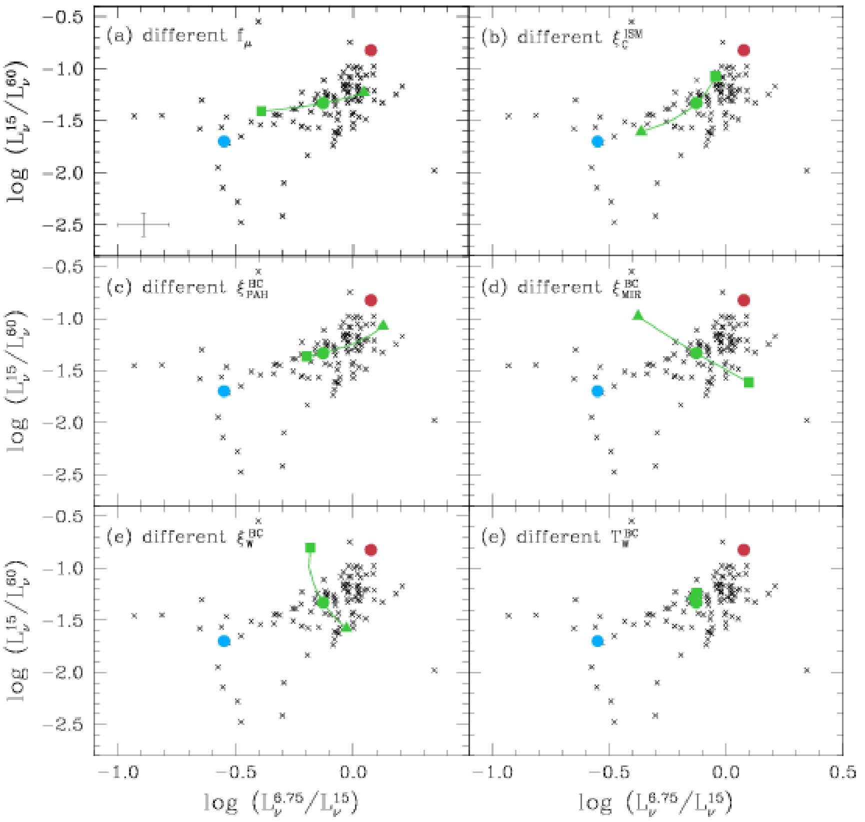

Figure 2.4: Ratio of 15-μm to 60-μm *ISO* and *IRAS* luminosity density plotted against ratio of 6.75-μm to 15-μm *ISO* luminosity density. The data points in all panels (black crosses) are from the Elbaz et al. (2002) sample discussed in Section 2.2.2. In each panel, the green line shows the effect of varying one parameter of the model from the lower end of the range (square) to the standard value (green circle) to the upper end of the range (triangle), with all other parameters fixed at their standard values. The models are the same as in Fig. 2.3. In all panels, the red circle corresponds to the same quiescent model galaxy dominated by cold dust emission, while the blue circle corresponds to an actively star-forming galaxy dominated hot dust emission (see Table 2.1 and Section 2.2.2 for a description of these models).

L_ν^{15}/L_ν^{60} and low L_ν^{60}/L_ν^{100}. In contrast, actively star-forming galaxies, in which the mid-infrared emission is dominated by continuum radiation by hot dust and the far-infrared emission by warm dust in star-forming regions, tend to have low L_ν^{12}/L_ν^{25}, $L_\nu^{6.75}/L_\nu^{15}$ and L_ν^{15}/L_ν^{60} and high L_ν^{60}/L_ν^{100}.

We now use these observations to explore the influence of each parameter of our model on the various infrared colours. We explore the effect of varying a single parameter at a time, keeping all the other parameters fixed at ‘standard’ values. After some experimentation, we adopted the following standard parameters (corresponding to the model shown in Fig. 2.2):

$$\begin{aligned} f_\mu &= 0.60 \\ \xi^{\rm BC}_{\rm PAH} &= 0.05 \\ \xi^{\rm BC}_{\rm MIR} &= 0.15 \\ \xi^{\rm BC}_{\rm W} &= 0.80 \\ \xi^{\rm ISM}_{\rm C} &= 0.80 \\ T^{\rm BC}_{\rm W} &= 48\,{\rm K} \\ T^{\rm ISM}_{\rm C} &= 22\,{\rm K}\,. \end{aligned} \tag{2.25}$$

These values allow the standard model to match roughly the observed typical (i.e. median) infrared colours of nearby star-forming galaxies in Figs. 2.3 and 2.4 (green circle). Each panel of Figs. 2.3 and 2.4 shows the effect of varying one parameter of the model, with the other parameters held fixed at their standard values.[4] We can summarise the role of each parameter as follows.

Fraction of total infrared luminosity contributed by dust in the ambient ISM. The dominant effect of increasing f_μ is to increase the contribution to the total infrared luminosity by cold dust. This raises the infrared luminosity around 100 μm (Fig. 2.2), causing L^{60}_ν/L^{100}_ν and even L^{15}_ν/L^{60}_ν to decrease (Figs. 2.3a and 2.4a). In addition, a larger f_μ leads to an increase in L^{12}_ν/L^{25}_ν and $L^{6.75}_\nu/L^{15}_\nu$, due to the increased contribution by PAH emission features (which dominate the mid-infrared emission of the ISM) to the total mid-infrared emission.

Contribution by cold dust in thermal equilibrium to the infrared emission from the ambient ISM. Increasing $\xi^{\rm ISM}_{\rm C}$ causes L^{12}_ν/L^{25}_ν and $L^{6.75}_\nu/L^{15}_\nu$ to decrease in Figs. 2.3b and 2.4b, because of the corresponding drop in PAH emission from the ambient ISM (see footnote 4). Also, both L^{15}_ν/L^{60}_ν and L^{60}_ν/L^{100}_ν decrease because of the larger contribution by cold dust to the 60 μm flux, and even more so to the 100 μm flux.

Contribution by PAHs to the infrared emission from stellar birth clouds. Increasing $\xi^{\rm BC}_{\rm PAH}$ raises the contribution by PAH features to $L^{6.75}_\nu$ and L^{12}_ν, and to a lesser extent L^{15}_ν (Fig. 2.2). This leads to a marked increase in $L^{6.75}_\nu/L^{15}_\nu$ and L^{12}_ν/L^{25}_ν and a milder one in L^{15}_ν/L^{60}_ν in Figs. 2.3c and 2.4c. The slight decrease in L^{60}_ν/L^{100}_ν when $\xi^{\rm BC}_{\rm PAH}$ increases in Fig. 2.3c is caused by the associated drop in $\xi^{\rm BC}_{\rm BG}$ (footnote 4).

Contribution by the hot mid-infrared continuum to the infrared emission from stellar birth clouds. The main effect of increasing $\xi^{\rm BC}_{\rm MIR}$ is to make L^{15}_ν and L^{25}_ν

---

[4] In practice, an increase in any of $\xi^{\rm BC}_{\rm PAH}$, $\xi^{\rm BC}_{\rm MIR}$ and $\xi^{\rm BC}_{\rm W}$ will be accompanied by a drop in the other two fractions by virtue of equation (2.14). Likewise, an increase in $\xi^{\rm ISM}_{\rm C}$ implies a drop in the sum $\xi^{\rm ISM}_{\rm PAH}+\xi^{\rm ISM}_{\rm MIR}+\xi^{\rm ISM}_{\rm W}$ (equation 2.16). When exploring such variations, we keep the relative ratios of the unexplored fractions fixed.

larger (Fig. 2.2). This causes a drop in L_ν^{12}/L_ν^{25} and $L_\nu^{6.75}/L_\nu^{15}$, while L_ν^{15}/L_ν^{60} increases (Figs. 2.3d and 2.4d). The slight decrease in L_ν^{60}/L_ν^{100} when $\xi_{\rm MIR}^{\rm BC}$ increases in Fig. 2.3c is again caused by the associated drop in $\xi_{\rm BG}^{\rm BC}$ (footnote 4).

Contribution by warm dust in thermal equilibrium to the infrared emission from stellar birth clouds. Increasing $\xi_{\rm W}^{\rm BC}$ makes L_ν^{60} larger, and to a lesser extent also L_ν^{25} and L_ν^{100} (Fig. 2.2). Remarkably, this causes L_ν^{12}/L_ν^{25} to drop and L_ν^{60}/L_ν^{100} to rise in Fig. 2.3e, almost along the observational relation. In Fig. 2.4e, an increase in $\xi_{\rm W}^{\rm BC}$ makes L_ν^{15} smaller (because of the associated drop in $\xi_{\rm MIR}^{\rm BC}$; see footnote 4), and hence, L_ν^{15}/L_ν^{60} smaller and $L_\nu^{6.75}/L_\nu^{15}$ larger.

Equilibrium temperature of warm dust in stellar birth clouds. Increasing $T_{\rm W}^{\rm BC}$ across the range from 30 to 60 K moves the wavelength of peak luminosity of dust in thermal equilibrium in the stellar birth clouds roughly from 70 to 40 μm. This causes L_ν^{12}/L_ν^{25} to drop and L_ν^{60}/L_ν^{100} to rise in Fig. 2.3f. In Fig. 2.4f, the effects on $L_\nu^{6.75}/L_\nu^{15}$ and L_ν^{15}/L_ν^{60} are negligible.

Equilibrium temperature of cold dust in the ambient ISM (not shown). The most significant effect of increasing $T_{\rm C}^{\rm ISM}$ at fixed $\xi_{\rm C}^{\rm ISM}$ in Figs. 2.3 and 2.4 is a small rise in L_ν^{60}/L_ν^{100} caused by a blue shift of the peak infrared luminosity of cold dust in the ambient ISM (from about 140 to 80 μm as $T_{\rm C}^{\rm ISM}$ increases from 15 to 25 K). Variations in $T_{\rm C}^{\rm ISM}$ also have a significant influence on the emission redward of 100 μm.

The green lines in Figs. 2.3 and 2.4 show that the extremities of the observational relations between the different infrared colours of galaxies cannot be reached by varying a single model parameter at a time. This suggests that variations in the different dust components of galaxies are related to each other. However, we have checked that the properties of every galaxy in Figs. 2.3 and 2.4 could be reproduced with at least one combination of parameters of our model. We illustrate this by showing two models lying at the ends of the observational relations: a 'cold' infrared spectrum characteristic of a quiescent galaxy with little star formation (red circle); and a 'hot' infrared spectrum characteristic of an actively star-forming, starburst galaxy (blue circle). The parameters of these models are listed in Table 2.1. We emphasise that these are not unique sets of parameters optimised to fit specific galaxy spectral energy distributions. Rather, they are examples of how the colours in those regions of the diagrams can be reproduced using our model.

Figs. 2.3 and 2.4 allow us to draw some general conclusions about the influence of the various parameters of our model on the observed infrared colours of galaxies. For example, as expected from Fig. 2.2, the L_ν^{60}/L_ν^{100} colour appears to be controlled primarily by the fraction f_μ of total infrared luminosity contributed by dust in the ambient ISM and the properties of dust in thermal equilibrium: the relative contribution $\xi_{\rm C}^{\rm ISM}$ by cold dust to the infrared luminosity of the ambient ISM (and the temperature $T_{\rm C}^{\rm ISM}$ of this dust) and the relative contribution $\xi_{\rm W}^{\rm BC}$ by

Table 2.1: Parameters of the 'standard', 'cold' and 'hot' models plotted in Figs. 2.3 and 2.4.

Model	'cold'	'standard'	'hot'
f_μ	0.75	0.60	0.20
$\xi_{\rm C}^{\rm ISM}$	0.75	0.80	0.90
$\xi_{\rm PAH}^{\rm BC}$	0.45	0.05	0.01
$\xi_{\rm MIR}^{\rm BC}$	0.15	0.15	0.09
$\xi_{\rm W}^{\rm BC}$	0.40	0.80	0.95
$T_{\rm W}^{\rm BC}$ (K)	40	48	55
$T_{\rm C}^{\rm ISM}$ (K)	18	22	25

warm dust to the infrared luminosity of stellar birth clouds (and the temperature $T_{\rm W}^{\rm BC}$ of this dust). These parameters also have distinct effects on the mid-infrared colours L_ν^{12}/L_ν^{25}, $L_\nu^{6.75}/L_\nu^{15}$ and L_ν^{15}/L_ν^{60}, indicating that they can be constrained independently from fits of extended infrared spectral energy distributions. The mid-infrared colours are primarily controlled by the different components of hot dust: the relative contributions $\xi_{\rm PAH}^{\rm BC}$ and $\xi_{\rm MIR}^{\rm BC}$ of PAHs and the hot mid-infrared continuum to the the infrared luminosity of stellar birth clouds, and the contribution by PAHs to the infrared luminosity of the ambient ISM, which is controlled indirectly by $\xi_{\rm C}^{\rm ISM}$. In the next chapter, we show how well these various model parameters can be constrained in galaxies with observed infrared spectral energy distributions.

2.2.2.3 Constraints on dust mass

It is also of interest to derive constraints on the dust mass in galaxies. The mass $M_{\rm d}(T_{\rm d})$ in dust grains in thermal equilibrium at the temperature $T_{\rm d}$ can be estimated from the far-infrared radiation $L_\lambda^{T_{\rm d}}$ of these grains using the formula (Hildebrand 1983)

$$L_\lambda^{T_{\rm d}} = 4\pi\, M_{\rm d}(T_{\rm d})\, \kappa_\lambda\, B_\lambda(T_{\rm d})\,, \tag{2.26}$$

where κ_λ and B_λ have been defined before (equation 2.10). We adopt this formula to estimate the mass contributed by dust in thermal equilibrium in stellar birth clouds (with temperature $T_{\rm d} = T_{\rm W}^{\rm BC}$) and in the ambient ISM (with temperatures $T_{\rm d} = T_{\rm W}^{\rm ISM}$ and $T_{\rm d} = T_{\rm C}^{\rm ISM}$) in our model. We adopt as before a dust emissivity index $\beta = 1.5$ for warm dust and $\beta = 2$ for cold dust and normalise κ_λ at 850 μm assuming $\kappa_{850\mu m} = 0.77\,{\rm g^{-1}cm^2}$ (Dunne et al. 2000). Using equations (2.10), (2.13), (2.15) and (2.26), we compute the mass contributed by warm dust in stellar birth clouds and in the ambient ISM as

$$M_{\rm W}^{\rm BC} = \xi_{\rm W}^{\rm BC}\,(1-f_\mu)\,L_{\rm d}^{\rm tot}\left[4\pi\int_0^\infty d\lambda\,\kappa_\lambda\,B_\lambda(T_{\rm W}^{\rm BC})\right]^{-1} \tag{2.27}$$

and

$$M_{\rm W}^{\rm ISM} = \xi_{\rm W}^{\rm ISM}\,f_\mu\,L_{\rm d}^{\rm tot}\left[4\pi\int_0^\infty d\lambda\,\kappa_\lambda\,B_\lambda(T_{\rm W}^{\rm ISM})\right]^{-1}\,, \tag{2.28}$$

and that contributed by cold dust in the ambient ISM as

$$M_{\rm C}^{\rm ISM} = \xi_{\rm C}^{\rm ISM}\,f_\mu\,L_{\rm d}^{\rm tot}\left[4\pi\int_0^\infty d\lambda\,\kappa_\lambda\,B_\lambda(T_{\rm C}^{\rm ISM})\right]^{-1}\,. \tag{2.29}$$

To include the contribution by stochastically heated dust grains (not in thermal equilibrium; see Section 2.2.2.1), we adopt a standard Mathis, Rumpl & Nordsieck (1977) distribution of grain sizes $N(a) \propto a^{-3.5}$ over the range $0.005\,\mu{\rm m} \leq a \leq 0.25\,\mu{\rm m}$. We assume that the stochastically heated dust grains are very small ($a \leq 0.01\,\mu{\rm m}$) and have mass densities typical of graphite, $\rho \approx 2.26\,{\rm g\,cm^{-3}}$, while bigger grains in thermal equilibrium have mass densities typical of silicates, $\rho \approx 3.30\,{\rm g\,cm^{-3}}$ (Draine & Lee 1984). For these assumptions, the mass contributed by grains of all sizes is about 5 per cent larger than that contributed by big grains alone ($a > 0.01\,\mu{\rm m}$). The contribution by PAHs to the overall dust mass is also very small, of the order of a few per cent (Draine et al. 2007). We therefore estimate the total dust mass of a galaxy as

$$M_{\rm d} \approx 1.1\,(M_{\rm W}^{\rm BC} + M_{\rm W}^{\rm ISM} + M_{\rm C}^{\rm ISM})\,, \tag{2.30}$$

where $M_{\rm W}^{\rm BC}$, $M_{\rm W}^{\rm ISM}$ and $M_{\rm C}^{\rm ISM}$ are given by equations (2.27), (2.28) and (2.29).

2.2.3 Combined ultraviolet, optical and infrared spectral energy distributions

A main feature of our model is the consistent modelling of ultraviolet, optical and infrared spectral energy distributions of galaxies. This is achieved by first computing the total energy absorbed by dust in stellar birth clouds and in the ambient ISM, $L_{\rm d}^{\rm BC}$ and $L_{\rm d}^{\rm ISM}$ (Section 2.2.1), and then re-distributing it at infrared wavelengths (Section 2.2.2). The main assumptions are the conservation of the energy absorbed and reradiated by dust, and that the dust in the ISM of galaxies is heated only by starlight (in particular, we ignore the possible influence of an active galactic nucleus). Different combinations of star formation histories, metallicities and dust contents can lead to the same absorbed energies $L_{\rm d}^{\rm BC}$ and $L_{\rm d}^{\rm ISM}$ in a model galaxy. Furthermore, these energies can be distributed in wavelength using different combinations of dust parameters in the stellar birth clouds ($\xi_{\rm PAH}^{\rm BC}$, $\xi_{\rm MIR}^{\rm BC}$, $\xi_{\rm W}^{\rm BC}$ and $T_{\rm W}^{\rm BC}$) and the ambient ISM ($\xi_{\rm C}^{\rm ISM}$ and $T_{\rm C}^{\rm ISM}$). In our model, therefore, a wide range of ultraviolet and optical spectral energy distributions can be associated to a wide range of infrared spectral energy distributions, at fixed $L_{\rm d}^{\rm BC}$ and $L_{\rm d}^{\rm ISM}$ (or equivalently, at fixed f_μ and $L_{\rm d}^{\rm tot}$; see equations 5.5 and 2.8). In the next chapters of this thesis, we show how combined observations at ultraviolet, optical and infrared wavelengths can be used to uniquely constrain the star formation histories and dust properties of galaxies using this model.

To illustrate the combination of ultraviolet, optical and infrared spectral energy distributions with our model, we compute examples of attenuated stellar population spectra consistent with the f_μ parameters of the cold, standard and hot infrared models of Table 2.1 (Section 2.2.2.2). For simplicity, we assume solar metallicity and select models with exponentially declining star formation rates

$$\psi(t) \propto \exp(-\gamma\, t)\,, \tag{2.31}$$

where γ is the star formation timescale parameter. We choose models with $\gamma = 0$, 0.07 and 0.25 $\rm Gyr^{-1}$ at the ages $t = 1.4$, 10 and 10 Gyr, respectively, to represent a starburst, a normal star-forming and a quiescent star-forming galaxy (e.g. Kauffmann & Charlot 1998). For the attenuation of starlight by dust (equations 5.4 and 5.3), we adopt effective dust absorption optical depths $\hat{\tau}_V = 2.0$, 1.5 and 1.0, for the starburst, normal star-forming and quiescent star-forming models, respectively. These values are consistent with the expectation that more actively star-forming galaxies are more obscured (e.g. Wang & Heckman 1996; Hopkins et al. 2001; Sullivan et al. 2001). We adopt fractions $\mu = 0.1$, 0.3 and 0.5 of $\hat{\tau}_V$ arising from dust in the ambient ISM. The resulting model galaxies have $f_\mu \approx 0.2$, 0.6 and 0.75, respectively, consistent with the parameters of the hot, standard and cold infrared models of Table 2.1.

In Fig. 2.5, we show the combined spectral energy distributions of the starburst + hot infrared, normal star-forming + standard infrared, and quiescent star-forming + cold infrared models, after scaling in each case the infrared luminosity to the total luminosity $L_{\rm d}^{\rm tot}$ absorbed by dust. As we shall see in the next chapters, the ability to compute such combined ultraviolet, optical and infrared spectral energy distributions for wide ranges of physical parameters of galaxies has important implications for statistical estimates of star formation histories and dust properties.

2.3 Applicability of the model

Our model is designed primarily to interpret ultraviolet, optical and infrared observations of large samples of (randomly oriented) galaxies in terms of effective (i.e galaxy-wide) physical parameters, such as star formation rate, stellar mass, dust mass, total infrared luminosity, breakdown of this luminosity between different dust components and between star-forming clouds and the diffuse ISM (Section 3.3). Constraints on these quantities for statistical samples of galaxies at various redshifts are expected to provide useful insight into the processes that were important in the evolution of the galaxies we see today.

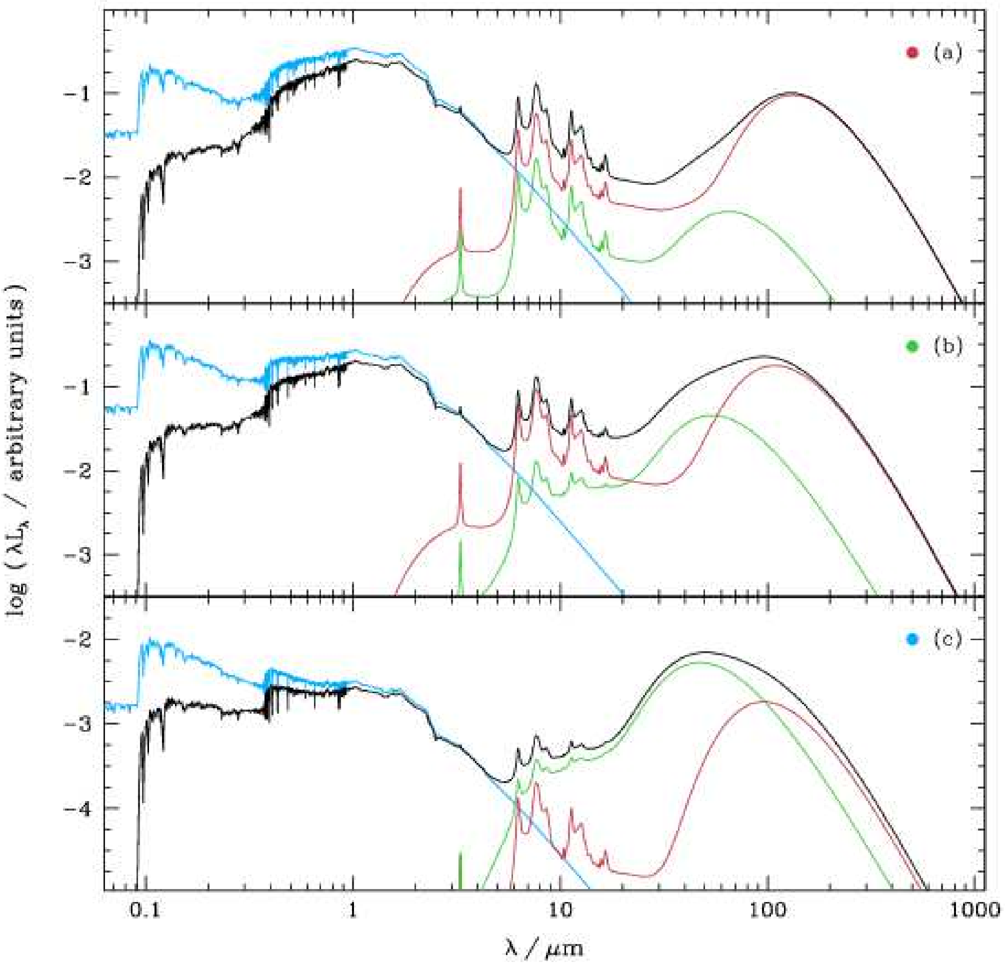

Figure 2.5: Examples of spectral energy distributions obtained by combining the infrared models of Table 2.1 with attenuated stellar population spectra corresponding to the same contributions by dust in stellar birth clouds $(1 - f_\mu)$ and in the ambient ISM (f_μ) to the total energy $L_{\mathrm{d}}^{\mathrm{tot}}$ absorbed and reradiated by dust (Section 2.2.3). (a) Quiescent star-forming galaxy spectrum combined with the 'cold' infrared model of Table 2.1; (b) normal star-forming galaxy spectrum combined with the 'standard' infrared model of Table 2.1; (c) starburst galaxy spectrum combined with the 'hot' infrared model of Table 2.1 (see text for details about the parameters of the stellar population models). Each panel shows the unattenuated stellar spectrum (blue line), the emission by dust in stellar birth clouds (green line), the emission by dust in the ambient ISM (red line) and the total emission from the galaxy, corresponding to the sum of the attenuated stellar spectrum and the total infrared emission (black line).

Our model is not optimised to interpret in detail multi-wavelength observations of individual galaxies, for which the consideration of geometrical factors becomes important. Studies of this type generally require complex radiative transfer calculations for specific optical properties of dust grains and specific spatial distributions of stars and dust. We refer the reader to the more sophisticated models of, for example, Silva et al. (1998) and Popescu et al. (2000) for such purposes. Also, for detailed investigations of the ambient physical conditions of gas and dust in starburst galaxies, where orientation effects are expected to be less crucial, the model of Dopita et al. (2005, see also Groves et al. 2007), which includes radiative transfer in expanding H II regions, represents a suitable alternative.

2.4 Summary and conclusion

In this chapter, we have developed a simple but versatile model to interpret the mid- and far-infrared spectral energy distributions of galaxies consistently with the emission at ultraviolet, optical and near-infrared wavelengths. Our model relies on the Bruzual & Charlot (2003) population synthesis code to compute the spectral evolution of stellar populations, and on the two-component model of Charlot & Fall (2000) to compute the total infrared luminosity absorbed and reradiated by dust in stellar birth clouds and in the ambient ISM. We distribute this total infrared energy in wavelength over the range from 3 to 1000 μm by considering the contributions by four main dust components: PAH emission, mid-infrared continuum emission from hot dust, warm dust with adjustable equilibrium temperature in the range 30–60 K and cold dust with adjustable equilibrium temperature in the range 15–25 K. We keep as adjustable parameters the relative contributions by PAHs, the hot mid-infrared continuum and warm dust to the infrared luminosity of stellar birth clouds. Cold dust resides (in an adjustabe amount) only in the ambient ISM, where the relative ratios of the other three components are fixed to the values reproducing the observed mid-infrared cirrus emission of the Milky Way. We find that this minimum number of components is required to account for the infrared spectral energy distributions of galaxies in wide ranges of star formation histories.

The simple but versatile model presented in this chapter allows us to derive statistical estimates of physical parameters such as star formation rate, stellar mass, dust content and dust properties, from combined ultraviolet, optical and infrared galaxy spectra. To achieve this, in the next chapter, we adopt a Bayesian approach similar to that successfully employed by, e.g., Kauffmann et al. (2003b), Brinchmann et al. (2004), Gallazzi et al. (2005) and Salim et al. (2007) to interpret ultraviolet, optical and near-infrared galaxy spectra using only the Bruzual & Charlot (2003) and Charlot & Fall (2000) models. As an example, we derive median-likelihood estimates of a set of physical parameters describing the stellar and dust contents of 66 star-forming galaxies from the Spitzer Infrared Nearby Galaxy Survey (SINGS, Kennicutt et al. 2003).

Chapter 3

The physical properties of a sample of nearby galaxies

This chapter is extracted from the paper *A simple model to interpret the ultraviolet, optical and infrared emission from galaxies*, by Elisabete da Cunha, Stéphane Charlot and David Elbaz, published in the Monthly Notices of the Royal Astronomical Society (da Cunha, Charlot & Elbaz 2008).

3.1 Introduction

In this chapter, we show how the simple model described in Chapter 2 can be used to extract star formation histories and dust properties from ultraviolet, optical and infrared observations of galaxies. In Section 3.2, we first describe our methodology to derive statistical constraints on galaxy physical parameters from multi-wavelength observations. Then, in Section 3.3, we use this methodology to constrain the physical parameters of star-forming galaxies in the Spitzer Infrared Nearby Galaxy Survey (SINGS) sample. We compare our results to those that would be obtained using previous models in Section 3.4. Finally, we discuss possible sources of systematic errors associated with our approach in Section 3.5 and summarize the applicability of this model in Section 2.3.

3.2 Methodology

The model of Section 2.2 allows one to compute the ultraviolet, optical and infrared emission from galaxies. This model contains a minimum number of adjustable parameters required to account for the observed relations between various integrated spectral properties of galaxies: age, star formation history, stellar metallicity, two components for the attenuation by dust and four contributors to the infrared emission (PAHs, hot mid-infrared continuum, warm and cold dust in thermal equilibrium). The large number of observable quantities to which the model can be compared insures that these different adjustable parameters can be constrained in a meaningful way (see below). A usual limitation of this type of study is that several different combinations of physical parameters can lead to similar spectral energy distributions of galaxies. For example, age, metallicity and dust attenuation have similar effects on the ultraviolet and optical spectra of galaxies. An efficient way to derive statistical constraints on the various parameters in these conditions is to consider a wide library of models encompassing all plausible parameter combinations.

Given an observed galaxy, we can build the likelihood distribution of any physical parameter by evaluating how well each model in the library can account for the observed properties of the galaxy. This Bayesian approach is similar to that used, for example, by Kauffmann et al. (2003b) to interpret the optical spectra of SDSS galaxies. The underlying assumption is that the library of models is the distribution from which the data were randomly drawn. Thus, the prior distribution of models must be such that the entire observational space is reasonably well sampled, and that no a priori implausible corner of parameter space accounts for a large fraction of the models.

3.2.1 Model library

We build a comprehensive library of models by generating separately a random library of stellar population models, for wide ranges of star formation histories, metallicities and dust contents, and a random library of infrared spectra, for wide ranges of dust temperatures and fractional contributions by the different dust components to the total infrared luminosity. We then combine these libraries following the procedure outline in Section 2.2.3.

For simplicity, we follow Kauffmann et al. (2003b) and parametrise each star formation history in the stellar population library in terms of two components: an underlying continuous model, characterised by an age $t_{\rm g}$ and a star formation time-scale parameter γ (equation 2.31), and random bursts superimposed on this continuous model. We take $t_{\rm g}$ to be uniformly distributed over the interval from 0.1 and 13.5 Gyr. To avoid oversampling galaxies with negligible current star formation, we distribute γ using the probability density function $p(\gamma) = 1 - \tanh(8\,\gamma - 6)$, which is approximately uniform over the interval from 0 to 0.6 Gyr^{-1} and drops exponentially to zero around $\gamma = 1\ \text{Gyr}^{-1}$. Random bursts occur with equal probability at all times until $t_{\rm g}$. We set the probability so that 50 per cent of the galaxies in the library have experienced a burst in the past 2 Gyr. We parametrise the amplitude of each burst as $A = M_{\rm burst}/M_{\rm cont}$, where $M_{\rm burst}$ is the mass of stars formed in the burst and $M_{\rm cont}$ is the total mass of stars formed by the continuous model over the time $t_{\rm g}$. This ratio is distributed logarithmically between 0.03 and 4.0. During a burst, stars form at a constant rate over the time $t_{\rm burst}$, which we distribute uniformly between 3×10^7 and 3×10^8 yr. We distribute the models uniformly in metallicity between 0.02 and 2 times solar.

We sample attenuation by dust in the library by randomly drawing the total effective V-band absorption optical depth, $\hat{\tau}_V$, and the fraction of this contributed by dust in the ambient ISM, μ (equations 5.4 and 5.3). We distribute $\hat{\tau}_V$ according to the probability density function $p(\hat{\tau}_V) = 1 - \tanh(1.5\,\hat{\tau}_V - 6.7)$, which is approximately uniform over the interval from 0 to 4 and drops exponentially to zero around $\hat{\tau}_V = 6$. For μ, we adopt the same probability density function as for γ above, i.e. $p(\mu) = 1 - \tanh(8\,\mu - 6)$. We note that these priors for attenuation encompass the dust properties of SDSS galaxies, for which $\hat{\tau}_V$ and μ peak around 1.0 and 0.3, respectively, with broad scatter (Brinchmann et al. 2004; Kong et al.

2004). Our final stellar population library consists of 50,000 different models.

In parallel, we generate a random library of infrared spectra as follows. We take the fraction f_μ of the total infrared luminosity contributed by dust in the ambient ISM to be uniformly distributed over the interval from 0 to 1. We adopt a similar distribution for the fractional contribution by warm dust in thermal equilibrium to the infrared luminosity of stellar birth clouds, $\xi_{\mathrm{W}}^{\mathrm{BC}}$. For each random drawing of $\xi_{\mathrm{W}}^{\mathrm{BC}}$, we successively draw the contributions by the other dust components to the infrared luminosity of stellar birth clouds (i.e. , hot mid-infrared continuum and PAHs) to satisfy the condition in equation (2.14): we draw $\xi_{\mathrm{MIR}}^{\mathrm{BC}}$ from a uniform distribution between 0 and $1-\xi_{\mathrm{W}}^{\mathrm{BC}}$, and we set $\xi_{\mathrm{PAH}}^{\mathrm{BC}}=1-\xi_{\mathrm{W}}^{\mathrm{BC}}-\xi_{\mathrm{MIR}}^{\mathrm{BC}}$. While this procedure does not exclude values of $\xi_{\mathrm{MIR}}^{\mathrm{BC}}$ and $\xi_{\mathrm{PAH}}^{\mathrm{BC}}$ close to unity, it does favour small values of these parameters, and hence, it avoids oversampling physically implausible models. We take the equilibrium temperature $T_{\mathrm{W}}^{\mathrm{BC}}$ of warm dust in the stellar birth clouds to be uniformly distributed between 30 and 60 K, and that $T_{\mathrm{C}}^{\mathrm{ISM}}$ of cold dust in the ambient ISM to be unifomly distributed between 15 and 25 K. We draw the fractional contribution $\xi_{\mathrm{C}}^{\mathrm{ISM}}$ by cold dust in thermal equilibrium to the infrared luminosity of the ambient ISM from a uniform distribution between 0.5 and 1 (this also defines the contributions $\xi_{\mathrm{PAH}}^{\mathrm{ISM}}$, $\xi_{\mathrm{MIR}}^{\mathrm{ISM}}$ and $\xi_{\mathrm{W}}^{\mathrm{ISM}}$ by PAHs, the hot mid-infrared continuum and warm dust to the infrared luminosity of the ambient ISM, as described in Section 2.2.2.1). Our final library of infrared spectra consists of 50,000 different models.

We combine the library of stellar population models and that of infrared spectra by associating together models with similar f_μ, which we scale according to the total infrared luminosity $L_{\mathrm{d}}^{\mathrm{tot}}$, as outlined in Section 2.2.3. In practice, we associate each model in the stellar population library to all the models in the infrared spectral library that have similar f_μ to within some error interval δf_μ.[1] That is, we associate each stellar population spectrum, characterised by ${f_\mu}^{\mathrm{SFH}}$, to all the infrared spectra characterised by ${f_\mu}^{\mathrm{IR}}$, such that ${f_\mu}^{\mathrm{IR}}=f_\mu^{\mathrm{SFH}}\pm\delta f_\mu$. Each spectral combination satisfying this condition is included in the final model library and is assigned a value $f_\mu=({f_\mu}^{\mathrm{SFH}}+{f_\mu}^{\mathrm{IR}})/2$. We adopt $\delta f_\mu=0.15$, which allows good reproductions of combined ultraviolet, optical and infrared observations of galaxies (Section 3.3).

Our final library of combined ultraviolet, optical and infrared spectral energy distributions consists of about 661 million models. It is important to note that such a large number of models is required to properly sample the multi-dimensional observational space.

3.2.2 Statistical constraints on physical parameters

We now investigate the accuracy to which the model library described in the previous section can help us constrain the star formation histories and dust properties of galaxies for which multi-wavelength observations are available. To assess this, we evaluate how well we can recover the parameters of a random set of models

---

[1] This allows us to include the uncertainties that could arise, for example, from orientation effects, in the connection between the stellar and dust emission.

with known properties, based on spectral fits. We consider the following observable quantities: the *GALEX* far-ultraviolet (*FUV*, 1520 Å) and near-ultraviolet (*NUV*, 2310 Å) luminosities; the optical *UBV* luminosities; the 2MASS near-infrared *JHKs* (1.25, 1.65 and 2.17 μm) luminosities; the *Spitzer*/IRAC 3.6, 4.5, 5.8 and 8.0 μm luminosities; the *ISO*/ISOCAM 6.75 and 15 μm luminosities; the *IRAS* 12, 25, 60 and 100 μm luminosities; the *Spitzer*/MIPS (Rieke et al. 2004) 24, 70 and 160 μm luminosities; and the SCUBA (Holland et al. 1999) 850 μm luminosity. We also include the hydrogen Hα and Hβ recombination-line luminosities.

We compute these observable quantities from the spectra of all 661 million models in the library and randomly select a subset of 100 models. To mimic observational conditions, we perturb the luminosities of this subset of models assuming a fixed uncertainty of 10 per cent. We then perform spectral fits to recover the likelihood distributions of the physical parameters of these 'mock galaxies' as follows. We first compare the luminosities of each mock galaxy in the sample to the luminosities of every model j in the library to measure the χ^2 goodness-of-fit of that model (e.g. , Bevington & Robinson 2003)

$$\chi^2_j = \sum_i \left(\frac{L^i_\nu - w_j \times L^i_{\nu,j}}{\sigma_i} \right)^2 , \tag{3.1}$$

where L^i_ν and $L^i_{\nu,j}$ are the luminosities in the ith band of the mock galaxy and the jth model, respectively, σ_i is the (10 percent) uncertainty in L^i_ν, and

$$w_j = \left(\sum_i \frac{L^i_\nu L^i_{\nu,j}}{\sigma_i^2} \right) \left[\sum_i \left(\frac{L^i_{\nu,j}}{\sigma_i} \right)^2 \right]^{-1} \tag{3.2}$$

is the model scaling factor that minimizes χ^2_j. Then, we build the probability density function of any physical parameter of the mock galaxy by weighting the value of that parameter in the jth model by the probability $\exp(-\chi^2_j/2)$. We take our 'best estimate' of the parameter to be the median of the resulting probability density function and the associated confidence interval to be the 16th–84th percentile range (this would be equivalent to the $\pm 1\sigma$ range in the case of a Gaussian distribution).

In Fig. 3.1, we compare the median-likelihood estimates to the true values of 12 parameters recovered in this way for the 100 mock galaxies in our sample. These parameters are: the fraction of total infrared luminosity contributed by dust in the ambient ISM, f_μ; the total effective V-band absorption optical depth of the dust, $\hat{\tau}_V$; the fraction of this contributed by dust in the ambient ISM, μ; the specific star formation rate, $\psi_{\rm S}$, defined as the ratio

$$\psi_{\rm S}(t) = \frac{\int_{t-t_8}^{t} dt'\, \psi(t')}{t_8\, M_*} \tag{3.3}$$

of the star formation rate averaged over the past $t_8 = 10^8$yr to the current stellar

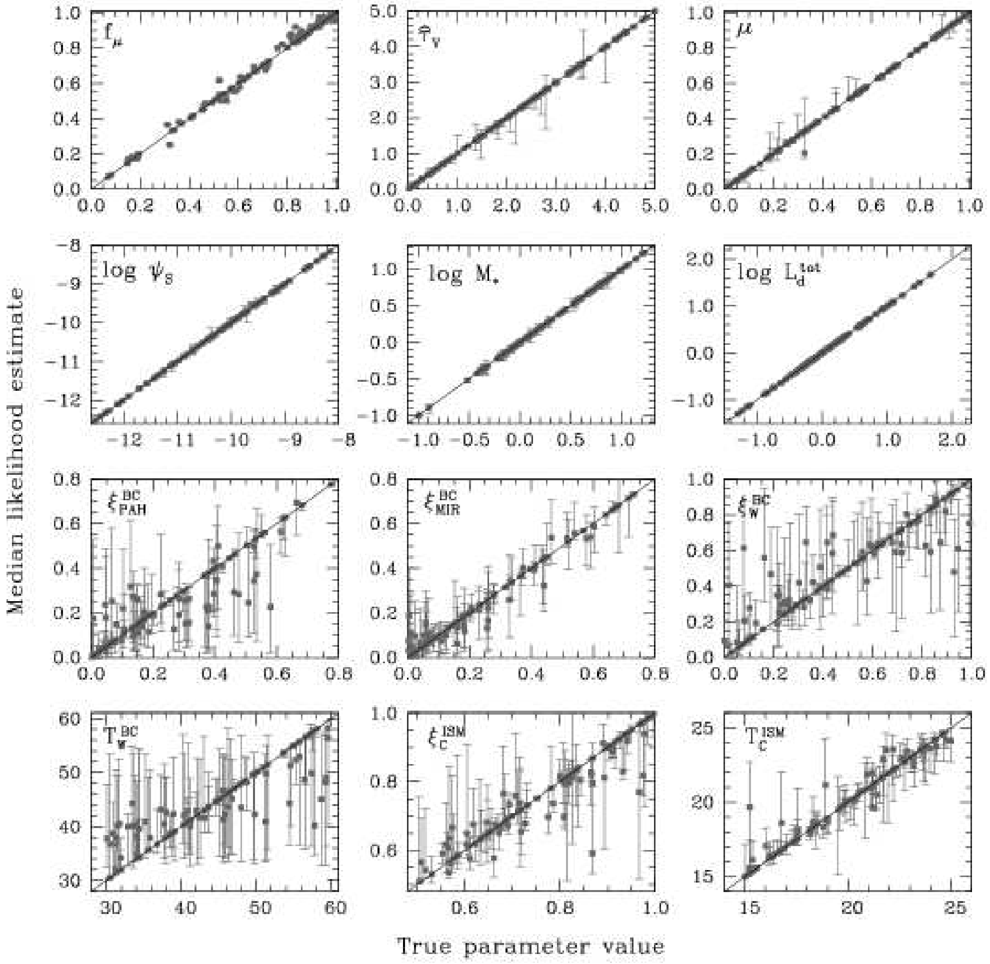

Figure 3.1: Median-likelihood estimates of 12 parameters (indicated in the upper left corner of each panel) recovered from the spectral fits of 100 mock galaxies, compared to the true values of these parameters (see Section 3.2.2). The error bars indicate the 16th–84th percentile ranges in the recovered probability distributions of the parameters. These results were obtained by fitting simulated *GALEX* (*FUV* and *NUV*), optical (*UBV*), 2MASS (*JHKs*), *Spitzer*/IRAC (3.6, 4.5, 5.8 and 8.0 μm), *ISO*/ISOCAM (6.75 and 15μm), *IRAS* (12, 25, 60, 100 μm), *Spitzer*/MIPS (24, 70, and 160 μm), SCUBA (850 μm), and Hα and Hβ luminosities.

mass M_* of the galaxy; the stellar mass, M_* (this accounts for the mass returned to the ISM by evolved stars); the total infrared luminosity, $L_{\rm d}^{\rm tot}$; the fractional contributions by PAHs, the hot mid-infrared continuum and warm dust in thermal equilibrium to the infrared luminosity of stellar birth clouds, $\xi_{\rm PAH}^{\rm BC}$, $\xi_{\rm MIR}^{\rm BC}$ and $\xi_{\rm W}^{\rm BC}$; the equilibrium temperature of warm grains in stellar birth clouds, $T_{\rm W}^{\rm BC}$; the contribution by cold dust to the total infrared luminosity of the ambient ISM, $\xi_{\rm C}^{\rm ISM}$, and the equilibrium temperature of this dust, $T_{\rm C}^{\rm ISM}$. Most of these parameters are recovered remarkably well by our model. In particular, f_μ, $\hat{\tau}_V$, μ, $\psi_{\rm S}$, M_*, $L_{\rm d}^{\rm tot}$, $\xi_{\rm MIR}^{\rm BC}$, $\xi_{\rm C}^{\rm ISM}$ and $T_{\rm C}^{\rm ISM}$ are recovered to very high accuracy. The most uncertain parameters are $\xi_{\rm PAH}^{\rm BC}$, $\xi_{\rm W}^{\rm BC}$ and $T_{\rm W}^{\rm BC}$, for which the typical confidence intervals reach almost 0.14, 0.18 and 11 K, respectively. We conclude that our model is a valuable tool for deriving statistical constraints on the star formation histories and dust properties of galaxies for which multi-wavelength (ultraviolet, optical and infrared) observations are available.

3.3 Application to the SINGS sample

3.3.1 The sample

Here, we exploit our model to interpret a wide range of ultraviolet, optical and infrared observations of a sample of well-studied nearby galaxies: the Spitzer Infrared Nearby Galaxy Survey (SINGS; Kennicutt et al. 2003). This sample contains 75 galaxies at a median distance of 9.5 Mpc (we adopt a Hubble constant $\rm H_0 = 70\,km\,s^{-1}Mpc^{-1}$). The galaxies span wide ranges in morphology (from E-S0 to Im-I0) and star formation activity (from quiescent to starburst). Some galaxies include low-luminosity active galactic nuclei (AGNs).[2] We note that this sample extends out to lower total infrared luminosities than the Elbaz et al. (2002) sample used to calibrate the infrared properties of our model in Section 2.2.2.2 ($L_{\rm d}^{\rm tot} \lesssim 10^{11} L_\odot$ instead of $L_{\rm d}^{\rm tot} \lesssim 10^{12} L_\odot$), but it includes observations across a much wider range of wavelengths.

Observations at ultraviolet, optical and infrared wavelengths are available for most galaxies in this sample. *GALEX* ultraviolet (*NUV* and *FUV*) observations are available for 70 galaxies (Dale et al. 2007). In the optical, we adopt *UBV* fluxes from the RC3 for 65 galaxies (de Vaucouleurs et al. 1991).[3] Near-infrared *JHKs* fluxes are available for all galaxies from the 2MASS Large Galaxy Atlas (Jarrett et al. 2003). In the mid- and far-infrared, we use the *Spitzer* observations published by Dale et al. (2007). This includes IRAC photometry at 3.6, 4.5, 5.8 and 8.0 μm and MIPS photometry at 24, 70 and 160 μm. *ISO*, *IRAS* and SCUBA 850 μm observations are also available for 13, 65 and 22 SINGS galaxies, respectively. These observations are typically of lower quality than *Spitzer* data, with photometric uncertainties around 20 per cent for *ISO* and *IRAS* and 30 per cent for SCUBA. More detail about the photometry of SINGS galaxies can be found in Dale et al. (2005, 2007).

It is important to note that these multi-wavelength observations can be combined in a meaningful way, since the fluxes all pertain to the total emission from a galaxy. For example, the *GALEX* (*FUV* and *NUV*), RC3 (*UBV*) and 2MASS

---

[2] The low-luminosity AGNs should have a negligible impact on the integrated broad-band fluxes of the galaxies. We distinguish galaxies hosting low-luminosity AGNs from normal star-forming galaxies in the spectral analyses presented later in this paper.

[3] We choose not to use the optical *BVRI* fluxes tabulated by Dale et al. (2007), because of calibration problems in the optical photometry of the SINGS Fifth Enhanced Data Release (D. Dale & A. Gil de Paz, priv. comm.)

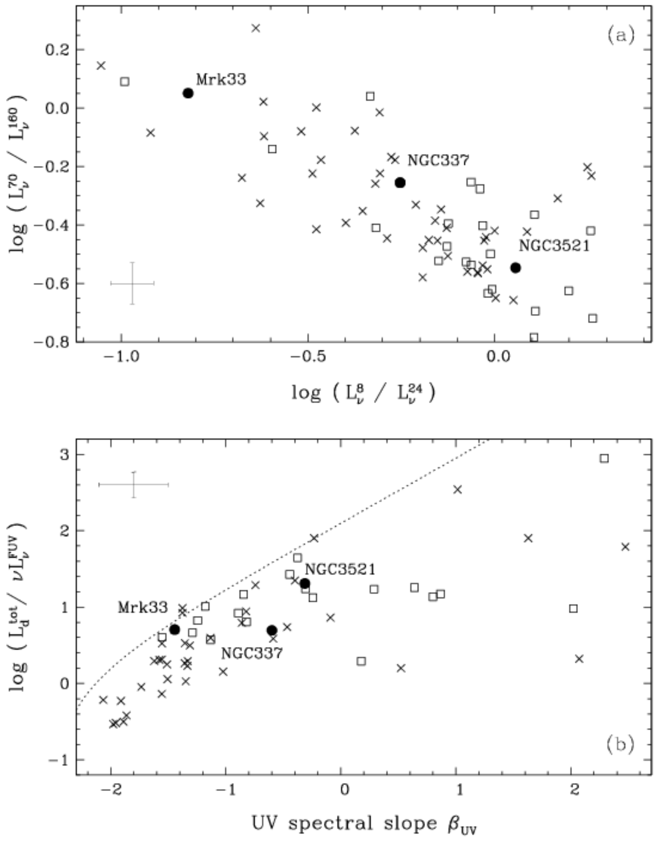

Figure 3.2: Selected properties of the SINGS galaxy sample discussed in Section 3.3. (a) Ratio of 70-μm to 160-μm luminosity plotted against ratio of 8-μm to 24-μm luminosity. (b) Ratio of total-infrared to ultraviolet luminosity as a function of ultraviolet spectral slope (the IRX–UV diagram). The dotted line in this diagram shows a fit by Kong et al. (2004) to the relation followed by starburst galaxies (Meurer, Heckman & Calzetti 1999). In both panels, crosses refer to galaxies with no AGN activity according to Kennicutt et al. (2003), while open squares refer to galaxies hosting low-luminosity AGNs (LINER and Seyfert). Filled circled indicate three galaxies selected along the L_ν^{70}/L_ν^{160} versus L_ν^{8}/L_ν^{24} relation, for which a wide set of observations are available (Section 3.3.2). Typical measurement errors are indicated in each diagram.

(*JHKs*) fluxes were obtained by integrating extrapolated surface brightness profiles to include the entire emission from a galaxy (see de Vaucouleurs et al. 1991; Jarrett et al. 2003; Gil de Paz et al. 2006). Also, the infrared *Spitzer* IRAC and MIPS fluxes include extended-source aperture corrections (amounting typically to 10 per cent; see Dale et al. 2005, 2007). Following Draine et al. (2007), we exclude 9 galaxies with bad IRAC and MIPS detections (because of contamination by external sources; very low surface brightness compared to foreground cirrus emission; and saturation issues): NGC 584, NGC 3034, NGC 1404, NGC 4552, M81 DwarfA, M81 DwarfB, DDO 154, DDO 165 and Holmberg IX. For 19 galaxies, we include Hα and Hβ emission-line fluxes (corrected for contamination by stellar absorption) from the integrated spectroscopy of Moustakas & Kennicutt (2006). Our final sample includes 66 galaxies, of which 61 have *GALEX* measurements. As before, for the purpose of comparisons with models, we neglect possible anisotropies and equate flux ratios at all wavelengths to the corresponding luminosity ratios.

We illustrate the ultraviolet and infrared properties of the SINGS galaxies in Fig. 3.2. Fig. 3.2a shows the MIPS L_ν^{70}/L_ν^{160} luminosity ratio plotted against the IRAC+MIPS L_ν^{8}/L_ν^{24} luminosity ratio. SINGS galaxies in this diagram follow a sequence very similar to that followed by the galaxies of the Elbaz et al. (2002) sample of Section 2.2.2 in the analogous *IRAS* L_ν^{60}/L_ν^{100} versus L_ν^{12}/L_ν^{25} diagram (Fig. 2.3). In Fig. 3.2b, we plot ratio of total-infrared to ultraviolet luminosity $L_{\rm d}^{\rm tot}/L_{\rm FUV}$ as a function of ultraviolet spectral slope $\beta_{\rm UV}$ (the 'IRX-UV diagram'). We used equation (4) of Dale & Helou (2002) to estimate $L_{\rm d}^{\rm tot}$ from the MIPS observations at 24, 70 and 160 μm, and equation (1) of Kong et al. (2004) to compute $\beta_{\rm UV}$ from the *GALEX FUV* and *NUV* luminosities. Previous studies have shown that starburst galaxies follow a tight sequence in this diagram (indicated by the dotted line in Fig. 3.2b), while more quiescent star-forming galaxies tend to exhibit redder ultraviolet spectra (i.e. larger $\beta_{\rm UV}$) than starburst galaxies at fixed $L_{\rm d}^{\rm tot}/L_{\rm FUV}$ (Meurer, Heckman & Calzetti 1999; Bell 2002; Kong et al. 2004). Fig. 3.2 confirms that the SINGS galaxies are representative of the ultraviolet and infrared properties of nearby galaxies.

3.3.2 Example of constraints on physical parameters

We now use the methodology outlined in Section 3.2 to constrain the star formation histories and dust properties of the SINGS galaxies. We first assess how well our model can reproduce the observed multi-wavelength observations of these galaxies. For each observed galaxy, we select the model of the library presented in Section 3.2 that minimizes χ_j^2 (equation 3.1), as computed by including as many luminosities as available in the following bands: *GALEX* (*FUV* and *NUV*), optical (*UBV*), 2MASS (*JHKs*), *Spitzer*/IRAC (3.6, 4.5, 5.8 and 8.0 μm), *ISO*/ISOCAM (6.75 and 15μm), *IRAS* (12, 25, 60 and 100 μm), *Spitzer*/MIPS (24, 70 and 160 μm), SCUBA (850 μm) and Hα and Hβ. Fig. 3.3 shows the resulting distribution of the difference between the observed luminosity $L_\nu^{\rm obs}$ and the best-fit model luminosity $L_\nu^{\rm mod}$, in units of the observational error $\sigma^{\rm obs}$, for the 66 galaxies in the sample (plain histograms). Each panel shows the result for a different photometric band. For reference, the shaded histograms show the results obtained when excluding the 22 galaxies identified as hosts of low-luminosity AGNs by Kennicutt et al. (2003).

Fig. 3.3 shows that our model can reproduce simultaneously the ultraviolet, optical and near-, mid- and far-infrared observations of all but a few SINGS galaxies to within the observational errors. This is remarkable, considering the relative simplicity of the model. We find that the galaxies the least well fitted at ultraviolet

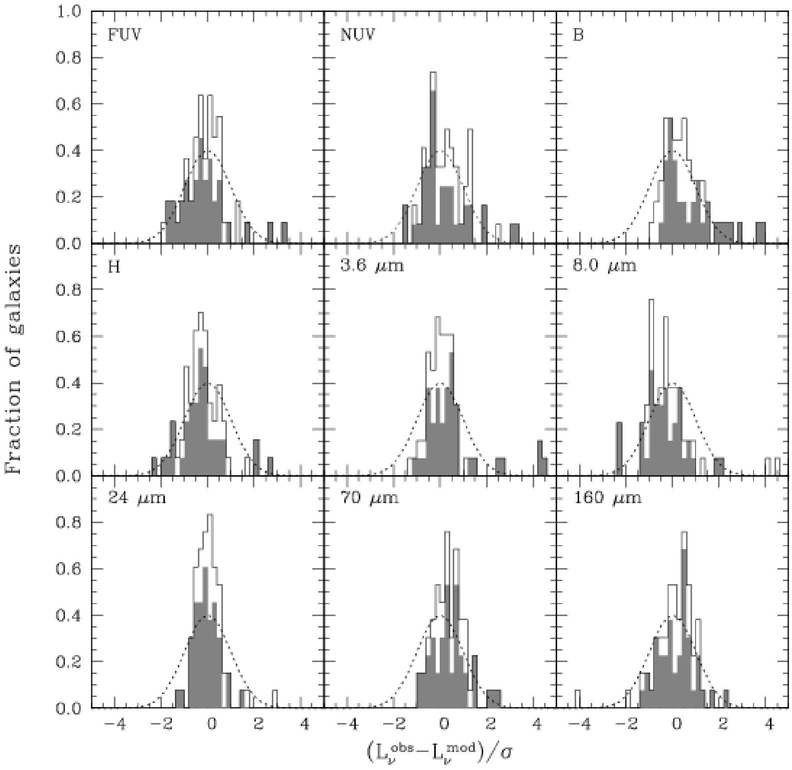

Figure 3.3: Distribution of the difference between observed luminosity $L_\nu^{\rm obs}$ and best-fit model luminosity $L_\nu^{\rm mod}$, in units of the observational error $\sigma^{\rm obs}$, for the 66 galaxies of the SINGS sample studied in Section 3.3 Each panel refers to a different photometric band (as indicated). The best-fit model for each galaxy was selected by fitting as many luminosities as available in the following bands: *GALEX* (*FUV* and *NUV*), optical (*UBV*), 2MASS (*JHKs*), *Spitzer*/IRAC (3.6, 4.5, 5.8 and 8.0 μm), *ISO*/ISOCAM (6.75 and 15μm), *IRAS* (12, 25, 60 and 100 μm), *Spitzer*/MIPS (24, 70 and 160 μm), SCUBA (850 μm) and Hα and Hβ. In each panel, the plain histogram shows the result for the full sample of 66 SINGS galaxies, while the shaded histogram shows the result for the subsample of 44 galaxies with no AGN activity according to Kennicutt et al. (2003). The dotted curve shows a Gaussian distribution with unit standard deviation, for reference.

and optical wavelengths tend to be low-metallicity dwarf galaxies, such as the blue compact dwarf galaxy NGC 2915 (e.g. Lee, Grebel & Hodge 2003) and the diffuse dwarf irregular galaxy Holmberg II (e.g. Hoessel, Saha & Danielson 1998). The difficulty in reproducing these observations may arise either from a limitation of the spectral synthesis code, or of the simple dust prescription, or from an underestimate of observational errors. The three galaxies for which the models significantly underestimate the 3.6 μm emission in Fig. 3.3 are also low-metallicity dwarf galaxies (NGC4236, IC4710 and NGC6822). For these galaxies, our simple scaling of the near-infrared continuum strength around 4 μm with the flux density of the 7.7 μm PAH feature may not be appropriate (see Section 2.2.2.1). Fig. 3.3 further shows that the galaxies with 8 μm mid-infrared luminosities least well reproduced by the model tend to be hosts of low-luminosity AGNs. In these galaxies, the contribution to the infrared emission by dust heated by the AGN may be significant. Despite these few outliers, we conclude from Fig. 3.3 that our model is adequate to investigate the constraints set on the physical properties of SINGS galaxies by their ultraviolet, optical and infrared spectral energy distributions.

To investigate the implications of these fits for the determination of physical parameters, we focus on three galaxies spanning different dust properties along the L_ν^{70}/L_ν^{160} versus L_ν^{8}/L_ν^{24} colour-colour relation in Fig. 3.2a, for which a wide set of observations are available: NGC 3521, a spiral (SABbc) galaxy at a distance of 9 Mpc; NGC 337, a spiral (SBd) galaxy at a distance of 24.7 Mpc; and Mrk 33, a dwarf irregular (Im) starburst galaxy at a distance of 21.7 Mpc. For all three galaxies, observations from *GALEX* (*FUV* and *NUV*), 2MASS (*JHKs*), *Spitzer* (IRAC and MIPS), *IRAS* and SCUBA are available, along with integrated Hα and Hβ spectroscopy from Moustakas & Kennicutt (2006). For NGC 3521 and NGC 337, additional constraints are available from RC3 (*UBV*) and *ISO* (ISOCAM 6.75 and 15μm) photometry.

Fig. 3.4 shows the models (in black) providing the best fits to the observed ultraviolet, optical, Hα and Hβ, and infrared spectral energy distributions of these three galaxies (in red). The quality of the fits is remarkable, as quantified by the residuals shown at the bottom of each spectrum. We note that, according to the best-fit models, the sequence of increasing F_ν^{70}/F_ν^{160} and decreasing F_ν^{8}/F_ν^{24} colours from NGC 3521 to NGC 337 to Mrk 33, which reflects a drop in the relative intensity of PAHs and a blueshift of the peak infrared luminosity (i.e. a rise in the overall dust temperature), is associated to an increase in star formation activity. This is apparent from the relative strengthening of the unattenuated ultraviolet and optical spectrum (in blue) from NGC 3521 to NGC 337 to Mrk 33 in Fig. 3.4. We investigate this trend further in Section 3.3.3 below.

We can study in more detail the constraints set on the star formation histories and dust properties of the galaxies by looking at the probability distributions of the corresponding model parameters. In Figs. 3.5 and 3.6, we show the likelihood distributions of 14 quantities constrained by the observed spectral energy distributions of NGC 3521, NGC 337 and Mrk 33. These distributions were derived using the model library of Section 3.2.1, following the procedure outlined in Section 3.2.2. Fig. 3.5 shows the likelihood distributions of parameters pertaining to the star formation history and dust content: fraction of the total infrared luminosity contributed by dust in the ambient ISM (f_μ); fraction of the total effective V-band absorption optical depth of the dust contributed by the ambient ISM (μ); effective V-band absorption optical depth of the dust ($\hat{\tau}_V$); effective V-band absorption optical depth of the dust in the ambient ISM ($\mu\hat{\tau}_V$); specific star formation rate (ψ_S; equation 3.3); stellar mass (M_*); and dust mass (M_d; equation 2.30). Fig. 3.6 shows the likelihood distributions of parameters pertaining to the dust emission: total infrared

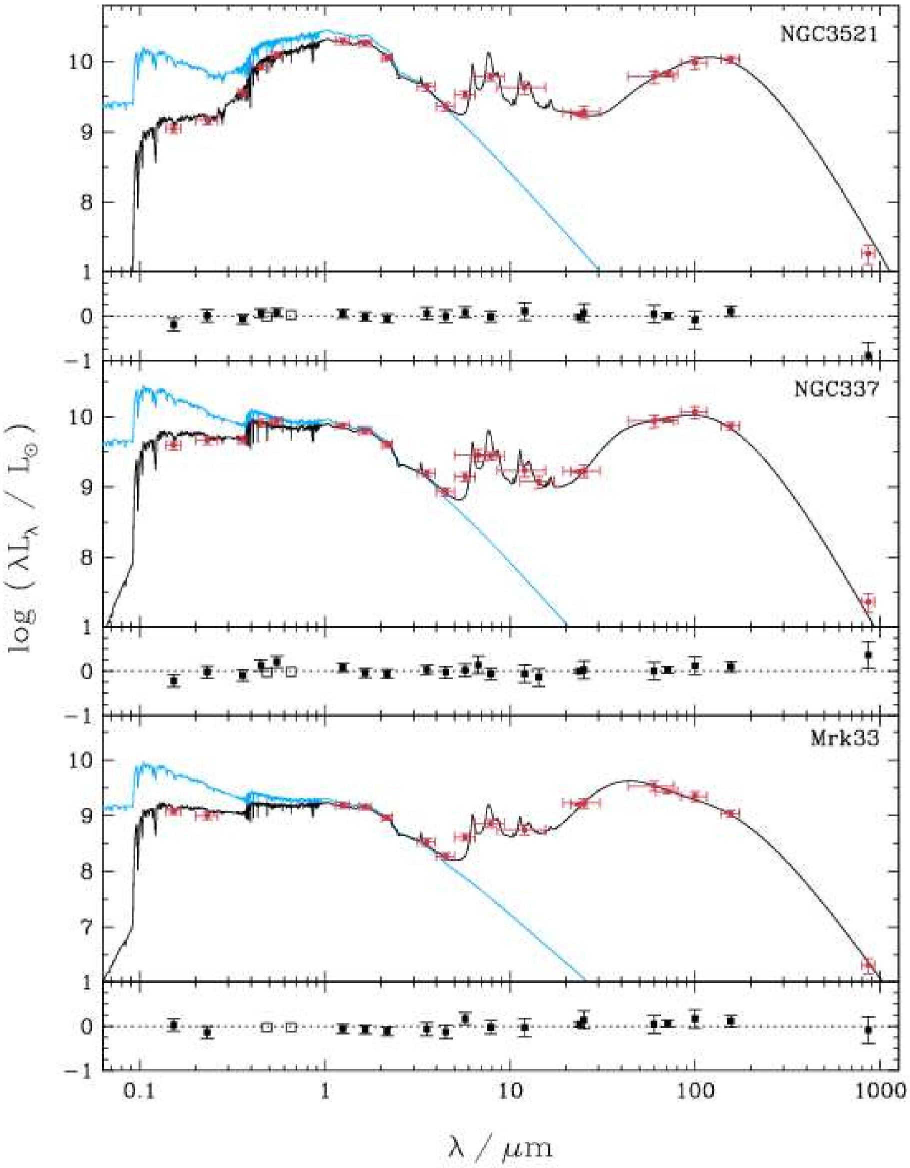

Figure 3.4: Best model fits (in black) to the observed spectral energy distributions (in red) of the three galaxies NGC 3521 (top panel), NGC 337 (middle panel) and Mrk 33 (bottom panel) spanning the infrared colour-colour relation of Fig. 3.2a. In each panel, the blue line shows the unattenuated stellar population spectrum. For each observational point, the vertical error bar indicates the measurement error, while the horizontal error bar shows the effective width of the corresponding photometric bands. The residuals $(L_\lambda^{\rm obs} - L_\lambda^{\rm mod})/L_\lambda^{\rm obs}$ are shown at the bottom of each panel. Filled squares refer to broad-band luminosties (*GALEX FUV* and *NUV*; RC3 *UBV*; 2MASS *JHKs*; *Spitzer* IRAC and MIPS; *ISO*, *IRAS* and SCUBA); open squares to the integrated Hα and Hβ luminosities.

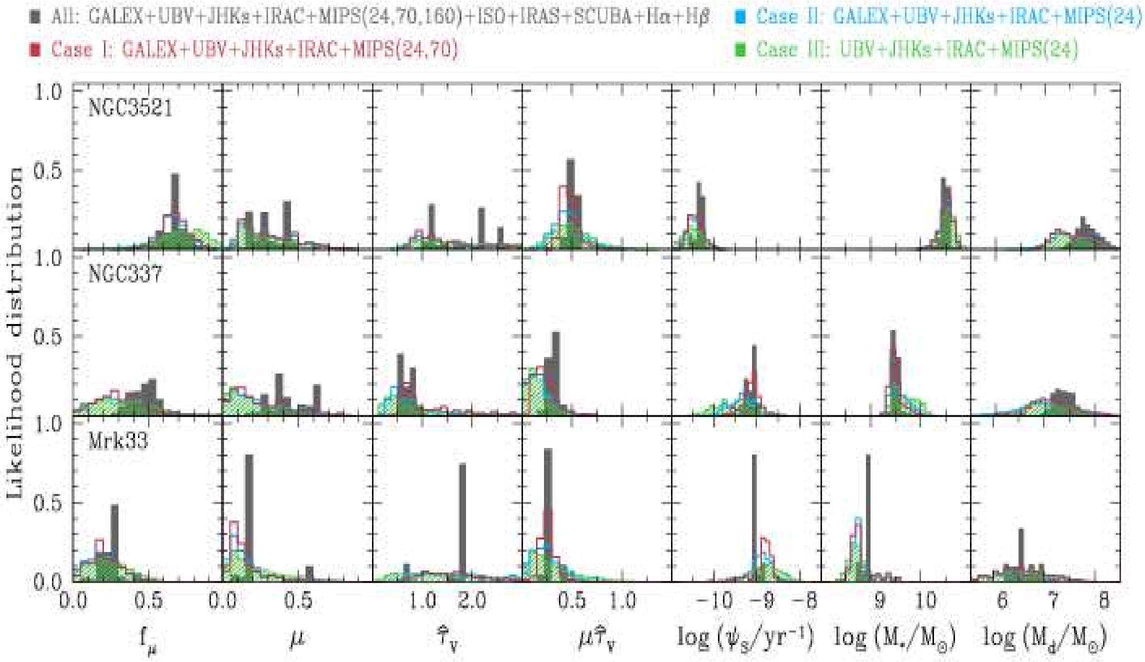

Figure 3.5: Likelihood distributions of physical quantities derived from fits to the observed ultraviolet, optical and infrared spectral energy distributions of NGC 3521 (top row), NGC 337 (middle row) and Mrk 33 (bottom row): fraction of the total infrared luminosity contributed by dust in the ambient ISM (f_μ); total effective V-band absorption optical depth of the dust ($\hat{\tau}_V$); fraction of the total V-band absorption optical depth of the dust contributed by the ambient ISM (μ); effective V-band absorption optical depth of the dust in the ambient ISM ($\mu\hat{\tau}_V$); specific star formation rate (ψ_S); stellar mass (M_*); and dust mass (M_d). The different histograms correspond to the different sets of observational constraints indicated at the top of the figure (see text of Section 3.3.2 for more detail).

luminosity ($L_\mathrm{d}^\mathrm{tot}$); global contributions (i.e. including stellar birth clouds and the ambient ISM) by PAHs ($\xi_\mathrm{PAH}^\mathrm{tot}$), the hot mid-infrared continuum ($\xi_\mathrm{MIR}^\mathrm{tot}$) and warm dust in thermal equilibrium ($\xi_\mathrm{W}^\mathrm{tot}$) to the total infrared luminosity (equations 2.19, 2.20 and 2.21); equilibrium temperature of warm dust in stellar birth clouds (T_W^BC); contribution by cold dust in thermal equilibrium to the total infrared luminosity ($\xi_\mathrm{C}^\mathrm{tot}$, equation 2.22); and equilibrium temperature of cold dust in the ambient ISM ($T_\mathrm{C}^\mathrm{ISM}$).

The different histograms in Figs. 3.5 and 3.6 refer to different assumptions about the available set of observations. The grey shaded histograms show the results obtained when using all the observational measurements from Fig. 3.4. In this case, all the parameters are well constrained by the observed ultraviolet, optical and infrared spectral energy distributions of the galaxies, except for the equilibrium temperature

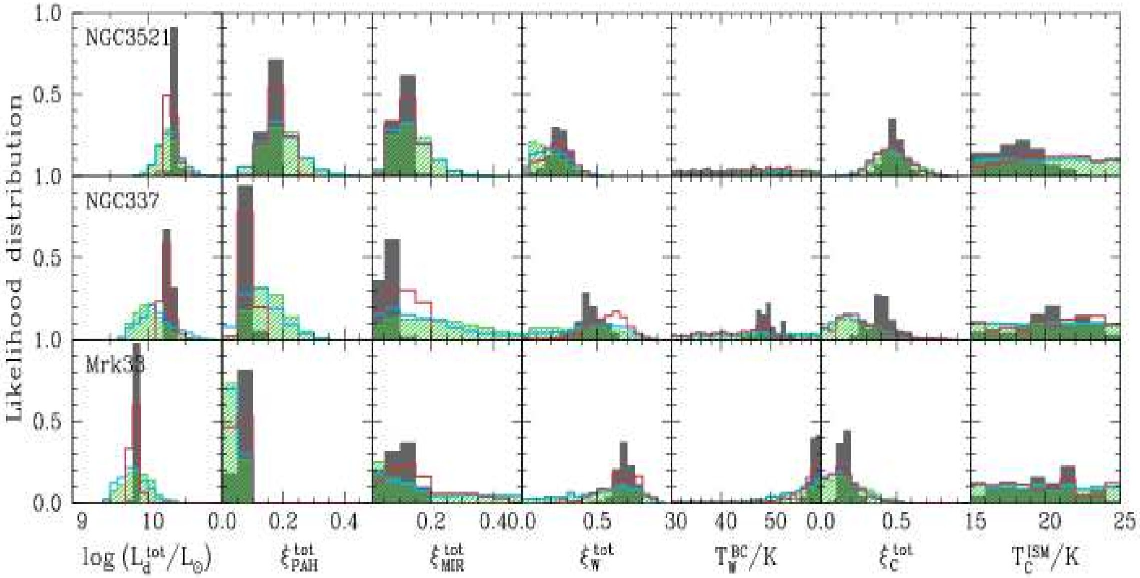

Figure 3.6: Likelihood distributions of physical quantities derived from fits to the observed ultraviolet, optical and infrared spectral energy distributions of NGC 3521 (top row), NGC 337 (middle row) and Mrk 33 (bottom row): total infrared luminosity of the dust ($L_{\mathrm{d}}^{\mathrm{tot}}$); global contributions (i.e. including stellar birth clouds and the ambient ISM) by PAHs ($\xi_{\mathrm{PAH}}^{\mathrm{tot}}$), the hot mid-infrared continuum ($\xi_{\mathrm{MIR}}^{\mathrm{tot}}$) and warm dust in thermal equilibrium ($\xi_{\mathrm{W}}^{\mathrm{tot}}$) to the total infrared luminosity; equilibrium temperature of warm dust in stellar birth clouds ($T_{\mathrm{W}}^{\mathrm{BC}}$); contribution by cold dust in thermal equilibrium to the total infrared luminosity ($\xi_{\mathrm{C}}^{\mathrm{tot}}$); and equilibrium temperature of cold dust in the ambient ISM ($T_{\mathrm{C}}^{\mathrm{ISM}}$). The different histograms correspond to the different sets of observational constraints indicated at the top of Fig. 3.5 (see text of Section 3.3.2 for more detail).

$T_{\mathrm{W}}^{\mathrm{BC}}$ of warm dust in stellar birth clouds in NGC 3521. This is not surprising, since the total infrared emission from this galaxy is largely dominated by dust in the ambient ISM (as can be appreciated, for example, from the analogous spectrum of the quiescent star-forming galaxy of Fig. 2.5a). We find that, as anticipated from Fig. 3.4, the transition from NGC 3521 to NGC 337 to Mrk 33 corresponds to a combined rise in specific star formation rate (ψ_{S}) and dust temperature ($T_{\mathrm{W}}^{\mathrm{BC}}$ and $T_{\mathrm{C}}^{\mathrm{ISM}}$), a larger contribution to the total infrared luminosity by warm dust ($\xi_{\mathrm{W}}^{\mathrm{tot}}$) relative to cold dust ($\xi_{\mathrm{C}}^{\mathrm{tot}}$), and by stellar birth clouds relative to the ambient ISM (f_μ), and a weakening of PAH features ($\xi_{\mathrm{PAH}}^{\mathrm{tot}}$). These results are consistent with the finding by Draine et al. (2007), on the basis of a more sophisticated physical dust model, that the intensity of the dust-heating starlight increases, and the fraction of dust mass contributed by PAHs decreases, from NGC 3521 to NGC 337 to Mrk 33. We emphasise the importance of finding tight constraints on all the adjustable model parameters in Figs. 3.5 and 3.6. This confirms that the problem is well defined and that our model can be used to derive meaningful constraints on the star formation histories and dust properties of galaxies from multi-wavelength observations.

In many situations, observations may not be available across the full range from ultraviolet to far-infrared wavelengths to constrain the physical parameters of galaxies. It is useful, therefore, to explore the constraints that can be derived on the physical parameters of Figs. 3.5 and 3.6 when reducing the set of available observations. We illustrate this by considering three potentially common situations:

(i) *Case I* (red histograms in Figs. 3.5 and 3.6): we relax the constraints on the Hα and Hβ, *ISO*/ISOCAM (6.75 and 15 μm), *IRAS* (12, 25, 60 and 100 μm), *Spitzer*/MIPS 160 μm and SCUBA 850 μm luminosities. This leaves constraints from *GALEX* (*FUV* and *NUV*), RC3 (*UBV*), 2MASS (*JHKs*), *Spitzer*/IRAC (3.6, 4.5, 5.8 and 8.0 μm) and *Spitzer*/MIPS (24 and 70 μm).

The most important effect of excluding the constraints on $L_{\mathrm{H}\alpha}$ and $L_{\mathrm{H}\beta}$ is to lose the determination of the total effective V-band absorption optical depth $\hat{\tau}_V$ in Fig. 3.5. This is because emission lines are the best tracers of dust in stellar birth clouds. In fact, the product $\mu\hat{\tau}_V$, i.e. the part of $\hat{\tau}_V$ arising from dust in the ambient ISM, remains reasonably well constrained by ultraviolet, optical and infrared photometry alone. In Fig. 3.6, the loss of far-infrared information redward of 70 μm (*IRAS* 100 μm, MIPS 160 μm and SCUBA 850 μm) has the most dramatic effect on determinations of the contribution by cold dust to the total infrared luminosity ($\xi_{\mathrm{C}}^{\mathrm{tot}}$) and on the equilibrium temperature of both cold ($T_{\mathrm{C}}^{\mathrm{ISM}}$) and warm ($T_{\mathrm{W}}^{\mathrm{BC}}$) dust. The IRAC data at wavelengths 3.6, 4.5, 5.8 and 8.0 μm still provide valuable constraints on $\xi_{\mathrm{PAH}}^{\mathrm{tot}}$, while the loss of *ISO* 6.75 and 15 μm and *IRAS* 12 μm information makes determinations of $\xi_{\mathrm{MIR}}^{\mathrm{tot}}$ and $\xi_{\mathrm{W}}^{\mathrm{tot}}$ more uncertain. The lack of far-infrared information also weakens the constraints on the dust mass M_{d} in Fig. 3.5.

(ii) *Case II* (blue histograms in Figs. 3.5 and 3.6): this is similar to Case I, but we also relax the constraint on the *Spitzer*/MIPS 70-μm luminosity. The main effect is to significantly worsen estimates of the contributions to the total infrared luminosity by warm dust in thermal equilibrium ($\xi_{\mathrm{W}}^{\mathrm{tot}}$) and by the hot mid-infrared continuum ($\xi_{\mathrm{MIR}}^{\mathrm{tot}}$). The constraints on the total infrared luminosity $L_{\mathrm{d}}^{\mathrm{tot}}$ itself are also slightly worse.

(iii) *Case III* (green histograms in Figs. 3.5 and 3.6): this is similar to Case II, but we also relax the constraints on the *GALEX FUV* and *NUV* luminosities. Not including information about the ultraviolet radiation from young stars has only a weak influence on the results of Figs. 3.5 and 3.6, when optical, near-infrared and mid-infrared data out to 24 μm are already available. The constraints on the specific star formation rate (ψ_{S}), the attenuation parameters (μ, $\hat{\tau}_V$ and the product $\mu\hat{\tau}_V$) and the relative contribution by dust in the ambient ISM to the total infrared luminosity (f_μ) become marginally worse.

The total infrared luminosity $L_{\rm d}^{\rm tot}$ and the stellar mass M_* remain reasonably well constrained.

We note that, if a galaxy has mid-infrared colours characteristic of Galactic cirrus emission, and if no other spectral information is available at shorter and longer wavelengths to constrain f_μ, it may be difficult to disentangle the contributions by stellar birth clouds and the ambient ISM to the total infrared luminosity. Galaxies with cirrus-like mid-infrared emission in the SINGS sample tend to have low specific star formation rates and infrared spectra dominated by the emission from ambient-ISM dust (as is the case, for example, for NGC 3521 in Fig. 3.4a). The inclusion of either far-infrared observations to constrain the temperature of the dust in thermal equilibrium or ultraviolet and optical observations to constrain the attenuation of starlight by dust can lift the ambiguity about the origin of the infrared emission (this is illustrated by the reasonably tight constraints obtained on f_μ for NGC 3521 in all the cases considered in Fig. 3.5). We have checked that the predicted mid-infrared emission of the ambient ISM in these analyses is always consistent with the expectation that stellar ultraviolet photons (with $\lambda < 3500$ Å) are the main contributors to the excitation of PAH molecules and the stochastic heating of dust grains responsible for the hot mid-infrared continuum. This is because stars slightly older than 10^7 yr, which have migrated from their birth clouds into the ambient ISM, are still bright in the ultraviolet. In the SINGS sample, for example, ultraviolet photons generated by stars older than 10^7 yr account for about 5 per cent of the heating of ambient-ISM dust for galaxies with the lowest specific star formation rates ($\psi_{\rm S}$). This fraction reaches about 85 per cent for galaxies with the highest $\psi_{\rm S}$. At the same time, PAHs and the hot mid-infrared continuum are found to produce from about 1 per cent to about 35 per cent, respectively, of the infrared luminosity of the ambient ISM in these galaxies. Thus, enough stellar ultraviolet photons are produced to account for the mid-infrared emission from PAHs and hot dust in the ambient ISM of these galaxies, even if a large part are absorbed by cooler grains in thermal equilibrium.

The above examples illustrate the usefulness of our model to interpret multi-wavelength observations of star-forming galaxies, and how particular observations may be important to constrain specific galaxy parameters. To further investigate the need for infrared information in the determination of $L_{\rm d}^{\rm tot}$, we compare in Fig. 3.7 estimates of this quantity obtained by fitting *GALEX*, RC3 and 2MASS data alone to those obtained when adding all the *Spitzer* mid- and far-infrared constraints (from IRAC and MIPS), for 61 SINGS galaxies with *GALEX* measurements in our sample. For most galaxies, both estimates are consistent with each other, although the estimates based on stellar emission alone are far more uncertain than those including infrared constraints (as can be seen from the much larger vertical than horizontal error bars in Fig 3.7). There is a tendency for starlight-based estimates of $L_{\rm d}^{\rm tot}$ to lie systematically under the more precise estimates including infrared constraints for the most luminous galaxies. This could arise, for example, if the SINGS galaxies with the largest infrared luminosities contained significant amounts of enshrouded

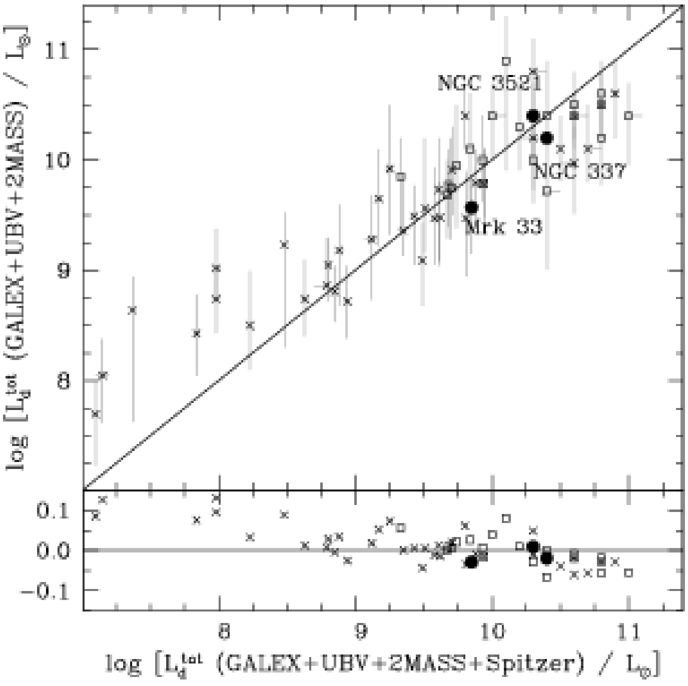

Figure 3.7: Estimates of the total infrared luminosity $L_{\rm d}^{\rm tot}$ derived from fits of the observed ultraviolet (*GALEX FUV* and *NUV*), optical (RC3 *UBV*) and near-infrared (2MASS *JHKs*) luminosities, plotted against estimates of the same quantity when including also the constraints from *Spitzer* (IRAC 3.6, 4.5, 5.8 and 8.0 μm and MIPS 24, 70, and 160 μm), for 61 galaxies with *GALEX* measurements in the sample studied in Section 3.3. The different symbols have the same meaning as in Fig. 3.2. The errors bars (in both the horizontal and vertical directions) represent the 16–84 percentile range in $L_{\rm d}^{\rm tot}$ derived from the likelihood distributions. The bottom panel shows the logarithm of the difference $L_{\rm d}^{\rm tot}(GALEX + UBV + {\rm 2MASS})$ minus $L_{\rm d}^{\rm tot}(GALEX + UBV + {\rm 2MASS} + Spitzer)$ divided by $L_{\rm d}^{\rm tot}(GALEX + UBV + {\rm 2MASS} + Spitzer)$.

stars with little contribution to the emergent optical and near-infrared light. At low $L_{\rm d}^{\rm tot}$, starlight-based estimates of the infrared luminosities of blue compact dwarf galaxies in our sample are very uncertain in Fig 3.7. We conclude that rough estimates of $L_{\rm d}^{\rm tot}$ may be obtained based on ultraviolet, optical and near-infrared observations alone (at least for values in the range from a few $\times 10^8$ to a few $\times 10^{10} L_\odot$), but reliable estimates of this parameter require longer-wavelength infrared observations. We note that the total dust luminosities estimated including infrared observations are typically within 10 per cent of those estimated by Draine et al. (2007) on the basis of their more sophisticated physical dust model.

3.3.3 Sample statistics

We can estimate the physical parameters of all the 66 SINGS galaxies in our sample in the same way as exemplified in Figs. 3.5 and 3.6 above for NGC 3521, NGC 337 and Mrk 33[4]. By doing so, we can explore potential correlations between different parameters of star-forming galaxies and infrared colours. In Table 3.1, we present the results of this investigation. We list the Spearman rank correlation coefficients for the relations between three *Spitzer* infrared colours, L_ν^8/L_ν^{24}, L_ν^{24}/L_ν^{70} and L_ν^{70}/L_ν^{160}, and 11 parameters derived from our spectral fits of SINGS galaxies: the specific star formation rate, ψ_S; the fraction of total infrared luminosity contributed by dust in the ambient ISM, f_μ; the global contributions (i.e. including stellar birth clouds and the ambient ISM) by PAHs ($\xi_\mathrm{PAH}^\mathrm{tot}$), the hot mid-infrared continuum ($\xi_\mathrm{MIR}^\mathrm{tot}$) and warm dust in thermal equilibrium ($\xi_\mathrm{W}^\mathrm{tot}$) to the total infrared luminosity (equations 2.19, 2.20 and 2.21); the equilibrium temperature of warm dust in stellar birth clouds, T_W^BC; the contribution by cold dust in thermal equilibrium to the total infrared luminosity, $\xi_\mathrm{C}^\mathrm{tot}$ (equation 2.22); the equilibrium temperature of cold dust in the ambient ISM, $T_\mathrm{C}^\mathrm{ISM}$; the star formation rate averaged over the past 100 Myr, $\psi = M_*\psi_S$ (see equation 3.3); the stellar mass, M_*; and the ratio of dust mass to stellar mass, M_d/M_* (see equation 2.30). We also indicate in Table 3.1 the significance levels of these correlations for our sample size of 66 galaxies.

Table 3.1 shows that the infrared colours L_ν^8/L_ν^{24} and L_ν^{70}/L_ν^{160} correlate well with several model quantities, such as ψ_S, f_μ, $\xi_\mathrm{PAH}^\mathrm{tot}$, $\xi_\mathrm{W}^\mathrm{tot}$, T_W^BC, $\xi_\mathrm{C}^\mathrm{tot}$ and $T_\mathrm{C}^\mathrm{ISM}$, while L_ν^{24}/L_ν^{70} does not. Furthermore, it is interesting to note that the specific star formation rate, but *not* the star formation rate itself, correlates well with L_ν^8/L_ν^{24} and L_ν^{70}/L_ν^{160}. This is illustrated in Fig. 3.8, where we show L_ν^8/L_ν^{24} and L_ν^{70}/L_ν^{160} as a function of both ψ_S and ψ for the 66 galaxies in our sample. We find that, as anticipated in Section 3.3.2, the correlation between infrared colours and specific star formation rate arises from a drop in the relative intensity of PAHs and a blueshift of the peak infrared luminosity (i.e. a rise in the overall dust temperature) when the star formation activity increases.

In Fig. 3.9, we explore the relations between ψ_S and other physical properties of the SINGS galaxies, which correlate well with infrared colours: f_μ, $\xi_\mathrm{PAH}^\mathrm{tot}$, $\xi_\mathrm{W}^\mathrm{tot}$, $\xi_\mathrm{C}^\mathrm{tot}$ and M_d/M_* (Table 3.1). The Spearman rank coefficients for these correlations are $r_S = -0.764$ (indicating a 6σ significance level for the sample size), -0.551 (4σ), 0.739 (6σ), -0.647 (5σ) and 0.780 (6σ), respectively. For completeness, we also show in Fig. 3.9 the relation between dust-to-gas mass ratio, $M_\mathrm{d}/M_\mathrm{H}$, and ψ_S, for the 35 galaxies with gas masses $M_\mathrm{H} = M(\mathrm{H\,I} + \mathrm{H_2})$ available from Draine et al. (2007). In this case, the Spearman rank coefficient is $r_S = -0.537$, indicating a 3σ correlation only for the reduced sample size. We note that the dust masses in Fig. 3.9 are typically within 50 per cent of those estimated by Draine et al. (2007) on the basis of their more sophisticated physical dust model.

---

[4] The median-likelihood estimations for each parameter of the model as well as the respective confidence intervals are listed for each galaxy in Appendix B.

Table 3.1: Correlations between three *Spitzer* infrared colours L_ν^8/L_ν^{24}, L_ν^{24}/L_ν^{70} and L_ν^{70}/L_ν^{160} and the median likelihood estimates of several physical parameters constrained using our model, for the 66 SINGS galaxies in our sample. For each combination of infrared colour and parameter, the first row indicates the Spearman rank correlation coefficient r_S of the relation between the two quantities, while the second row indicates the significance level of the correlation for the sample size.

	L_ν^8/L_ν^{24}	L_ν^{24}/L_ν^{70}	L_ν^{24}/L_ν^{70}
ψ_S	-0.723	0.018	0.466
	6σ	$< 1\sigma$	4σ
f_μ	0.679	-0.201	-0.464
	5σ	2σ	4σ
$\xi_{\rm PAH}^{\rm tot}$	0.715	0.182	-0.556
	6σ	1σ	4σ
$\xi_{\rm MIR}^{\rm tot}$	0.108	0.253	-0.162
	1σ	2σ	1σ
$\xi_{\rm W}^{\rm tot}$	-0.858	0.212	0.741
	7σ	2σ	6σ
$T_{\rm W}^{\rm BC}$	-0.437	0.423	0.509
	4σ	3σ	4σ
$\xi_{\rm C}^{\rm tot}$	0.663	-0.390	0.577
	5σ	3σ	5σ
$T_{\rm C}^{\rm ISM}$	-0.318	-0.081	0.692
	3σ	$< 1\sigma$	6σ
ψ	-0.007	0.503	-0.123
	$< 1\sigma$	4σ	1σ
M_*	0.634	0.243	-0.450
	3σ	1σ	$< 1\sigma$
$M_{\rm d}/M_*$	-0.377	0.133	0.040
	3σ	1σ	$< 1\sigma$

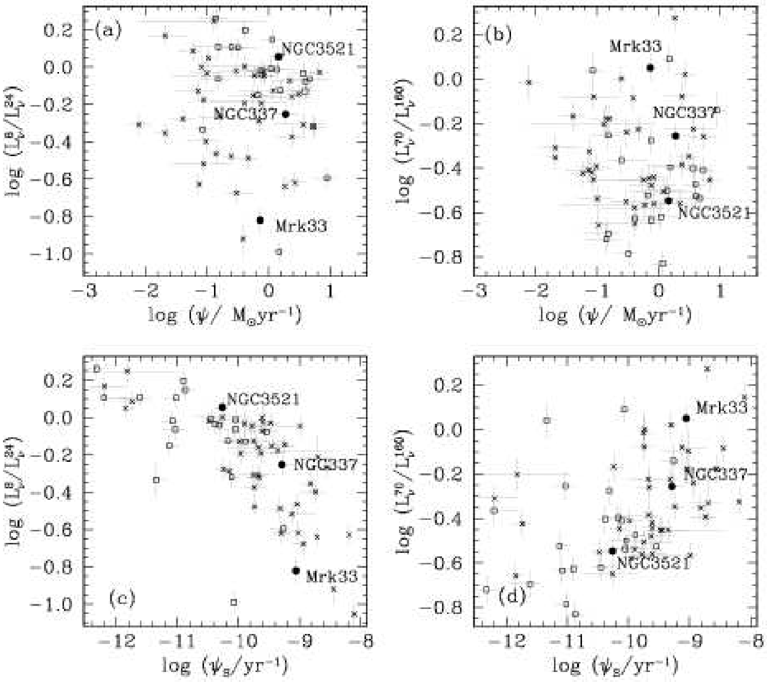

Figure 3.8: *Spitzer* infrared colours plotted against median-likelihood estimates of the star formation rate, for the 66 SINGS galaxies of the sample discussed in Section 3.3. (a) Ratio of 8-μm to 24-μm luminosity plotted against star formation rate averaged over the past 100 Myr, $\psi = M_* \psi_S$ (see equation 3.3). (b) Ratio of 70-μm to 160-μm luminosity plotted against ψ. (c) Ratio of 8-μm to 24-μm luminosity plotted against specific star formation rate ψ_S. (d) Ratio of 70-μm to 160-μm luminosity plotted against ψ_S. The different symbols have the same meaning as in Fig. 3.2. For each point, the vertical error bars represent the $\pm 1\sigma$ observational uncertainties, while the horizontal error bars represent the 16th–84th percentile range derived from the likelihood distribution of the quantity on the x-axis.

The strong correlations between infrared colours and several physical quantities of the SINGS galaxies in Fig. 3.8 and 3.9 provide important insight into the link between star formation and ISM properties in galaxies. For example, we also find a 7σ correlation between the star formation rate ψ and the dust mass M_d for the 66 SINGS galaxies in our full sample, and a 5σ correlation between ψ and the gas mass M_H for the 35 galaxies with H I and H_2 measurements (not shown). To some extent, the rise in the contribution by stellar birth clouds (i.e. giant molecular clouds) to the infrared emission from a galaxy when ψ_S increases (Fig. 3.9a), the accompanying rise in the contribution by warm dust (Fig. 3.9c), the drop in that by cold dust (Fig. 3.9d) and the weakening of PAH features (Fig. 3.9b) have been anticipated in several previous studies (e.g. , Helou 1986; Cesarsky et al. 1996; Silva et al. 1998; Dale et al. 2001, 2007). The originality of our approach is to *quantify*

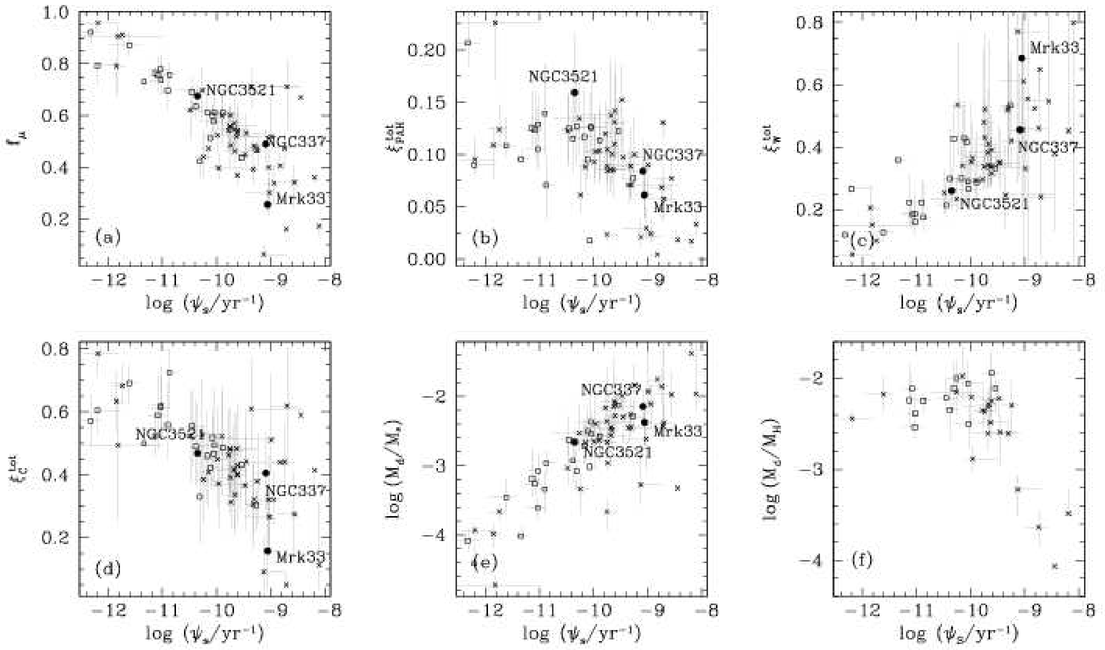

Figure 3.9: Median-likelihood estimates of galaxy properties plotted against specific star formation rate, for the 66 SINGS galaxies of the sample discussed in Section 3.3. (a) Fraction of total infrared luminosity contributed by dust in the ambient ISM, f_μ. (b) Global contribution (i.e. including stellar birth clouds and the ambient ISM) by PAHs to the total infrared luminosity, $\xi^{\rm tot}_{\rm PAH}$. (c) Global contribution by warm dust in thermal equilibrium to the total infrared luminosity $\xi^{\rm tot}_{\rm W}$. (d) Contribution by cold dust in thermal equilibrium to the total infrared luminosity, $\xi^{\rm tot}_{\rm C}$. (e) Ratio of dust mass to stellar mass, $M_{\rm d}/M_*$. (f) Ratio of dust mass to gas mass, $M_{\rm d}/M_{\rm H}$, for the 35 galaxies with gas masses $M_{\rm H} = M({\rm H\,I} + {\rm H_2})$ available from Draine et al. (2007). The different symbols have the same meaning as in Fig. 3.2. The error bars represent the 16–84 percentile ranges derived from the likelihood distributions of the estimated parameters.

these effects by means of a simple but versatile model, which allows statistical studies of the star formation and dust properties of large samples of galaxies. It is worth emphasising that our method does not introduce these relations a priori and that they arise from our consistent treatment of stellar populations and dust in galaxies.

3.4 Comparison with previous models

The model we have developed allows one to interpret the infrared spectral energy distributions of galaxies consistently with the ultraviolet and optical emission, in terms of combined constraints on the star formation and dust properties. At the same time, the model is versatile enough that it can be used to statistically derive such properties for large samples of observed galaxies. So far, the tools most widely used to extract minimum physical quantities from infrared spectra of large samples of observed galaxies are the spectral libraries of Chary & Elbaz (2001) and Dale & Helou (2002). As an illustration, we compare here the constraints derived from our model to those that would be obtained using these libraries for the three galaxies studied in detail in Section 3.3.2 (Fig. 3.4).

Chary & Elbaz (2001) propose a library of template spectra to reproduce the observed correlations between the total infrared luminosity $L_{\rm d}^{\rm tot}$ ($L_{\rm IR}$ in their notation) and the luminosities in individual *ISO* and *IRAS* bands, for local galaxies. This leads them to assign a unique luminosity to a given infrared spectral shape. In Fig. 3.10, we compare the best-fit spectral energy distributions inferred from our model for NGC 3521, NGC 337 and Mrk 33 (in black, from Fig. 3.4) with template spectra from Chary & Elbaz (2001,in green). Since the three galaxies have similar infrared luminosities (Fig. 3.6), they are assigned similar infrared spectra in the prescription of Chary & Elbaz (2001,shown as dotted green lines in Fig. 3.10). However, as Figs. 3.2 and 3.4 show, NGC 3521, NGC 337 and Mrk 33 have different infrared colours. As a result, the Chary & Elbaz (2001) template spectra that best fit the *ISO* and *IRAS* colours of these galaxies (plotted as solid green lines in Fig. 3.10) correspond to widely different infrared luminosities. For example, the Chary & Elbaz (2001) template that best fits the observed colours of the dwarf starburst galaxy Mrk 33 corresponds to a spectral energy distribution typical of an ultraluminous infrared galaxy (ULIRG, with $L_{\rm IR} \geq 10^{12} L_{\odot}$). This inconsistency illustrates the impossibility with the Chary & Elbaz (2001) library to account for the intrinsic dispersion of infrared colours among galaxies of comparable infrared luminosity.

Dale & Helou (2002) parametrise the spectral energy distributions of normal star-forming galaxies in terms of a single parameter $\alpha_{\rm SED}$, which is inversely proportional to the intensity of the interstellar radiation field heating dust grains. Variations in $\alpha_{\rm SED}$ can account for the observed range of F_{60}/F_{100} colours of normal star-forming galaxies. Dale et al. (2007) find that the Dale & Helou (2002) models that best fit the MIPS colours of NGC 3521, NGC 337 and Mrk 33 have $\alpha_{\rm SED} = 3.32$, 2.23 and 1.44, respectively (these models are shown as blue lines in Fig. 3.10). This sequence in $\alpha_{\rm SED}$ is consistent with that in the specific star formation rate $\psi_{\rm S}$ inferred from our analysis of these galaxies (see Fig. 3.5). As mentioned above, our model can provide greater insight into the star formation histories and dust properties of galaxies.

3.5 Potential sources of systematic errors

3.5.1 Star formation prior

We have checked the sensitivity of our results to the prior distributions of star formation histories in the model library of Section 3.2. We have repeated our results

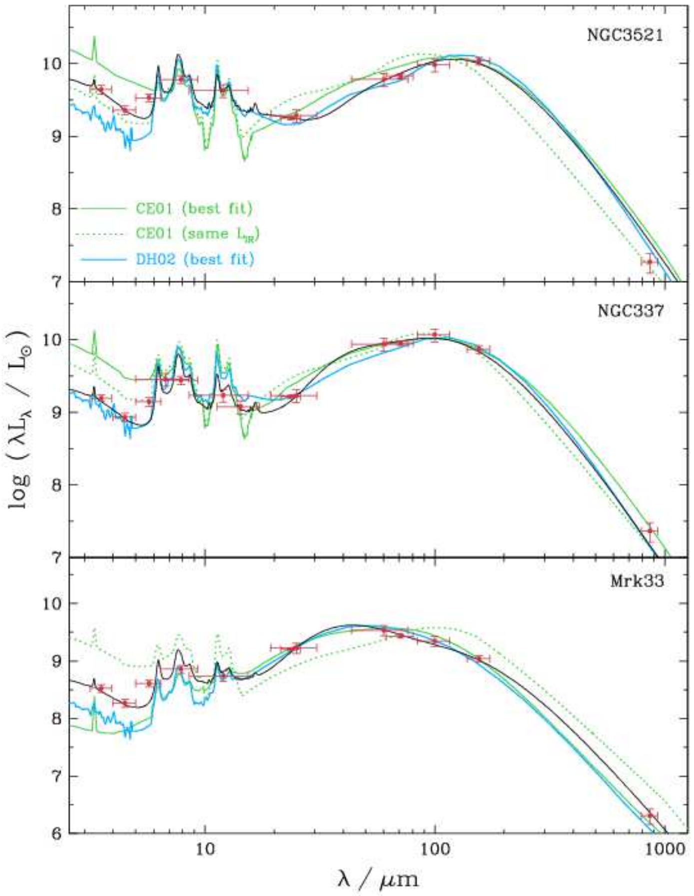

Figure 3.10: Fits by various models to the observed infrared (*Spitzer* IRAC and MIPS, *ISO*, *IRAS* and SCUBA) spectral energy distributions of the same three galaxies as in Fig. 3.4 (in red). In each panel, the black line shows the best-fit model from Fig. 3.4; the dotted green line is the Chary & Elbaz (2001) template spectrum corresponding to the same total infrared luminosity as the black line; the solid green line is the Chary & Elbaz (2001) template that best fits the *IRAS* and *ISO* observations of the galaxy; and the blue line is the Dale & Helou (2002) model that best fits the MIPS observations of the galaxy (see text for detail).

using continuous star formations histories (i.e. omitting superimposed stochastic starbursts). We find that, in this case, the overall quality of the fits to the ultraviolet, optical and infrared spectral energy distributions of SINGS galaxies decreases, and that the star formation rates of the galaxies are systematically lower by up to 40 per cent. We have also tested the influence of the initial mass function. Adopting a Salpeter (1955) IMF instead of the Chabrier IMF would lead to stellar mass estimates about 1.4 times larger.

3.5.2 Attenuation law

In this study, we have assumed that the effective dust absorption optical depth in stellar birth clouds scales with wavelength as $\hat{\tau}_\lambda^{\rm BC} \propto \lambda^{-1.3}$ (see Section 2.2.1). Adopting instead $\hat{\tau}_\lambda^{\rm BC} \propto \lambda^{-0.7}$ (i.e. , the same wavelength dependence as the attenuation law in the ambient ISM; see Charlot & Fall 2000) does not change significantly the overall quality of the fits to the broad-band spectral energy distributions of the SINGS galaxies. However, for the galaxies with spectroscopic observations, the Hα/Hβ ratios predicted using $\hat{\tau}_\lambda^{\rm BC} \propto \lambda^{-0.7}$ tend to be lower than observed by typically 15 per cent (see also Wild et al. 2007). This has negligible implications for the constraints on the dust parameters μ and $\hat{\tau}_V$ derived for the SINGS galaxies.

3.5.3 Inclination

The predictions of our model are averaged over viewing angles. In practice, however, because of the non-uniform spatial distribution of dust, observed fluxes at ultraviolet, optical and infrared wavelengths may depend on the angle under which a star-forming galaxy is seen. We account to some extent for this effect in our model when introducing the uncertainty δf_μ in the connection between stellar and dust emission (see Section 3.2). Also, we do not find any systematic trend in the quality of spectral fits with the inclination of the SINGS galaxies. In Chapter 5, we further investigate the effect of orientation by applying our model to a larger sample of galaxies spanning wide ranges in physical properties and inclinations.

3.6 Summary and conclusion

In this chapter, we have generated a comprehensive library of model galaxy spectra by combining a library of attenuated stellar population spectra (built from stochastic star formation histories and dust contents) with a library of infrared emission spectra. As Fig. 3.4 illustrates, these models provide appropriate fits to the observed ultraviolet, optical and infrared spectral energy distributions of nearby galaxies in the SINGS sample, for which data are available from *GALEX*, RC3, 2MASS, *Spitzer*, *ISO*, *IRAS* and SCUBA (Kennicutt et al. 2003). We have used this model library to derive median-likelihood estimates of the star formation rate, stellar mass, dust attenuation, dust mass and relative contributions by different dust components to the total infrared luminosity of every SINGS galaxy in our sample. The accuracy of these estimates depends on the available spectral information. We find that, for example, although the total infrared luminosity $L_{\rm d}^{\rm tot}$ of a galaxy can be roughly estimated using ultraviolet, optical and near-infrared data alone (at least for values in the range from a few $\times 10^8$ to a few $\times 10^{10} L_\odot$), reliable estimates of this parameter require infrared observations at longer wavelengths.

A main advantage provided by our model is the capacity to study the relation between different physical parameters of observed galaxies in a quantitative and statistically meaningful way. We find that, for example, the specific star formation rate of SINGS galaxies correlates strongly not only with observed infrared colours, but also with several other properties of the galaxies, such as the fraction of total infrared luminosity contributed by dust in the ambient ISM, the contributions by PAHs, warm dust and cold dust to the total infrared luminosity and the ratio of dust mass to stellar mass. These correlations provide important insight into the link between star formation and ISM properties in galaxies. In particular, they allow one to quantify the relations between star formation rate, gas mass, dust mass, stellar mass, dust temperature and distribution of the dust between giant molecular clouds and the diffuse interstellar medium. Studies of these relations at different redshifts will have important implications for our understanding of the physical processes that dominate galaxy evolution.

Acknowledgments

We thank the anonymous referee for important suggestions, which helped improve the quality of this paper. We also thank Brent Groves, Jarle Brinchmann and Tim Heckman for comments on the manuscript, and Jakob Walcher, Armando Gil de Paz, Hervé Aussel and Hélène Roussel for helpful discussions. We are grateful to Eli Dwek for providing us with an electronic version of the *COBE*/FIRAS spectrum of the diffuse cirrus emission of the Milky Way. EdC is financed by the EU Marie Curie Research Training Network MAGPOP. This research made use of the NASA/IPAC Extragalactic Database (NED) which is operated by the Jet Propulsion Laboratory, California Institute of Technology, under contract with the National Aeronautics and Space Administration.

Chapter 4

The physical properties of star-forming galaxies at z $\sim$ 0.1

4.1 Introduction

In the previous chapter, we have seen how the model we have developed in Chapter 2 can be useful to interpret the observed ultraviolet, optical and infrared spectral energy distributions of galaxies in terms of their star formation activity and dust content. We have illustrated this by analysing the properties of nearby star-forming galaxies from the SINGS sample. In this chapter, we carry out a slightly different analysis of a new galaxy sample at slightly higher redshift ($z \sim 0.1$), the *Spitzer-SDSS-GALEX Spectroscopic Survey* (SSGSS; Schiminovich et al., in preparation)[1]. This is being accomplished in collaboration with the SSGSS team, in particular David Schiminovich, Stéphane Charlot, Ben Jonhson and Matt O'Dowd. Here we show some preliminary results of this ongoing work.

The observed properties available for the SSGSS sample differ from those of the SINGS sample in that, for the SSGSS sample, in addition to multi-wavelength broad-band photometry, SDSS optical spectra and *Spitzer*/Infrared Spectrograph (IRS; Houck et al. 2004) mid-infrared spectra were taken encompassing a large fraction of the galaxies[2].

In the following, we first use photometric data to study the physical properties of the SSGSS galaxies and compare them to those of the SINGS galaxies. Then we concentrate on what can be learnt from the additional information provided by the *Spitzer*/IRS spectroscopy of these galaxies. We discuss how the IRS spectra provide insight into the physical conditions in the ISM of galaxies, such as

- the properties and amount of interstellar dust through the silicate absorption features at 9.7 and 18 μm;
- the properties of interstellar polycyclic aromatic (PAHs) through the detailed study of the mid-infrared emission features;
- the dust-heating conditions in galaxies and possible contribution of AGN to this heating;

---

[1] See also http://www.astro.columbia.edu/ssgss

[2] Existing *Spitzer*/IRS spectra of the SINGS galaxies are available only for the nucleus of the galaxies and small extra-nuclear regions (Kennicutt et al. 2003)

- the physical state of interstellar gas in the galaxies (ionization, temperature, density and abundances of different elements), through the study mid-infrared nebular emission lines.

4.2 The sample

The SSGSS sample consists of 101 galaxies with ultraviolet, optical and infrared wavelength coverage. The sample is extracted from the SDSS spectroscopic sample (Strauss et al. 2002), optically selected with $r < 17.77$ AB magnitudes, for which *ugriz* photometry is available. Additional photometric observations in the ultraviolet and infrared from *GALEX* (*FUV* and *NUV*), 2MASS (*JHKs*), *Spitzer*/IRAC (3.6, 4.5, 5.8, 8.0 μm) and *Spitzer*/MIPS (24, 70 and 160 μm) were taken as part of different surveys in the Lockman Hole[3] (Johnson et al. 2007). The SSGSS team has performed a careful match of this multi-wavelength photometry in aperture. This enables the *GALEX*, SDSS, 2MASS and *Spitzer* fluxes to be consistently interpreted using our model (Schiminovich et al., in preparation).

In addition to this multi-wavelength photometry, the SSGSS sample is characterized by the availability of *Spitzer*/IRS spectra between 5 and 38 μm for all galaxies. This spectroscopic sample is selected from the photometric sample described above by performing a flux cut at 24 μm, $F_\nu(24\ \mu\mathrm{m}) > 1.5$ mJy. This ensures high-quality infrared spectroscopic observations with IRS. The IRS instrument also allows to perform imaging in the 'blue peak-up' band, centered at 16 μm. Photometry in this band is important to constrain the detailed shape of the mid-infrared emission from galaxies, since it fills the gap between the IRAC band at 8 μm and the MIPS band at 24 μm. The IRS observations were performed to match in aperture with the SDSS fibre. Therefore, the aperture in which the IRS 16-μm flux was obtained does not coincide with the aperture of the other photometric observations described above. The SSGSS team has applied an aperture correction to the IRS 16-μm flux so that we can include it in our analysis.

The physical properties of the SSGSS galaxies have been roughly characterized by Johnson et al. (2007) using previously available models. Johnson et al. (2007) use the observed *NUV*-IRAC(3.6 μm) colour, the $\mathrm{D}_n(4000)$ spectral break[4] measured from the optical SDSS spectra and the stellar masses derived by Kauffmann et al. (2003b) to characterize the sample. In Fig. 4.1, we show the *NUV*-IRAC(3.6 μm)

---

[3] The Lockman Hole is a region of the sky in the constellation of Ursa Major. This region presents very low column densities of Galactic interstellar dust along the line of sight, and therefore it is ideal for extragalactic studies. The Lockman Hole is one of the better studied regions of the sky, as it has been intensively observed in a wide wavelength range.

[4] The $\mathrm{D}_n(4000)$ spectral break originates from the accumulation of a large number of stellar absorption lines in the optical spectra of galaxies in a narrow region around 4000 Å. The main contribution to the opacity of these lines comes from ionized metals in the stellar atmospheres. In young, hot stars with very high surface temperatures, the metals are multiply ionised and the opacity of these lines is low, therefore the $\mathrm{D}_n(4000)$ break is weak. On the contrary, in old, metal-rich stars, the opacity of these lines is large, and the 4000-Å break is strong (e.g. Bruzual A. 1983; Balogh et al. 1999; Kauffmann et al. 2003b). Therefore, the $\mathrm{D}_n(4000)$ spectral break can be used to infer the mean age of stellar populations in galaxies.

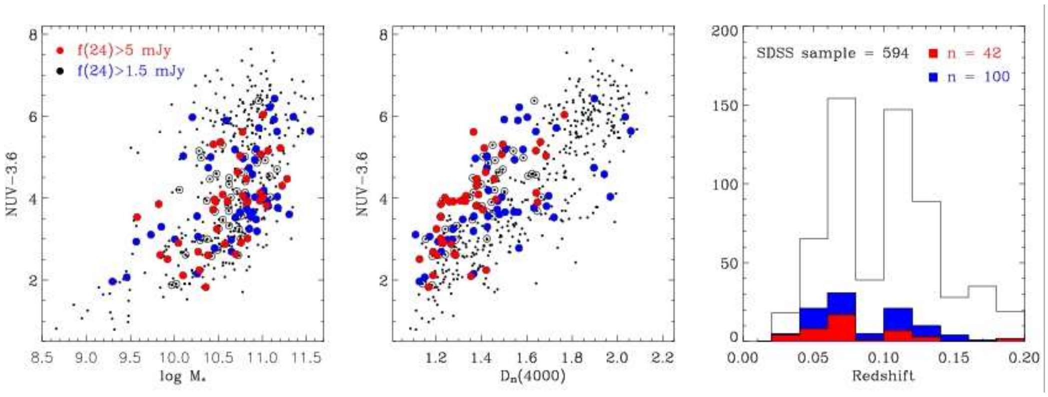

Figure 4.1: *NUV*-IRAC(3.6 μm) color plotted against stellar mass M_* (left panel), and *NUV*-IRAC(3.6 μm) plotted against $\mathrm{D}_n(4000)$ (right panel) for Lockman Hole photometric sample (in black). The SSGSS sample is selected by performing a 24-μm flux cut at 1.5 mJy (in blue, and 5 mJy for bright sample, in red). This yields a large number of galaxies with a representative distribution of mass, colour, and star formation history out to redshift $z < 0.2$ (right panel). Figure from Schiminovich et al. (in preparation).

colour plotted against the rough estimates of stellar mass M_* and $\mathrm{D}_n(4000)$. The galaxies of the primary photometric sample from Johnson et al. (2007) are plotted as black dots, and the SSGSS galaxies are plotted as coloured circles.

The stellar mass estimates for the sample galaxies shown in Fig. 4.1 are computed by Kauffmann et al. (2003b) using stellar absorption indices measured in the SDSS fiber and adopting a simple power-law $\lambda^{-0.7}$ to account for the attenuation by dust. These stellar mass estimates are therefore limited by (i) the fact that the SDSS fiber may not include the total emission from galaxies, and therefore aperture corrections are made which assume a constant mass-to-light ratio, and (ii) the fact that the attenuation law implies that stars of all ages in the galaxy are attenuated in the same way (i.e. it does not take into account the fact that young stars are embedded in dense birth clouds as described in the previous chapters of this thesis). In Section 4.3, we will analyse in detail the observed photometric properties of the SSGSS galaxies using the more sophisticated model presented in Chapter 2. This will enable us to provide more accurate constraints on the stellar mass, star formation and dust properties of these galaxies.

4.2.1 Composition of the SSGSS sample

An important difference of the SSGSS sample relative to the SINGS sample studied in Chapter 3 is that it contains galaxies hosts of bright AGN. We classify the galaxies of the SSGSS sample in three categories: star-forming galaxies; AGN hosts; and ‘composite’ galaxies. We perform this classification using the optical emission line ratios [N II]$\lambda\,6584\,\text{Å}/\mathrm{H}\alpha$ and [O III]$\lambda\,5007\,\text{Å}/\mathrm{H}\beta$, measured in the SDSS spectra. These emission line ratios provide a powerful diagnostic of the ionization state of

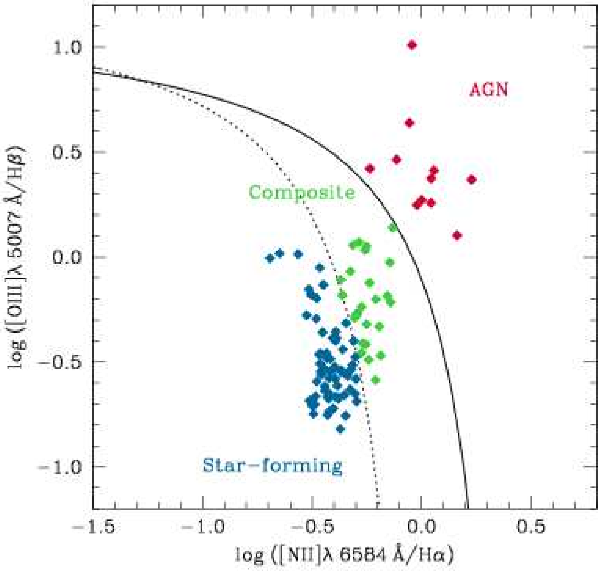

Figure 4.2: Baldwin, Phillips & Terlevich (1981) diagram for the SSGSS galaxies. This shows optical emission line ratios [N II]λ 6584 Å/Hα against [O III]λ 5007 Å/Hβ. The solid line corresponds to the division computed by Kewley & Dopita 2002 (equation 4.1). Above this line, galaxies are classified as AGN. The dotted line is the empirical division of Kauffmann et al. 2003a (equation 4.2). Under this line, galaxies are classified as purely star-forming. Galaxies located between the two lines form the composite class.

the gas (Baldwin, Phillips & Terlevich 1981). They allow one to distinguish gas ionization caused by the soft radiation from young stars (in typical H II regions) from that produced by the harder radiation of AGN.[5]

Fig. 4.2 shows the location of the SSGSS galaxies in the BPT diagnostic diagram. Kewley & Dopita (2002) define a theoretical 'maximum starburst' line in this diagram (solid line in Fig. 4.2), parametrized as

$$\log([\mathrm{O\,III}]\lambda\,5007\,\text{Å}/\mathrm{H}\beta) = \big(0.61/([\mathrm{N\,II}]\lambda\,6584\,\text{Å}/\mathrm{H}\alpha - 0.47)\big) + 1.19\,. \tag{4.1}$$

Above this line, the observed values of [N II]λ 6584 Å/Hα and [O III]λ 5007 Å/Hβ must originate from ionization by an AGN. Therefore, we classify galaxies above this line as AGN hosts. Kauffmann et al. (2003a) propose an alternative, empirical separation between star-forming and AGN host galaxies in the BPT diagram (dotted line in Fig. 4.2), using ∼ 120 000 galactic spectra from SDSS:

$$\log([\mathrm{O\,III}]\lambda\,5007\,\text{Å}/\mathrm{H}\beta) = \big(0.61/([\mathrm{N\,II}]\lambda\,6584\,\text{Å}/\mathrm{H}\alpha - 0.05)\big) + 1.30\,. \tag{4.2}$$

---

[5] The plot of [N II]λ 6584 Å/Hα against [O III]λ 5007 Å/Hβ is known as the 'BPT diagram' as a reference to the work of Baldwin, Phillips & Terlevich (1981).

This empirical line does not coincide with the line theoretically predicted by Kewley & Dopita (2002). We classify galaxies lying under this line as purely star-forming galaxies. When galaxies are located between the empirical line of Kauffmann et al. (2003a) and the theoretical line of Kewley & Dopita (2002), the classification is more ambiguous. We classify such galaxies as 'composite'. According to the above classification, the SSGSS sample is composed of:

(i) 66 star-forming galaxies (blue symbols in Fig. 4.2);

(ii) 24 composite (green symbols in Fig. 4.2);

(iii) 11 AGN (red symbols in Fig. 4.2).

We note that the model we have developed in Chapter 2 does not include the contribution by AGN to the emission from galaxies. Therefore, this model is strictly applicable only to galaxies dominated by star formation. We investigate in Section 4.4 how the presence of an AGN can affect the determination of galaxy physical parameters using this model.

4.2.2 Comparison of the SSGSS and SINGS samples

In Fig. 4.3, we compare observed ultraviolet and infrared properties of the SSGSS with the SINGS sample. Fig. 4.3a shows the MIPS L_ν^{70}/L_ν^{160} luminosity ratio plotted against the IRAC+MIPS L_ν^{8}/L_ν^{24} luminosity ratio. The SSGSS and SINGS galaxies follow the same infrared colour distributions in this diagram. However, we note that SSGSS galaxies are typically slightly more concentrated towards redder (i.e. cooler) infrared colours than the SINGS galaxies. We show in Section 4.3.3 below that this is because SSGSS galaxies do not extend to as high specific star formation rates as the SINGS galaxies. In Fig. 4.3b, we plot the ratio of total-infrared to ultraviolet luminosity $L_\mathrm{d}^\mathrm{tot}/L_\mathrm{FUV}$ (i.e. infrared excess) as a function of ultraviolet spectral slope β_UV. As in Fig. 3.2, we have used equation (4) of Dale & Helou (2002) to estimate $L_\mathrm{d}^\mathrm{tot}$ from the MIPS observations at 24, 70 and 160 μm, and equation (1) of Kong et al. (2004) to compute β_UV from the *GALEX FUV* and *NUV* luminosities. The SSGSS galaxies do not present as high dispersion around the starburst line as the SINGS galaxies. We also note that the galaxies of the SSGSS sample do not reach the lower left-hand corner of the diagram, corresponding to low values of β_UV and $L_\mathrm{d}^\mathrm{tot}/L_\mathrm{FUV}$. The SINGS galaxies populating this corner tend to be blue, star-forming dwarf galaxies. This type of galaxy tends to drop below the magnitude cutoff of the SDSS spectroscopic sample.

4.2.3 PAH emission of SSGSS galaxies

From the detailed study of the *Spitzer/IRS* mid-infrared spectra of the SSGSS galaxies, O'Dowd et al. (in preparation) have measured the average PAH emission spectrum of these galaxies. This PAH spectrum was extracted from the average mid-infrared spectrum of the sample using the PAHFIT code of Smith et al. (2007).

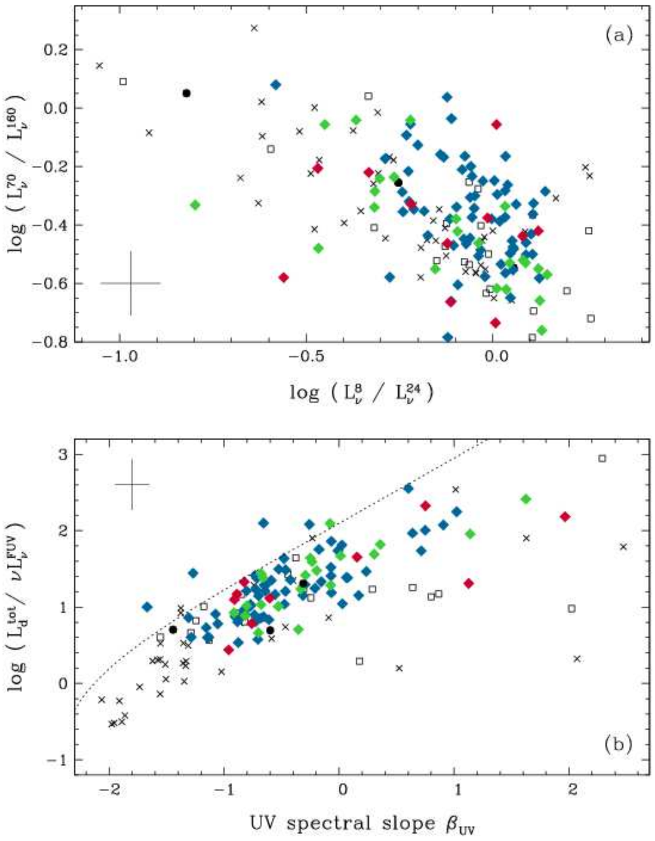

Figure 4.3: Comparison between the observed properties of the SSGSS and the SINGS sample: (a) Ratio of 70-μm to 160-μm luminosity plotted against ratio of 8-μm to 24-μm luminosity. (b) Ratio of total-infrared to ultraviolet luminosity as a function of ultraviolet spectral slope (the IRX–UV diagram). The dotted line in this diagram shows a fit by Kong et al. (2004) to the relation followed by starburst galaxies (Meurer, Heckman & Calzetti 1999). In both panels, the black symbols correspond to the SINGS galaxies, with the same meaning as in Fig. 3.2. The SSGSS galaxies are plotted as coloured diamonds, according to the classification of Section 4.2.1: blue – star-forming galaxies; green – composite galaxies; red – AGN hosts. The median error bars for the SSGSS sample are plotted in the left corner of each diagram.

This code decomposes an observed mid-infrared spectrum in several components; the main ingredients are:

- a stellar continuum: reproduced using a black body at a fixed temperature of 5000 K;
- a thermal mid-infrared continuum, which is the sum of up to 8 modified black bodies of different temperatures between 35 and 300 K;

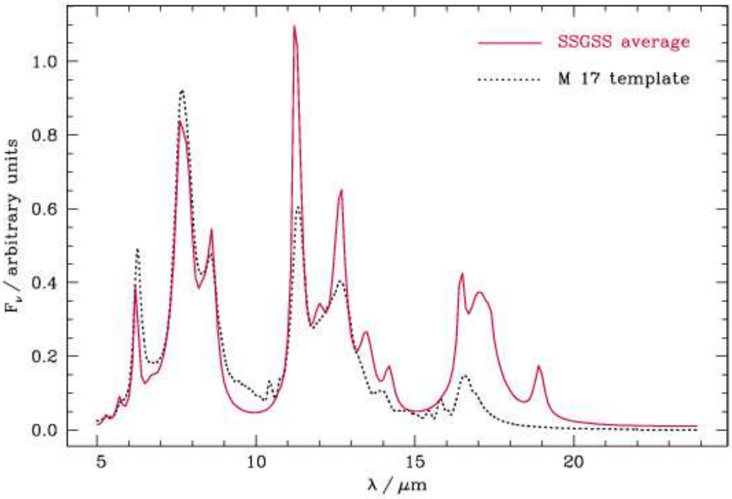

Figure 4.4: Comparison between the average PAH spectrum of the SSGSS sample (O'Dowd et al., in preparation) and the M 17 PDR mid-infrared spectrum used as a PAH emission template in Chapter 2. For comparison, both spectra are normalized to total area between 5 and 24 μm.

- an infrared extinction curve, composed of a power-law plus silicate absorption features at 9.7 and 18 μm;
- nebular emission lines (mainly forbidden lines of ionized species and rotational lines of H_2), represented by Gaussian profiles;
- and PAH emission features, represented by Drude profiles.

  We note that Drude profiles, as with the Lorentzian profiles widely used to fit PAH features (e.g. Boulanger et al. 1998; Verstraete et al. 2001), have more power in the extended wings than Gaussian profiles. The physical motivation to fit PAH features using these profiles is that they represent the theoretical frequency profiles for classical damped harmonic oscillators (Li & Draine 2001; Smith et al. 2007).

O'Dowd et al. build the average PAH emission spectrum of the sample by adding the set of Drude profiles which best fit the average SSGSS mid-infrared spectrum. In Fig. 4.4, we plot the resulting PAH emission spectrum (in red). Also shown for comparison is the M 17 template spectrum used to model PAH emission in Chapters 2 and 3. The average PAH emission spectrum of the SSGSS galaxies deviates significantly from the M 17 mid-infrared spectrum. In particular, the mid-infrared spectrum of M 17 fails to reproduce the average ratio of 7.7-μm to 11.3-μm features observed in the SSGSS IRS spectra. Also, the average SSGSS spectrum shows a stronger emission in the 17-μm feature complex.

According to the physical models of Li & Draine (2001), a lower ratio of 7.7-μm to 11.3-μm emission features may result from a higher contribution of neutral PAHs compared to ionized PAHs. This possibly indicates that the average radiation field in the SSGSS galaxies is softer than the radiation field in the M 17 star-forming region, or that the bulk of the emitting PAHs in these galaxies reside in regions where they are more shielded from strong ultraviolet radiation. Having a different 7.7-μm to 11.3-μm ratio should not significantly affect our results unless we attempt to reproduce detailed mid-infrared spectra instead of broad-band photometry.

We take advantage of this information and choose to replace the M 17 template spectrum with the average SSGSS PAH spectrum when interpreting the SSGSS data with our model. We expect that the main effect of stronger emission in 17-μm feature complex will be to attribute a slightly higher fraction of the total mid-infrared luminosity of the galaxies to PAHs. We will discuss later the main implications of this choice on the interpretation of the spectral energy distributions of the galaxies and on the median-likelihood estimates of physical parameters.

4.3 Statistical constraints on physical parameters

The exquisite spectral coverage of the SSGSS sample from far-ultraviolet to far-infrared wavelengths is ideal to constrain the physical parameters of the galaxies using the model presented in Chapter 2.

4.3.1 The method

We use the method described in Chapter 3 to derive the median-likelihood estimates of the star formation rates, stellar masses, dust attenuation, dust masses and the relative contributions by different dust components to the total infrared luminosity of SSGSS galaxies.

At the typical redshifts of the sample, the SDSS optical fluxes in the g, r and i bands (centered at 0.45, 0.62 and 0.75 μm, respectively) may include light coming from nebular emission lines, specially for actively star-forming galaxies (see e.g. Kauffmann et al. 2003b). Since the spectral models we use to interpret the photometry do not include nebular emission lines, we correct the observed g, r and i magnitudes for emission lines contamination, using corrections kindly provided by Jarle Brinchmann (private communication). These corrections are computed by comparing the photometry of the purely stellar model which best fits the spectra with the observed photometry.

The typical observational uncertainties (including matching uncertainties) for each photometric band are: FUV – 5 per cent; NUV – 3 per cent; u – 10 per cent; *griz* – 5 per cent; *JHKs* – 8 per cent; IRAC 3.6, 4.5, 5.8, 8.0-μm – 5 per cent; MIPS 24, 70-μm – 10 per cent; MIPS 160-μm – 30 per cent. We also include the flux measured in the *Spitzer*/IRS blue peak-up band at 16 μm. This is measured within the same aperture as the IRS spectra, and therefore may not include the total emission from galaxies. To take this into account, an aperture correction is applied (Schiminovich et al., in preparation) and we take a typical uncertainty of 10 per cent for the photometry in this band.

We follow the method described in Chapter 3 to interpret the photometric observations of the galaxies using our simple model described Chapter 2. We build random libraries of stellar population models for wide ranges of star formation histories, metallicities and dust contents, and random libraries of dust emission models for wide ranges of dust temperatures and fractional contributions of each component to the total dust luminosity (for more details see Chapter 3). To account for the redshift distribution of the sample (right panel in Fig. 4.1), we generate random libraries at four different redshifts: $z = 0.05$, 0.10, 0.15 and 0.20. For each library of models at each redshift, we use the same prior distributions for all the parameters except the age of the galaxy, t_g. For each redshift, the t_g is uniformly distributed from 0.1 Gyr to a maximum value which corresponds to the age of the universe $t(z)$ at that redshift, computed using (e.g. Peebles 1993):

$$t(z) = \frac{1}{H_0} \int_0^\infty \frac{dz'}{(1+z')E(z')} \,, \tag{4.3}$$

where $E(z) = \sqrt{\Omega_M(1+z)^3 + (1-\Omega_M-\Omega_\Lambda)(1+z)^2 + \Omega_\Lambda}$. We adopt $\Omega_M = 0.30$, $\Omega_\Lambda = 0.70$ and $H_0 = 70\ \mathrm{km\,s^{-1}\ Mpc^{-1}}$. This gives $t(z = 0.05) = 12.8$, $t(z = 0.10) = 12.2$, $t(z = 0.15) = 11.6$, and $t(z = 0.20) = 11.0$ Gyr.

For each model in a random library at given redshift, we compute the ultraviolet, optical and infrared luminosity densities in the *GALEX*, SDSS, 2MASS and *Spitzer* photometric bands, by generalizing equation (2.23) to include the dependence on redshift:

$$L_\nu^{\lambda_0} = C_{\nu_0} \frac{\int d\nu\, \nu^{-1}\,(1+z)\, L_{\nu(1+z)}\, R_\nu}{\int d\nu\, \nu^{-1}\, C_\nu\, R_\nu} = \frac{\lambda_0^2}{c}\, C_{\lambda_0} \frac{\int d\lambda\, (1+z)^{-1}\, L_{\lambda/(1+z)}\, \lambda\, R_\lambda}{\int d\lambda\, C_\lambda\, \lambda\, R_\lambda} \,, \tag{4.4}$$

where λ_0 is the effective wavelength of the filter of response R_λ (R_ν), and the calibration spectrum C_λ (C_ν) depends on the photometric system (see more details in Section 2.2.2.1).

We divide the SSGSS sample into four redshift bins centered at $z = 0.05$, 0.10, 0.15 and 0.20. For each galaxy in each redshift bin, we compare the observed luminosities with the model luminosities at the corresponding redshift bin[6]. To do this, we compute the χ_j^2 goodness-of-fit of each model j (equation 3.1), as outlined in Section 3.2. By analogy with our approach in previous chapters, we build the probability density function of each physical parameter of our observed galaxies by weighting the value of that parameter in the jth model by the probability $\exp(-\chi_j^2/2)$. We take the median of the resulting probability density function as

---

[6] We note that this approach can introduce errors when interpreting the detailed spectra of galaxies located at different redshifts than the center of the corresponding redshift bin (for which the models were actually computed), due to the k-correction. However, since for now we aim at interpreting the broad-band photometry of the galaxies, this grid of redshift is fine enough that possible errors introduced by our method remain smaller than the observational uncertainties.

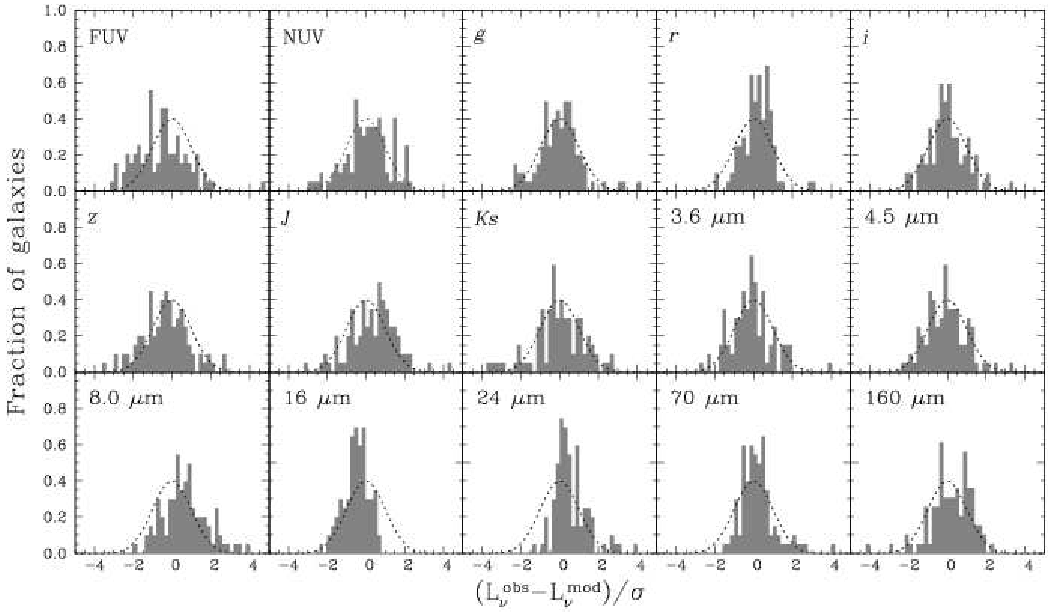

Figure 4.5: Distribution of the difference between observed luminosity $L_\nu^{\rm obs}$ and best-fit model luminosity $L_\nu^{\rm mod}$, in units of the observational error σ, for the 101 galaxies of the SSGSS sample. Each panel refers to a different photometric band (as indicated). The best-fit model for each galaxy was selected by fitting as many luminosities as available in the following bands: *GALEX* (*FUV* and *NUV*), optical SDSS (*griz*), 2MASS (*J* and *Ks*), *Spitzer*/IRAC (3.6, 4.5 and 8.0 μm), *Spitzer*/IRS blue peak-up band at 16 μm, and *Spitzer*/MIPS (24, 70 and 160 μm). We have checked that the distribution of these residuals does not show any particular trends when only star-forming, composite or AGN host galaxies are considered. In each panel, the dotted curve shows a Gaussian distribution with unit standard deviation, for reference.

our best estimate of the parameter, and the 16th–18th percentile range as the confidence interval.

4.3.2 Results

We now examine how well the model presented in Chapter 2 can reproduce the observed multi-wavelength photometric observations of the SSGSS galaxies. For each observed galaxy, we select the model of the random library that minimizes χ_j^2 (equation 3.1), computed using the observed luminosities in the following bands: *GALEX* (*FUV* and *NUV*), optical SDSS (*ugriz*), 2MASS (*JHKs*), *Spitzer*/IRAC (3.6, 4.5, 5.8 and 8.0 μm), *Spitzer*/IRS blue peak-up band (16 μm), and *Spitzer*/MIPS (24, 70 and 160 μm). In Fig. 4.5, we plot the resulting distribution of the difference between the observed luminosity $L_\nu^{\rm obs}$ and the best-fit model luminosity $L_\nu^{\rm mod}$, in units of the observational error σ, for the 100 galaxies in the sample. Each panel

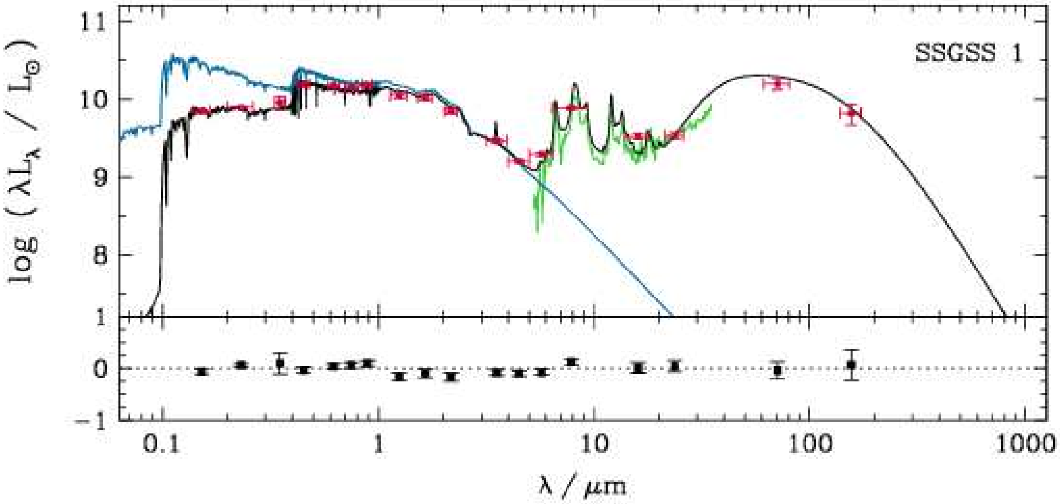

Figure 4.6: Example of best model fit (in black) to the observed spectral energy distribution (in red) of one of the galaxies of the SSGSS sample, at redshift $z = 0.066$ and with specific star formation rate $\log(\psi_S/\mathrm{yr}^{-1}) = -9.05$. The blue line shows the unattenuated stellar population spectrum. For each observational point, the vertical error bar indicates the measurement error, while the horizontal error bar shows the effective width of the corresponding photometric band. The residuals $(L_\lambda^{\mathrm{obs}} - L_\lambda^{\mathrm{mod}})/L_\lambda^{\mathrm{obs}}$ are shown at the bottom. The squares refer to broad-band luminosties (*GALEX FUV* and *NUV*; SDSS *ugriz*; 2MASS *JHKs*; *Spitzer* IRAC, IRS 16-μm band and MIPS). The green line shows the observed *Spitzer*/IRS spectrum, not included in the fit.

shows the result for a different photometric band. Fig. 4.5 shows that our model can reproduce simultaneously the ultraviolet, optical and near-, mid- and far-infrared photometric observations of the SSGSS galaxies to within the observational errors.

Our best fit model tends to systematically overestimate the flux in the IRS band at 16 μm. We have mentioned in Section 4.2 that the flux in this band requires a significant aperture correction in order to be compared with the integrated photometry in the other photometric bands. The bias of the corresponding histogram of residuals towards slightly negative values in Fig. 4.5 suggests that the photometric aperture correction we have applied to the data might be slightly underestimated. In Fig. 4.6, we show an example of best-fit model (in black) to the observed spectral energy distribution of one of the galaxies of the sample (in red), SSGSS 1, at redshift $z = 0.066$, with specific star formation rate $\log(\psi_S/\mathrm{yr}^{-1}) = -9.05$. The residuals, plotted in the bottom panel, show that the fit is accurate across the whole spectral range from far-ultraviolet to far-infrared wavelengths. The green line in Fig. 4.6 shows the observed IRS spectrum of the galaxy. We note that the IRS spectrum is not use to constrain the (purely photometric) fit and that no re-scaling was applied to account for the different aperture between the photometric and spectroscopic

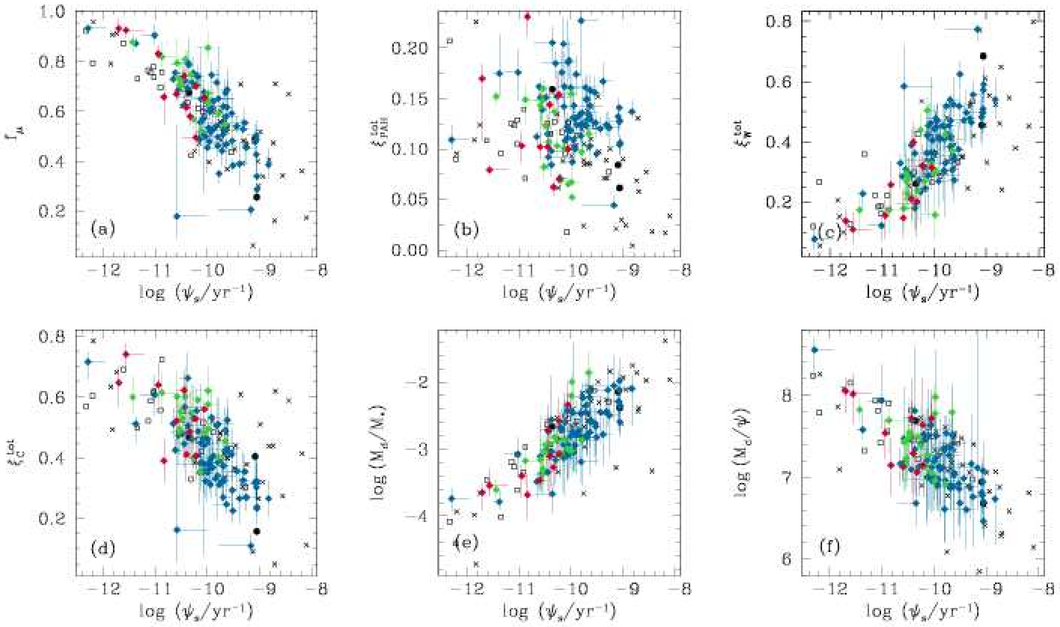

Figure 4.7: Median-likelihood estimates of galaxy properties plotted against specific star formation rate ψ_{S}, for the 100 SSGSS galaxies (coloured symbols; different colours have the same meaning as in Fig. 4.3), compared with the 66 SINGS galaxies (black symbols) of Chapter 3. (a) Fraction of total infrared luminosity contributed by dust in the ambient ISM, f_μ. (b) Global contribution (i.e. including stellar birth clouds and the ambient ISM) by PAHs to the total infrared luminosity, $\xi^{\mathrm{tot}}_{\mathrm{PAH}}$. (c) Global contribution by warm dust in thermal equilibrium to the total infrared luminosity $\xi^{\mathrm{tot}}_{\mathrm{W}}$. (d) Contribution by cold dust in thermal equilibrium to the total infrared luminosity, $\xi^{\mathrm{tot}}_{\mathrm{C}}$. (e) Ratio of dust mass to stellar mass, M_{d}/M_*. (f) Ratio of dust mass to star formation rate averaged over the last 10^8 yr, M_{d}/ψ. The error bars represent the 16–84 percentile ranges derived from the likelihood distributions of the estimated parameters.

observations (see Section 4.4.1 below).

4.3.3 Comparison of the physical properties of SSGSS and SINGS galaxies

We now compare the median-likelihood estimates of several physical parameters derived from the spectral fits in the previous section to those obtained previously for the SINGS galaxies. Fig. 4.7 is the analog of Fig. 3.9 from Section 3.3.3, in which we show how the median-likelihood estimates of several parameters correlate with specific star formation rate. Fig. 4.7 shows that the median-likelihood estimates of the physical parameters of the SSGSS galaxies follow roughly the same relations found for the SINGS sample. This is not surprising, since both samples contain mainly local star-forming galaxies.

Fig. 4.7 shows that the SSGSS galaxies do not span as wide a range in specific star formation rate $\psi_{\rm S}$ as the SINGS galaxies. For example, we find no SSGSS galaxy with $\log(\psi_{\rm S}/{\rm M}_{\odot}) > -8.8~{\rm yr}^{-1}$, and only four SSGSS galaxies with $\log(\psi_{\rm S}/{\rm M}_{\odot}) < -11.0~{\rm yr}^{-1}$. This difference results from the selection of the samples. SSGSS galaxies were flux-selected to be a representative sample of the local universe, whereas SINGS galaxies were selected amongst nearby galaxies to encompass the full range of observed properties of galaxies, such as star formation rate, infrared-to-blue ratio and morphological type (Kennicutt et al. 2003).

Another important difference between SSGSS and SINGS galaxies is the distribution of the fraction of total infrared luminosity contributed by PAHs, $\xi_{\rm PAH}^{\rm BC}$, as a function of specific star formation rate $\psi_{\rm S}$ (Fig. 4.7b). The SSGSS galaxies exhibit slightly higher $\xi_{\rm PAH}^{\rm BC}$ than the SINGS galaxies, at fixed $\psi_{\rm S}$. Conversely, in SSGSS galaxies, the hot mid-infrared continuum (characterized by $\xi_{\rm MIR}^{\rm BC}$) contributes typically less to the total dust luminosity than in SINGS galaxies (not shown). We think that this difference arises from to two main effects. The first is an observational bias. Fig. 4.3 shows that, at fixed $L_{\nu}^{70}/L_{\nu}^{160}$, SSGSS galaxies have a slightly higher L_{ν}^{8}/L_{ν}^{24} than SINGS galaxies. This indicates a higher contribution by PAHs to the mid-infrared luminosity. The second effect contributing to the offset in $\xi_{\rm PAH}^{\rm BC}$ might be the different PAH emission template used in this chapter. As discussed in Section 4.2.3, this template includes more flux in the 17-μm feature complex than the M 17 template used in the previous chapters. This can cause the overall increase of the contribution by PAHs to the total infrared luminosity.

The use of a different PAH template here to that of Chapter 3 does not have a strong influence in the quality of the photometric fits even at mid-infrared wavelengths (see Figs. 3.3 and 4.5). However, these results suggest a possible degeneracy between the contributions by PAHs and hot mid-infrared continuum to the mid-infrared emission. We note that this uncertainty is naturally taken into account using our statistical method to derive the confidence intervals of the parameters.

4.4 Observed mid-infrared spectra

4.4.1 Comparison with the best fit models to observed photometry

In this section, we compare the best-fit models derived from purely photometric fits to the observed *Spitzer*/IRS spectra of the galaxies between 5 and 38 μm. We stress that the observed spectra and the photometry are not matched in aperture. Nevertheless, the IRS spectra encompass most of the galaxies, and therefore we do not expect to have very large offsets between the photometry and the spectroscopy.

Fig. 4.8 shows shows such a comparison for six galaxies of the sample. These examples are typical. They show that the model and observed mid-infrared spectra agree quite well in general. This is remarkable, given the simplicity of our model, and shows that the combination of adjustable mid-infrared continuum emission with a fixed PAH template spectrum provides a fair representation of SSGSS galaxy spectra.

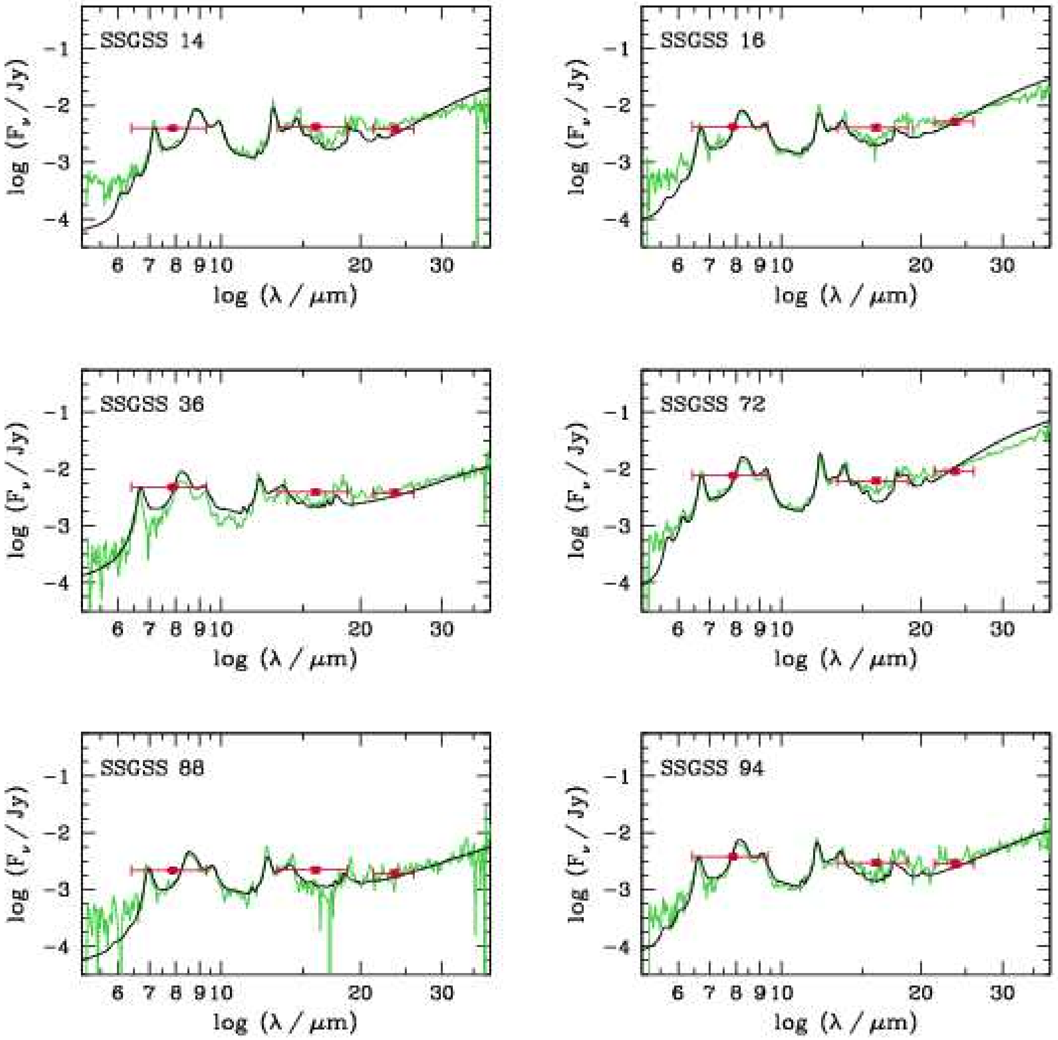

Figure 4.8: Comparison between the best fit model (in black) to the observed photometry (in red) and the observed *Spitzer*/IRS spectrum (in green) for six galaxies of the SSGSS sample: SSGSS 14, SSGSS 16, SSGSS 36, SSGSS 72, SSGSS 88 and SSGSS 94. These examples show cases where the models which best fit the photometric data are in good agreement with the observed IRS spectra.

For almost all of the galaxies in the sample, the observed relative minimum between strong PAH features in the (rest-frame) emission around 10 μm is well reproduced with by our model. In Fig. 4.9, we show the only two galaxies of the sample for which this is not the case. The observed mid-infrared spectra of these galaxies exhibit stronger absorption around 10 μm than can be accommodated by the model. This deep absorption in the observed spectra is the 9.7 μm silicate

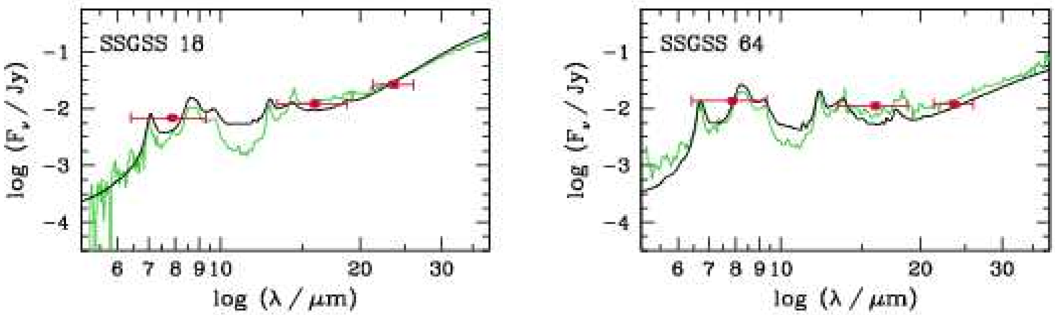

Figure 4.9: Comparison between the best fit model (in black) to the observed photometry (in red) and the observed *Spitzer*/IRS spectrum (in green) for two galaxies of the SSGSS sample: SSGSS 18 (left panel) and SSGSS 64 (right panel). For these two galaxies, the fit to the photometric points using our model fails at reproducing the detailed shape of the mid-infrared spectrum, particularly the silicate absorption feature at 9.7 μm.

absorption feature (Section 1.4.3). This feature is not included in our model spectra, since we assume for simplicity that the ISM of galaxies is optically thin at mid- and far-infrared wavelengths. The analysis of the SSGSS sample shows that this approximation is valid for most galaxies. Only in the two cases of Fig. 4.9 would silicate absorption be required to reproduce in detail the observed IRS spectra of the galaxies. These galaxies are the amongst the most actively-starforming and the most dust-rich star-forming galaxies of the sample. Therefore this result is not surprising, since galaxies with high star formation rates and dust contents tend to have pronounced silicate absorption in their mid-infrared spectra (e.g. Brandl et al. 2006).

Another current limitation of our model is that we not include the potential contribution by an AGN to the emission from a galaxy. Therefore, the application of this model to the interpretation of the galaxies classified as AGN and composite in the SSGSS sample should be regarded with caution.

To illustrate this, we show in Fig. 4.10 the spectra of two galaxies classified as AGN hosts on the basis of the BPT diagram in Fig. 4.2. The observed IRS spectra of these galaxies display strong, nearly-flat continua, which are presumably produced by from hot, stochastically-heated small grains around the active nucleus. PAH features are nearly absent from these spectra. In these two cases, the observations are fitted by models with high $\xi_{\rm MIR}^{\rm BC}$, low $\xi_{\rm PAH}^{\rm BC}$ and high $T_{\rm W}^{\rm BC}$.

The excess of hot dust emission and lack of PAH emission in the mid-infrared spectra of these two SSGSS galaxies is likely to be caused by the presence of an AGN rather than by an excess of star formation, given the relatively low specific star formation rates derived from the photometric fits. In fact, the infrared luminosity of dust heated by the AGN is probably wrongly attributed to star formation in

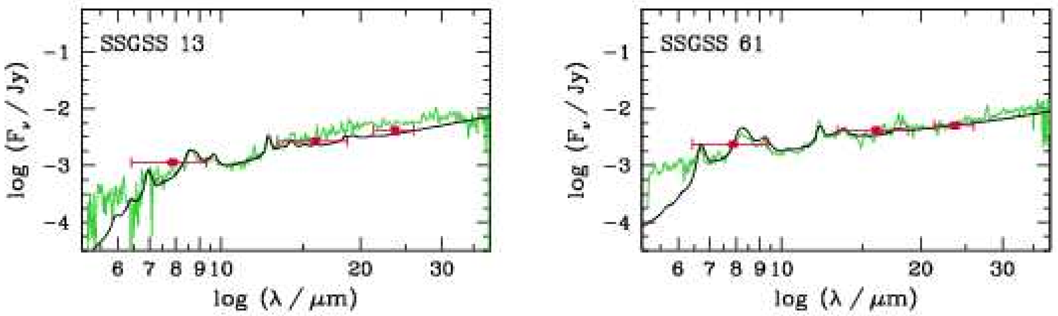

Figure 4.10: Comparison between the best fit model (in black) to the observed photometry (in red) and the observed *Spitzer*/IRS spectrum (in green) for two galaxies of the SSGSS sample classified as AGN: SSGSS 13 (left panel) and SSGSS 61 (right panel). These two galaxies are, of all the galaxies classified as AGN in the sample, the ones where the AGN contribution to the mid-infrared spectrum is most noticeable. This can be seen by the very strong continuum due to very hot dust and the almost lack of PAH features.

the photometric fits, which may bias our estimates of the physical parameters of these two galaxies. We consider the results of our model to be reliable only for star-forming galaxies in which starlight is the main source of dust heating. We plan to include the contribution of AGN to the infrared emission from galaxies in future applications of our model. This will be particularly important when interpreting observations from galaxies at high redshifts with very high infrared luminosities.

We stress that the examples shown in Fig. 4.10 are the most extreme cases of AGN hosts in the SSGSS sample for which we can observe clearly an excess of hot dust emission in the mid-infrared that would not be expected given the relatively low specific star formation rates of these galaxies. The vast majority of SSGSS galaxies classified as AGN hosts and composite galaxies have IRS spectra which are not dominated by a strong hot mid-infrared continuum. This suggests that most of the optically-detected (Fig. 4.2) AGN hosts in the sample may be optically thin and that the radiation from the AGN is not a significant source of dust heating.

4.4.2 Study of the detailed mid-infrared spectra

We have shown in the previous section that the detailed mid-infrared spectra of the SSGSS sample can provide important clues on the dust properties and heating conditions in galaxies. In the framework of this study, we also plan to use the *Spitzer*/IRS spectra to study the star formation properties and physical conditions in the ISM of SSGSS galaxies. One advantage of these observations is that the IRS spectra correspond to the same aperture as the optical spectra from SDSS, and therefore we will be able to study consistently both optical and mid-infrared

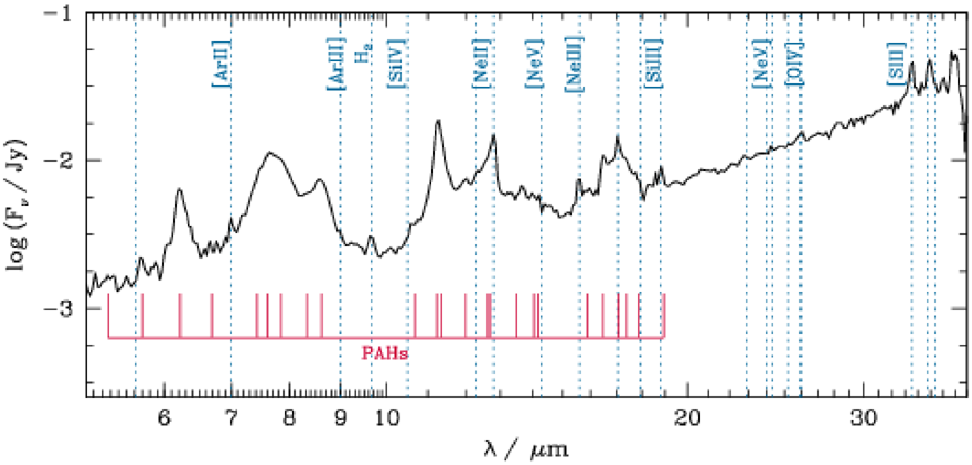

Figure 4.11: *Spitzer*/IRS spectrum of the closest galaxy in the SSGSS sample (SSGSS 67, at $z = 0.031$), corrected to rest-frame. In blue, we show the main nebular emission lines that can be observed in the IRS spectra of the SSGSS galaxies (see Table 4.1). Red lines show the main PAH emission features (e.g. Draine & Li 2007; Smith et al. 2007.)

Table 4.1: Main mid-infrared nebular emission lines detectable in the *Spitzer*/IRS spectra of galaxies.

λ/μm	Line	λ/μm	Line
5.61	[Mg V]	17.94	[Fe II]
6.99	[Ar II]	18.80	[S III]
8.99	[Ar III]	22.90	[Fe III]
8.99	[Mg VII]	24.00	[Fe I]
9.67	H_2	24.30	[Ne V]
10.50	[S IV]	25.20	[S I]
12.27	H_2	25.90	[O IV]
12.80	[Ne II]	26.00	[Fe II]
14.30	[Ne V]	33.50	[S III]
15.60	[Ne III]	34.80	[Si II]
17.03	H_2	35.30	[Fe II]

emission lines in the available spectral range.

In Fig. 4.11, we plot an example of high signal-to-noise IRS spectrum of one of the SSGSS galaxies (corrected to rest-frame). The main observed PAH features and emission lines are labelled. In Table 4.1, we list the wavelengths of the most important nebular lines. These observations will be used in a following study to investigate the star formation and the physical state of the ISM. We briefly summarize the main diagnostics that can be used.

- The rotational lines of H_2 are excited by penetrating high-energy photons (X-ray and ultraviolet) or shocks in PDRs, at the interface between ionized regions and molecular clouds (Section 1.4.2). Therefore, the study of these lines provides an important diagnostic on the physical conditions inside PDRs.

- Observations of the mid-infrared forbidden lines emitted by ionized gas can be used to infer the physical state of H II regions, such as density, the abundance of different chemical elements and the ionization state (e.g. Alexander et al. 1999; Groves, Dopita & Sutherland 2006). For example, the density of the gas can be computed from ratios such as [S III] λ 18.8 μm/[S III] λ 33.5 μm, [Ne III] λ 15.6 μm/[Ne III] λ 36.0 μm or [Ne V] λ 14.3 μm/[Ne V] λ 24.3 μm. The hardness of the radiation field can be estimated by comparing lines that arise from different ionization states of the same element, such as [Ne III] and [Ne II] lines.

- In star-forming galaxies, nebular forbidden lines can also provide an indicator of the star formation rate. We can use the models such as the ones of Charlot & Longhetti (2001), which combine stellar population synthesis models and photoionization codes, to interpret the observed mid-infrared line emission from star-forming galaxies in terms of the ionization of the gas by newly-formed stars. We can also compare the mid-infrared observed spectra with the model predictions based on the optical nebular lines observed in the optical SDSS spectra.

- The IRS spectra of the SSGSS galaxies allow us to investigate possible empirical diagnostics of AGN based on observed mid-infrared line ratios (see also, e.g. Groves, Dopita & Sutherland 2006). To do this, we can compare in detail the optical nebular lines provided by SDSS spectroscopy with the mid-infrared nebular lines of the IRS spectra.

- To investigate the mechanisms of ionization and destruction of PAH molecules in the ISM of star-forming galaxies and AGN hosts, we can perform detailed comparisons between PAH features and nebular line strengths which probe the physical conditions in the ISM such as the hardness of the radiation field (e.g. Engelbracht et al. 2008; Gordon et al. 2008).

4.5 Summary and conclusion

In this chapter, we have presented preliminary results of the analysis of a sample of 101 star-forming galaxies at $z \sim 0.1$, the SSGSS sample. This sample is primarily selected from the SDSS spectroscopic sample, and supplemented with a rich set of multi-wavelength photometry and mid-infrared *Spitzer*/IRS spectra between 5 and 38 μm.

One main advantage of the SSGSS sample is the availability of mid-infrared IRS spectra. This has allowed us to study the mid-infrared emission properties of the galaxies in this sample. As a result, we find that the average PAH emission of SSGSS galaxies differs from the M 17 spectrum used as a PAH template in previous chapters of this thesis. We have taken advantage of this information and replaced the M 17 template with the average SSGSS PAH spectrum. We have discussed the main implications of adopting this different PAH template.

Using the simple model of Chapter 2, we have interpreted the observed multi-wavelength photometry of the SSGSS galaxies. This has allowed us to derive median-likelihood estimates of the star formation rates, dust masses, dust attenuation and the contributions by different components to the total infrared luminosity of the dust. We have compared our results to the median-likelihood estimates derived for the SINGS sample in Chapter 3. We find that, in general, the physical properties of the SSGSS and SINGS sample are very similar. This is not surprising, since these two samples contain mainly local star-forming galaxies.

Finally, we have compared our best-fit models to the infrared photometry with the observed mid-infrared spectra of the SSGSS galaxies. We have found that, in general, our best-fit model provides a fair representation of the observed IRS spectrum. We have analysed in more detail the few cases in which our model does not reproduce optimally the shape of the mid-infrared spectrum. This is the case for galaxies with high star formation rates and with large amounts of dust in the ISM, for which the silicate absorption feature at 9.7 μm (which we do not include in our model) becomes important. We have also analysed the case of two AGN host spectra in which a strong hot mid-infrared continuum and very weak PAH features are observed. We have discussed the origin of this emission and stressed that, even though our model may reproduce the observations in these cases, the results should be regarded with caution, since we do not include possible contribution by AGN to the emission from galaxies. However, we have noted that the excess of mid-infrared continuum and weak PAH emission, characteristic of dust heated by AGN, are not observed for the vast majority of the galaxies classified as AGN hosts and composite galaxies in the SSGSS sample.

The availability of IRS spectra allows us to study in more detail the star formation properties and the physical state of the ISM in the SSGSS galaxies. In future work, we plan to study these properties by analysing in more detail these mid-infrared spectra, in particular the PAH features, the silicate absorption and the nebular emission lines.

Chapter 5

The relation between star formation activity and dust content in galaxies

---

This chapter is extracted from the paper *The relation between star formation and dust content*, by Celine Eminian, Stéphane Charlot, Elisabete da Cunha and Jérémy Blaizot, to be submitted for publication in the Monthly Notices of the Royal Astronomical Society.

5.1 Introduction

Interstellar dust and star formation activity in galaxies are strongly linked. Dust grains originate from star formation, since they form in the cold envelopes of evolved stars and in supernova ejecta. Furthermore, dust grains in the interstellar medium of galaxies play a fundamental role in the formation of molecular clouds, which collapse to form new stars: dust grains provide a surface for molecular hydrogen to form; they shield the newly-formed molecules from ultraviolet radiation; and they participate in the cooling of the gas (see Chapter 1.4).

Several studies relying on ultraviolet, optical and near-infrared observations of large samples of galaxies have shed some light on the relation between the star formation activity and the dust content of galaxies. These studies have shown that, in general, galaxies with the highest star formation rates also suffer the highest attenuation (e.g. Kauffmann et al. 2003b; Brinchmann et al. 2004). However, observations at ultraviolet, optical and near-infrared wavelengths set only limited constraints on the dust content of galaxies. As we have seen in the previous chapters, new insight into the dust properties of galaxies may be gained by using observations at mid- and far-infrared wavelengths, where the dust re-radiates the energy absorbed from starlight. This has been explored already in previous studies, which allied ultraviolet and optical observations with rough estimates of the total infrared luminosity to better constrain the dust content of galaxies (e.g. Wang & Heckman 1996; Hopkins et al. 2001; Sullivan et al. 2001; Kong et al. 2004). The models we proposed in Chapter 2 above allows us to go a step beyond these (largely empirical) studies, by offering a means of interpreting simultaneously ultraviolet, optical and infrared observations in terms of physical parameters pertaining to the stars, gas and dust in galaxies. Using this model, we have interpreted the observed ultraviolet, optical and infrared spectral energy distributions of the galaxies in the SINGS (Chapter 3) and in the SSGSS (Chapter 4) samples in terms constraints on the star formation histories and dust contents of the galaxies. We have derived in this way median-likelihood estimates of the stellar mass, star formation rate, dust attenuation and dust mass of the observed galaxies. We have shown that, for the galaxies in the SINGS and SSGSS samples, the dust-to-stellar mass ratio correlates strongly with the specific star formation rate. This confirms the expectation that dust mass and star formation rate go hand in hand in galaxies. Although these trends are clear, the galaxy samples used in these studies were restrained to relatively small numbers.

In the present chapter, we further investigate these relations by assembling a larger sample of about 3000 star-forming galaxies with photometric observations from ultraviolet to infrared wavelengths. By analogy with our approach in Chapters 3 and 4, we use the model presented in Chapter 2 to derive median-likelihood estimates of the total stellar mass, dust mass and star formation rate of the galaxies in this sample. We confirm the relations found in Chapters 3 and 4 between dust content and star formation activity in galaxies. The size of the sample presented in this chapter represents a significant improvement in comparison to previous studies. It allows us to study in detail the relations between the specific star formation rate, dust mass and dust-to-gas ratio. We quantify the observed relations between the star formation history and dust content and try to interpret them as an evolutive sequence. For the first time, we provide a simple recipe to estimate the dust mass of a galaxy as a function of the star formation rate.

We compare our findings with recent models of the chemical evolution of galaxies by Calura, Pipino & Matteucci (2008). We also compare the relations between the specific star formation rate, the ratio of dust luminosity to stellar mass and the ratio of dust luminosity to star formation rate obtained from our analysis with those predicted by cosmological simulations of galaxy formation by Hatton et al. (2003).

This chapter is organized as follows. We describe the matched *GALEX*-SDSS-2MASS-*IRAS* sample in Section 5.2. In Section 5.3, we outline the model used to analyze these data. We present our results concerning the correlations between the star formation, dust content and gas enrichment by dust of galaxies in Section 5.4. In Section 5.5, we discuss the implications of these results and compare them to the predictions of cosmological simulations. The conclusions of this study are presented in Section 5.6.

5.2 The galaxy sample

The sample analyzed in this chapter is drawn from SDSS DR6 main spectroscopic sample. We cross-correlate this sample with catalogues at ultraviolet, near-infrared and far-infrared wavelengths: the *GALEX* catalogue, the 2MASS All Sky Extended source catalogue and the *IRAS* Point Source Catalogue (PSCz) and Faint Source Catalogue (FSC). The specificity of our sample with respect to other large samples of galaxies is to be detected at ultraviolet, optical, near-infrared and far-infrared wavelengths.

5.2.1 Optical photometry

The SDSS DR6 spectroscopic sample (Adelman-McCarthy et al. 2008) provides the optical photometry and the redshifts of our galaxies. This sample contains 792,680 galaxies limited by Petrosian magnitude, $r < 17.77$. Optical photometry from SDSS images is available in the *ugriz* bands for these galaxies. We use the SDSS 'model magnitudes' in these bands[1]. These magnitudes include the integrated light from the whole galaxy, and are the best suited to compare with the total photometry from the other instruments. This is important to ensure consistent multi-wavelength information for each galaxy. We stress that consistent multi-wavelength photometry is a fundamental requirement in the application of the model described in Chapter 2. Many fundamental parameters of these galaxies have been derived from the spectroscopic data (e.g. Brinchmann et al. 2004), and are publicly available in an online database[2]. We use this information to restrict our sample to galaxies classified as 'star-forming' according to their emission lines. AGN in the sample are eliminated when one or both of two criteria are met: (i) the existence of broad emission lines from high-velocity gas around the AGN (e.g. Brinchmann et al. 2004); (ii) the existence of narrow emission lines with intensity ratios characteristic of an AGN in the Baldwin, Phillips & Terlevich diagram (BPT; Baldwin, Phillips & Terlevich 1981), according to the criterion of Kauffmann et al. (2003a)[3]. In Section 5.5.2, we discuss the possible contamination of our sample by optically thick AGN. If the emission lines are highly attenuated, the BPT diagnostic may fail to identify an obscured AGN. Observations in the X-rays or in the mid-infrared can be used to detect AGN in this case.

5.2.2 UV photometry

To supplement SDSS DR6 spectroscopic data with ultraviolet measurements, we cross-correlate the sample with the *Galaxy Evolution Explorer* (*GALEX*; Martin et al. 2005; Morrissey et al. 2005) latest data release. *GALEX* is an all-sky survey which images galaxies in two main photometric bands: the far-ultraviolet (*FUV*, 1520 Å) and the near-ultraviolet (*NUV*, 2310 Å). The match routine uses a search radius of 4 arcsecs around the SDSS position (we use data kindly provided in advance of publication by David Schiminovich). We retain galaxies which have a single *GALEX* detection in the search radius, i.e. we eliminate objects for which two *GALEX* detections may exist for the same SDSS source. At ultraviolet wavelengths, Galactic extinction is particularly important (see e.g. Chapter 1.4). Therefore, we

---

[1] These magnitudes are computed using a weighted combination of the de Vaucouleurs and the exponential light profiles

[2] http://pc-66.astro.up.pt/ jarle/GASS/

[3] The BPT diagram allows one to distinguish star-forming galaxies from AGN on the basis of the degree of ionization of the gas by comparing the narrow-line ratios [O III]λ 5007 Å/Hβ against [N II]λ 6584 Å/Hα (see also Section 4.2.1).

apply foreground Galactic reddening corrections to the *GALEX* magnitudes (Seibert et al. 2005): $A_{\rm FUV} = 8.29\ E(B-V)$ and $A_{\rm NUV} = 8.18\ E(B-V)$, where the color excess $E(B-V)$ is taken accordingly to the dust reddening maps of Schlegel, Finkbeiner & Davis (1998). We also correct the observed optical and near-infrared magnitudes for galactic extinction using this method.

5.2.3 Near-IR photometry

We further supplement our sample with near-infrared photometry in the $JHKs$ bands from the 2MASS (Skrutskie et al. 1997) All Sky Extended Source Catalog (XSC). We cross-identify the SDSS DR6 spectroscopic sample and the 2MASS XSC within a search radius of 5 arcsecs around SDSS coordinates. Only sources with no artifacts and not in close proximity to a large nearby galaxy are retained. Concerning the photometry, we follow the recommendations in the the User's Guide to the 2MASS All-Sky Data Release[4]: we adopt K20 fiducial isophotal elliptical aperture magnitudes for galaxies with $Ks < 13$, and fixed $R = 7$ arcsec circular aperture magnitudes for fainter galaxies.

5.2.4 Mid- and far-infrared photometry

We now turn to the most original feature of our sample: the inclusion of mid- and far-infrared photometry. Observations with *IRAS* are rather limited in sensitivity, but they have the advantage of providing an all-sky survey at 12, 25, 60 and 100 μm. In practice, most measurements at 12 and 25 μm are upper flux density limits, and we do not include them in our spectral fits. We use both the *IRAS* Point Source Catalogue (PSCz; Saunders et al. 2000) and the *IRAS* Faint Source Catalogue v2.0 (FSC; Moshir 1989). The PSCz catalogue is a complete and uniform catalogue assembled from the *IRAS* Point Source Catalogue (Beichman et al. 1988) and supplemented by various redshift surveys. It contains 15,411 galaxies with measured redshifts to a depth of 0.6 Jy at 60 μm. The Faint Source Catalogue contains 173,044 sources to a depth of roughly 0.25 Jy at 60 μm. Low galactic latitude regions ($|b| < 20$) are excluded from this catalogue because of the contamination by foreground galactic sources at this detection limit. In both catalogues, we rely on the quoted quality flags of the data to select sources which have a good flux quality at 60 μm (quality flag = 3) and at least a moderate flux quality at 100 μm (quality flag $\geqslant 2$); detections at 12 and 25 μm are not strictly required. To increase the reliability of the sample, we remove objects with a cirrus flag > 2 and a confusion flag > 0. We cross-identify our SDSS-*IRAS* sample with the *IRAS* PSCz and *IRAS* FSC using the same criteria as Pasquali, Kauffmann & Heckman (2005). We discard *IRAS* sources which have more than one SDSS matched object within a search radius of 30 arcsec. A test of our algorithm on the PSCz catalogue shows that only about 1 per cent of the sources are assigned to a different SDSS object than the one found in the PSCz catalogue. However, the contamination may be

---

[4] http://www.ipac.caltech.edu/2mass/releases/allsky/doc/

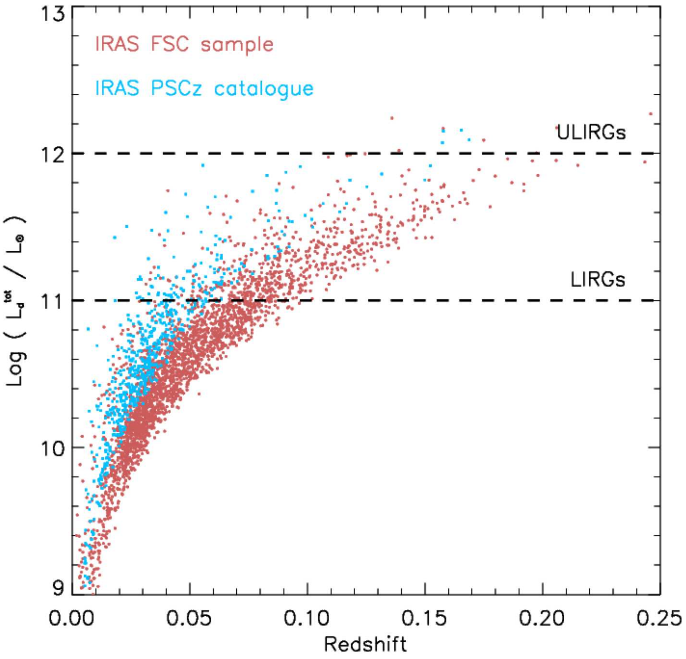

Figure 5.1: Total infrared luminosity $L_{\rm d}^{\rm tot}$ plotted against the redshift for our galaxies in the *IRAS* PSCz catalogue (blue symbols) and in the *IRAS* FSC catalogue(red symbols). $L_{\rm d}^{\rm tot}$ is obtained from the empirical formula given by Helou et al. (1988): $L_{\rm d}^{\rm tot} = F_{\rm c}\ L_{\rm FIR}$. $L_{\rm FIR}$ is computed using the *IRAS* 60- and 100-μm fluxes, $L_{\rm FIR} = 1.26 \times 10^{-14}(2.58F_\nu^{60} + F_\nu^{100})4\pi d_{\rm L}^2$, where $d_{\rm L}$ is the luminosity distance. We compute the correction factor using the prescription of Helou et al. (1988) $F_{\rm c}$ according to the F_ν^{60}/F_ν^{100} colour, for a dust emissivity index $\beta = 2$.

higher in our cross-identified FSC-SDSS catalogue due to the lower quality of the FSC observations. Using simulated data, Pasquali, Kauffmann & Heckman (2005) estimate that the percentage of wrong cross-identifications is at most 1.5 per cent for a matching radius of 30 arcsec.

5.2.5 Final sample

Our final *GALEX*-SDSS-2MASS-*IRAS* sample is composed of 3321 galaxies from the PSCz and FSC catalogues, covering a redshift range from $z = 0$ to $z = 0.22$ (see Fig. 5.2a). To summarise, for the galaxies in this sample, we have:

- at least one of ultraviolet *FUV* and *NUV* fluxes from *GALEX*;
- optical *ugriz* fluxes from SDSS;
- near-infrared *JHKs* fluxes from 2MASS;
- 12-, 25-, 60- and 100-μm fluxes from *IRAS* (all galaxies are detected at 60 and 100 μm at least).

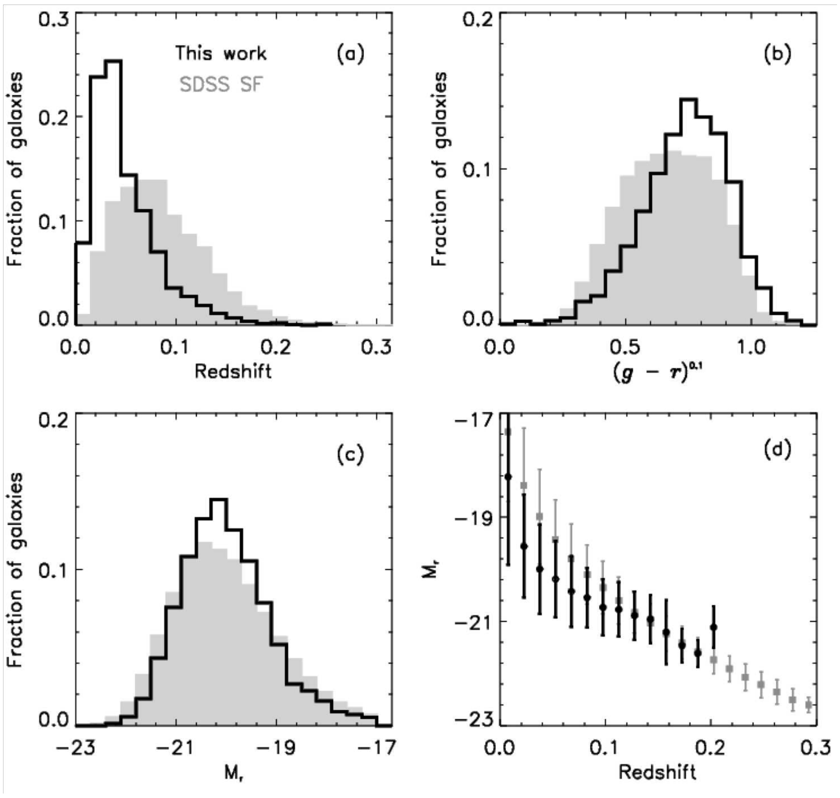

Figure 5.2: Properties of the SDSS DR6 star-forming galaxies (in grey) and the subsample considered in this paper (in black). In panels (a), (b), and (c), the histograms show the normalized distributions of the following parameters: (a) Redshift; (b) Galaxy $g - r$ model colour, k-corrected to $z = 0.1$; (c) Absolute r-band model magnitude. In panel (d), we plot the absolute r-band model magnitude as function of redshift for both samples.

We are interested here in the total emission from galaxies. Therefore, we choose to not include SDSS spectroscopic information (such as Hα and Hβ emission line fluxes), which is restricted to the inner 3 arcsec diameter aperture sampled by the SDSS spectroscopic fibre aperture. At the low redshifts of our galaxies, this limited sampling could introduce substantial bias on the inferred star formation rate and dust content (Kewley, Jansen & Geller 2005). In addition, central spectroscopic quantities cannot be compared directly with the multi-wavelength photometric data pertaining to whole galaxies.

It is instructive to examine the typical infrared luminosities of the galaxies in our sample. In Fig. 5.1, we plot the total infrared luminosity of our galaxies $L_{\rm d}^{\rm tot}$ as a function of redshift. For this purpose, we compute $L_{\rm d}^{\rm tot}$ from the 60- and 100-μm *IRAS* flux densities F_ν^{60} and F_ν^{100} using the empirical formula by Helou et al. (1988):

$$L_{\rm d}^{\rm tot} = F_{\rm c}\, L_{\rm FIR}\,, \tag{5.1}$$

with

$$L_{\rm FIR} = 1.26 \times 10^{-14} (2.58\, F_\nu^{60} + F_\nu^{100})\, 4\pi d_{\rm L}^2\,. \qquad (5.2)$$

Here, $d_{\rm L}$ is the luminosity distance in m, F_ν^{60} and F_ν^{100} are in Jy, and $L_{\rm d}^{\rm tot}$ and $L_{\rm FIR}$ are in W . We compute the correction factor F_c used to convert the quantity $L_{\rm FIR}$ into $L_{\rm d}^{\rm tot}$ as a function of the F_ν^{60}/F_ν^{100} ratio following the empirical prescription of Helou et al. (1988). Assuming a dust emissivity index $\beta = 2$ for our sample, the median correction factor is $F_c \approx 1.35$.

Fig. 5.7 shows that a large fraction of the galaxies in our sample (about 22 per cent) have $L_{\rm d}^{\rm tot} > 10^{11}$ $L_\odot$. Such galaxies are usually referred to as 'luminous infrared galaxies' (LIRGs). About 1 per cent of the galaxies have $L_{\rm d}^{\rm tot} > 10^{12}$ $L_\odot$. These galaxies with extreme infrared luminosities as usually referred to as 'ultra luminous infrared galaxies' (ULIRGs). They have been the object of extensive studies (e.g. Soifer et al. 1987; Veilleux et al. 1995; Veilleux, Kim & Sanders 1999; Rigopoulou et al. 1999; Cao et al. 2006; Armus et al. 2007). At least at low redshifts, most ULIRGs are known to be the result of interactions and merging processes. Visual inspection of the SDSS optical images of the ULIRGs in our sample confirms that ULIRGs in our sample have disturbed morphologies.

We further compare in Fig. 5.2 the properties of our sample with the overall properties of the SDSS star-forming galaxy sample. Fig. 5.2a shows that our sample is biased towards the low-redshift end of the SDSS star-forming sample. This is a selection effect due to the low sensitivity of *IRAS*. Fig. 5.2b shows that the colour distribution of the galaxies in our sample peaks at redder colours than whole SDSS star-forming sample. This is most probably a consequence of the higher average dust content of our galaxies, which makes them detectable by *IRAS* in the first place. In fact, Obrić et al. (2006, see their figure 19) point out that SDSS galaxies detected by *IRAS* have systematically higher dust attenuation than the average SDSS star-forming galaxy. Fig. 5.2c further shows that galaxies in our sample are typically slightly more luminous than the average SDSS star-forming galaxy. This effect is more striking in Fig. 5.2d, where the absolute r-band magnitude M_r is plotted against redshift for both samples: our sample is biased towards the most luminous SDSS star-forming galaxies. This effect is again explained by the *IRAS* selection.

5.3 Constraints on physical parameters

In this Section, we use the simple model developed in Chapter 2 to extract the star formation histories and dust contents of the galaxies in our sample from ultraviolet, optical and infrared observations. First, we briefly summarize the model. Then, we describe the statistical approach used to derive median-likelihood estimates on the model parameters.

5.3.1 Description of the model

The simple, physically motivated model of Chapter 2 allows us to interpret the mid- and far-infrared spectral energy distributions of galaxies consistently with the emission at ultraviolet, optical and near-infrared wavelengths. We briefly recall the main features of this model.

We compute the emission by stars in galaxies using the latest version of the Bruzual & Charlot (2003) population synthesis code (Charlot & Bruzual, in preparation). This code predicts the spectral evolution of stellar populations in galaxies from far-ultraviolet to far-infrared wavelengths and at ages between 1×10^5 and 2×10^{10} yr, for different metallicities, initial mass functions (IMFs) and star formation histories. In this work, we adopt the Chabrier (2003) Galactic-disc IMF (more details about these models can be found in Section 1.3).

The emission from stars is then attenuated using the simple two-component dust model of Charlot & Fall (2000). This accounts for the fact that stars are born in dense molecular clouds with typical lifetimes of 10^7 yr; after that time, they migrate to the ambient (diffuse) ISM. Thus, the light produced by stars younger than 10^7 yr is attenuated by dust in the birth clouds and in the ambient ISM, while the light produced by stars older than the lifetime of the birth clouds is attenuated only by dust in the ambient ISM. The model of Charlot & Fall (2000) uses an 'effective absorption' curve for each component, $\hat{\tau}_\lambda \propto \lambda^{-n}$. The slope of this curve, n, reflects both the optical properties and the spatial distribution of the dust (see Section 1.4). Following Charlot & Fall (2000), we adopt for the ambient ISM

$$\hat{\tau}_\lambda^{\mathrm{ISM}} = \mu \hat{\tau}_V (\lambda / 5500 \text{ Å})^{-0.7} \,, \tag{5.3}$$

where $\hat{\tau}_V$ is the total effective V-band absorption optical depth of the dust seen by young stars inside birth clouds, and $\mu = \hat{\tau}_V^{\mathrm{ISM}} / (\hat{\tau}_V^{\mathrm{BC}} + \hat{\tau}_V^{\mathrm{ISM}})$ is the fraction of this contributed by dust in the ambient ISM. For the stellar birth clouds, we adopt (Chapter 2):

$$\hat{\tau}_\lambda^{\mathrm{BC}} = (1 - \mu) \hat{\tau}_V (\lambda / 5500 \text{ Å})^{-1.3} \,. \tag{5.4}$$

We use this prescription to compute the total energy absorbed by dust in the birth clouds and in the ambient ISM; this energy is re-radiated by dust at infrared wavelengths. By analogy with Chapter 2, we define the total dust luminosity reradiated by dust in the birth clouds and in the ambient ISM as $L_{\mathrm{d}}^{\mathrm{BC}}$ and $L_{\mathrm{d}}^{\mathrm{ISM}}$, respectively. The total luminosity emitted by dust in the galaxy is then

$$L_{\mathrm{d}}^{\mathrm{tot}} = L_{\mathrm{d}}^{\mathrm{BC}} + L_{\mathrm{d}}^{\mathrm{ISM}} \,. \tag{5.5}$$

We distribute in wavelength the energy reradiated by dust in the infrared, $L_{\mathrm{d}}^{\mathrm{BC}}$ and $L_{\mathrm{d}}^{\mathrm{ISM}}$, over the range from 3 to 1000 μm, using four main components:

- the emission from polycyclic aromatic hydrocarbons (PAHs; i.e. mid-infrared emission features),

- the mid-infrared continuum emission from hot dust with temperatures in the range 130–250 K,
- the emission from warm dust in thermal equilibrium with adjustable temperature in the range 30–60 K,
- the emission from cold dust in thermal equilibrium with adjustable temperature in the range 15–25 K.

In stellar birth clouds, the relative contributions by PAHs, the hot mid-infrared continuum and warm dust to $L_{\mathrm{d}}^{\mathrm{BC}}$ are kept as adjustable parameters. These clouds do not contain any cold dust. In the ambient ISM, the contribution by cold dust to $L_{\mathrm{d}}^{\mathrm{ISM}}$ is kept as an adjustable parameter. The relative ratios of the other three components are fixed to the values reproducing the mid-infrared cirrus emission of the Milky Way. This minimum number of components is required to account for the infrared spectral energy distributions of galaxies in wide ranges of star formation histories (see Chapter 2 for more details).

5.3.2 Median-likelihood estimates of physical parameters

The model summarized above allows us to derive statistical estimates of physical parameters, such as stellar mass, star formation rate and dust mass from combined ultraviolet, optical and infrared galaxy observations. To achieve this, we adopt a Bayesian technique similar to that already employed in Chapter 3.

5.3.2.1 Model library

We build random libraries of models at different redshifts $z = 0.00$, 0.05, 0.10, 0.15, 0.20 and 0.25, as described in Section 4.3.1.

At each redshift, we generate a random library of stellar population models for wide ranges of star formation histories, metallicities and dust contents. Each star formation history is parametrized in terms of an underlying continuous model with exponentially declining star formation rate on top of which are superimposed random bursts (see also Kauffmann et al. 2003b). The models are distributed uniformly in metallicity between 0.2 and 2 times solar. The attenuation by dust is randomly sampled by drawing the total effective V-band absorption optical depth, $\hat{\tau}_V$, between 0 and 6, and the fraction of this contributed by dust in the ambient ISM, μ, between 0 and 1 (see Section 3.2.1 for more details on the prior distributions of these parameters). For each model, we compute the specific star formation rate averaged over the past $t_8 = 10^8$ yr:

$$\psi_{\mathrm{S}}(t) = \frac{\int_{t-t_8}^{t} dt'\psi(t')}{t_8 M_*(t)}\,, \tag{5.6}$$

where $M_*(t)$ is the stellar mass at time t.

In parallel, we generate for each redshift bin libraries of infrared spectra for wide ranges of dust temperatures and fractional contributions by different dust components to the total infrared luminosity. As in Chapter 3, the fraction of the total luminosity of dust contributed by the diffuse ISM, $f_\mu = L_{\rm d}^{\rm ISM}/L_{\rm d}^{\rm tot}$, and the fractional contribution by warm dust in thermal equilibrium to the total dust luminosity of the birth clouds, $\xi_{\rm W}^{\rm BC}$, are uniformly distributed between 0 and 1; the fractions of luminosity contributed by the other components in the birth clouds, $\xi_{\rm MIR}^{\rm BC}$ (hot mid-infrared continuum) and $\xi_{\rm PAH}^{\rm BC}$ (PAHs), are randomly draw from prior distributions such that $\xi_{\rm W}^{\rm BC} + \xi_{\rm MIR}^{\rm BC} + \xi_{\rm PAH}^{\rm BC} = 1$. We distribute uniformly the temperature of warm dust in thermal equilibrium in the birth clouds, $T_{\rm W}^{\rm BC}$, between 30 and 60 K, and the temperature of cold dust in thermal equilibrium in the diffuse ISM, $T_{\rm C}^{\rm ISM}$, between 15 and 25 K. Finally, we distribute uniformly the contribution by cold dust to the total infrared luminosity of the ISM, $\xi_{\rm C}^{\rm ISM}$, between 0.5 and 1.

For each model in the library of infrared spectra, we compute the total mass of dust as

$$M_{\rm d} = 1.1\,(M_{\rm W}^{\rm BC} + M_{\rm W}^{\rm ISM} + M_{\rm C}^{\rm ISM})\,, \tag{5.7}$$

where $M_{\rm W}^{\rm BC}$, $M_{\rm W}^{\rm ISM}$ and $M_{\rm C}^{\rm ISM}$ are the masses of the dust components in thermal equilibrium: warm dust in the birth clouds and the ambient ISM and cold dust in the ambient ISM, respectively. The multiplying factor 1.1 accounts for the small contribution by stochastically heated dust grains. Dust in thermal equilibrium constitutes the bulk of the mass of dust in galaxies (see Chapter 2 and references therein). The mass $M_{\rm d}(T_{\rm d})$ of dust in thermal equilibrium at temperature $T_{\rm d}$ is estimated from its far-infrared emission $L_\lambda^{T_{\rm d}}$ using (Hildebrand 1983):

$$L_\lambda^{T_{\rm d}} = 4\pi\, M_{\rm d}(T_{\rm d})\, \kappa_\lambda\, B_\lambda(T_{\rm d})\,, \tag{5.8}$$

where κ_λ is the dust mass absorption coefficient and $B_\lambda(T_{\rm d})$ is the Planck function of temperature $T_{\rm d}$.

We combine stochastic libraries of attenuated stellar spectra and infrared dust emission spectra at each redshift by associating models with the same value of f_μ, within some error interval $\delta f_\mu = 0.15$, scaled to the same total dust luminosity $L_{\rm d}^{\rm tot}$. For each combined spectrum, we compute the synthetic photometry in the *GALEX* FUV and NUV, SDSS *ugriz*, 2MASS *JHKs* and *IRAS* 12-, 25-, 60- and 100-μm bands (equation 4.4).

5.3.2.2 Corrections applied to the observed fluxes

In the redshift range of our sample, prominent optical nebular emission lines can significantly affect the observed fluxes in the SDSS *gri* bands. The model spectra we use to interpret these data do not include nebular emission lines. Therefore, to interpret the observed optical fluxes of our galaxies with our model, we first need to correct the SDSS *gri* observed magnitudes for contamination by nebular emission lines (e.g. Kauffmann et al. 2003b). We use the corrections computed by Jarle

Brinchmann (private communication), which are inferred from fits of the stellar emission of each SDSS optical spectrum with Bruzual & Charlot (2003) models (we assume that the corrections derived in this way within the aperture sampled by the SDSS fibre applies to the galaxy as a whole).

We also compute k-corrections to the ultraviolet, optical and near-infrared magnitudes of each galaxy in our sample. To minimise this correction, we k-correct the magnitudes from the galaxy redshift to the the closest redshift among the grid $z = 0.00$, 0.05, 0.10, 0.15, 0.20 and 0.25. We use the version v3 of the KCORRECT code of Blanton et al. (2003) and assume a standard cosmology with $\Omega_m = 0.30$, $\Omega_\Lambda = 0.70$ and $H_0 = 70$ km s^{-1} Mpc^{-1}. No k-corrections are applied to the *IRAS* 12-, 25-, 60- and 100-μm fluxes. Yet it remains a very good approximation to compare these fluxes with the fluxes computed at the fixed redshifts of the model libraries, given the large effective width of the *IRAS* filter response functions, and the relatively large observational uncertainties in these bands.

To account for the uncertainties linked to the k-correction and emission-line correction, we add the following uncertainties to the observed fluxes: 2 per cent for *GALEX*, 2MASS, and SDSS z bands, and 1.5 per cent for the SDSS gri bands. The SDSS u-band photometry is known to be quite uncertain; to account for this, we take an observational uncertainty of 10 per cent for the flux in this band.

5.3.2.3 Spectral fits

Each model in the libraries is characterized by a set of parameters randomly drawn physical quantities. We perform spectral fits by comparing the observed spectral energy distribution of a galaxy with every model in the library at the corresponding redshift. Specifically, for each observed galaxy, we compute the χ^2 goodness of fit of each model. Then, we build the likelihood distribution of any given physical parameter by weighting the value of that parameter in each model of the library by its probability, $\exp(-\chi^2/2)$. We take our estimate of the parameter to be the median of the likelihood distribution, and the associated confidence interval to be the 16th–84th percentile range (see more details in Chapter 3).

We use this approach to derive the likelihood distributions of several physical parameters of the galaxies in our sample, based on fits of the *GALEX FUV* and *NUV*, SDSS $ugriz$, 2MASS $JHKs$ and *IRAS* 12-, 25-, 60- and 100-μm fluxes for all the galaxies in our sample (in different redshift bins). The parameters we focus on are: the star formation rate, ψ; the specific star formation rate, ψ_S; the stellar mass, M_*; the dust mass, M_d; the total luminosity of the dust, $L_\mathrm{d}^\mathrm{tot}$; the fraction of this contributed by the diffuse ISM, f_μ; the effective absobtion optical depth, $\hat{\tau}_V$, and the fraction of it contributed by dust in the ambient ISM, μ.

We first check how well the model can reproduce the observed spectral energy distributions of the galaxies in our sample. The histograms in Fig. 5.3 show, for each photometric band, the distribution of the difference between the observed luminosity L_ν^obs and the best-fit model luminosity L_ν^mod, in units of observational error σ. The model can fit remarkably well the observed ultraviolet, optical, near-, mid- and far-

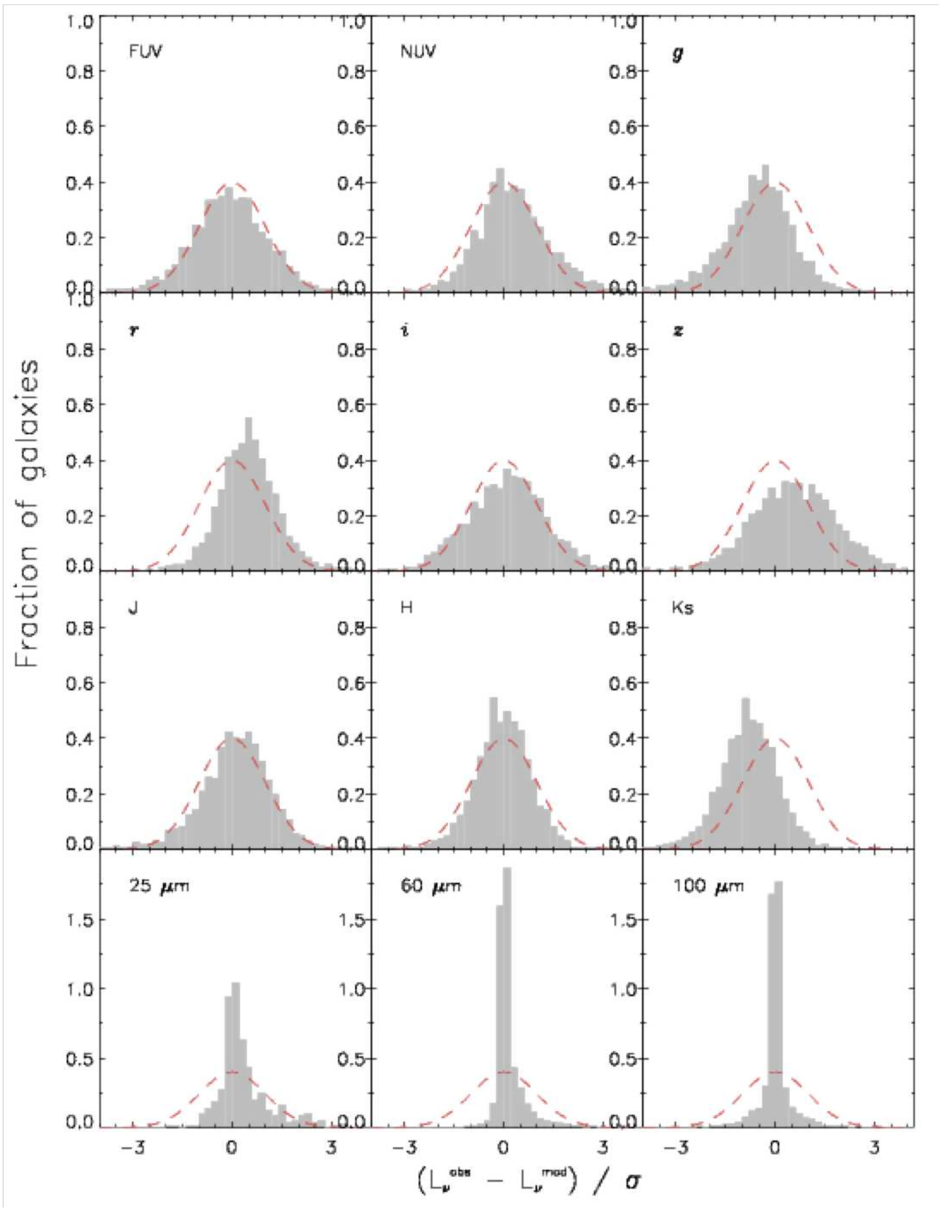

Figure 5.3: Distribution of the difference between observed luminosity $L_\nu^{\rm obs}$ and best-fit model luminosity $L_\nu^{\rm mod}$, in units of the observational error σ for the galaxies in our sample. Each panel refers to a different photometric band (as indicated). The best-fit model for each galaxy was selected by fitting as many luminosities as available in the following bands: *GALEX* (*FUV* and *NUV*), optical SDSS *ugriz*, 2MASS (*JHKs*), and *IRAS* (12, 25, 60 and 100 μm). The red dashed curve shows a Gaussian distribution with unit standard deviation, for reference.

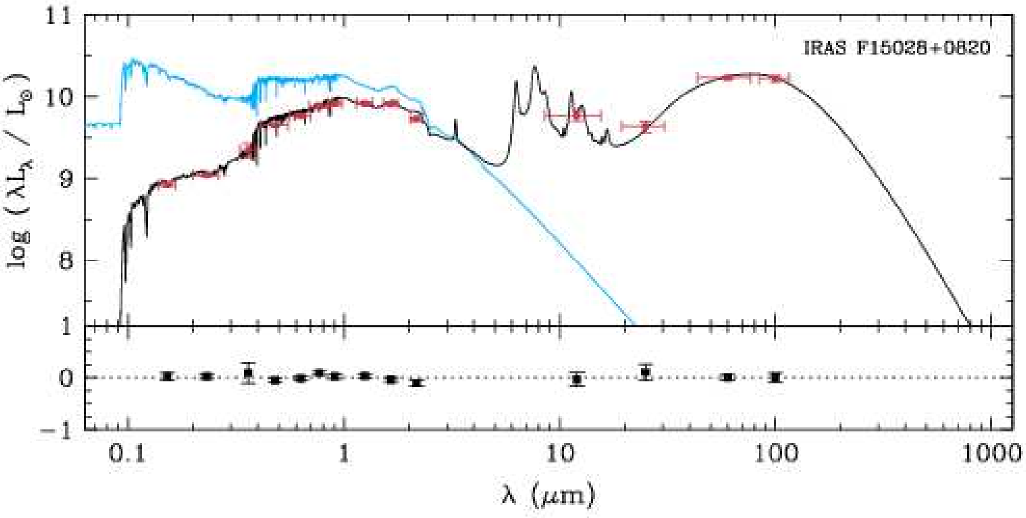

Figure 5.4: Best fit model (in black) to the observed spectral energy distribution (in red) of one galaxy in our sample with median properties in Fig. 5.6, IRAS F15028+0820. The blue line shows the unattenuated stellar spectrum. For each galaxy, the red squares show the observed broad band luminosity (*GALEX FUV*, *NUV*; SDSS *ugriz*; 2MASS *JHKs*; *IRAS* 12-, 25-, 60- and 100-μm) with its error as the vertical bar and the width of the filter as the horizontal bar. The residuals $(L_\lambda^{\rm obs} - L_\lambda^{\rm mod})/L_\lambda^{\rm obs}$ are shown at the bottom of each panel

infrared luminosities of the galaxies simultaneously. We note that the model appears to underestimate slightly (by a factor that corresponds to ~ 0.10 magnitudes) the observed Ks-band luminosity of the galaxies. This small offset is within the uncertainty of current population synthesis models, and it has negligible influence on our results (as inferred from removing the Ks-band constraint from the spectral fits.

In Fig. 5.4, we show, an example of best-fit spectral energy distribution (in black) to the observations of a galaxy in the sample (in red). For reference, this galaxy is located near the median of the relation between the dust-to-stellar mass ratio and the specific star formation rate illustrated in Fig. 5.6 below.

5.4 The relation between star formation activity and dust content in galaxies

5.4.1 Results

The method described above allows us to derive statistical constraints on the total dust luminosity, $L_{\rm d}^{\rm tot}$, the total dust mass, $M_{\rm d}$, the star formation rate, ψ, the stellar

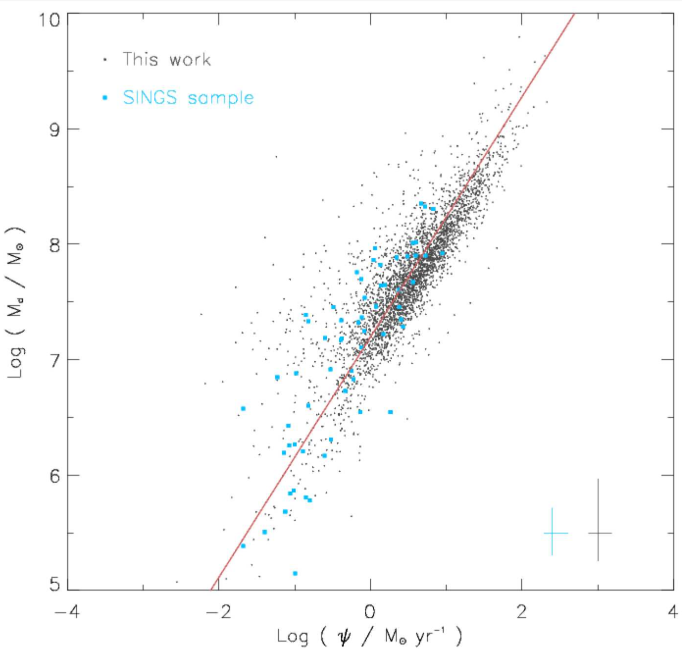

Figure 5.5: Median-likelihood estimate of the dust mass, $M_{\rm d}$, against star formation rate averaged over the last 10^8 yr, ψ, for the 3321 galaxies of our sample (gray symbols) and the SINGS galaxies (blue symbols). The median error bars for each sample are plotted in the lower-right corner using their respective colours. These error bars correspond to the median confidence intervals, computed using the 16th–84th percentile range of the likelihood distribution for $M_{\rm d}$ and ψ for each galaxy in each sample. The red line is a linear robust fit minimizing the absolute deviation along the x-axis.

mass, M_*, and the fraction of $L_{\rm d}^{\rm tot}$ contributed by dust in the diffuse interstellar medium, f_μ, for the 3321 galaxies in our *GALEX*-SDSS-2MASS-*IRAS* sample.

In Fig. 5.5, we show the relation between dust mass $M_{\rm d}$ and star formation rate ψ derived in this way for the galaxies in our sample (gray dots). The median dust mass is 4.8×10^7 $\rm M_\odot$. The correlation between dust mass and star formation rate is remarkably tight, spanning four orders of magnitudes in ψ and $M_{\rm d}$. We perform a linear fit to the points of Fig. 5.5 by computing the bisector of two least-square regression lines: one of the y-axis variable on the x-axis variable and one of the x-axis variable on the y-axis variable (Isobe et al. 1990). This gives (red line in Fig. 5.5)

$$M_{\rm d} = A\,\psi^\alpha\,, \tag{5.9}$$

with $A = (1.57 \pm 0.02) \times 10^7$ and $\alpha = 1.04 \pm 0.01$, where $M_{\rm d}$ is expressed in $\rm M_\odot$ and ψ in $\rm M_\odot$ $\rm yr^{-1}$. The quantity A can be regarded as the average efficiency of dust production in galaxies. We emphasize that the quoted uncertainties are formal uncertainties computed by taking into account the confidence range of each measurement. However, these uncertainties do not take the scatter of the relation directly into account; these formal uncertainties are much smaller than the typical scatter of the relation (about 0.7 dex in M_d). The expression in equation (5.9) can be used to estimate the typical dust mass in a galaxy, based on the star formation rate. We note that equation (5.9) can be combined with the Schmidt-Kennicutt law (Schmidt 1959; Kennicutt 1998b) to relate the dust mass to gas mass in a galaxy (currently under investigation). To our knowledge it is the first time that such an expression can be calibrated for a large sample of galaxies.

We also show for comparison in Fig. 5.5 the dust masses and star formation rates of the SINGS galaxies derived in Chapter 3. These local galaxies follow the same relation as the galaxies in our sample, and extend to slightly lower dust masses and star formation rates. The typical error bars on M_d and ψ for SINGS galaxies are smaller than for our sample. This is because a wider collection of constraints are available for the SINGS galaxies (see more details in Chapter 3).

In Fig. 5.6, we explore the relations between ψ_S and three particularly interesting physical parameters for the galaxies in our sample: the dust-to-stellar mass ratio M_d/M_*, the ratio of dust mass to star formation rate M_d/ψ, and the fraction of $L_\mathrm{d}^\mathrm{tot}$ contributed by dust in the diffuse ISM. The top panels show remarkably strong correlations between ψ_S and these quantities: the Spearman rank coefficients are $r_S = 0.86$, -0.63 and -0.75, respectively. All these correlations have a significance above 20σ for the sample size. In the bottom panels of Fig. 5.6, we show the same correlations for pairs of galaxies that have been closely matched in stellar mass[5]. These panels demonstrate that the stellar mass is not driving the strong correlations observed in the top panels of Fig. 5.6. We use red triangles to mark galaxies for which 12- and 25-μm *IRAS* fluxes are available in addition to the fluxes at 60 and 100 μm, hence for which the error bars on the derived parameters are smallest. These galaxies follow the same distribution as the rest of the sample. This indicates that the parameters derived for galaxies with only two *IRAS* fluxes are not systematically biased relatively to those derived using all four *IRAS* bands.

The strength of the correlations between ψ_S and M_d/M_*, M_d/ψ, and the fraction of $L_\mathrm{d}^\mathrm{tot}$ contributed by the diffuse ISM in Fig. 5.6 suggest that the specific star formation rate is a fundamental diagnostic of the properties of the ISM in galaxies. The left panels in Fig. 5.6 show that the most dust-rich galaxies are those with the highest specific star formation rates. This is not surprising, as dust is produced by supernovae and AGB stars in actively star-forming galaxies. In the middle panels, M_d/ψ can be regarded as proxy of the dust-to-gas ratio, as ψ is related to the gas mass (H I + H_2) by virtue of the Schmidt law. The anti-correlation between M_d/ψ and ψ_S suggests that the ISM is more enriched in dust in galaxies with low specific star formation rate i.e. which have presumably exhausted their gas reservoir. Finally, the right panels of Fig. 5.6 show that the fraction of $L_\mathrm{d}^\mathrm{tot}$ contributed by

---

[5] This match is achieved by comparing the physical properties of galaxy pairs with the same stellar mass M_*.

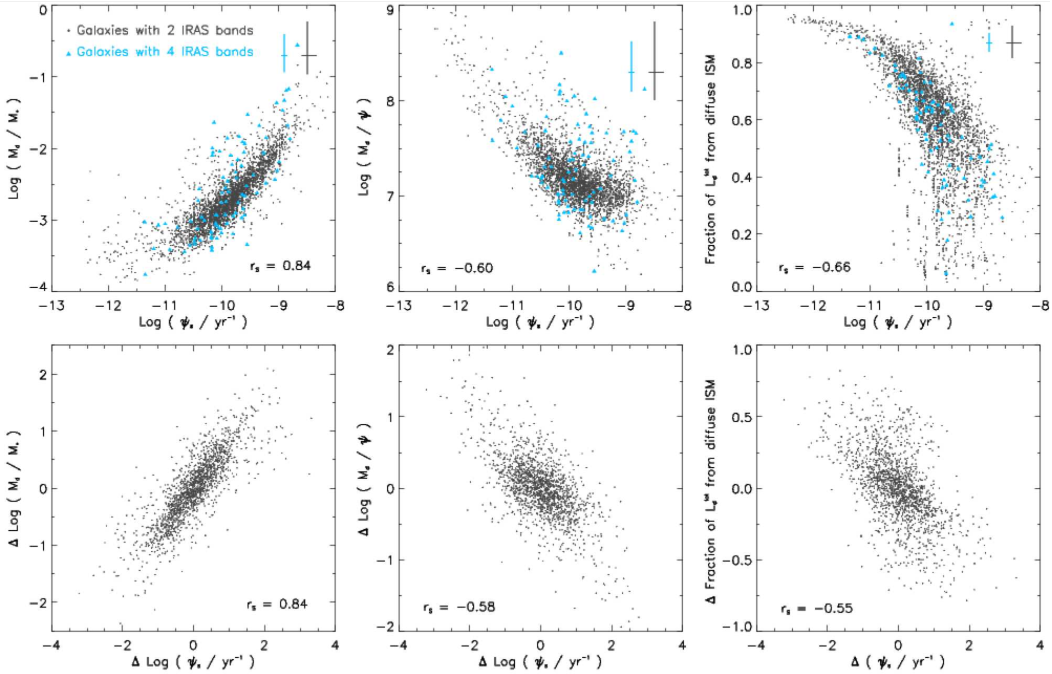

Figure 5.6: *Top:* Median-likelihood estimate of three galaxy properties against specific star formation rate, ψ_S. Left panel – ratio of dust mass to stellar mass, M_d/M_*; middle panel – ratio of dust mass to star formation rate, M_d/ψ (as discussed in Section 5.4.1, this is used as a proxy for the dust enrichment of the ISM); right panel – fration of total infrared luminosity contributed by dust in the ambient ISM. The blue triangles show galaxies in our sample with available measurement in the four *IRAS* bands. The error bars represent the median confidence ranges for each parameter. *Bottom:* In these panels, we show the same relations for galaxy pairs in our sample that are closely matched in stellar mass. The Spearman rank coefficient, r_S, is indicated in each panel.

dust drops in galaxies with highest specific star formation rates ψ_S. This trend was previously found for other local galaxy samples in Chapters 3 and Chapter 4. Indeed we expect that the main contribution to the total dust luminosity comes from dust heated by young stars inside birth clouds for highly star-forming galaxies, whereas the bulk of dust emission is attributed to dust in the diffuse ISM heated by old stars in more quiescent galaxies.

5.4.2 Results in stellar mass ranges

We now divide our sample in three stellar mass ranges to further explore the relations of Fig. 5.6. We have already demonstrated in the previous section that the correlations observed in Fig. 5.6 are not primarily driven by stellar mass. We now investigate possible systematic differences in the ISM properties of galaxies

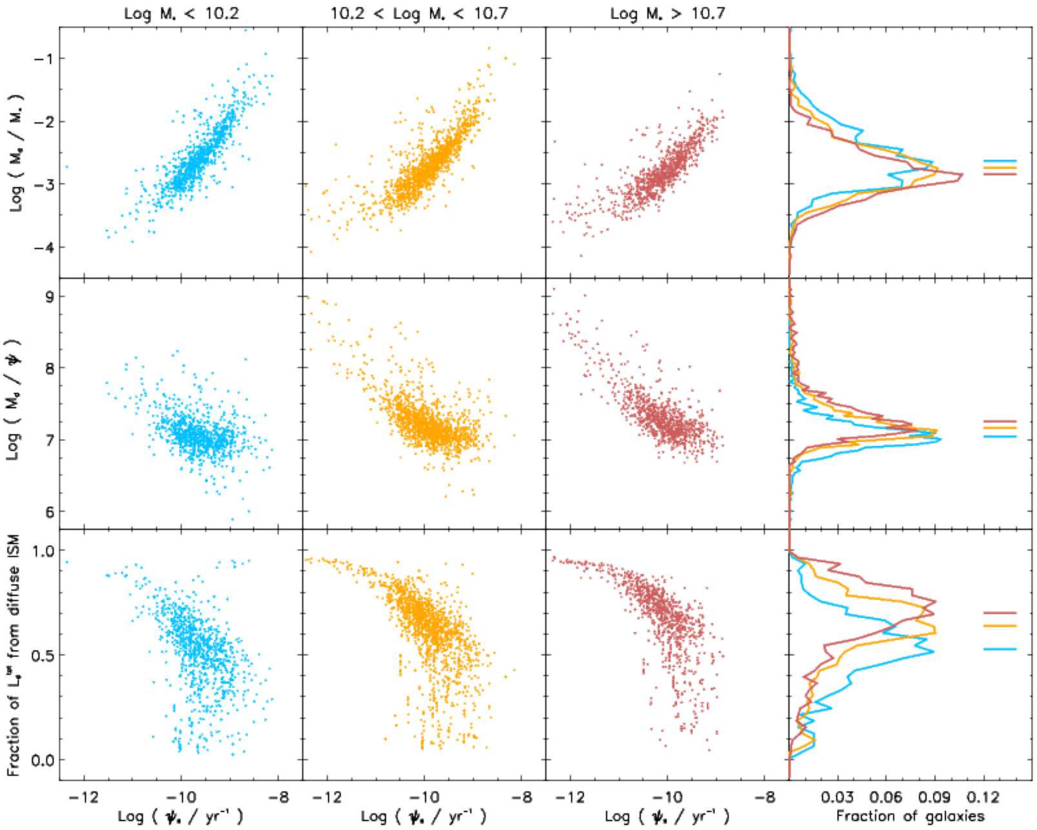

Figure 5.7: Same relations as in Fig. 5.6 in three stellar mass ranges indicated at the top of the figure (blue – log $(M_*/\mathrm{M}_\odot) < 0.2$; yellow – $10.2 <$ log $(M_*/\mathrm{M}_\odot) < 0.7$; red – log $(M_*/\mathrm{M}_\odot) > 0.7$). The right-hand panels illustrate how the distribution of the dust-to-stellar mass ratio, the dust mass to star formation rate ratio and the fraction of total infrared luminosity contributed by dust in the ambient ISM evolve with stellar mass. The median value of the distribution is indicated as a short line of the corresponding colour.

with different stellar masses, since it is known that the star formation activity of a galaxy tends to decrease with increasing stellar mass (e.g. Brinchmann et al. 2004). Fig. 5.7 shows the dust-to-stellar mass ratio M_d/M_*, the ratio of dust mass to star formation rate M_d/ψ, and the fraction of $L_\mathrm{d}^\mathrm{tot}$ contributed by dust in the diffuse ISM as a function of the specific star formation rate ψ_S, in three bins of stellar mass $(M_*/\mathrm{M}_\odot)$. The distribution of the y-axis quantity and its median value (colour coded) is displayed on the right-hand panels.

Fig. 5.7 shows that the relation between M_d/M_* and ψ_S barely changes with stellar mass. There is perhaps a slight tendency for the most massive galaxies to have slightly higher M_d/M_*. Also, we note that M_d/ψ, which measures the dust enrichment of the ISM, increases with stellar mass. The greatest variation with stellar mass in Fig. 5.7 in the fraction of $L_\mathrm{d}^\mathrm{tot}$ contributed by dust in the diffuse

ISM. The median of this parameter changes from 0.5 in the lowest stellar mass bin to 0.7 in the highest stellar mass bin. We note that the median stellar mass in the three bins presents a small dynamic range, thereby possibly hiding a stronger evolution of these properties with stellar mass. It is tempting to interpret the relations of Fig. 5.6 and Fig. 5.7 as evolutionary sequences, where the diffuse ISM of more massive galaxies is dust enriched from previous episodes of star formation. We return to this possibility in the next section.

5.4.3 Comparison with chemical evolution models

In this section, we compare our median-likelihood estimates for the star formation rate and dust content of the galaxies in our sample with the predictions of chemical evolution models. Based on the formalism develop by Dwek (1998), Calura, Pipino & Matteucci (2008) carry out a detailed study of the evolution of dust properties for the solar neighbourhood, as well as for dwarf irregular and elliptical galaxies. These authors take into account the production of dust in the cold envelopes of low- and intermediate-mass stars, and in type-II and type-Ia supernovae. The destruction of dust grains occurs through the shock waves caused by supernovae explosions. The models of Calura, Pipino & Matteucci (2008) allow one to predict the stellar mass and dust mass of galaxies with a given star formation history as a function of time.

In our analysis, we consider the models for the solar neighbourhood and for a dwarf irregular galaxy with continuous star formation. Detailed descriptions of these models can be found in Calura, Pipino & Matteucci (2008). We highlight only the most relevant features for our analysis here. First, the solar-neighbourhood model is designed to reproduce the properties of the Galactic disk component solely, in a 2 kpc-wide ring located at 8 kpc from the Galactic centre. In this model, the Galactic disk is formed in two main episodes, assuming gas infall but no outflow. The exact expression for the star formation rate is given in Chiappini, Matteucci & Gratton (1997), and it is mainly a function of the gas mass surface density with a critical threshold. In the dwarf-irregular model, the star formation rate is expressed as a Schmidt law and increases continuously with time. This model assumes gas infall and galactic winds.

In Fig. 5.8, we compare our median-likelihood estimates of M_d/M_* and M_d/ψ as a function of ψ_S for the galaxies in our sample with the predictions of the solar-neighbourhood model (red filled squares) and the dwarf-irregular model (blue filled circles) of Calura, Pipino & Matteucci (2008) at ages from 1 to 12 Gyr. Both models lie remarkably well in the range spanned by our data at $t = 12$ Gyr. The stellar mass of the dwarf model at 12 Gyr, 1.4×10^8 $\mathrm{M}_\odot$, corresponds to the lower stellar mass limit of our sample. For reference, we select a galaxy of our sample with derived physical properties similar to those of the dwarf model at 12 Gyr at plot it as an open blue circle in Fig. 5.8.

To compare the properties of the solar-neighbourhood model of Calura, Pipino & Matteucci (2008) with those of spiral galaxies in our sample, we must account for the fact that this model does not include a bulge component. The correction

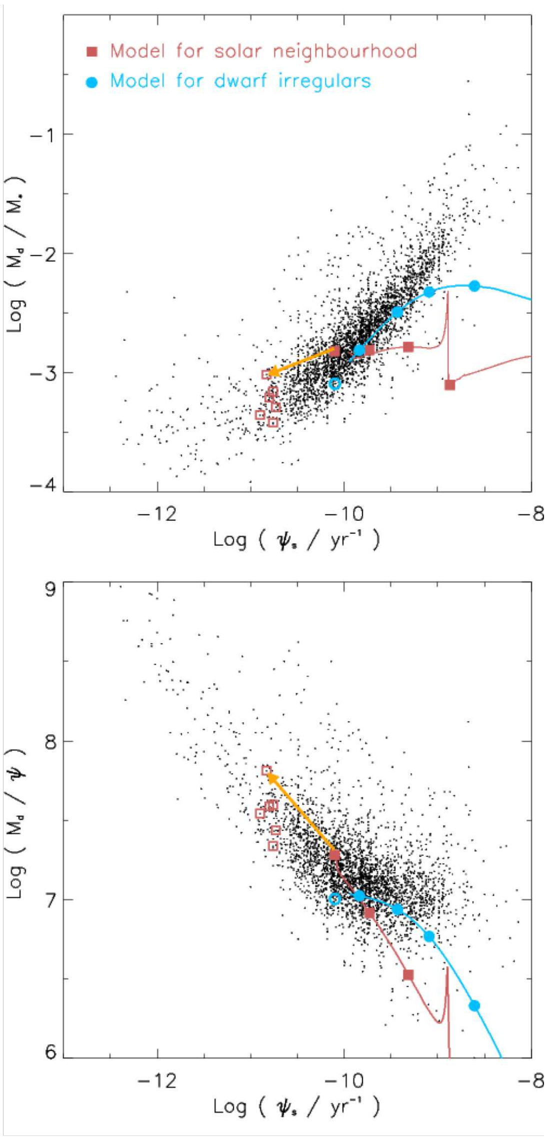

Figure 5.8: Comparison between our sample median-likelihood estimates and theoretical predictions from the chemical evolution models of Calura, Pipino & Matteucci (2008), for the dust-to-stellar mass ratio (top panel) and ratio of dust mass to star formation rate (bottom panel) against specific star formation rate. The time evolution of the solar neighbourhood model and of the dwarf irregular model of Calura, Pipino & Matteucci (2008) are plotted in red and in blue, respectively. The red filled squares and blue circles indicate galaxy ages of 1, 3, 6 and 12 Gyr. The yellow arrow displays the correction for 12 Gyr when adding the Galactic bulge component to the solar neighbourhood model (see Section 5.4.3). For comparison, we show as open symbols galaxies in our sample which have properties similar to the Galactic-bulge corrected solar neighbourhood model (red open squares) and to the dwarf irregular model (blue open circle).

to the dust mass is negligible, since bulges, like elliptical galaxies, tend to have little in interstellar medium. After we add the typical stellar mass of the bulge of the Milky Way to the solar-neighbourhood model of Calura, Pipino & Matteucci (2008), this corrected model presents characteristic values of our Galaxy ($M_* = 2 \times 10^{11}$ M$_\odot$, $\psi = 3$ M$_\odot$ yr^{-1}) with a dust mass of $M_\mathrm{d} = 2 \times 10^8$ M$_\odot$. The model corresponding to our Galaxy lies among the less star-forming and less dusty galaxies of our sample. The red open squares in Fig. 5.8 show galaxies from our sample selected for having similar stellar mass and star formation rate to those of our Galaxy. The solar-neighbourhood predictions corrected for the Galactic bulge component (orange arrow) are remarkably close to this subsample.

A valuable feature of chemical evolution models is that they allow one to predict the evolution of the dust content of galaxies as a function of time. This allows us to test the hypothesis that the sequences followed by galaxies in our sample in Figs. 5.6, 5.7 and 5.8 are driven by evolution. In the top panel of Fig. 5.8, the dwarf-irregular model from ages 3 to 12 Gyr follows the trends observed for the galaxies in our sample as the specific star formation rate decreases with time. A similar trend is not observed for the solar-neighbourhood model, but we emphasize here that the model does not account for the Galactic bulge. In the bottom panel of Fig. 5.8, we can see that both models indicate dust enrichment of the ISM with time, as observed in for sample. These comparisons suggest that the correlations found in Section 5.4.1 are the result of an evolutive sequence.

5.5 Discussion

5.5.1 The effect of inclination

Optical SDSS observations show that our sample is mainly composed of spiral galaxies. The concentration index C, defined as the ratio of the radii enclosing 90 per cent and 50 per cent of the r-band luminosity of a galaxy is computed for the galaxies in our sample. The results indicate that 64 per cent of the galaxies lie below the value $C = 2.6$, considered as the boundary between late- and early-type galaxies (Strateva et al. 2001). It is therefore important to look at possible systematic effects related with galaxy inclination in our sample. The predictions of the dust model described in Section 5.3 are averaged over viewing angle. However, the observed fluxes and colors of galaxies have been found to vary with inclination (e.g. Maller et al. 2008), due to the non-uniform distribution of dust in spiral galaxies.

In Fig. 5.9, we plot the several relevant galaxy properties used in this paper against the axis ratio b/a. This ratio is inversely proportional to inclination.

We first highlight a selection effect in our sample: at low b/a (i.e. high inclination), we do *not* observe galaxies fainter than magnitude $r \sim 16$ (Fig. 5.9a). This occurs because the optical light from these galaxies is attenuated by dust in the edge-on disk. We conclude that edge-on galaxies our sample are biased towards small attenuation, or dust content, as a consequence of optical selection. A galaxy with a dust content above a certain threshold can be optically-detected when it is

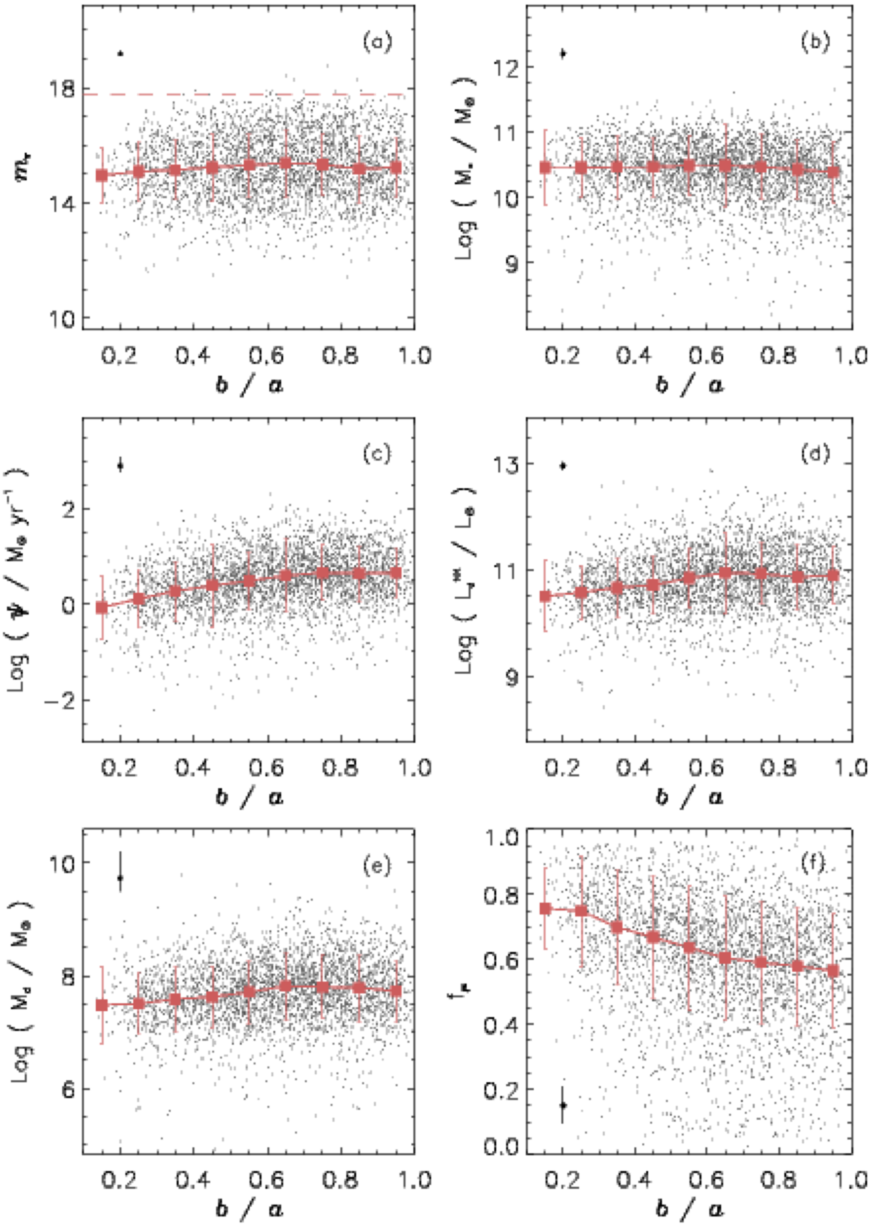

Figure 5.9: Galaxy properties against axis ratio b/a (i.e. inclination) for the galaxies in our sample: (a) apparent r-band magnitude, m_r; (b) stellar mass, M_*; (c) star formation rate, ψ; (d) total infrared luminosity, $L_{\rm d}^{\rm tot}$; (e) dust mass, $M_{\rm d}$; (f) fraction of $L_{\rm d}^{\rm tot}$ contributed by dust in the diffuse ISM, f_μ. The red squares and their error bars indicate the median values and the standard deviation in bins of b/a. The median observational error in m_r is indicated on the upper left corner of panel (a). Likewise, the median confidence interval for the sample on the median-likelihood estimates of the parameters in panels (b) to (e) is indicated on the upper left corner of each panel.

observed at low inclinations, but at similar intrinsic galaxy luminosity it will drop out of the sample if the galaxy is highly inclined. The SDSS spectroscopic sample limit $r < 17.77$ is reached at $b/a = 0.6$: for axis ratios equal or higher than this value, we are able to detect optically galaxies with a full range of dust contents.

We now explore relations of physical parameters derived in this chapter with galaxy axis ratio. The estimate of stellar mass, mainly constrained by the observed near-infrared fluxes, which practically not affected by dust, does not vary with axis ratio, meaning that it is not affected by inclination. The star formation rate is the quantity that varies the most: face-on galaxies ($b/a \simeq 1$) have a value typically 0.7 dex higher than edge-on galaxies. This increase is significant compared to the median error on the star formation rate estimate. Two effects contribute to this trend. First, the young stellar populations which contribute the most to the estimate of the star formation are more attenuated in edge-on galaxies, because their light has to travel longer path through the ISM (the optical depth increases). Secondly, the selection effect mentioned above means that we are missing dusty, actively star-forming galaxies at low axis ratio. In Figs. 5.9d and 5.9e, the estimates on dust mass and dust luminosity increase slightly with axis ratio and reach a plateau at $b/a = 0.6$. These trends are a consequence of our selection effect in the optical only. Finally, Fig. 5.9f shows an effect on the estimate of the contribution of the diffuse ISM to $L_{\rm d}^{\rm tot}$ with inclination. This is due to the model used to interpret the observations. In edge-on galaxies, the optical depth through the disk is so high that the short wavelength radiation from young stars is very attenuated (as discussed above). This makes the model underestimate the amount of stars heating the dust in birth clouds, and therefore it overestimates the contribution of the diffuse ISM heated by old stars to the total dust luminosity.

It is important to notice that these effects are weak compared to the scatter of the estimated parameters. At most, these effects will introduce only a slight scatter in the relations derived in this chapter.

5.5.2 Contamination by AGN hosts

We have seen in Chapter 4 that AGN hosts may present an excess of infrared emission that is not caused by dust heating by stellar light. In these cases, the model we use to interpret the observed spectral energy distributions of the galaxies is not applicable, since it does not include the contribution of AGN to dust heating. Our sample is restricted to purely star-forming galaxies on the basis of the analysis of their optical emission lines, as described in Section 5.2. However, optically-thick AGN would not be detected by the analysis of their optical emission lines. We therefore discuss the possible contamination of optically-thick AGN hosts in our sample. This question is a fair concern as the fraction of optically-selected AGN is known to increase with the total infrared luminosity (Veilleux et al. 1995; Cao et al. 2006). In addition, evidence for dust-enshrouded AGN activity has been found in some ULIRGs and LIRGs of the *IRAS* sample (Dudley & Wynn-Williams 1997; Imanishi & Dudley 2000).

In Section 5.2, we describe the selection criteria adopted to discard AGN hosts of our sample. These criteria are based on observations of the broad and narrow optical emission lines of the galaxies. However, as mentioned above this method does not prevent us from including dusty, optically-thick AGN in our sample. X-ray observations, which are less affected by extinction, would be necessary to identify this type of AGN, but they are not available for our whole sample. We hence rely on the results from previous studies of infrared galaxies to roughly estimate the contamination of our sample by AGN hosts. Elbaz et al. (2002) calculate the fraction of AGN hosts in their ISOCAM-HDFN sample supplemented by *Chandra X-ray Observatory* measurements. The sample studied by Elbaz et al. (2002) extends to much higher redshift (out to $z = 1.3$) and the total infrared luminosities of the galaxies are very similar to the values found for the galaxies in our sample. Elbaz et al. (2002) find that only 12 ± 5 per cent (5/41) of their infrared galaxies are classified as AGN hosts using *Chandra* X-ray observations. The optical spectra of the galaxies reveal that only 7 per cent (2/28) of the AGN hosts detected with *Chandra* show broad emission lines. We remind the reader that AGN hosts presenting both broad and narrow emission lines are excluded from our sample (Section 5.2). Based on these estimations, we can roughly infer that the fraction of optically-thick AGN in our sample is at most 5 per cent. Furthermore, AGN are likely to be less common in the local universe than at high redshift.

We investigate if optically-thick AGN can cause an excess of infrared emission in the galaxies of our sample (e.g. de Grijp et al. 1985; Pasquali, Kauffmann & Heckman 2005). AGN can contribute to the total infrared luminosity of their host galaxies by heating the dust in the vicinities of the active nucleus (in particular, in a dusty torus surrounding it). Using a matched sample of SDSS DR2 and *IRAS* objects, Pasquali, Kauffmann & Heckman (2005) confirm an excess in emission for the 60- and 100-μm fluxes of optically-selected AGNs. It is very likely that optically-thick AGNs display an even stronger emission in the infrared. For the most infrared luminous galaxies in our sample which are detected in the four IRAS bands, we do not find any significant excess of L_ν^{60}/L_ν^{100} and L_ν^{12}/L_ν^{25} infrared colours. Such an excess could indicate the presence of optically-thick AGN. However, we would need more detailed observations in the mid-infrared regime to definitively rule out the existence of AGN hosts in our sample (for example *Spitzer*/IRS mid-infrared spectra; see Chapter 4).

5.5.3 Comparison with the GALICS simulation

We now turn to a comparison of our results with the GALICS semi-analytic model from Hatton et al. (2003). The baseline of this model follows the now classical semi-analytic/hybrid approach, which we summarize briefly. Dark matter halo merger trees are constructed from a N-body simulation. We use here the same simulation that was used in the whole series of GALICS papers (Hatton et al. 2003; Blaizot et al. 2004, 2006). This simulation describes a cubic volume of side $100h^{-1}$ Mpc with a halo mass resolution of $\sim 1.6 \times 10^{11}$ $\mathrm{M}_\odot$. The model assumes gas to be shock-heated

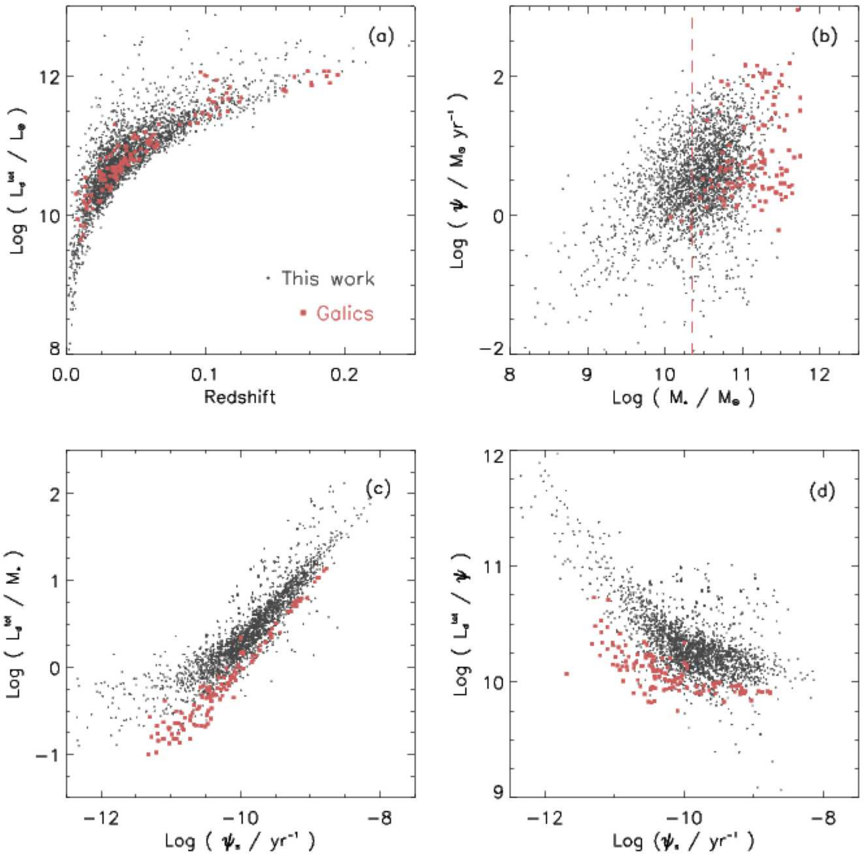

Figure 5.10: Comparison between the median-likelihood estimates for our sample (gray points) and the predictions of the GALICS simulations (red squares) for: (a) Total infrared luminosity $L_{\rm d}^{\rm tot}$ against observed redshift z; (b) Star formation rate ψ against stellar mass M_*; (c) Ratio of the total infrared luminosity to stellar mass $L_{\rm d}^{\rm tot}/M_*$ against specific star formation rate $\psi_{\rm S}$; (d) Ratio of the total infrared luminosity to star formation rate $L_{\rm d}^{\rm tot}/\psi$ against specific star formation rate $\psi_{\rm S}$.

to the virial temperature when falling into these haloes, and then lets it cool down onto galactic discs at a rate depending on its temperature and metallicity. These discs form stars at a rate given by the Kennicutt law (Kennicutt 1998a), and may expel part of their ISM due to supernovae explosions. When haloes merge, galaxies gather in the same potential wells and may merge together too, typically on a dynamical friction timescale. These mergers give birth to (or feed) the bulge and starburst components, which in turn evolve as a result of the competition between the Kennicutt law and supernova feedback. GALICS features some approximate implementation of AGN feedback to resist the over-cooling problem: gas cooling is stopped in haloes in which the bulge mass locked in galaxies is greater than $10^{11} M_\odot$. One of the specificities of the GALICS model is that it proposes predictions for the infrared emission by dust for all its galaxies. In short, the far-infrared emission of model galaxies is derived by assuming that all absorbed stellar light is re-emitted by dust. Extinction is computed as described in Hatton et al. (2003, see their section 6.2), and the spectral energy distribution of dust is then drawn from a series of templates from Devriendt, Guiderdoni & Sadat (1999) depending on the overall dust luminosity. Hatton et al. (2003) have show that this model is able to reproduce the *IRAS* luminosity functions, which we are interested in here.

To carry out the comparison of our results with GALICS we further make use of mock catalogues made with the MoMaF software (Blaizot et al. 2005). Specifically, these mocks allow us to select model galaxies on their apparent magnitudes, with $r < 17.77$ and $m_{60\mu m} < 10.4$ (corresponding to the 0.25 Jy completeness limit of *IRAS* FSC at 60 μm). This selection results in 133 objects among 51 GALICS light-cones of 1 square degree each. This number of galaxies (on average ~ 2.7 per square degree) is higher than what we observe (a rough estimate gives ~ 0.5 per square degree). However, the agreement is improved when we include all galaxies in the SDSS DR6 sample (with no selection on star formation or AGN contamination) and perform a match with *IRAS* data with a tolerance of 30 arcsec: we then find ~ 1.2 source per square degree. The remaining factor of two may in part be due to a slight overestimate of r-band counts by the GALICS model (see Blaizot et al. 2006, Fig. 2). We note that this disagreement is not a real concern for the comparison we wish to carry out in the present chapter, since our goal is to understand the properties of the selected galaxies, not their number.

We can now look at the physical properties of the model galaxies. Adjusting to the limited number of properties predicted by GALICS, we focus our investigation on the relations between (i) the total dust luminosity, (ii) the instantaneous star formation rate (averaged over only 10^6yr), and (iii) the stellar mass. Fig. 5.9 shows these relations for GALICS galaxies (red points) and our observed sample (black dots). Fig. 5.9a shows that GALICS reproduces rather well the distribution of dust luminosities that we observe from $z = 0$ to $z = 0.2$. The only possible disagreement (which has little statistical significance) is the fact that GALICS seems to have no galaxies with $L_{\rm d}^{\rm tot} < 10^9$ L$_\odot$. This is likely simply due to the selection of model galaxies. Fig. 5.9b shows the relation between stellar mass and star formation rate. Again, this plot shows a good agreement in the range where GALICS is valid, i.e. above the resolution limit indicated by the vertical dashed line. From this plot, we also see that GALICS tends to produce high-mass galaxies with lower ψ than observed. This is possibly due to the fact that GALICS star formation rates are measured over the last Myr and may often be lower than star formation rates which would be measured over a longer timescale (e.g. if the galaxy is finishing an exponential burst phase). The agreement found in Fig. 5.9a goes in this direction, since the model dust luminosity takes in ultraviolet light produced over a longer period (a few 100 Myr). Also, Fig. 5.9b seems to indicate that stellar masses of model galaxies are systematically higher than those observed (we are currently trying to understand the origin of this offset). Keeping this in mind, Figs. 5.9c and 5.9d show that the the relations between dust luminosity and star formation rate, are again in very good agreement with the galaxy sample.

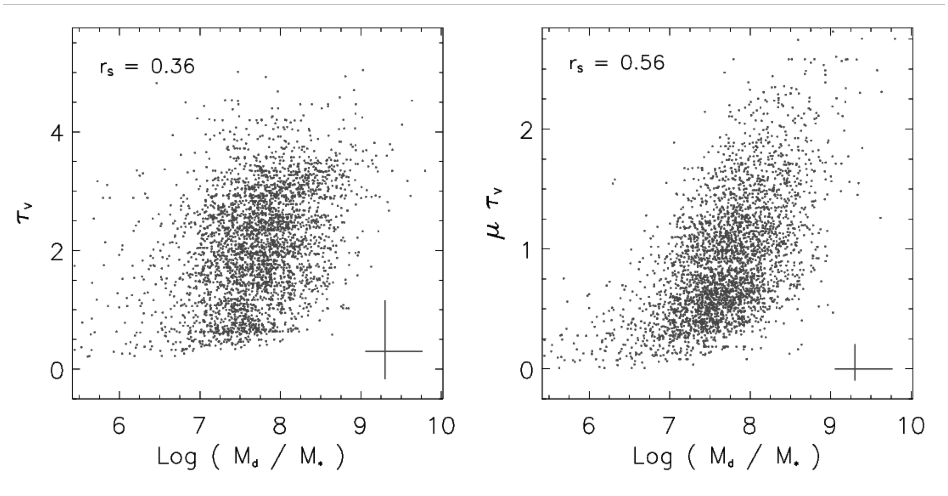

Figure 5.11: *Left panel:* median-likelihood estimate of the total effective V-band absorbtion optical depth of the dust seen by young stars inside stellar birth clouds, $\hat{\tau}_V$, against the dust mass, M_d, for the galaxies in our sample. *Right panel:* median-likelohood estimate of the effective V-band absorbtion optical depth of the dust seen by stars older than 10^7 yr in the ambient ISM, $\mu\hat{\tau}_V$, against the dust mass. The error bars represent the median confidence intervals for the estimated parameters. The Spearman rank coefficient, r_S, is indicated on the top left corner of each panel.

Overall, the agreement between GALICS predictions and our measured properties for observed galaxies is very satisfactory. This suggests that the semi-empirical description of dust emission from Hatton et al. (2003) is able to provide robust predictions for the far-infrared emission of galaxies from the local universe. The statistical results presented here, together with the model of Chapter 2, provide a new framework to model dust emission with more details and physical insight in such semi-analytic models.

5.5.4 Relation between dust mass and optical depth

It is interesting to explore the relation between the dust mass and the attenuation of stellar light in galaxies. The simple attenuation model of Charlot & Fall (2000) allows us to distinguish between the effective V-band absorption optical depth seen by young stars inside birth clouds, $\hat{\tau}_V$, and the effective V-band absorption optical depth seen by stars older than 10^7 yrs which heat the dust only in the diffuse ISM, $\mu\hat{\tau}_V$.

Stellar birth clouds are in general optically thick, and therefore the stellar continuum from young stars is practically all absorbed by dust inside these regions. As a consequence, the most effective way to probe the optical depth $\hat{\tau}_V$ seen by stars younger than 10^7 yr is to use the ratio of emission lines originating from the ionized gas surrounding OB stars inside birth clouds. The most widely-used diagnostic of this kind is the Balmer decrement Hα/Hβ. Another more indirect way of probing the amount of dust inside birth clouds is to observe the infrared emission from the galaxies. This allows one to distinguish between the emission coming from dust heated by young stars inside birth clouds, and the emission coming from dust heated by older stars in the diffuse ISM. However, this distinction is not trivial, since the emission by dust in these regions depends not only on the amount of dust (i.e. the optical depth), but also on the heating conditions, geometry and on the properties of the dust grain population. The model presented in Chapter 2 allows us to use multi-wavelength observations to statistically constrain the amount of dust in the birth clouds and in the ISM. The effective V-band optical depth seen by stars in the diffuse ISM, $\mu\hat{\tau}_V$, is well constrained using only broad-band photometric observations which probe the stellar continuum and dust emission, as in the analysis presented in this chapter. However, photometric observations alone do not allow us to derive tight constraints on the optical depth seen by young stars in birth clouds, $\hat{\tau}_V$. Constraining this parameter would require emission line observations to probe the H II regions inside the birth clouds.

In Fig. 5.11, we plot the median-likelihood estimates of the dust mass, M_d, the effective V-band absorption optical depth seen by young stars in birth clouds, $\hat{\tau}_V$, and the effective V-band absorption optical depth seen by stars in the diffuse ISM, $\mu\hat{\tau}_V$, for the galaxies in our sample. The figure shows that the correlation between $\hat{\tau}_V$ and M_d is not as strong as the correlation between $\mu\hat{\tau}_V$ and M_d. This is because we cannot estimate accurately $\hat{\tau}_V$ using only broad-band photometric observations, as discussed above. Also, the bulk of the mass of dust in galaxies is expected to reside in the diffuse ISM. Therefore, it is not surprising that the correlation of M_d with $\mu\hat{\tau}_V$ is stronger than the correlation of M_d with $\hat{\tau}_V$. Nevertheless, both the correlations shown in Fig. 5.11 between the mass of dust and the V-band absorption optical depth are statistically significant. We note that substantial scatter is introduced in these correlations are due to two main factors: (i) the large confidence intervals for M_d and $\hat{\tau}_V$, which are a result of the limited observational constraints used in the fit; (ii) the absorption optical depth does not only depend on the quantity of dust in the ISM, i.e. the total mass of dust M_d, but also on the spatial distribution of the dust in the ISM.

5.5.5 Implications for studies of galaxies at high redshifts

We now discuss the implications of our study for studies of galaxies at higher redshifts. These studies are crucial to understand the cosmic evolution of the star formation activity and ISM properties of galaxies.

We demonstrate in this chapter that the dust mass in galaxies is strongly correlated with the star formation rate. It is therefore not surprising that high-redshift, strongly star-forming objects show high dust attenuation. However, because these galaxies are younger, their metallicity is assumed to be typically lower than at $z = 0$. This can play an important role for dust particle formation, explain!!! (e.g. Engelbracht et al. 2008). If we consider both of these effects, it is not clear whether high-redshift galaxies are intrinsically more dusty than present-day galaxies. Moreover, the measurement of the dust attenuation in these objects suffers from several limitations.

Observations at high redshifts show that more distant galaxies tend to be more actively star-forming than local galaxies, and that the star formation in the Universe shows a peak around $z \simeq 2-3$. A very strong fraction of this star formation occurs in very dusty objects which contribute significantly to the observed cosmic infrared background. In a recent study, Magnelli et al. (2008) present evidence for an excess emission at 3.3 μm in 5 galaxies at $0.6 < z < 1.7$. Investigating the origin of this excess, they conclude that it likely corresponds to the 3.3-μm PAH feature, in agreement with dust model expectations. The excess also correlates with the star formation rate in the galaxies.

These findings agree with the results of our study for local galaxies. Future observations will bring more insight into the dust content of high redshift galaxies and allow to compare the relation between star formation rate and dust mass at high redshift to the one found in Fig. 5.5 for local galaxies.

5.6 Summary and conclusion

In this chapter, we have assembled a sample of ~ 3000 local galaxies with photometric observations from the far-ultraviolet to the far-infrared. These galaxies were primarily selected from the SDSS DR6 spectroscopic sample cross-correlated with *IRAS* all sky catalogues. The optical and infrared observations were supplemented with matched ultraviolet and near-infrared data from *GALEX* and 2MASS, respectively. The size of this sample represents a significant improvement over previous studies (e.g. Chapter 3). We have used the model developed in Chapter 2 to derive statistical constraints on the star formation rate, stellar mass, dust attenuation, dust luminosity, dust mass and fraction of dust luminosity contributed by dust in the diffuse ISM for all the galaxies in our sample.

The size of our sample has allowed us to investigate significant correlations between the derived physical properties of the galaxies. In particular, we find that the star formation rate correlates remarkably well with the dust mass of galaxies over four orders of magnitude in both quantities. This is in agreement with results from previous studies which suggest that more actively star-forming galaxies have higher dust contents. We quantify the relation between the star formation and dust mass of galaxies by providing a liner fit to the observed trend (equation 5.9). This can be regarded as a simple empirical recipe to estimate the total dust mass of galaxies from the star formation rate. We also find that the dust-to-stellar mass ratio, the dust mass to star formation ratio and the fraction of dust luminosity contributed by dust in the diffuse ISM correlate strongly with the specific star formation rate of the galaxies. These results confirm previous results found in Chapters 3 and 4 for smaller local galaxy samples. The higher number of galaxies in this sample has allowed us to check the significance of such correlations.

We have compared our results with the predictions of the recent chemical evolution models of Calura, Pipino & Matteucci (2008), which include the production of interstellar dust grains in the cold envelopes of evolved stars (mainly AGB stars) and in the cool ejecta of supernova, as well as the destruction of the dust grains through shock waves from supernova explosions. The predictions of this model agree quite well with the relations between specific star formation rate, dust-to-stellar mass ratio and dust mass to star formation rate that we find for our sample. We suggest that these relations may be interpreted as an evolutive sequence: as galaxies form stars during their lifetimes, their specific star formation rate decreases and their interstellar medium is enriched with dust.

Optical measurements of the axis ratio of our galaxies have allowed us to investigate possible systematic effects with inclination which could bias our results. We find that, for $b/a \lesssim 0.6$ (i.e. high inclinations), the optical SDSS selection fails to detect the stellar light from relatively dusty galaxies. This observational bias produces the most important systematic effects with inclination on the median-likelihood estimates of parameters such as the total dust luminosity and the star formation rate. In addition, for highly-inclined galaxies, the ultraviolet and optical radiation from young stellar populations is more attenuated. As a result, we underestimate the star formation rate and overestimate the contribution by dust in the diffuse ISM to the total dust luminosity in these galaxies. We note, however, that the main effect of this bias is, at most, to introduce scatter in the observed relations between physical parameters.

We have compared our results with hybrid galaxy simulation models which treat the evolution of baryons in galaxies using simple, semi-analytic recipes, the GALICS simulation (Hatton et al. 2003). We select mock galaxies from the simulations using the same criteria that were used to select the observational sample. We find that the agreement between GALICS predictions and our measured properties for observed galaxies is very satisfactory. This validates the semi-empirical recipes used in this simulation.

In general, the results of this study confirm and quantify already known relations between the star formation rate and the dust content of galaxies in the local universe. At high redshifts, these relations are more difficult to understand. On one hand, high-redshift galaxies form stars at very high rates and a big fraction of this star formation is obscured by dust. In fact, the number of galaxies for which the infrared dominates the energy output increases with redshift and reaches a maximum around $z = 2$. On the other hand, galaxies at higher redshifts are expected to have lower metallicities, and hence, less metals available to form dust grains. Future statistical studies such as the one presented here, but including galaxies at high redshifts, will become possible in the forthcoming years with space observatories such as the *Herschel Space Telescope* and the *James Webb Space Telescope*. Hopefully, these future studies will shed more light into the cosmic evolution of the dust content of galaxies. The results presented in this chapter can provide a local reference for comparison with local galaxies in such studies.

Acknowledgements

We are extremely grateful to David Schiminovich for matching our SDSS-*IRAS* sample with the latest *GALEX* data release and kindly providing us the data. We thank Jarle Brinchmann for useful discussions and for providing us the corrections to account for emission-line contamination in the optical SDSS bands. We also thank David Elbaz, Vivienne Wild and Jakob Walcher for useful discussions. We thank Francesco Calura and Antonio Pipino for providing us the data of their chemical evolution model. CE was supported by the Marie Curie EARA-EST host fellowship while this work was carried out and acknowledges the IAP for hospitality. CE is partly supported by the Swiss Sunburst Fund. EdC is financed by the EU Marie Curie Research Training Network MAGPOP.

Funding for the SDSS has been provided by the Alfred P. Sloan Foundation, the Participating Institutions, the National Science Foundation, the US Department of Energy, the National Aeronautics and Space Administration, the Japanese Monbukagakusho, the Max Planck Society, and the Higher Education Funding Council for England. The SDSS Web site is http://www.sdss.org. The SDSS is managed by the Astrophysical Research Consortium for the Participating Institutions. The Participating Institutions are the American Museum of Natural History, the Astrophysical Institute Potsdam, the University of Basel, Cambridge University, Case Western Reserve University, the University of Chicago, Drexel University, Fermilab, the Institute for Advanced Study, the Japan Participation Group, Johns Hopkins University, the Joint Institute for Nuclear Astrophysics, the Kavli Institute for Particle Astrophysics and Cosmology, the Korean Scientist Group, the Chinese Academy of Sciences, Los Alamos National Laboratory, the Max Planck Institute for Astronomy, the Max Planck Institute for Astrophysics, New Mexico State University, Ohio State University, the University of Pittsburgh, the University of Portsmouth, Princeton University, the US Naval Observatory, and the University of Washington.

CHAPTER 6

Conclusion

Studies of the light emitted by galaxies at different wavelengths are crucial to understand the formation and evolution of galaxies. We have seen in this thesis that the detailed study of the spectral energy distributions of galaxies at ultraviolet, optical and infrared wavelengths provides important information on the radiation produced by stellar populations and on how this radiation is affected by gas and dust in the interstellar medium.

In recent years, observations at different wavelengths have started to become available for large samples of galaxies. These observations include mostly local galaxies, but current and future deep surveys will provide observations of large galaxy samples at higher redshifts. Extracting constraints on the stellar populations and ISM of galaxies from these multi-wavelength observations requires the consistent modelling of the emission by stars, gas and dust.

At the starting point of this thesis, sophisticated radiative transfer models were available to compute consistently the emission from stars and dust in galaxies were available. These models are useful to interpret in detail the emission from individual galaxies in terms of constraints on stellar populations and the spatial distribution and physical properties of the dust. However, because of the complexity of radiative transfer computations, these models are not optimised to derive statistical constraints from observations of large samples of galaxies. In order to exploit the new observational surveys and set the best constraints on galaxy formation and evolution scenarios, we require a model that is optimised to interpret consistently the whole multi-wavelength emission from large samples of galaxies in terms of physical parameters, such as star formation rate, stellar mass and dust content. Our primary goal in this thesis was to build such a model.

We have developed a simple but versatile model to interpret the mid- and far-infrared spectral energy distributions of galaxies consistently with the emission at ultraviolet, optical and near-infrared wavelengths. Our model relies on the Bruzual & Charlot (2003) population synthesis code to compute the spectral evolution of stellar populations, and on the two-component model of Charlot & Fall (2000) to compute the total infrared luminosity absorbed and reradiated by dust in stellar birth clouds and in the ambient ISM. We distribute this total infrared energy in wavelength over the range from 3 to 1000 μm by considering the contributions by four main dust components: PAH emission, mid-infrared continuum emission from hot dust, warm dust with adjustable equilibrium temperature in the range 30–60 K and cold dust with adjustable equilibrium temperature in the range 15–25 K.

We keep as adjustable parameters the relative contributions by PAHs, the hot mid-infrared continuum and warm dust to the infrared luminosity of stellar birth clouds. Cold dust resides (in an adjustabe amount) only in the ambient ISM, where the relative ratios of the other three components are fixed to the values reproducing the observed mid-infrared cirrus emission of the Milky Way. We find that this minimum number of components is required to account for the infrared spectral energy distributions of galaxies in wide ranges of star formation histories.

We have shown that this simple but versatile model allows us to derive statistical estimates of physical parameters such as star formation rate, stellar mass, dust content and dust properties, from combined ultraviolet, optical and infrared galaxy spectra. To achieve this, we have adopted a Bayesian approach similar to that successfully employed by previous studies to interpret ultraviolet, optical and near-infrared galaxy spectra using only the Bruzual & Charlot (2003) and Charlot & Fall (2000) models. Using this technique, we have derived median-likelihood estimates of a set of physical parameters describing the stellar and dust contents of local star-forming galaxies from three different samples:

(i) 66 galaxies from the *Spitzer Infrared Nearby Galaxy Survey* (SINGS; Kennicutt et al. 2003), in Chapter 3;

(ii) 101 galaxies from the *Spitzer-SDSS-GALEX Spectroscopic Survey* (SSGSS; Schiminovich et. al, in preparation), in Chapter 4;

(iii) a new, larger sample of 3321 galaxies observed with *GALEX*, SDSS, 2MASS and *IRAS*, in Chapter 5.

Our model reproduces well the observed spectral energy distributions of these galaxies across the entire wavelength range from the far-ultraviolet to the far-infrared, and the star formation histories and dust contents of the galaxies are well constrained.

A main advantage provided by this model is the capacity to study the relation between different physical parameters of observed galaxies in a quantitative and statistically meaningful way. In the first two applications of this model (Chapters 3 and 4), we have found that, for example, the specific star formation rate of the star-forming galaxies correlates strongly not only with observed infrared colours, but also with several other properties of the galaxies, such as the fraction of total infrared luminosity contributed by dust in the ambient ISM, the contributions by PAHs, warm dust and cold dust to the total infrared luminosity and the ratio of dust mass to stellar mass. These correlations provide important insight into the link between star formation and ISM properties in galaxies.

To further investigate and quantify the relation between the star formation activity and the dust content of galaxies, we have assembled in Chapter 5 a large sample of 3321 galaxies with photometric observations from ultraviolet to infrared wavelengths. We have found that the star formation rate correlates remarkably well with galaxy dust mass over four orders of magnitude in both quantities. We have provided a simple empirical recipe to estimate the total dust mass of galaxies from the star formation rate. The study of this sample has also confirmed that the dust-to-stellar mass ratio, the dust mass to star formation ratio and the fraction of dust luminosity contributed by dust in the diffuse ISM all correlate strongly with the specific star formation rate of the galaxies. We have compared our results with the predictions of chemical evolution models by Calura, Pipino & Matteucci (2008) and discussed the possibility of interpreting these relations as an evolutionary sequence.

We have also compared our results with hybrid, state-of-the-art galaxy simulations in which the evolution of baryons is treated using simple, semi-analytic recipes, the GALICS simulation (Hatton et al. 2003). We have found that the agreement between the predictions of these simulations and our measured properties for observed galaxies is very satisfactory. This illustrates the usefulness of our model to test the validity of the semi-empirical recipes used in cosmological simulations.

The model developed in this thesis is optimised to interpret the spectral energy distributions of star-forming galaxies using a minimum set of free parameters. Our model does not include the potential contribution by AGNs to dust heating. This constitutes a current limitation of the model, especially because the fraction of AGN hosts is known to increase at higher redshifts. For future applications of the model to higher redshifts studies, it will be important to include the contribution by AGN to the heating of dust.

Another possible way to extend this model is to combine it with a simple prescription to compute the emission by nebular lines from ultraviolet to infrared wavelengths (such as the model of Charlot & Longhetti 2001). This would allow us to explore in more detail than what has been done so far the potential of mid- and far-infrared emission lines to constrain the physical conditions of star-forming regions in galaxies.

The model presented in this thesis should be useful to interpret data from any modern galaxy survey at ultraviolet, optical and infrared wavelengths. It can also be used to design new observations by optimizing the set of observables required to constrain specific physical parameters of galaxies.

The future *Herschel Space Telescope* and *James Webb Space Teslescope* will soon collect observations of large samples of galaxies at higher redshifts which the model presented in this thesis should be useful to interpret. The comparison of the relations linking the physical properties of galaxies at these early epochs with those identified at low redshifts will have important implications for our understanding of the physical processes that dominate galaxy evolution.

Appendix A

Physical constants

Table A.1: Physical and astronomical constants used in this thesis.

Physical constants		
Speed of light	c	2.9979×10^{10} $\mathrm{cm\,s^{-1}}$
Planck constant	h	6.6261×10^{-27} $\mathrm{erg\,s^{-1}}$
Boltzmann constant	k	1.3807×10^{-34} $\mathrm{J\,s}$
Stefan-Boltzmann constant	σ	5.6708×10^{-5} $\mathrm{erg\,cm^{-2}\,K^{-4}\,s^{-1}}$

Astronomical constants		
Solar luminosity	$\mathrm{L}_\odot$	3.839×10^{33} $\mathrm{erg\,s^{-1}}$
Solar mass	$\mathrm{M}_\odot$	1.989×10^{33} g
Parsec	pc	3.086×10^{18} cm
Jansky	Jy	10^{-23} $\mathrm{erg\,s^{-1}\,cm^{-2}\,Hz^{-1}}$

Cosmological parameters		
Total matter density	Ω_m	0.30
Cosmological constant	Ω_Λ	0.70
Hubble constant	H_0	70 $\mathrm{km\,s^{-1}\,Mpc^{-1}}$

APPENDIX B

Derived physical parameters of the SINGS galaxies

In this appendix, we list the median-likelihood estimates of several physical parameters for the galaxies of the SINGS sample derived from fits to observed ultraviolet, optical and infrared observations using the method described in Chapter 3. For each parameter, we list the estimate given by median of the likelihood distribution and the confidence interval associated with this estimate, given by the 16th–18th percentile range of the likelihood distribution.

Table B.1: Median-likelihood estimates and confidence intervals of five parameters derived for the SINGS galaxies: fraction of the total infrared luminosity contributed by dust in the ambient ISM (f_μ); fraction of the total V-band absorption optical depth of the dust contributed by the ambient ISM (μ); total effective V-band absorption optical depth of the dust ($\hat{\tau}_V$); effective V-band absorption optical depth of the dust in the ambient ISM ($\mu\hat{\tau}_V$); logarithm of the specific star formation rate (ψ_S).

Galaxy	f_μ	μ	$\hat{\tau}_V$	$\mu\hat{\tau}_V$	$\log(\psi_{\rm S}/{\rm yr}^{-1})$
NGC 0024	$0.600^{+0.090}_{-0.069}$	$0.508^{+0.105}_{-0.210}$	$0.277^{+0.150}_{-0.040}$	$0.142^{+0.035}_{-0.025}$	$-9.898^{+0.205}_{-0.242}$
NGC 0337	$0.490^{+0.053}_{-0.074}$	$0.420^{+0.207}_{-0.142}$	$0.682^{+0.185}_{-0.170}$	$0.312^{+0.010}_{-0.065}$	$-9.088^{+0.070}_{-0.200}$
NGC 0628	$0.534^{+0.101}_{-0.076}$	$0.394^{+0.202}_{-0.234}$	$0.552^{+0.515}_{-0.095}$	$0.232^{+0.065}_{-0.060}$	$-9.613^{+0.225}_{-0.225}$
NGC 0855	$0.440^{+0.095}_{-0.083}$	$0.201^{+0.214}_{-0.126}$	$0.752^{+1.460}_{-0.275}$	$0.172^{+0.030}_{-0.030}$	$-10.240^{+0.170}_{-0.120}$
NGC 0925	$0.518^{+0.079}_{-0.069}$	$0.426^{+0.207}_{-0.180}$	$0.322^{+0.140}_{-0.060}$	$0.147^{+0.030}_{-0.010}$	$-9.628^{+0.390}_{-0.175}$
NGC 1097	$0.512^{+0.040}_{-0.044}$	$0.153^{+0.162}_{-0.029}$	$2.577^{+0.835}_{-1.275}$	$0.412^{+0.055}_{-0.040}$	$-10.110^{+0.127}_{-0.110}$
NGC 1266	$0.600^{+0.045}_{-0.000}$	$0.363^{+0.156}_{-0.000}$	$5.027^{+0.000}_{-1.475}$	$1.822^{+0.040}_{-0.000}$	$-10.070^{+0.092}_{-0.000}$
NGC 1291	$0.791^{+0.025}_{-0.120}$	$0.242^{+0.000}_{-0.190}$	$0.292^{+1.240}_{-0.000}$	$0.072^{+0.005}_{-0.020}$	$-11.850^{+0.150}_{-0.000}$
NGC 1316	$0.793^{+0.005}_{-0.072}$	$0.025^{+0.015}_{-0.005}$	$2.722^{+0.235}_{-1.070}$	$0.057^{+0.025}_{-0.000}$	$-12.200^{+0.410}_{-0.000}$
NGC 1377	$0.161^{+0.002}_{-0.002}$	$0.084^{+0.000}_{-0.000}$	$4.897^{+0.000}_{-0.000}$	$0.407^{+0.000}_{-0.000}$	$-8.713^{+0.000}_{-0.000}$

Table B.1: (continued)

Galaxy	f_μ	μ	$\hat{\tau}_V$	$\mu\hat{\tau}_V$	$\log(\psi_{\rm S}/{\rm yr}^{-1})$
NGC 1482	$0.602^{+0.028}_{-0.019}$	$0.485^{+0.138}_{-0.093}$	$3.357^{+0.775}_{-0.695}$	$1.637^{+0.035}_{-0.040}$	$-9.743^{+0.195}_{-0.200}$
NGC 1512	$0.621^{+0.092}_{-0.110}$	$0.476^{+0.161}_{-0.208}$	$0.352^{+0.175}_{-0.060}$	$0.172^{+0.025}_{-0.040}$	$-10.480^{+0.230}_{-0.130}$
NGC 1566	$0.610^{+0.078}_{-0.121}$	$0.599^{+0.112}_{-0.349}$	$0.532^{+0.415}_{-0.075}$	$0.307^{+0.045}_{-0.075}$	$-9.883^{+0.145}_{-0.137}$
NGC 1705	$0.064^{+0.044}_{-0.018}$	$0.028^{+0.151}_{-0.000}$	$0.097^{+0.000}_{-0.035}$	$0.002^{+0.010}_{-0.000}$	$-9.128^{+0.410}_{-0.000}$
NGC 2403	$0.532^{+0.072}_{-0.068}$	$0.497^{+0.115}_{-0.202}$	$0.342^{+0.135}_{-0.015}$	$0.172^{+0.035}_{-0.030}$	$-9.453^{+0.380}_{-0.270}$
Holmberg II	$0.669^{+0.013}_{-0.000}$	$0.195^{+0.000}_{-0.000}$	$0.307^{+0.000}_{-0.000}$	$0.062^{+0.000}_{-0.000}$	$-8.443^{+0.000}_{-0.000}$
DDO 053	$0.301^{+0.052}_{-0.086}$	$0.340^{+0.014}_{-0.129}$	$0.152^{+0.020}_{-0.010}$	$0.052^{+0.010}_{-0.020}$	$-9.023^{+0.040}_{-0.435}$
NGC 2798	$0.483^{+0.027}_{-0.034}$	$0.362^{+0.129}_{-0.098}$	$3.192^{+1.200}_{-0.815}$	$1.167^{+0.060}_{-0.045}$	$-9.303^{+0.145}_{-0.120}$
NGC 2841	$0.737^{+0.070}_{-0.058}$	$0.309^{+0.140}_{-0.206}$	$0.642^{+1.070}_{-0.185}$	$0.182^{+0.030}_{-0.010}$	$-11.020^{+0.050}_{-0.190}$
NGC 2915	$0.558^{+0.000}_{-0.156}$	$0.744^{+0.000}_{-0.289}$	$0.097^{+0.010}_{-0.000}$	$0.072^{+0.000}_{-0.025}$	$-9.753^{+0.195}_{-0.000}$
Holmberg I	$0.711^{+0.106}_{-0.163}$	$0.227^{+0.446}_{-0.168}$	$0.307^{+0.630}_{-0.240}$	$0.057^{+0.015}_{-0.010}$	$-8.698^{+0.205}_{-0.310}$
NGC 2976	$0.524^{+0.089}_{-0.072}$	$0.208^{+0.225}_{-0.096}$	$1.302^{+1.200}_{-0.590}$	$0.287^{+0.060}_{-0.035}$	$-9.983^{+0.230}_{-0.237}$
NGC 3049	$0.392^{+0.049}_{-0.060}$	$0.281^{+0.134}_{-0.129}$	$0.997^{+0.680}_{-0.265}$	$0.282^{+0.045}_{-0.060}$	$-9.318^{+0.105}_{-0.160}$
NGC 3031	$0.696^{+0.072}_{-0.070}$	$0.411^{+0.159}_{-0.161}$	$0.322^{+0.140}_{-0.055}$	$0.122^{+0.030}_{-0.010}$	$-10.900^{+0.040}_{-0.100}$
NGC 3190	$0.911^{+0.026}_{-0.027}$	$0.297^{+0.257}_{-0.152}$	$1.152^{+1.545}_{-0.475}$	$0.347^{+0.025}_{-0.010}$	$-11.740^{+0.140}_{-0.200}$
NGC 3184	$0.698^{+0.088}_{-0.105}$	$0.335^{+0.283}_{-0.201}$	$1.017^{+1.305}_{-0.590}$	$0.312^{+0.095}_{-0.105}$	$-10.260^{+0.417}_{-0.480}$
NGC 3198	$0.396^{+0.053}_{-0.041}$	$0.068^{+0.017}_{-0.001}$	$2.342^{+1.240}_{-0.140}$	$0.197^{+0.040}_{-0.050}$	$-9.963^{+0.485}_{-0.157}$
IC 2574	$0.360^{+0.000}_{-0.021}$	$0.487^{+0.000}_{-0.000}$	$0.092^{+0.000}_{-0.000}$	$0.047^{+0.000}_{-0.000}$	$-8.188^{+0.000}_{-0.000}$
NGC 3265	$0.485^{+0.034}_{-0.038}$	$0.317^{+0.113}_{-0.070}$	$1.942^{+0.445}_{-0.465}$	$0.637^{+0.025}_{-0.030}$	$-9.733^{+0.075}_{-0.085}$
Mrk 33	$0.256^{+0.035}_{-0.028}$	$0.156^{+0.000}_{-0.000}$	$1.817^{+0.000}_{-0.225}$	$0.282^{+0.000}_{-0.000}$	$-9.058^{+0.140}_{-0.000}$
NGC 3351	$0.473^{+0.064}_{-0.042}$	$0.115^{+0.023}_{-0.027}$	$2.262^{+0.705}_{-0.155}$	$0.252^{+0.080}_{-0.010}$	$-10.150^{+0.070}_{-0.140}$
NGC 3521	$0.675^{+0.041}_{-0.046}$	$0.267^{+0.137}_{-0.087}$	$1.842^{+0.750}_{-0.615}$	$0.492^{+0.055}_{-0.025}$	$-10.350^{+0.090}_{-0.080}$
NGC 3621	$0.543^{+0.096}_{-0.091}$	$0.592^{+0.147}_{-0.226}$	$0.527^{+0.110}_{-0.080}$	$0.322^{+0.030}_{-0.095}$	$-9.608^{+0.175}_{-0.180}$
NGC 3627	$0.613^{+0.063}_{-0.063}$	$0.249^{+0.261}_{-0.105}$	$1.937^{+1.555}_{-0.970}$	$0.502^{+0.035}_{-0.040}$	$-10.170^{+0.217}_{-0.150}$
NGC 3773	$0.400^{+0.063}_{-0.122}$	$0.517^{+0.122}_{-0.348}$	$0.302^{+0.130}_{-0.020}$	$0.152^{+0.040}_{-0.060}$	$-9.038^{+0.055}_{-0.100}$
NGC 3938	$0.541^{+0.085}_{-0.083}$	$0.395^{+0.114}_{-0.243}$	$0.627^{+0.745}_{-0.125}$	$0.257^{+0.035}_{-0.075}$	$-9.778^{+0.195}_{-0.135}$
NGC 4125	$0.905^{+0.040}_{-0.217}$	$0.024^{+0.011}_{-0.004}$	$2.247^{+0.000}_{-1.215}$	$0.042^{+0.010}_{-0.010}$	$-11.820^{+0.205}_{-1.090}$
NGC 4236	$0.473^{+0.063}_{-0.069}$	$0.563^{+0.130}_{-0.135}$	$0.142^{+0.010}_{-0.025}$	$0.077^{+0.025}_{-0.025}$	$-8.738^{+0.165}_{-0.250}$
NGC 4254	$0.450^{+0.065}_{-0.052}$	$0.229^{+0.036}_{-0.082}$	$1.802^{+0.395}_{-0.340}$	$0.387^{+0.100}_{-0.070}$	$-9.473^{+0.140}_{-0.115}$

Table B.1: (continued)

Galaxy	f_μ	μ	$\hat{\tau}_V$	$\mu\hat{\tau}_V$	$\log(\psi_\mathrm{S}/\mathrm{yr}^{-1})$
NGC 4321	$0.579^{+0.059}_{-0.040}$	$0.123^{+0.044}_{-0.010}$	$3.257^{+0.245}_{-0.945}$	$0.387^{+0.045}_{-0.020}$	$-10.050^{+0.297}_{-0.280}$
NGC 4450	$0.873^{+0.048}_{-0.043}$	$0.181^{+0.252}_{-0.099}$	$0.857^{+1.420}_{-0.495}$	$0.157^{+0.025}_{-0.030}$	$-11.610^{+0.180}_{-0.350}$
NGC 4536	$0.462^{+0.058}_{-0.051}$	$0.193^{+0.117}_{-0.075}$	$2.372^{+1.470}_{-0.945}$	$0.447^{+0.055}_{-0.035}$	$-9.663^{+0.125}_{-0.195}$
NGC 4559	$0.559^{+0.083}_{-0.063}$	$0.517^{+0.163}_{-0.289}$	$0.327^{+0.155}_{-0.005}$	$0.202^{+0.020}_{-0.065}$	$-9.748^{+0.485}_{-0.135}$
NGC 4569	$0.764^{+0.025}_{-0.046}$	$0.089^{+0.057}_{-0.021}$	$3.612^{+0.695}_{-1.810}$	$0.317^{+0.005}_{-0.040}$	$-11.130^{+0.170}_{-0.000}$
NGC 4579	$0.756^{+0.073}_{-0.062}$	$0.235^{+0.260}_{-0.146}$	$0.872^{+1.635}_{-0.380}$	$0.217^{+0.035}_{-0.015}$	$-11.080^{+0.140}_{-0.180}$
NGC 4594	$0.922^{+0.035}_{-0.045}$	$0.055^{+0.041}_{-0.012}$	$2.032^{+0.885}_{-1.200}$	$0.107^{+0.015}_{-0.030}$	$-12.320^{+0.200}_{-0.260}$
NGC 4625	$0.368^{+0.022}_{-0.031}$	$0.150^{+0.000}_{-0.000}$	$0.942^{+0.000}_{-0.000}$	$0.142^{+0.000}_{-0.000}$	$-9.613^{+0.000}_{-0.000}$
NGC 4631	$0.465^{+0.056}_{-0.063}$	$0.239^{+0.224}_{-0.102}$	$1.707^{+1.405}_{-0.745}$	$0.422^{+0.065}_{-0.045}$	$-9.243^{+0.120}_{-0.170}$
NGC 4725	$0.758^{+0.047}_{-0.056}$	$0.526^{+0.076}_{-0.127}$	$0.322^{+0.100}_{-0.045}$	$0.167^{+0.020}_{-0.025}$	$-10.870^{+0.160}_{-0.100}$
NGC 4736	$0.422^{+0.029}_{-0.051}$	$0.094^{+0.000}_{-0.000}$	$1.992^{+0.000}_{-0.000}$	$0.187^{+0.000}_{-0.000}$	$-10.310^{+0.000}_{-0.000}$
NGC 4826	$0.780^{+0.059}_{-0.046}$	$0.171^{+0.238}_{-0.060}$	$1.612^{+0.820}_{-1.000}$	$0.267^{+0.035}_{-0.020}$	$-11.030^{+0.160}_{-0.230}$
NGC 5033	$0.612^{+0.103}_{-0.092}$	$0.336^{+0.274}_{-0.176}$	$1.327^{+1.540}_{-0.660}$	$0.427^{+0.130}_{-0.110}$	$-10.040^{+0.247}_{-0.290}$
NGC 5055	$0.691^{+0.056}_{-0.060}$	$0.272^{+0.255}_{-0.134}$	$1.497^{+1.650}_{-0.635}$	$0.422^{+0.040}_{-0.040}$	$-10.450^{+0.240}_{-0.150}$
NGC 5194	$0.435^{+0.019}_{-0.025}$	$0.136^{+0.002}_{-0.007}$	$2.197^{+0.060}_{-0.285}$	$0.287^{+0.015}_{-0.025}$	$-9.538^{+0.045}_{-0.035}$
NGC 5195	$0.731^{+0.009}_{-0.029}$	$0.069^{+0.117}_{-0.004}$	$3.812^{+0.920}_{-2.790}$	$0.272^{+0.035}_{-0.080}$	$-11.340^{+0.160}_{-0.080}$
Tololo 89	$0.340^{+0.065}_{-0.076}$	$0.435^{+0.088}_{-0.153}$	$0.257^{+0.030}_{-0.020}$	$0.107^{+0.030}_{-0.035}$	$-8.938^{+0.080}_{-0.175}$
NGC 5408	$0.173^{+0.017}_{-0.035}$	$0.331^{+0.000}_{-0.044}$	$0.092^{+0.000}_{-0.015}$	$0.027^{+0.000}_{-0.005}$	$-8.103^{+0.045}_{-0.000}$
NGC 5474	$0.709^{+0.072}_{-0.083}$	$0.312^{+0.232}_{-0.101}$	$0.407^{+0.320}_{-0.075}$	$0.127^{+0.050}_{-0.000}$	$-9.353^{+0.900}_{-0.000}$
NGC 5713	$0.547^{+0.069}_{-0.054}$	$0.328^{+0.183}_{-0.104}$	$2.142^{+0.995}_{-0.805}$	$0.702^{+0.025}_{-0.055}$	$-9.678^{+0.270}_{-0.322}$
NGC 5866	$0.958^{+0.022}_{-0.034}$	$0.225^{+0.322}_{-0.133}$	$0.937^{+1.625}_{-0.555}$	$0.212^{+0.020}_{-0.010}$	$-12.190^{+0.100}_{-0.260}$
IC 4710	$0.343^{+0.067}_{-0.100}$	$0.468^{+0.161}_{-0.243}$	$0.112^{+0.070}_{-0.020}$	$0.047^{+0.045}_{-0.020}$	$-8.558^{+0.040}_{-0.310}$
NGC 6822	$0.405^{+0.049}_{-0.022}$	$0.493^{+0.082}_{-0.079}$	$0.182^{+0.010}_{-0.005}$	$0.092^{+0.005}_{-0.020}$	$-8.818^{+0.055}_{-0.150}$
NGC 6946	$0.571^{+0.136}_{-0.095}$	$0.693^{+0.207}_{-0.107}$	$0.712^{+0.105}_{-0.130}$	$0.477^{+0.165}_{-0.075}$	$-9.673^{+0.150}_{-0.497}$
NGC 7331	$0.635^{+0.053}_{-0.051}$	$0.270^{+0.268}_{-0.114}$	$2.067^{+1.395}_{-0.965}$	$0.582^{+0.030}_{-0.050}$	$-10.380^{+0.160}_{-0.110}$
NGC 7552	$0.470^{+0.022}_{-0.022}$	$0.310^{+0.141}_{-0.079}$	$2.857^{+1.255}_{-0.665}$	$0.942^{+0.050}_{-0.045}$	$-9.263^{+0.100}_{-0.210}$
NGC 7793	$0.518^{+0.150}_{-0.015}$	$0.426^{+0.071}_{-0.198}$	$0.462^{+0.310}_{-0.140}$	$0.177^{+0.030}_{-0.040}$	$-8.988^{+0.095}_{-0.815}$

Table B.2: Median-likelihood estimates and confidence intervals of three more parameters derived for the SINGS galaxies: logarithm of the stellar mass (M_*); logarithm of the dust mass (M_d); and logarithm of the total dust luminosity ($L_\mathrm{d}^\mathrm{tot}$).

Galaxy	$\log(M_*/M_\odot)$	$\log(M_\mathrm{d}/M_\odot)$	$\log(L_\mathrm{d}^\mathrm{tot}/L_\odot)$
NGC 0024	$8.897^{+0.190}_{-0.110}$	$6.267^{+0.265}_{-0.250}$	$8.787^{+0.030}_{-0.035}$
NGC 0337	$9.492^{+0.085}_{-0.060}$	$7.347^{+0.265}_{-0.195}$	$10.290^{+0.020}_{-0.010}$
NGC 0628	$9.957^{+0.173}_{-0.160}$	$7.887^{+0.175}_{-0.275}$	$10.270^{+0.040}_{-0.030}$
NGC 0855	$8.847^{+0.115}_{-0.160}$	$5.507^{+0.360}_{-0.105}$	$8.607^{+0.020}_{-0.025}$
NGC 0925	$9.512^{+0.150}_{-0.305}$	$7.367^{+0.195}_{-0.440}$	$9.707^{+0.035}_{-0.030}$
NGC 1097	$10.830^{+0.110}_{-0.110}$	$8.327^{+0.100}_{-0.330}$	$10.800^{+0.020}_{-0.020}$
NGC 1266	$10.240^{+0.000}_{-0.110}$	$7.222^{+0.000}_{-0.030}$	$10.450^{+0.010}_{-0.000}$
NGC 1291	$10.870^{+0.070}_{-0.010}$	$6.882^{+0.190}_{-0.135}$	$9.437^{+0.010}_{-0.070}$
NGC 1316	$11.600^{+0.080}_{-0.230}$	$7.187^{+0.080}_{-0.090}$	$10.060^{+0.050}_{-0.010}$
NGC 1377	$8.977^{+0.005}_{-0.000}$	$6.547^{+0.000}_{-0.315}$	$10.180^{+0.000}_{-0.000}$
NGC 1482	$10.120^{+0.180}_{-0.143}$	$7.457^{+0.085}_{-0.040}$	$10.660^{+0.020}_{-0.010}$
NGC 1512	$9.952^{+0.128}_{-0.180}$	$6.917^{+0.240}_{-0.265}$	$9.447^{+0.020}_{-0.025}$
NGC 1566	$10.480^{+0.080}_{-0.130}$	$7.902^{+0.290}_{-0.180}$	$10.600^{+0.030}_{-0.020}$
NGC 1705	$8.072^{+0.020}_{-0.540}$	$4.797^{+0.285}_{-0.140}$	$7.992^{+0.010}_{-0.015}$
NGC 2403	$9.202^{+0.115}_{-0.205}$	$6.902^{+0.370}_{-0.185}$	$9.562^{+0.040}_{-0.020}$
Holmberg II	$8.027^{+0.000}_{-0.010}$	$4.702^{+0.035}_{-0.000}$	$7.962^{+0.000}_{-0.010}$
DDO 053	$6.536^{+0.000}_{-0.500}$	$3.922^{+0.455}_{-0.235}$	$7.087^{+0.015}_{-0.030}$
NGC 2798	$9.732^{+0.105}_{-0.100}$	$7.287^{+0.090}_{-0.095}$	$10.560^{+0.020}_{-0.020}$
NGC 2841	$10.530^{+0.130}_{-0.060}$	$7.457^{+0.160}_{-0.230}$	$9.752^{+0.030}_{-0.030}$
NGC 2915	$7.647^{+0.000}_{-0.175}$	$3.982^{+0.275}_{-0.000}$	$7.327^{+0.025}_{-0.000}$
Holmberg I	$6.819^{+0.000}_{-0.500}$	$4.437^{+0.250}_{-0.345}$	$7.102^{+0.050}_{-0.085}$
NGC 2976	$8.842^{+0.160}_{-0.225}$	$6.192^{+0.360}_{-0.195}$	$8.932^{+0.020}_{-0.030}$
NGC 3049	$8.987^{+0.095}_{-0.080}$	$6.727^{+0.215}_{-0.215}$	$9.592^{+0.020}_{-0.015}$

Table B.2: (continued)

Galaxy	$\log(M_*/M_\odot)$	$\log(M_\mathrm{d}/M_\odot)$	$\log(L_\mathrm{d}^\mathrm{tot}/L_\odot)$
NGC 3031	$10.520^{+0.100}_{-0.070}$	$7.182^{+0.350}_{-0.230}$	$9.672^{+0.015}_{-0.055}$
NGC 3190	$10.510^{+0.080}_{-0.060}$	$6.847^{+0.105}_{-0.090}$	$9.732^{+0.035}_{-0.010}$
NGC 3184	$9.872^{+0.138}_{-0.270}$	$7.342^{+0.255}_{-0.240}$	$9.757^{+0.030}_{-0.035}$
NGC 3198	$9.572^{+0.115}_{-0.470}$	$7.172^{+0.150}_{-0.155}$	$9.617^{+0.010}_{-0.050}$
IC 2574	$7.062^{+0.000}_{-0.000}$	$5.682^{+0.000}_{-0.275}$	$8.257^{+0.000}_{-0.000}$
NGC 3265	$9.127^{+0.035}_{-0.110}$	$6.167^{+0.095}_{-0.025}$	$9.477^{+0.015}_{-0.015}$
Mrk 33	$8.922^{+0.005}_{-0.040}$	$6.547^{+0.325}_{-0.180}$	$9.817^{+0.010}_{-0.010}$
NGC 3351	$9.992^{+0.088}_{-0.065}$	$7.322^{+0.275}_{-0.340}$	$9.887^{+0.040}_{-0.030}$
NGC 3521	$10.480^{+0.060}_{-0.070}$	$7.822^{+0.250}_{-0.195}$	$10.360^{+0.030}_{-0.030}$
NGC 3621	$9.527^{+0.180}_{-0.135}$	$7.247^{+0.265}_{-0.240}$	$9.847^{+0.025}_{-0.025}$
NGC 3627	$10.360^{+0.130}_{-0.160}$	$7.647^{+0.235}_{-0.260}$	$10.410^{+0.020}_{-0.030}$
NGC 3773	$8.187^{+0.080}_{-0.035}$	$5.807^{+0.375}_{-0.195}$	$8.867^{+0.025}_{-0.030}$
NGC 3938	$9.702^{+0.110}_{-0.170}$	$7.537^{+0.195}_{-0.250}$	$9.947^{+0.015}_{-0.030}$
NGC 4125	$10.930^{+0.090}_{-0.090}$	$6.207^{+0.090}_{-0.090}$	$9.217^{+0.030}_{-0.030}$
NGC 4236	$7.727^{+0.170}_{-0.145}$	$5.867^{+0.210}_{-0.190}$	$8.492^{+0.020}_{-0.020}$
NGC 4254	$10.300^{+0.080}_{-0.070}$	$8.307^{+0.215}_{-0.195}$	$10.880^{+0.020}_{-0.030}$
NGC 4321	$10.720^{+0.190}_{-0.270}$	$8.352^{+0.145}_{-0.245}$	$10.820^{+0.030}_{-0.030}$
NGC 4450	$10.790^{+0.070}_{-0.140}$	$7.332^{+0.190}_{-0.190}$	$9.812^{+0.025}_{-0.040}$
NGC 4536	$10.390^{+0.200}_{-0.100}$	$7.902^{+0.350}_{-0.190}$	$10.820^{+0.020}_{-0.030}$
NGC 4559	$9.822^{+0.055}_{-0.480}$	$7.462^{+0.300}_{-0.305}$	$9.932^{+0.035}_{-0.025}$
NGC 4569	$10.950^{+0.020}_{-0.070}$	$7.757^{+0.265}_{-0.405}$	$10.370^{+0.020}_{-0.100}$
NGC 4579	$10.960^{+0.080}_{-0.110}$	$7.697^{+0.170}_{-0.175}$	$10.230^{+0.030}_{-0.020}$
NGC 4594	$11.470^{+0.020}_{-0.110}$	$7.387^{+0.165}_{-0.120}$	$9.917^{+0.030}_{-0.010}$
NGC 4625	$8.527^{+0.000}_{-0.000}$	$6.427^{+0.050}_{-0.000}$	$8.852^{+0.000}_{-0.005}$
NGC 4631	$9.732^{+0.115}_{-0.100}$	$7.892^{+0.345}_{-0.275}$	$10.510^{+0.030}_{-0.030}$
NGC 4725	$10.930^{+0.090}_{-0.150}$	$7.967^{+0.145}_{-0.075}$	$10.190^{+0.020}_{-0.040}$
NGC 4736	$10.190^{+0.000}_{-0.020}$	$7.107^{+0.260}_{-0.305}$	$9.877^{+0.010}_{-0.010}$
NGC 4826	$10.210^{+0.150}_{-0.120}$	$6.602^{+0.110}_{-0.065}$	$9.667^{+0.020}_{-0.020}$
NGC 5033	$10.180^{+0.170}_{-0.170}$	$7.642^{+0.275}_{-0.225}$	$10.270^{+0.030}_{-0.020}$

Table B.2: (continued)

Galaxy	$\log(M_*/M_\odot)$	$\log(M_\mathrm{d}/M_\odot)$	$\log(L_\mathrm{d}^\mathrm{tot}/L_\odot)$
NGC 5055	$10.490^{+0.130}_{-0.200}$	$7.862^{+0.185}_{-0.230}$	$10.330^{+0.020}_{-0.030}$
NGC 5194	$10.140^{+0.020}_{-0.080}$	$8.017^{+0.260}_{-0.130}$	$10.600^{+0.010}_{-0.030}$
NGC 5195	$10.270^{+0.060}_{-0.110}$	$6.257^{+0.025}_{-0.065}$	$9.432^{+0.015}_{-0.060}$
Tololo 89	$8.417^{+0.255}_{-0.055}$	$6.307^{+0.325}_{-0.245}$	$9.167^{+0.015}_{-0.025}$
NGC 5408	$7.108^{+0.000}_{-0.500}$	$5.147^{+0.240}_{-0.535}$	$8.247^{+0.020}_{-0.015}$
NGC 5474	$8.297^{+0.025}_{-0.110}$	$5.842^{+0.200}_{-0.125}$	$8.712^{+0.015}_{-0.015}$
NGC 5713	$10.240^{+0.220}_{-0.220}$	$7.672^{+0.180}_{-0.150}$	$10.710^{+0.030}_{-0.010}$
NGC 5866	$10.510^{+0.100}_{-0.060}$	$6.577^{+0.095}_{-0.085}$	$9.572^{+0.015}_{-0.020}$
IC 4710	$7.757^{+0.125}_{-0.040}$	$5.782^{+0.315}_{-0.320}$	$8.642^{+0.020}_{-0.030}$
NGC 6822	$7.137^{+0.045}_{-0.005}$	$5.387^{+0.025}_{-0.005}$	$7.797^{+0.030}_{-0.005}$
NGC 6946	$10.050^{+0.290}_{-0.153}$	$7.602^{+0.225}_{-0.180}$	$10.370^{+0.020}_{-0.020}$
NGC 7331	$10.940^{+0.090}_{-0.130}$	$8.012^{+0.325}_{-0.225}$	$10.770^{+0.030}_{-0.040}$
NGC 7552	$10.210^{+0.140}_{-0.070}$	$7.922^{+0.205}_{-0.075}$	$11.060^{+0.010}_{-0.020}$
NGC 7793	$8.762^{+0.305}_{-0.255}$	$6.832^{+0.155}_{-0.470}$	$9.122^{+0.025}_{-0.035}$

Table B.3: Median-likelihood estimates and confidence intervals of six more parameters derived for the SINGS galaxies: global contributions (i.e. including stellar birth clouds and the ambient ISM) by PAHs ($\xi_{\rm PAH}^{\rm tot}$), the hot mid-infrared continuum ($\xi_{\rm MIR}^{\rm tot}$) and warm dust in thermal equilibrium ($\xi_{\rm W}^{\rm tot}$) to the total infrared luminosity; equilibrium temperature of warm dust in stellar birth clouds ($T_{\rm W}^{\rm BC}$); contribution by cold dust in thermal equilibrium to the total infrared luminosity ($\xi_{\rm C}^{\rm tot}$); and equilibrium temperature of cold dust in the ambient ISM ($T_{\rm C}^{\rm ISM}$).

Galaxy	$\xi_{\rm PAH}^{\rm tot}$	$\xi_{\rm MIR}^{\rm tot}$	$\xi_{\rm W}^{\rm tot}$	$T_{\rm W}^{\rm BC}$	$\xi_{\rm C}^{\rm tot}$	$T_{\rm C}^{\rm ISM}$
NGC0024	$0.104^{+0.040}_{-0.033}$	$0.081^{+0.030}_{-0.032}$	$0.292^{+0.067}_{-0.067}$	$43.2^{+6.8}_{-9.3}$	$0.521^{+0.119}_{-0.109}$	$18.0^{+2.3}_{-2.0}$
NGC0337	$0.084^{+0.031}_{-0.025}$	$0.055^{+0.031}_{-0.019}$	$0.455^{+0.081}_{-0.094}$	$49.5^{+2.9}_{-2.4}$	$0.405^{+0.084}_{-0.086}$	$20.5^{+2.4}_{-2.4}$
NGC0628	$0.131^{+0.048}_{-0.037}$	$0.124^{+0.031}_{-0.043}$	$0.315^{+0.081}_{-0.056}$	$43.9^{+8.6}_{-11.7}$	$0.429^{+0.129}_{-0.106}$	$17.0^{+1.8}_{-1.8}$
NGC0855	$0.061^{+0.032}_{-0.019}$	$0.027^{+0.011}_{-0.014}$	$0.535^{+0.188}_{-0.135}$	$49.7^{+3.6}_{-2.0}$	$0.385^{+0.139}_{-0.098}$	$21.3^{+2.0}_{-3.5}$
NGC0925	$0.085^{+0.026}_{-0.029}$	$0.094^{+0.027}_{-0.034}$	$0.338^{+0.058}_{-0.078}$	$42.6^{+7.5}_{-7.4}$	$0.483^{+0.076}_{-0.119}$	$16.3^{+3.3}_{-1.1}$
NGC1097	$0.095^{+0.016}_{-0.020}$	$0.047^{+0.018}_{-0.010}$	$0.428^{+0.047}_{-0.054}$	$54.7^{+3.2}_{-1.5}$	$0.422^{+0.052}_{-0.057}$	$17.2^{+2.2}_{-0.8}$
NGC1266	$0.018^{+0.001}_{-0.002}$	$0.048^{+0.021}_{-0.000}$	$0.416^{+0.046}_{-0.017}$	$53.8^{+1.1}_{-0.0}$	$0.518^{+0.059}_{-0.012}$	$23.6^{+0.7}_{-0.0}$
NGC1291	$0.109^{+0.017}_{-0.032}$	$0.051^{+0.043}_{-0.013}$	$0.205^{+0.041}_{-0.051}$	$55.9^{+1.9}_{-2.2}$	$0.634^{+0.074}_{-0.078}$	$18.4^{+1.1}_{-0.9}$
NGC1316	$0.090^{+0.016}_{-0.010}$	$0.038^{+0.003}_{-0.003}$	$0.266^{+0.008}_{-0.027}$	$59.1^{+0.5}_{-2.5}$	$0.604^{+0.012}_{-0.057}$	$21.2^{+0.9}_{-0.6}$
NGC1377	$0.130^{+0.004}_{-0.015}$	$0.170^{+0.048}_{-0.007}$	$0.649^{+0.022}_{-0.043}$	$59.8^{+0.0}_{-1.5}$	$0.050^{+0.003}_{-0.004}$	$19.5^{+4.1}_{-0.0}$
NGC1482	$0.105^{+0.007}_{-0.017}$	$0.074^{+0.015}_{-0.017}$	$0.430^{+0.043}_{-0.015}$	$59.0^{+0.6}_{-1.1}$	$0.391^{+0.031}_{-0.004}$	$24.0^{+0.1}_{-1.1}$
NGC1512	$0.122^{+0.036}_{-0.036}$	$0.106^{+0.036}_{-0.024}$	$0.253^{+0.055}_{-0.077}$	$37.1^{+9.5}_{-5.8}$	$0.524^{+0.110}_{-0.110}$	$17.8^{+2.9}_{-1.7}$
NGC1566	$0.114^{+0.038}_{-0.039}$	$0.115^{+0.041}_{-0.050}$	$0.287^{+0.088}_{-0.072}$	$46.4^{+10.0}_{-9.3}$	$0.485^{+0.129}_{-0.121}$	$19.1^{+2.1}_{-2.5}$
NGC1705	$0.021^{+0.011}_{-0.011}$	$0.127^{+0.057}_{-0.044}$	$0.770^{+0.351}_{-0.252}$	$32.2^{+4.6}_{-0.7}$	$0.091^{+0.043}_{-0.032}$	$20.8^{+4.1}_{-3.9}$
NGC2403	$0.097^{+0.038}_{-0.023}$	$0.109^{+0.031}_{-0.031}$	$0.351^{+0.072}_{-0.085}$	$41.1^{+7.5}_{-5.8}$	$0.441^{+0.112}_{-0.116}$	$18.7^{+1.6}_{-2.9}$
HolII	$0.018^{+0.005}_{-0.000}$	$0.013^{+0.019}_{-0.000}$	$0.379^{+0.017}_{-0.024}$	$57.9^{+0.0}_{-0.5}$	$0.590^{+0.026}_{-0.000}$	$24.3^{+0.0}_{-0.2}$
DDO053	$0.029^{+0.021}_{-0.011}$	$0.080^{+0.084}_{-0.058}$	$0.611^{+0.203}_{-0.163}$	$50.0^{+2.3}_{-6.4}$	$0.266^{+0.085}_{-0.069}$	$20.8^{+3.0}_{-4.0}$
NGC2798	$0.071^{+0.029}_{-0.014}$	$0.079^{+0.025}_{-0.036}$	$0.526^{+0.055}_{-0.085}$	$57.8^{+1.3}_{-2.0}$	$0.321^{+0.066}_{-0.076}$	$23.3^{+1.1}_{-1.1}$
NGC2841	$0.129^{+0.029}_{-0.043}$	$0.088^{+0.033}_{-0.017}$	$0.160^{+0.051}_{-0.044}$	$41.6^{+10.4}_{-8.8}$	$0.621^{+0.103}_{-0.068}$	$17.0^{+1.8}_{-1.1}$
NGC2915	$0.024^{+0.000}_{-0.010}$	$0.014^{+0.000}_{-0.006}$	$0.480^{+0.012}_{-0.190}$	$52.7^{+0.0}_{-2.7}$	$0.483^{+0.000}_{-0.194}$	$24.7^{+0.0}_{-3.1}$
HolI	$0.057^{+0.032}_{-0.021}$	$0.082^{+0.071}_{-0.033}$	$0.240^{+0.073}_{-0.111}$	$38.4^{+15.3}_{-7.5}$	$0.619^{+0.168}_{-0.168}$	$19.3^{+2.3}_{-2.2}$

Table B.3: (continued)

Galaxy	$\xi^{\mathrm{tot}}_{\mathrm{PAH}}$	$\xi^{\mathrm{tot}}_{\mathrm{MIR}}$	$\xi^{\mathrm{tot}}_{\mathrm{W}}$	$T^{\mathrm{BC}}_{\mathrm{W}}$	$\xi^{\mathrm{tot}}_{\mathrm{C}}$	$T^{\mathrm{ISM}}_{\mathrm{C}}$
NGC2976	$0.093^{+0.046}_{-0.023}$	$0.104^{+0.031}_{-0.056}$	$0.353^{+0.094}_{-0.086}$	$42.6^{+8.4}_{-6.5}$	$0.449^{+0.120}_{-0.110}$	$19.3^{+1.8}_{-3.0}$
NGC3049	$0.089^{+0.039}_{-0.031}$	$0.075^{+0.060}_{-0.032}$	$0.517^{+0.123}_{-0.103}$	$56.8^{+1.9}_{-3.0}$	$0.305^{+0.076}_{-0.064}$	$19.0^{+2.0}_{-2.0}$
NGC3031	$0.139^{+0.048}_{-0.041}$	$0.083^{+0.022}_{-0.026}$	$0.221^{+0.054}_{-0.061}$	$38.4^{+9.5}_{-6.0}$	$0.558^{+0.101}_{-0.090}$	$18.3^{+1.6}_{-2.7}$
NGC3190	$0.124^{+0.026}_{-0.013}$	$0.094^{+0.027}_{-0.025}$	$0.099^{+0.030}_{-0.052}$	$46.8^{+8.4}_{-9.8}$	$0.682^{+0.061}_{-0.059}$	$22.4^{+0.9}_{-0.9}$
NGC3184	$0.135^{+0.042}_{-0.037}$	$0.107^{+0.033}_{-0.037}$	$0.233^{+0.055}_{-0.062}$	$41.2^{+11.3}_{-8.6}$	$0.526^{+0.129}_{-0.125}$	$17.2^{+2.0}_{-1.6}$
NGC3198	$0.102^{+0.037}_{-0.025}$	$0.157^{+0.032}_{-0.015}$	$0.366^{+0.079}_{-0.039}$	$37.4^{+4.0}_{-5.9}$	$0.372^{+0.096}_{-0.067}$	$16.2^{+0.8}_{-0.3}$
IC2574	$0.017^{+0.000}_{-0.008}$	$0.116^{+0.003}_{-0.024}$	$0.452^{+0.021}_{-0.046}$	$37.2^{+0.0}_{-5.9}$	$0.415^{+0.000}_{-0.042}$	$17.7^{+2.5}_{-0.0}$
NGC3265	$0.084^{+0.056}_{-0.013}$	$0.084^{+0.015}_{-0.035}$	$0.521^{+0.062}_{-0.084}$	$56.4^{+2.7}_{-0.7}$	$0.313^{+0.084}_{-0.088}$	$23.9^{+0.7}_{-1.3}$
Mrk33	$0.061^{+0.027}_{-0.025}$	$0.106^{+0.037}_{-0.075}$	$0.685^{+0.221}_{-0.177}$	$58.9^{+0.8}_{-1.0}$	$0.158^{+0.066}_{-0.059}$	$20.0^{+1.9}_{-2.9}$
NGC3351	$0.088^{+0.030}_{-0.025}$	$0.165^{+0.038}_{-0.043}$	$0.339^{+0.068}_{-0.079}$	$40.6^{+8.6}_{-5.3}$	$0.408^{+0.081}_{-0.089}$	$17.7^{+2.6}_{-1.8}$
NGC3521	$0.159^{+0.059}_{-0.034}$	$0.112^{+0.030}_{-0.034}$	$0.259^{+0.051}_{-0.072}$	$43.9^{+7.8}_{-8.2}$	$0.468^{+0.108}_{-0.111}$	$18.1^{+1.6}_{-2.0}$
NGC3621	$0.142^{+0.053}_{-0.047}$	$0.123^{+0.034}_{-0.033}$	$0.337^{+0.103}_{-0.080}$	$38.3^{+9.5}_{-6.3}$	$0.399^{+0.141}_{-0.119}$	$18.0^{+2.5}_{-2.2}$
NGC3627	$0.117^{+0.047}_{-0.033}$	$0.123^{+0.044}_{-0.052}$	$0.299^{+0.070}_{-0.084}$	$46.2^{+6.5}_{-8.3}$	$0.459^{+0.096}_{-0.109}$	$19.5^{+2.7}_{-2.0}$
NGC3773	$0.062^{+0.029}_{-0.022}$	$0.162^{+0.053}_{-0.075}$	$0.455^{+0.122}_{-0.164}$	$45.1^{+5.8}_{-9.2}$	$0.321^{+0.088}_{-0.116}$	$20.6^{+2.5}_{-3.8}$
NGC3938	$0.120^{+0.034}_{-0.029}$	$0.112^{+0.023}_{-0.024}$	$0.297^{+0.068}_{-0.056}$	$38.0^{+8.0}_{-6.6}$	$0.463^{+0.109}_{-0.099}$	$17.0^{+2.1}_{-1.6}$
NGC4125	$0.226^{+0.049}_{-0.062}$	$0.124^{+0.037}_{-0.034}$	$0.149^{+0.040}_{-0.050}$	$47.8^{+7.3}_{-11.1}$	$0.494^{+0.100}_{-0.161}$	$23.8^{+0.8}_{-1.6}$
NGC4236	$0.068^{+0.012}_{-0.031}$	$0.029^{+0.016}_{-0.005}$	$0.461^{+0.100}_{-0.043}$	$51.6^{+1.6}_{-2.8}$	$0.440^{+0.098}_{-0.051}$	$18.0^{+1.7}_{-1.9}$
NGC4254	$0.152^{+0.035}_{-0.052}$	$0.133^{+0.030}_{-0.026}$	$0.349^{+0.072}_{-0.077}$	$35.9^{+9.1}_{-3.5}$	$0.366^{+0.091}_{-0.100}$	$17.5^{+1.8}_{-1.9}$
NGC4321	$0.126^{+0.035}_{-0.031}$	$0.115^{+0.037}_{-0.020}$	$0.289^{+0.053}_{-0.054}$	$40.1^{+6.8}_{-6.6}$	$0.467^{+0.099}_{-0.088}$	$17.6^{+1.8}_{-1.6}$
NGC4450	$0.108^{+0.027}_{-0.011}$	$0.072^{+0.016}_{-0.016}$	$0.126^{+0.024}_{-0.035}$	$49.1^{+6.2}_{-9.7}$	$0.691^{+0.049}_{-0.063}$	$18.7^{+1.3}_{-1.4}$
NGC4536	$0.100^{+0.038}_{-0.030}$	$0.145^{+0.073}_{-0.080}$	$0.409^{+0.112}_{-0.100}$	$49.7^{+5.5}_{-10.2}$	$0.336^{+0.087}_{-0.085}$	$19.9^{+2.1}_{-3.1}$
NGC4559	$0.089^{+0.032}_{-0.028}$	$0.093^{+0.023}_{-0.042}$	$0.336^{+0.055}_{-0.067}$	$41.3^{+7.3}_{-5.6}$	$0.481^{+0.087}_{-0.106}$	$17.5^{+1.9}_{-2.0}$
NGC4569	$0.125^{+0.035}_{-0.018}$	$0.122^{+0.075}_{-0.035}$	$0.222^{+0.051}_{-0.089}$	$51.9^{+5.1}_{-8.6}$	$0.523^{+0.061}_{-0.062}$	$19.0^{+2.8}_{-2.2}$
NGC4579	$0.123^{+0.037}_{-0.028}$	$0.104^{+0.049}_{-0.019}$	$0.184^{+0.041}_{-0.071}$	$42.3^{+9.6}_{-9.5}$	$0.588^{+0.098}_{-0.092}$	$18.7^{+1.6}_{-1.6}$
NGC4594	$0.207^{+0.031}_{-0.026}$	$0.104^{+0.018}_{-0.013}$	$0.118^{+0.023}_{-0.036}$	$40.5^{+11.2}_{-6.7}$	$0.571^{+0.065}_{-0.068}$	$18.8^{+1.1}_{-1.3}$
NGC4625	$0.110^{+0.045}_{-0.015}$	$0.096^{+0.010}_{-0.014}$	$0.390^{+0.041}_{-0.068}$	$37.6^{+7.3}_{-5.8}$	$0.401^{+0.044}_{-0.061}$	$16.2^{+0.3}_{-0.0}$
NGC4631	$0.100^{+0.037}_{-0.031}$	$0.102^{+0.023}_{-0.058}$	$0.419^{+0.094}_{-0.090}$	$45.7^{+4.4}_{-8.1}$	$0.379^{+0.088}_{-0.099}$	$17.8^{+2.6}_{-2.1}$
NGC4725	$0.071^{+0.028}_{-0.034}$	$0.028^{+0.011}_{-0.009}$	$0.174^{+0.049}_{-0.038}$	$58.4^{+1.2}_{-2.5}$	$0.723^{+0.073}_{-0.064}$	$17.0^{+0.1}_{-1.2}$
NGC4736	$0.127^{+0.051}_{-0.040}$	$0.119^{+0.024}_{-0.031}$	$0.426^{+0.061}_{-0.108}$	$38.7^{+7.5}_{-4.3}$	$0.330^{+0.093}_{-0.112}$	$18.8^{+3.0}_{-2.5}$

Table B.3: (continued)

Galaxy	$\xi_{\rm PAH}^{\rm tot}$	$\xi_{\rm MIR}^{\rm tot}$	$\xi_{\rm W}^{\rm tot}$	$T_{\rm W}^{\rm BC}$	$\xi_{\rm C}^{\rm tot}$	$T_{\rm C}^{\rm ISM}$
NGC4826	$0.105^{+0.039}_{-0.019}$	$0.097^{+0.048}_{-0.041}$	$0.186^{+0.042}_{-0.079}$	$50.5^{+5.4}_{-11.1}$	$0.615^{+0.078}_{-0.090}$	$23.8^{+0.7}_{-1.2}$
NGC5033	$0.126^{+0.049}_{-0.038}$	$0.108^{+0.037}_{-0.026}$	$0.265^{+0.081}_{-0.078}$	$40.1^{+12.1}_{-7.5}$	$0.494^{+0.133}_{-0.113}$	$18.7^{+2.3}_{-2.6}$
NGC5055	$0.125^{+0.035}_{-0.034}$	$0.106^{+0.027}_{-0.024}$	$0.214^{+0.043}_{-0.056}$	$39.6^{+11.9}_{-7.2}$	$0.555^{+0.083}_{-0.102}$	$17.9^{+1.9}_{-1.7}$
NGC5194	$0.122^{+0.030}_{-0.036}$	$0.116^{+0.016}_{-0.018}$	$0.332^{+0.040}_{-0.039}$	$42.0^{+6.5}_{-9.8}$	$0.430^{+0.041}_{-0.051}$	$17.5^{+1.4}_{-2.0}$
NGC5195	$0.096^{+0.009}_{-0.003}$	$0.046^{+0.010}_{-0.000}$	$0.358^{+0.009}_{-0.015}$	$59.1^{+0.0}_{-3.6}$	$0.499^{+0.024}_{-0.020}$	$24.5^{+0.0}_{-0.7}$
Tol89	$0.024^{+0.014}_{-0.007}$	$0.088^{+0.064}_{-0.043}$	$0.554^{+0.154}_{-0.090}$	$55.9^{+2.0}_{-2.2}$	$0.321^{+0.085}_{-0.046}$	$19.3^{+1.0}_{-2.9}$
NGC5408	$0.033^{+0.011}_{-0.013}$	$0.064^{+0.063}_{-0.056}$	$0.798^{+0.181}_{-0.296}$	$55.0^{+1.5}_{-2.5}$	$0.113^{+0.038}_{-0.050}$	$17.6^{+5.2}_{-1.9}$
NGC5474	$0.071^{+0.035}_{-0.019}$	$0.067^{+0.054}_{-0.038}$	$0.246^{+0.067}_{-0.072}$	$49.5^{+6.5}_{-10.3}$	$0.609^{+0.136}_{-0.113}$	$21.3^{+1.6}_{-2.2}$
NGC5713	$0.085^{+0.029}_{-0.022}$	$0.116^{+0.050}_{-0.045}$	$0.382^{+0.091}_{-0.073}$	$54.0^{+3.6}_{-4.0}$	$0.416^{+0.098}_{-0.072}$	$21.9^{+1.8}_{-2.4}$
NGC5866	$0.095^{+0.021}_{-0.012}$	$0.059^{+0.017}_{-0.014}$	$0.055^{+0.026}_{-0.026}$	$42.3^{+10.9}_{-7.8}$	$0.785^{+0.060}_{-0.074}$	$23.8^{+0.8}_{-1.1}$
IC4710	$0.077^{+0.027}_{-0.029}$	$0.103^{+0.033}_{-0.064}$	$0.546^{+0.164}_{-0.170}$	$40.5^{+6.8}_{-6.3}$	$0.275^{+0.084}_{-0.092}$	$19.2^{+2.6}_{-3.3}$
NGC6822	$0.004^{+0.000}_{-0.000}$	$0.032^{+0.000}_{-0.000}$	$0.524^{+0.000}_{-0.000}$	$47.9^{+0.0}_{-0.0}$	$0.439^{+0.000}_{-0.000}$	$16.7^{+0.0}_{-0.0}$
NGC6946	$0.138^{+0.048}_{-0.042}$	$0.099^{+0.045}_{-0.045}$	$0.342^{+0.083}_{-0.109}$	$51.5^{+4.3}_{-5.1}$	$0.417^{+0.117}_{-0.149}$	$19.3^{+2.2}_{-2.1}$
NGC7331	$0.115^{+0.050}_{-0.033}$	$0.093^{+0.041}_{-0.042}$	$0.298^{+0.073}_{-0.071}$	$44.2^{+7.4}_{-7.8}$	$0.490^{+0.104}_{-0.100}$	$19.7^{+2.6}_{-2.8}$
NGC7552	$0.077^{+0.009}_{-0.012}$	$0.083^{+0.019}_{-0.019}$	$0.534^{+0.026}_{-0.053}$	$58.3^{+0.8}_{-0.8}$	$0.304^{+0.021}_{-0.029}$	$21.7^{+0.5}_{-2.2}$
NGC7793	$0.090^{+0.030}_{-0.030}$	$0.071^{+0.039}_{-0.033}$	$0.331^{+0.124}_{-0.041}$	$44.9^{+7.2}_{-11.0}$	$0.511^{+0.188}_{-0.039}$	$16.4^{+3.9}_{-0.9}$

Bibliography

Aannestad, P. A., Kenyon, S. J.: *Temperature fluctuations and the size distribution of interstellar grains*, ApJ, vol. 230, 771–781, 1979.

Adelman-McCarthy, J. K., Agüeros, M. A., Allam, S. S., et al.: *The Sixth Data Release of the Sloan Digital Sky Survey*, ApJS, vol. 175, 297–313, 2008.

Agladze, N. I., Sievers, A. J., Jones, S. A., Burlitch, J. M., Beckwith, S. V. W.: *Laboratory Results on Millimeter-Wave Absorption in Silicate Grain Materials at Cryogenic Temperatures*, ApJ, vol. 462, 1026–+, 1996.

Alexander, T., Sturm, E., Lutz, D., Sternberg, A., Netzer, H., Genzel, R.: *Infrared Spectroscopy of NGC 4151: Probing the Obscured Ionizing Active Galactic Nucleus Continuum*, ApJ, vol. 512, 204–223, 1999.

Allamandola, L. J., Hudgins, D. M., Sandford, S. A.: *Modeling the Unidentified Infrared Emission with Combinations of Polycyclic Aromatic Hydrocarbons*, ApJ, vol. 511, L115–L119, 1999.

Allamandola, L. J., Tielens, A. G. G. M., Barker, J. R.: *Polycyclic aromatic hydrocarbons and the unidentified infrared emission bands - Auto exhaust along the Milky Way*, ApJ, vol. 290, L25–L28, 1985.

Alongi, M., Bertelli, G., Bressan, A., Chiosi, C., Fagotto, F., Greggio, L., Nasi, E.: *Evolutionary sequences of stellar models with semiconvection and convective overshoot. I - Z = 0.008*, A&AS, vol. 97, 851–871, 1993.

Andriesse, C. D.: *Far-infrared properties of interstellar grains*, A&A, vol. 37, 257–262, 1974.

Arendt, R. G., Odegard, N., Weiland, J. L., Sodroski, T. J., Hauser, M. G., Dwek, E., Kelsall, T., Moseley, S. H., Silverberg, R. F., Leisawitz, D., Mitchell, K., Reach, W. T., Wright, E. L.: *The COBE Diffuse Infrared Background Experiment Search for the Cosmic Infrared Background. III. Separation of Galactic Emission from the Infrared Sky Brightness*, ApJ, vol. 508, 74–105, 1998.

Arimoto, N., Yoshii, Y.: *Chemical and photometric properties of a galactic wind model for elliptical galaxies*, A&A, vol. 173, 23–38, 1987.

Armus, L., Charmandaris, V., Bernard-Salas, J., Spoon, H. W. W., Marshall, J. A., Higdon, S. J. U., Desai, V., Teplitz, H. I., Hao, L., Devost, D., Brandl, B. R., Wu, Y., Sloan, G. C., Soifer, B. T., Houck, J. R., Herter, T. L.: *Observations of Ultraluminous Infrared Galaxies with the Infrared Spectrograph on the Spitzer Space Telescope. II. The IRAS Bright Galaxy Sample*, ApJ, vol. 656, 148–167, 2007.

Baade, W.: *The Resolution of Messier 32, NGC 205, and the Central Region of the Andromeda Nebula.*, ApJ, vol. 100, 137–+, 1944.

Baker, J. G., Menzel, D. H.: *Physical Processes in Gaseous Nebulae. III. The Balmer Decrement.*, ApJ, vol. 88, 52–+, 1938.

Baldwin, J. A., Ferland, G. J., Martin, P. G., Corbin, M. R., Cota, S. A., Peterson, B. M., Slettebak, A.: *Physical conditions in the Orion Nebula and an assessment of its helium abundance*, ApJ, vol. 374, 580–609, 1991.

Baldwin, J. A., Phillips, M. M., Terlevich, R.: *Classification parameters for the emission-line spectra of extragalactic objects*, PASP, vol. 93, 5–19, 1981.

Balogh, M. L., Morris, S. L., Yee, H. K. C., Carlberg, R. G., Ellingson, E.: *Differential Galaxy Evolution in Cluster and Field Galaxies at z˜0.3*, ApJ, vol. 527, 54–79, 1999.

Beichman, C. A., Neugebauer, G., Habing, H. J., Clegg, P. E., Chester, T. J., editors: *Infrared astronomical satellite (IRAS) catalogs and atlases. Volume 1: Explanatory supplement*, vol. 1, 1988.

Bell, E. F.: *Dust-induced Systematic Errors in Ultraviolet-derived Star Formation Rates*, ApJ, vol. 577, 150–154, 2002.

Bell, E. F.: *Estimating Star Formation Rates from Infrared and Radio Luminosities: The Origin of the Radio-Infrared Correlation*, ApJ, vol. 586, 794–813, 2003.

Bevington, P. R., Robinson, D. K.: *Data reduction and error analysis for the physical sciences*, Data reduction and error analysis for the physical sciences, 3rd ed., by Philip R. Bevington, and Keith D. Robinson. Boston, MA: McGraw-Hill, ISBN 0-07-247227-8, 2003., 2003.

Blaizot, J., Guiderdoni, B., Devriendt, J. E. G., Bouchet, F. R., Hatton, S. J., Stoehr, F.: *GALICS- III. Properties of Lyman-break galaxies at a redshift of 3*, MNRAS, vol. 352, 571–588, 2004.

Blaizot, J., Szapudi, I., Colombi, S., Budavàri, T., Bouchet, F. R., Devriendt, J. E. G., Guiderdoni, B., Pan, J., Szalay, A.: *GALICS - V: Low- and high-order clustering in mock Sloan Digital Sky Surveys*, MNRAS, vol. 369, 1009–1020, 2006.

Blaizot, J., Wadadekar, Y., Guiderdoni, B., Colombi, S. T., Bertin, E., Bouchet, F. R., Devriendt, J. E. G., Hatton, S.: *MoMaF: the Mock Map Facility*, MNRAS, vol. 360, 159–175, 2005.

Blanton, M. R., Brinkmann, J., Csabai, I., Doi, M., Eisenstein, D., Fukugita, M., Gunn, J. E., Hogg, D. W., Schlegel, D. J.: *Estimating Fixed-Frame Galaxy Magnitudes in the Sloan Digital Sky Survey*, AJ, vol. 125, 2348–2360, 2003.

Blitz, L., Shu, F. H.: *The origin and lifetime of giant molecular cloud complexes*, ApJ, vol. 238, 148–157, 1980.

Blommaert, J. A. D. L., Siebenmorgen, R., Coulais, A., Metcalfe, L., Miville-Deschenes, M.-A., Okumura, K., Ott, S., Pollock, A., Sauvage, M., Starck, J.-L.: *The ISO Handbook, Volume II - CAM - The ISO Camera*, The ISO Handbook', Volume II - CAM - The ISO Camera Version 2.0 (June, 2003). Series edited by T.G. Mueller, J.A.D.L. Blommaert, and P. Garcia-Lario. ESA SP-1262, ISBN No. 92-9092-968-5, ISSN No. 0379-6566. European Space Agency, 2003., 2003.

Boselli, A., Lequeux, J., Sauvage, M., Boulade, O., Boulanger, F., Cesarsky, D., Dupraz, C., Madden, S., Viallefond, F., Vigroux, L.: *Mid-IR emission of galaxies in the Virgo cluster. II. Integrated properties*, A&A, vol. 335, 53–68, 1998.

Boulanger, F., Abergel, A., Bernard, J.-P., Burton, W. B., Desert, F.-X., Hartmann, D., Lagache, G., Puget, J.-L.: *The dust/gas correlation at high Galactic latitude.*, A&A, vol. 312, 256–262, 1996.

Boulanger, F., Boissel, P., Cesarsky, D., Ryter, C.: *The shape of the unidentified infra-red bands: analytical fit to ISOCAM spectra*, A&A, vol. 339, 194–200, 1998.

Boulanger, F., Perault, M.: *Diffuse infrared emission from the galaxy. I - Solar neighborhood*, ApJ, vol. 330, 964–985, 1988.

Brandl, B. R., Bernard-Salas, J., Spoon, H. W. W., Devost, D., Sloan, G. C., Guilles, S., Wu, Y., Houck, J. R., et al.: *The Mid-Infrared Properties of Starburst Galaxies from Spitzer-IRS Spectroscopy*, ApJ, vol. 653, 1129–1144, 2006.

Bressan, A., Chiosi, C., Fagotto, F.: *Spectrophotometric evolution of elliptical galaxies. 1: Ultraviolet excess and color-magnitude-redshift relations*, ApJS, vol. 94, 63–115, 1994.

Bressan, A., Fagotto, F., Bertelli, G., Chiosi, C.: *Evolutionary sequences of stellar models with new radiative opacities. II - Z = 0.02*, A&AS, vol. 100, 647–664, 1993.

Brinchmann, J., Charlot, S., White, S. D. M., Tremonti, C., Kauffmann, G., Heckman, T., Brinkmann, J.: *The physical properties of star-forming galaxies in the low-redshift Universe*, MNRAS, vol. 351, 1151–1179, 2004.

Bruzual, A. G.: *On TP-AGB stars and the mass of galaxies*, in *IAU Symposium*, vol. 241 of *IAU Symposium*, pp. 125–132, 2007.

Bruzual, G.: *Spectral evolution of galaxies. I - Early-type systems*, ApJ, vol. 273, 105–127, 1983.

Bruzual, G., Charlot, S.: *Spectral evolution of stellar populations using isochrone synthesis*, ApJ, vol. 405, 538–553, 1993.

Bruzual, G., Charlot, S.: *Stellar population synthesis at the resolution of 2003*, MNRAS, vol. 344, 1000–1028, 2003.

Bruzual, G. A., Magris, G., Calvet, N.: *A model for the effects of dust on the spectra of disk galaxies. I - General treatment*, ApJ, vol. 333, 673–688, 1988.

Bruzual A., G.: *Spectral evolution of galaxies. I - Early-type systems*, ApJ, vol. 273, 105–127, 1983.

Buzzoni, A.: *Evolutionary population synthesis in stellar systems. I - A global approach*, ApJS, vol. 71, 817–869, 1989.

Calura, F., Pipino, A., Matteucci, F.: *The cycle of interstellar dust in galaxies of different morphological types*, A&A, vol. 479, 669–685, 2008.

Calzetti, D.: *The Dust Opacity of Star-forming Galaxies*, PASP, vol. 113, 1449–1485, 2001.

Calzetti, D., Kinney, A. L., Storchi-Bergmann, T.: *Dust extinction of the stellar continua in starburst galaxies: The ultraviolet and optical extinction law*, ApJ, vol. 429, 582–601, 1994.

Cao, C., Wu, H., Wang, J.-L., Hao, C.-N., Deng, Z.-G., Xia, X.-Y., Zou, Z.-L.: *A Catalog of Luminous Infrared Galaxies in the IRAS Survey and Second Data Release of SDSS*, Chinese Journal of Astronomy and Astrophysics, vol. 6, 197–209, 2006.

Cesarsky, D., Lequeux, J., Abergel, A., Perault, M., Palazzi, E., Madden, S., Tran, D.: *Infrared spectrophotometry of NGC 7023 with ISOCAM.*, A&A, vol. 315, L305–L308, 1996.

Chabrier, G.: *Galactic Stellar and Substellar Initial Mass Function*, PASP, vol. 115, 763–795, 2003.

Charlot, S., Bruzual, A. G.: *Stellar population synthesis revisited*, ApJ, vol. 367, 126–140, 1991.

Charlot, S., Fall, S. M.: *A Simple Model for the Absorption of Starlight by Dust in Galaxies*, ApJ, vol. 539, 718–731, 2000.

Charlot, S., Kauffmann, G., Longhetti, M., Tresse, L., White, S. D. M., Maddox, S. J., Fall, S. M.: *Star formation, metallicity and dust properties derived from the Stromlo-APM galaxy survey spectra*, MNRAS, vol. 330, 876–888, 2002.

Charlot, S., Longhetti, M.: *Nebular emission from star-forming galaxies*, MNRAS, vol. 323, 887–903, 2001.

Chary, R., Elbaz, D.: *Interpreting the Cosmic Infrared Background: Constraints on the Evolution of the Dust-enshrouded Star Formation Rate*, ApJ, vol. 556, 562–581, 2001.

Chiappini, C., Matteucci, F., Gratton, R.: *The Chemical Evolution of the Galaxy: The Two-Infall Model*, ApJ, vol. 477, 765–+, 1997.

Coelho, P.: *Model stars for the modelling of galaxies: α-enhancement in stellar populations models*, ArXiv e-prints, vol. 802, 2008.

Colless, M., Dalton, G., Maddox, S., Sutherland, W., Norberg, P., Cole, S., Bland-Hawthorn, J., Bridges, T., et al.: *The 2dF Galaxy Redshift Survey: spectra and redshifts*, MNRAS, vol. 328, 1039–1063, 2001.

Condon, J. J.: *Radio emission from normal galaxies*, ARA&A, vol. 30, 575–611, 1992.

da Cunha, E., Charlot, S., Elbaz, D.: *A simple model to interpret the ultraviolet, optical and infrared emission from galaxies*, MNRAS, vol. 388, 1595–1617, 2008.

Dale, D. A., Bendo, G. J., Engelbracht, C. W., Gordon, K. D., Regan, M. W., Armus, L., Cannon, J. M., Calzetti, D., Draine, B. T., Helou, G., Joseph, R. D., Kennicutt, R. C., Li, A., Murphy, E. J., Roussel, H., Walter, F., Hanson, H. M., Hollenbach, D. J., Jarrett, T. H., Kewley, L. J., Lamanna, C. A., Leitherer, C., Meyer, M. J., Rieke, G. H., Rieke, M. J., Sheth, K., Smith, J. D. T., Thornley, M. D.: *Infrared Spectral Energy Distributions of Nearby Galaxies*, ApJ, vol. 633, 857–870, 2005.

Dale, D. A., Gil de Paz, A., Gordon, K. D., Hanson, H. M., Armus, L., Bendo, G. J., Bianchi, L., Block, M., Boissier, S., Boselli, A., Buckalew, B. A., Buat, V., Burgarella, D., Calzetti, D., Cannon, J. M., Engelbracht, C. W., Helou, G., Hollenbach, D. J., Jarrett, T. H., Kennicutt, R. C., Leitherer, C., Li, A., Madore, B. F., Martin, D. C., Meyer, M. J., Murphy, E. J., Regan, M. W., Roussel, H., Smith, J. D. T., Sosey, M. L., Thilker, D. A., Walter, F.: *An Ultraviolet-to-Radio Broadband Spectral Atlas of Nearby Galaxies*, ApJ, vol. 655, 863–884, 2007.

Dale, D. A., Helou, G.: *The Infrared Spectral Energy Distribution of Normal Star-forming Galaxies: Calibration at Far-Infrared and Submillimeter Wavelengths*, ApJ, vol. 576, 159–168, 2002.

Dale, D. A., Helou, G., Contursi, A., Silbermann, N. A., Kolhatkar, S.: *The Infrared Spectral Energy Distribution of Normal Star-forming Galaxies*, ApJ, vol. 549, 215–227, 2001.

Dale, D. A., Silbermann, N. A., Helou, G., Valjavec, E., Malhotra, S., Beichman, C. A., Brauher, J., Contursi, A., Dinerstein, H. L., Hollenbach, D. J., Hunter, D. A., Kolhatkar, S., Lo, K.-Y., Lord, S. D., Lu, N. Y., Rubin, R. H., Stacey, G. J., Thronson, H. A., Jr., Werner, M. W., Corwin, H. G., Jr.: *ISO Mid-Infrared Observations of Normal Star-Forming Galaxies: The Key Project Sample*, AJ, vol. 120, 583–603, 2000.

Davis, M., Guhathakurta, P., Konidaris, N. P., Newman, J. A., Ashby, M. L. N., Biggs, A. D., Barmby, P., Bundy, K., Chapman, S. C., Coil, A. L., Conselice, C. J., Cooper, M. C., Croton, D. J., Eisenhardt, P. R. M., Ellis, R. S., Faber, S. M., Fang, T., Fazio, G. G., Georgakakis, A., Gerke, B. F., Goss, W. M., Gwyn, S., Harker, J., Hopkins, A. M., Huang, J.-S., Ivison, R. J., Kassin, S. A., Kirby, E. N., Koekemoer, A. M., Koo, D. C., Laird, E. S., Le Floc'h, E., Lin, L., Lotz, J. M., Marshall, P. J., Martin, D. C., Metevier, A. J., Moustakas, L. A., Nandra, K., Noeske, K. G., Papovich, C., Phillips, A. C., Rich, R. M., Rieke, G. H., Rigopoulou, D., Salim, S., Schiminovich, D., Simard, L., Smail, I., Small, T. A., Weiner, B. J., Willmer, C. N. A., Willner, S. P., Wilson, G., Wright, E. L., Yan, R.: *The All-Wavelength Extended Groth Strip International Survey (AEGIS) Data Sets*, ApJ, vol. 660, L1–L6, 2007.

de Grijp, M. H. K., Miley, G. K., Lub, J., de Jong, T.: *Infrared Seyferts - A new population of active galaxies?*, Nature, vol. 314, 240–242, 1985.

de Vaucouleurs, G.: *Structure, dynamics and statistical properties of galaxies*, in J. R. Shakeshaft, editor, *The Formation and Dynamics of Galaxies*, vol. 58 of *IAU Symposium*, pp. 1–52, 1974.

de Vaucouleurs, G., de Vaucouleurs, A., Corwin, H. G., Jr., Buta, R. J., Paturel, G., Fouque, P.: *Third Reference Catalogue of Bright Galaxies*, Volume 1-3, XII, 2069 pp. 7 figs.. Springer-Verlag Berlin Heidelberg New York, 1991.

Désert, F.-X., Boulanger, F., Puget, J. L.: *Interstellar dust models for extinction and emission*, A&A, vol. 237, 215–236, 1990.

Devriendt, J. E. G., Guiderdoni, B., Sadat, R.: *Galaxy modelling. I. Spectral energy distributions from far-UV to sub-mm wavelengths*, A&A, vol. 350, 381–398, 1999.

Dickinson, M., GOODS Legacy Team: *The Great Observatories Origins Deep Survey (GOODS)*, in *Bulletin of the American Astronomical Society*, vol. 33 of *Bulletin of the American Astronomical Society*, pp. 820–+, 2001.

Dinerstein, H. L., Lester, D. F., Werner, M. W.: *Far-infrared line observations of planetary nebulae. I - The forbidden O III spectrum*, ApJ, vol. 291, 561–570, 1985.

Dopita, M. A., Groves, B. A., Fischera, J., Sutherland, R. S., Tuffs, R. J., Popescu, C. C., Kewley, L. J., Reuland, M., Leitherer, C.: *Modeling the Pan-Spectral Energy Distribution of Starburst Galaxies. I. The Role of ISM Pressure and the Molecular Cloud Dissipation Timescale*, ApJ, vol. 619, 755–778, 2005.

Draine, B. T.: *Interstellar Dust Grains*, ARA&A, vol. 41, 241–289, 2003.

Draine, B. T., Anderson, N.: *Temperature fluctuations and infrared emission from interstellar grains*, ApJ, vol. 292, 494–499, 1985.

Draine, B. T., Dale, D. A., Bendo, G., Gordon, K. D., Smith, J. D. T., Armus, L., Engelbracht, C. W., Helou, G., Kennicutt, R. C., Jr., Li, A., Roussel, H., Walter, F., Calzetti, D., Moustakas, J., Murphy, E. J., Rieke, G. H., Bot, C., Hollenbach, D. J., Sheth, K., Teplitz, H. I.: *Dust Masses, PAH Abundances, and Starlight Intensities in the SINGS Galaxy Sample*, ApJ, vol. 663, 866–894, 2007.

Draine, B. T., Lee, H. M.: *Optical properties of interstellar graphite and silicate grains*, ApJ, vol. 285, 89–108, 1984.

Draine, B. T., Li, A.: *Infrared Emission from Interstellar Dust. I. Stochastic Heating of Small Grains*, ApJ, vol. 551, 807–824, 2001.

Draine, B. T., Li, A.: *Infrared Emission from Interstellar Dust. IV. The Silicate-Graphite-PAH Model in the Post-Spitzer Era*, ApJ, vol. 657, 810–837, 2007.

Dudley, C. C., Wynn-Williams, C. G.: *The Deep Silicate Absorption Feature in IRAS 08572+3915 and Other Infrared Galaxies*, ApJ, vol. 488, 720–+, 1997.

Dunne, L., Eales, S., Edmunds, M., Ivison, R., Alexander, P., Clements, D. L.: *The SCUBA Local Universe Galaxy Survey - I. First measurements of the submillimetre luminosity and dust mass functions*, MNRAS, vol. 315, 115–139, 2000.

Dunne, L., Eales, S. A.: *The SCUBA Local Universe Galaxy Survey - II. 450-μm data: evidence for cold dust in bright IRAS galaxies*, MNRAS, vol. 327, 697–714, 2001.

Dwek, E.: *The Evolution of the Elemental Abundances in the Gas and Dust Phases of the Galaxy*, ApJ, vol. 501, 643–+, 1998.

Dwek, E., Arendt, R. G., Fixsen, D. J., Sodroski, T. J., Odegard, N., Weiland, J. L., Reach, W. T., Hauser, M. G., Kelsall, T., Moseley, S. H., Silverberg, R. F., Shafer, R. A., Ballester, J., Bazell, D., Isaacman, R.: *Detection and Characterization of Cold Interstellar Dust and Polycyclic Aromatic Hydrocarbon Emission, from COBE Observations*, ApJ, vol. 475, 565–+, 1997.

Efstathiou, A., Rowan-Robinson, M.: *Radiative transfer in axisymmetric dust clouds*, MNRAS, vol. 245, 275–288, 1990.

Elbaz, D., Cesarsky, C. J., Chanial, P., Aussel, H., Franceschini, A., Fadda, D., Chary, R. R.: *The bulk of the cosmic infrared background resolved by ISOCAM*, A&A, vol. 384, 848–865, 2002.

Engelbracht, C. W., Gordon, K. D., Rieke, G. H., Werner, M. W., Dale, D. A., Latter, W. B.: *Metallicity Effects on Mid-Infrared Colors and the 8 μm PAH Emission in Galaxies*, ApJ, vol. 628, L29–L32, 2005.

Engelbracht, C. W., Rieke, G. H., Gordon, K. D., Smith, J.-D. T., Werner, M. W., Moustakas, J., Willmer, C. N. A., Vanzi, L.: *Metallicity Effects on Dust Properties in Starbursting Galaxies*, ApJ, vol. 678, 804–827, 2008.

Ewen, H. I., Purcell, E. M.: *Observation of a Line in the Galactic Radio Spectrum: Radiation from Galactic Hydrogen at 1,420 Mc./sec.*, Nature, vol. 168, 356–+, 1951.

Faber, S. M.: *Quadratic programming applied to the problem of galaxy population synthesis.*, A&A, vol. 20, 361–374, 1972.

Fagotto, F., Bressan, A., Bertelli, G., Chiosi, C.: *Evolutionary sequences of stellar models with new radiative opacities. III. Z=0.0004 and Z=0.05*, A&AS, vol. 104, 365–376, 1994a.

Fagotto, F., Bressan, A., Bertelli, G., Chiosi, C.: *Evolutionary sequences of stellar models with new radiative opacities. IV. Z=0.004 and Z=0.008*, A&AS, vol. 105, 29–38, 1994b.

Ferland, G. J.: *Hazy, A Brief Introduction to Cloudy 90*, University of Kentucky Internal Report, 565 pages, 1996.

Field, G. B., Goldsmith, D. W., Habing, H. J.: *Cosmic-Ray Heating of the Interstellar Gas*, ApJ, vol. 155, L149+, 1969.

Finkbeiner, D. P., Davis, M., Schlegel, D. J.: *Extrapolation of Galactic Dust Emission at 100 Microns to Cosmic Microwave Background Radiation Frequencies Using FIRAS*, ApJ, vol. 524, 867–886, 1999.

Fioc, M., Rocca-Volmerange, B.: *PEGASE: a UV to NIR spectral evolution model of galaxies. Application to the calibration of bright galaxy counts.*, A&A, vol. 326, 950–962, 1997.

Flagey, N., Boulanger, F., Verstraete, L., Miville Deschênes, M. A., Noriega Crespo, A., Reach, W. T.: *Spitzer/IRAC and ISOCAM/CVF insights on the origin of the near to mid-IR Galactic diffuse emission*, A&A, vol. 453, 969–978, 2006.

Franceschini, A., Aussel, H., Cesarsky, C. J., Elbaz, D., Fadda, D.: *A long-wavelength view on galaxy evolution from deep surveys by the Infrared Space Observatory*, A&A, vol. 378, 1–29, 2001.

Gallagher, J. S., III, Hunter, D. A., Tutukov, A. V.: *Star formation histories of irregular galaxies*, ApJ, vol. 284, 544–556, 1984.

Gallazzi, A., Charlot, S., Brinchmann, J., White, S. D. M., Tremonti, C. A.: *The ages and metallicities of galaxies in the local universe*, MNRAS, vol. 362, 41–58, 2005.

Galliano, F., Dwek, E., Chanial, P.: *Stellar Evolutionary Effects on the Abundances of PAH and SN-Condensed Dust in Galaxies*, ArXiv e-prints, vol. 708, 2007.

Gil de Paz, A., Boissier, S., Madore, B. F., Seibert, M., Joe, Y. H., Boselli, A., Wyder, T. K., Thilker, D., et al.: *The GALEX Ultraviolet Atlas of Nearby Galaxies*, ArXiv Astrophysics e-prints, 2006.

Gordon, K. D., Engelbracht, C. W., Rieke, G. H., Misselt, K. A., Smith, J.-D. T., Kennicutt, R. C., Jr.: *The Behavior of the Aromatic Features in M101 H II Regions: Evidence for Dust Processing*, ApJ, vol. 682, 336–354, 2008.

Gordon, K. D., Misselt, K. A., Witt, A. N., Clayton, G. C.: *The DIRTY Model. I. Monte Carlo Radiative Transfer through Dust*, ApJ, vol. 551, 269–276, 2001.

Groves, B., Dopita, M., Sutherland, R.: *The infrared emission from the narrow line region*, A&A, vol. 458, 405–416, 2006.

Groves, B., Dopita, M., Sutherland, R., Kewley, L., Fischera, J., Leitherer, C., Brandl, B., van Breugal, W.: *Modelling the Pan-Spectral Energy Distribution of Starburst Galaxies: IV The Controlling Parameters of the Starburst SED*, ArXiv e-prints, vol. 712, 2007.

Guhathakurta, P., Draine, B. T.: *Temperature fluctuations in interstellar grains. I - Computational method and sublimation of small grains*, ApJ, vol. 345, 230–244, 1989.

Guiderdoni, B., Rocca-Volmerange, B.: *A model of spectrophotometric evolution for high-redshift galaxies*, A&A, vol. 186, 1–2, 1987.

Gustafsson, B., Heiter, U., Edvardsson, B.: *Libraries of synthetic stellar spectra - or are we building palaces upon sand?*, in A. Vazdekis, R. F. Peletier, editors, *IAU Symposium*, vol. 241 of *IAU Symposium*, pp. 47–57, 2007.

Hartmann, J.: *Investigations on the spectrum and orbit of delta Orionis.*, ApJ, vol. 19, 268–286, 1904.

Hatton, S., Devriendt, J. E. G., Ninin, S., Bouchet, F. R., Guiderdoni, B., Vibert, D.: *GALICS- I. A hybrid N-body/semi-analytic model of hierarchical galaxy formation*, MNRAS, vol. 343, 75–106, 2003.

Helou, G.: *The IRAS colors of normal galaxies*, ApJ, vol. 311, L33–L36, 1986.

Helou, G., Khan, I. R., Malek, L., Boehmer, L.: *IRAS observations of galaxies in the Virgo cluster area*, ApJS, vol. 68, 151–172, 1988.

Helou, G., Lu, N. Y., Werner, M. W., Malhotra, S., Silbermann, N.: *The Mid-Infrared Spectra of Normal Galaxies*, ApJ, vol. 532, L21–L24, 2000.

Hildebrand, R. H.: *The Determination of Cloud Masses and Dust Characteristics from Submillimetre Thermal Emission*, QJRAS, vol. 24, 267–+, 1983.

Hoessel, J. G., Saha, A., Danielson, G. E.: *Variable stars in the Holmberg II dwarf galaxy*, AJ, vol. 115, 573–+, 1998.

Holland, W. S., Robson, E. I., Gear, W. K., Cunningham, C. R., Lightfoot, J. F., Jenness, T., Ivison, R. J., Stevens, J. A., Ade, P. A. R., Griffin, M. J., Duncan, W. D., Murphy, J. A., Naylor, D. A.: *SCUBA: a common-user submillimetre camera operating on the James Clerk Maxwell Telescope*, MNRAS, vol. 303, 659–672, 1999.

Hollenbach, D., Salpeter, E. E.: *Surface Recombination of Hydrogen Molecules*, ApJ, vol. 163, 155–+, 1971.

Hollenbach, D. J., Tielens, A. G. G. M.: *Dense Photodissociation Regions (PDRs)*, ARA&A, vol. 35, 179–216, 1997.

Hopkins, A. M., Connolly, A. J., Haarsma, D. B., Cram, L. E.: *Toward a Resolution of the Discrepancy between Different Estimators of Star Formation Rate*, AJ, vol. 122, 288–296, 2001.

Houck, J. R., Roellig, T. L., van Cleve, J., Forrest, W. J., Herter, T., Lawrence, C. R., Matthews, K., Reitsema, H. J., Soifer, B. T., Watson, D. M., Weedman, D., Huisjen, M., Troeltzsch, J., Barry, D. J., Bernard-Salas, J., Blacken, C. E., Brandl, B. R., Charmandaris, V., Devost, D., Gull, G. E., Hall, P., Henderson, C. P., Higdon, S. J. U., Pirger, B. E., Schoenwald, J., Sloan, G. C., Uchida, K. I., Appleton, P. N., Armus, L., Burgdorf, M. J., Fajardo-Acosta, S. B., Grillmair, C. J., Ingalls, J. G., Morris, P. W., Teplitz, H. I.: *The Infrared Spectrograph (IRS) on the Spitzer Space Telescope*, ApJS, vol. 154, 18–24, 2004.

Hubble, E.: *A Relation between Distance and Radial Velocity among Extra-Galactic Nebulae*, Proceedings of the National Academy of Science, vol. 15, 168–173, 1929.

Hubble, E., Humason, M. L.: *The Velocity-Distance Relation among Extra-Galactic Nebulae*, ApJ, vol. 74, 43–+, 1931.

Hubble, E. P.: *NGC 6822, a remote stellar system.*, ApJ, vol. 62, 409–433, 1925.

Hubble, E. P.: *Extragalactic nebulae.*, ApJ, vol. 64, 321–369, 1926.

Iben, I. J.: *Single and binary star evolution*, ApJS, vol. 76, 55–114, 1991.

Imanishi, M., Dudley, C. C.: *Energy Diagnoses of Nine Infrared Luminous Galaxies Based on 3-4 Micron Spectra*, ApJ, vol. 545, 701–711, 2000.

Isobe, T., Feigelson, E. D., Akritas, M. G., Babu, G. J.: *Linear regression in astronomy.*, ApJ, vol. 364, 104–113, 1990.

Jarrett, T. H., Chester, T., Cutri, R., Schneider, S. E., Huchra, J. P.: *The 2MASS Large Galaxy Atlas*, AJ, vol. 125, 525–554, 2003.

Johnson, B. D., Schiminovich, D., Seibert, M., Treyer, M., Martin, D. C., Barlow, T. A., Forster, K., Friedman, P. G., Morrissey, P., Neff, S. G., Small, T., Wyder,

T. K., Bianchi, L., Donas, J., Heckman, T. M., Lee, Y.-W., Madore, B. F., Milliard, B., Rich, R. M., Szalay, A. S., Welsh, B. Y., Yi, S. K.: *Ultraviolet, Optical, and Infrared Constraints on Models of Stellar Populations and Dust Attenuation*, ApJS, vol. 173, 377–391, 2007.

Kauffmann, G., Charlot, S.: *The K-band luminosity function at z=1: a powerful constraint on galaxy formation theory*, MNRAS, vol. 297, L23+, 1998.

Kauffmann, G., Heckman, T. M., Tremonti, C., Brinchmann, J., Charlot, S., White, S. D. M., Ridgway, S. E., Brinkmann, J., Fukugita, M., Hall, P. B., Ivezić, Ž., Richards, G. T., Schneider, D. P.: *The host galaxies of active galactic nuclei*, MNRAS, vol. 346, 1055–1077, 2003a.

Kauffmann, G., Heckman, T. M., White, S. D. M., Charlot, S., Tremonti, C., Brinchmann, J., Bruzual, G., Peng, E. W., Seibert, M., Bernardi, M., Blanton, M., Brinkmann, J., Castander, F., Csábai, I., Fukugita, M., Ivezic, Z., Munn, J. A., Nichol, R. C., Padmanabhan, N., Thakar, A. R., Weinberg, D. H., York, D.: *Stellar masses and star formation histories for* 10^5 *galaxies from the Sloan Digital Sky Survey*, MNRAS, vol. 341, 33–53, 2003b.

Kennicutt, R. C., Jr.: *The integrated spectra of nearby galaxies - General properties and emission-line spectra*, ApJ, vol. 388, 310–327, 1992.

Kennicutt, R. C., Jr.: *Star Formation in Galaxies Along the Hubble Sequence*, ARA&A, vol. 36, 189–232, 1998a.

Kennicutt, R. C., Jr.: *The Global Schmidt Law in Star-forming Galaxies*, ApJ, vol. 498, 541–+, 1998b.

Kennicutt, R. C., Jr., Armus, L., Bendo, G., Calzetti, D., Dale, D. A., Draine, B. T., Engelbracht, C. W., Gordon, K. D., Grauer, A. D., Helou, G., Hollenbach, D. J., Jarrett, T. H., Kewley, L. J., Leitherer, C., Li, A., Malhotra, S., Regan, M. W., Rieke, G. H., Rieke, M. J., Roussel, H., Smith, J.-D. T., Thornley, M. D., Walter, F.: *SINGS: The SIRTF Nearby Galaxies Survey*, PASP, vol. 115, 928–952, 2003.

Kessler, M. F., Steinz, J. A., Anderegg, M. E., Clavel, J., Drechsel, G., Estaria, P., Faelker, J., Riedinger, J. R., et al.: *The Infrared Space Observatory (ISO) mission.*, A&A, vol. 315, L27–L31, 1996.

Kewley, L. J., Dopita, M. A.: *Using Strong Lines to Estimate Abundances in Extragalactic H II Regions and Starburst Galaxies*, ApJS, vol. 142, 35–52, 2002.

Kewley, L. J., Jansen, R. A., Geller, M. J.: *Aperture Effects on Star Formation Rate, Metallicity, and Reddening*, PASP, vol. 117, 227–244, 2005.

Kong, X., Charlot, S., Brinchmann, J., Fall, S. M.: *Star formation history and dust content of galaxies drawn from ultraviolet surveys*, MNRAS, vol. 349, 769–778, 2004.

Kroupa, P.: *On the variation of the initial mass function*, MNRAS, vol. 322, 231–246, 2001.

Lagache, G., Dole, H., Puget, J.-L.: *Modelling infrared galaxy evolution using a phenomenological approach*, MNRAS, vol. 338, 555–571, 2003.

Lagache, G., Dole, H., Puget, J.-L., Pérez-González, P. G., Le Floc'h, E., Rieke, G. H., Papovich, C., Egami, E., Alonso-Herrero, A., Engelbracht, C. W., Gordon, K. D., Misselt, K. A., Morrison, J. E.: *Polycyclic Aromatic Hydrocarbon Contribution to the Infrared Output Energy of the Universe at z ˜= 2*, ApJS, vol. 154, 112–117, 2004.

Latter, W. B., NHSC, HSC Teams: *The Herschel Space Observatory: An Overview*, in *Bulletin of the American Astronomical Society*, vol. 38 of *Bulletin of the American Astronomical Society*, pp. 107–+, 2007.

Laurent, O., Mirabel, I. F., Charmandaris, V., Gallais, P., Madden, S. C., Sauvage, M., Vigroux, L., Cesarsky, C.: *Mid-infrared diagnostics to distinguish AGNs from starbursts*, A&A, vol. 359, 887–899, 2000.

Le Borgne, J.-F., Bruzual, G., Pelló, R., Lançon, A., Rocca-Volmerange, B., Sanahuja, B., Schaerer, D., Soubiran, C., Vílchez-Gómez, R.: *STELIB: A library of stellar spectra at R ˜ 2000*, A&A, vol. 402, 433–442, 2003.

Lee, H., Grebel, E. K., Hodge, P. W.: *Nebular abundances of nearby southern dwarf galaxies*, A&A, vol. 401, 141–159, 2003.

Leger, A., D'Hendecourt, L., Defourneau, D.: *Physics of IR emission by interstellar PAH molecules*, A&A, vol. 216, 148–164, 1989.

Leger, A., Puget, J. L.: *Identification of the 'unidentified' IR emission features of interstellar dust?*, A&A, vol. 137, L5–L8, 1984.

Leitherer, C., Heckman, T. M.: *Synthetic properties of starburst galaxies*, ApJS, vol. 96, 9–38, 1995.

Li, A., Draine, B. T.: *Infrared Emission from Interstellar Dust. II. The Diffuse Interstellar Medium*, ApJ, vol. 554, 778–802, 2001.

Lu, N., Helou, G., Werner, M. W., Dinerstein, H. L., Dale, D. A., Silbermann, N. A., Malhotra, S., Beichman, C. A., Jarrett, T. H.: *Infrared Emission of Normal Galaxies from 2.5 to 12 Micron: Infrared Space Observatory Spectra, Near-Infrared Continuum, and Mid-Infrared Emission Features*, ApJ, vol. 588, 199–217, 2003.

Madden, S. C., Galliano, F., Jones, A. P., Sauvage, M.: *ISM properties in low-metallicity environments*, A&A, vol. 446, 877–896, 2006.

Magnelli, B., Chary, R. R., Pope, A., Elbaz, D., Morrison, G., Dickinson, M.: *IRAC Excess in Distant Star-Forming Galaxies: Tentative Evidence for the 3.3 μm Polycyclic Aromatic Hydrocarbon Feature?*, ApJ, vol. 681, 258–268, 2008.

Maller, A. H., Berlind, A. A., Blanton, M., Hogg, D. W.: *Intrinsic Properties of Low-z SDSS Galaxies*, ArXiv e-prints, vol. 801, 2008.

Maraston, C.: *Evolutionary synthesis of stellar populations: a modular tool*, MNRAS, vol. 300, 872–892, 1998.

Marcillac, D., Elbaz, D., Chary, R. R., Dickinson, M., Galliano, F., Morrison, G.: *Mid infrared properties of distant infrared luminous galaxies*, A&A, vol. 451, 57–69, 2006.

Marigo, P., Girardi, L.: *Evolution of asymptotic giant branch stars. I. Updated synthetic TP-AGB models and their basic calibration*, A&A, vol. 469, 239–263, 2007.

Marigo, P., Girardi, L., Bressan, A., Groenewegen, M. A. T., Silva, L., Granato, G. L.: *Evolution of asymptotic giant branch stars. II. Optical to far-infrared isochrones with improved TP-AGB models*, A&A, vol. 482, 883–905, 2008.

Martin, D. C., Fanson, J., Schiminovich, D., Morrissey, P., Friedman, P. G., Barlow, T. A., Conrow, T., Grange, R., Jelinsky, P. N., Milliard, B., Siegmund, O. H. W., Bianchi, L., Byun, Y.-I., Donas, J., Forster, K., Heckman, T. M., Lee, Y.-W., Madore, B. F., Malina, R. F., Neff, S. G., Rich, R. M., Small, T., Surber, F., Szalay, A. S., Welsh, B., Wyder, T. K.: *The Galaxy Evolution Explorer: A Space Ultraviolet Survey Mission*, ApJ, vol. 619, L1–L6, 2005.

Martins, L. P., Coelho, P.: *Testing the accuracy of synthetic stellar libraries*, MNRAS, vol. 381, 1329–1346, 2007.

Mathis, J. S.: *Interstellar dust and extinction*, ARA&A, vol. 28, 37–70, 1990.

Mathis, J. S., Mezger, P. G., Panagia, N.: *Interstellar radiation field and dust temperatures in the diffuse interstellar matter and in giant molecular clouds*, A&A, vol. 128, 212–229, 1983.

Mathis, J. S., Rumpl, W., Nordsieck, K. H.: *The size distribution of interstellar grains*, ApJ, vol. 217, 425–433, 1977.

Mennella, V., Brucato, J. R., Colangeli, L., Palumbo, P., Rotundi, A., Bussoletti, E.: *Temperature Dependence of the Absorption Coefficient of Cosmic Analog Grains in the Wavelength Range 20 Microns to 2 Millimeters*, ApJ, vol. 496, 1058–+, 1998.

Menzel, D. H., Aller, L. H., Hebb, M. H.: *Physical Processes in Gaseous Nebulae. XIII.*, ApJ, vol. 93, 230–+, 1941.

Meurer, G. R., Heckman, T. M., Calzetti, D.: *Dust Absorption and the Ultraviolet Luminosity Density at Z˜3 as Calibrated by Local Starburst Galaxies*, ApJ, vol. 521, 64–80, 1999.

Mezger, P. G., Mathis, J. S., Panagia, N.: *The origin of the diffuse galactic far infrared and sub-millimeter emission*, A&A, vol. 105, 372–388, 1982.

Misiriotis, A., Popescu, C. C., Tuffs, R., Kylafis, N. D.: *Modeling the spectral energy distribution of galaxies. II. Disk opacity and star formation in 5 edge-on spirals*, A&A, vol. 372, 775–783, 2001.

Misselt, K. A., Gordon, K. D., Clayton, G. C., Wolff, M. J.: *The DIRTY Model. II. Self-consistent Treatment of Dust Heating and Emission in a Three-dimensional Radiative Transfer Code*, ApJ, vol. 551, 277–293, 2001.

Morrissey, P., Schiminovich, D., Barlow, T. A., Martin, D. C., Blakkolb, B., Conrow, T., Cooke, B., Erickson, K., Fanson, J., Friedman, P. G., Grange, R., Jelinsky, P. N., Lee, S.-C., Liu, D., Mazer, A., McLean, R., Milliard, B., Randall, D., Schmitigal, W., Sen, A., Siegmund, O. H. W., Surber, F., Vaughan, A., Viton, M., Welsh, B. Y., Bianchi, L., Byun, Y.-I., Donas, J., Forster, K., Heckman, T. M., Lee, Y.-W., Madore, B. F., Malina, R. F., Neff, S. G., Rich, R. M., Small, T., Szalay, A. S., Wyder, T. K.: *The On-Orbit Performance of the Galaxy Evolution Explorer*, ApJ, vol. 619, L7–L10, 2005.

Moshir, M.: *IRAS Faint Source Survey, Explanatory supplement version 1 and tape*, Pasadena: Infrared Processing and Analysis Center, California Institute of Technology, 1989, edited by Moshir, M., 1989.

Moustakas, J., Kennicutt, R. C., Jr.: *An Integrated Spectrophotometric Survey of Nearby Star-forming Galaxies*, ApJS, vol. 164, 81–98, 2006.

Natta, A., Panagia, N.: *Extinction in inhomogeneous clouds*, ApJ, vol. 287, 228–237, 1984.

Obrić, M., Ivezić, Ž., Best, P. N., Lupton, R. H., Tremonti, C., Brinchmann, J., Agüeros, M. A., Knapp, G. R., Gunn, J. E., Rockosi, C. M., Schlegel, D., Finkbeiner, D., Gaćeša, M., Smolčić, V., Anderson, S. F., Voges, W., Jurić, M., Siverd, R. J., Steinhardt, W., Jagoda, A. S., Blanton, M. R., Schneider, D. P.: *Panchromatic properties of 99000 galaxies detected by SDSS, and (some by) ROSAT, GALEX, 2MASS, IRAS, GB6, FIRST, NVSS and WENSS surveys*, MNRAS, vol. 370, 1677–1698, 2006.

O'Connell, R. W.: *Galaxy spectral synthesis. I - Stellar populations in the nuclei of giant ellipticals*, ApJ, vol. 206, 370–390, 1976.

Oke, J. B., Gunn, J. E.: *Secondary standard stars for absolute spectrophotometry*, ApJ, vol. 266, 713–717, 1983.

Omont, A.: *Physics and chemistry of interstellar polycyclic aromatic molecules*, A&A, vol. 164, 159–178, 1986.

Onaka, T., Yamamura, I., Tanabe, T., Roellig, T. L., Yuen, L.: *Detection of the Mid-Infrared Unidentified Bands in the Diffuse Galactic Emission by IRTS*, PASJ, vol. 48, L59–L63, 1996.

Osterbrock, D. E.: *Astrophysics of gaseous nebulae and active galactic nuclei*, Research supported by the University of California, John Simon Guggenheim Memorial Foundation, University of Minnesota, et al. Mill Valley, CA, University Science Books, 1989, 422 p., 1989.

Pasquali, A., Kauffmann, G., Heckman, T. M.: *The excess far-infrared emission of active galactic nuclei in the local Universe*, MNRAS, vol. 361, 1121–1130, 2005.

Peebles, P. J. E.: *Principles of physical cosmology*, Princeton Series in Physics, Princeton, NJ: Princeton University Press, —c1993, 1993.

Peeters, E., Martín-Hernández, N. L., Damour, F., Cox, P., Roelfsema, P. R., Baluteau, J.-P., Tielens, A. G. G. M., Churchwell, E., Kessler, M. F., Mathis, J. S., Morisset, C., Schaerer, D.: *ISO spectroscopy of compact H II regions in the Galaxy. I. The catalogue*, A&A, vol. 381, 571–605, 2002.

Pei, Y. C.: *Interstellar dust from the Milky Way to the Magellanic Clouds*, ApJ, vol. 395, 130–139, 1992.

Petrosian, V., Silk, J., Field, G. B.: *A Simple Analytic Approximation for Dusty STRÖMGREN Spheres*, ApJ, vol. 177, L69+, 1972.

Pope, A., Scott, D., Dickinson, M., Chary, R.-R., Morrison, G., Borys, C., Sajina, A., Alexander, D. M., Daddi, E., Frayer, D., MacDonald, E., Stern, D.: *The Hubble Deep Field-North SCUBA Super-map - IV. Characterizing submillimetre galaxies using deep Spitzer imaging*, MNRAS, vol. 370, 1185–1207, 2006.

Popescu, C. C., Misiriotis, A., Kylafis, N. D., Tuffs, R. J., Fischera, J.: *Modelling the spectral energy distribution of galaxies. I. Radiation fields and grain heating in the edge-on spiral NGC 891*, A&A, vol. 362, 138–150, 2000.

Purcell, E. M.: *Temperature fluctuations in very small interstellar grains*, ApJ, vol. 206, 685–690, 1976.

Rapacioli, M., Joblin, C., Boissel, P.: *Spectroscopy of polycyclic aromatic hydrocarbons and very small grains in photodissociation regions*, A&A, vol. 429, 193–204, 2005.

Reach, W. T., Dwek, E., Fixsen, D. J., Hewagama, T., Mather, J. C., Shafer, R. A., Banday, A. J., Bennett, C. L., et al.: *Far-Infrared Spectral Observations of the Galaxy by COBE*, ApJ, vol. 451, 188–+, 1995.

Reach, W. T., Megeath, S. T., Cohen, M., Hora, J., Carey, S., Surace, J., Willner, S. P., Barmby, P., Wilson, G., Glaccum, W., Lowrance, P., Marengo, M., Fazio, G. G.: *Absolute Calibration of the Infrared Array Camera on the Spitzer Space Telescope*, PASP, vol. 117, 978–990, 2005.

Rieke, G. H., Young, E. T., Engelbracht, C. W., Kelly, D. M., Low, F. J., Haller, E. E., et al.: *The Multiband Imaging Photometer for Spitzer (MIPS)*, ApJS, vol. 154, 25–29, 2004.

Rigopoulou et al.: *Ultraluminous IRAS galaxies as seen with ISO*, in P. Cox, M. Kessler, editors, *The Universe as Seen by ISO*, vol. 427 of *ESA Special Publication*, pp. 833–+, 1999.

Roberts, M. S., Haynes, M. P.: *Physical Parameters along the Hubble Sequence*, ARA&A, vol. 32, 115–152, 1994.

Roussel, H., Vigroux, L., Bosma, A., Sauvage, M., Bonoli, C., Gallais, P., Hawarden, T., Lequeux, J., Madden, S., Mazzei, P.: *An atlas of mid-infrared dust emission in spiral galaxies*, A&A, vol. 369, 473–509, 2001.

Rowan-Robinson, M.: *Radiative transfer in dust clouds. I - Hot-centered clouds associated with regions of massive star formation*, ApJS, vol. 44, 403–426, 1980.

Salim, S., Rich, R. M., Charlot, S., Brinchmann, J., Johnson, B. D., Schiminovich, D., Seibert, M., Mallery, R., Heckman, T. M., Forster, K., Friedman, P. G., Martin, D. C., Morrissey, P., Neff, S. G., Small, T., Wyder, T. K., Bianchi, L., Donas, J., Lee, Y.-W., Madore, B. F., Milliard, B., Szalay, A. S., Welsh, B. Y., Yi, S. K.: *UV Star Formation Rates in the Local Universe*, ApJS, vol. 173, 267–292, 2007.

Salpeter, E. E.: *The Luminosity Function and Stellar Evolution.*, ApJ, vol. 121, 161–+, 1955.

Sandage, A.: *Star formation rates, galaxy morphology, and the Hubble sequence*, A&A, vol. 161, 89–101, 1986.

Saunders, W., Sutherland, W. J., Maddox, S. J., Keeble, O., Oliver, S. J., Rowan-Robinson, M., McMahon, R. G., Efstathiou, G. P., Tadros, H., White, S. D. M., Frenk, C. S., Carramiñana, A., Hawkins, M. R. S.: *The PSCz catalogue*, MNRAS, vol. 317, 55–63, 2000.

Scalo, J. M.: *The stellar initial mass function*, Fundamentals of Cosmic Physics, vol. 11, 1–278, 1986.

Schlegel, D. J., Finkbeiner, D. P., Davis, M.: *Maps of Dust Infrared Emission for Use in Estimation of Reddening and Cosmic Microwave Background Radiation Foregrounds*, ApJ, vol. 500, 525–+, 1998.

Schmidt, M.: *The Rate of Star Formation.*, ApJ, vol. 129, 243–+, 1959.

Scoville, N., Aussel, H., Brusa, M., Capak, P., Carollo, C. M., Elvis, M., Giavalisco, M., Guzzo, L., Hasinger, G., Impey, C., Kneib, J.-P., LeFevre, O., Lilly, S. J., Mobasher, B., Renzini, A., Rich, R. M., Sanders, D. B., Schinnerer, E., Schminovich, D., Shopbell, P., Taniguchi, Y., Tyson, N. D.: *The Cosmic Evolution Survey (COSMOS): Overview*, ApJS, vol. 172, 1–8, 2007.

Seibert et al.: *Testing the Empirical Relation between Ultraviolet Color and Attenuation of Galaxies*, ApJ, vol. 619, L55–L58, 2005.

Sellgren, K.: *The near-infrared continuum emission of visual reflection nebulae*, ApJ, vol. 277, 623–633, 1984.

Sellgren, K., Werner, M. W., Dinerstein, H. L.: *Extended near-infrared emission from visual reflection nebulae*, ApJ, vol. 271, L13–L17, 1983.

Shapley, H.: *A Contribution to the Study of Galactic Dimensions*, Proceedings of the National Academy of Science, vol. 19, 29–34, 1933.

Silva, L., Granato, G. L., Bressan, A., Danese, L.: *Modeling the Effects of Dust on Galactic Spectral Energy Distributions from the Ultraviolet to the Millimeter Band*, ApJ, vol. 509, 103–117, 1998.

Skrutskie, M. F., Schneider, S. E., Stiening, R., Strom, S. E., Weinberg, M. D., Beichman, C., Chester, T., Cutri, R., et al.: *The Two Micron All Sky Survey (2MASS): Overview and Status.*, in F. Garzon, N. Epchtein, A. Omont, B. Burton, P. Persi, editors, *Astrophysics and Space Science Library*, vol. 210 of *Astrophysics and Space Science Library*, pp. 25–+, 1997.

Smith, J. D. T., Draine, B. T., Dale, D. A., Moustakas, J., Kennicutt, R. C., Jr., Helou, G., Armus, L., Roussel, H., Sheth, K., Bendo, G. J., Buckalew, B. A., Calzetti, D., Engelbracht, C. W., Gordon, K. D., Hollenbach, D. J., Li, A., Malhotra, S., Murphy, E. J., Walter, F.: *The Mid-Infrared Spectrum of Star-forming Galaxies: Global Properties of Polycyclic Aromatic Hydrocarbon Emission*, ApJ, vol. 656, 770–791, 2007.

Smoot, G. F., Bennett, C. L., Kogut, A., Wright, E. L., Aymon, J., Boggess, N. W., Cheng, E. S., de Amici, G., Gulkis, S., Hauser, M. G., Hinshaw, G., Jackson, P. D., Janssen, M., Kaita, E., Kelsall, T., Keegstra, P., Lineweaver, C., Loewenstein, K., Lubin, P., Mather, J., Meyer, S. S., Moseley, S. H., Murdock, T., Rokke, L., Silverberg, R. F., Tenorio, L., Weiss, R., Wilkinson, D. T.: *Structure in the COBE differential microwave radiometer first-year maps*, ApJ, vol. 396, L1–L5, 1992.

Soifer, B. T., Sanders, D. B., Madore, B. F., Neugebauer, G., Danielson, G. E., Elias, J. H., Lonsdale, C. J., Rice, W. L.: *The IRAS bright galaxy sample. II - The sample and luminosity function*, ApJ, vol. 320, 238–257, 1987.

Spinrad, H., Taylor, B. J.: *The Stellar Content of the Nuclei of Nearby Galaxies. I. M31, M32, and M81*, ApJS, vol. 22, 445–+, 1971.

Spitzer, L. J.: *On a Possible Interstellar Galactic Corona.*, ApJ, vol. 124, 20–+, 1956.

Spitzer, L. J., Fitzpatrick, E. L.: *Composition of interstellar clouds in the disk and halo. I - HD 93521*, ApJ, vol. 409, 299–318, 1993.

Stoughton, C., Lupton, R. H., Bernardi, M., Blanton, M. R., Burles, S., Castander, F. J., Connolly, A. J., Eisenstein, D. J., et al.: *Sloan Digital Sky Survey: Early Data Release*, AJ, vol. 123, 485–548, 2002.

Strateva, I., Ivezić, Ž., Knapp, G. R., Narayanan, V. K., Strauss, M. A., Gunn, J. E., Lupton, R. H., Schlegel, D., Bahcall, N. A., Brinkmann, J., Brunner, R. J., Budavári, T., Csabai, I., Castander, F. J., Doi, M., Fukugita, M., Győry, Z., Hamabe, M., Hennessy, G., Ichikawa, T., Kunszt, P. Z., Lamb, D. Q., McKay, T. A., Okamura, S., Racusin, J., Sekiguchi, M., Schneider, D. P., Shimasaku, K., York, D.: *Color Separation of Galaxy Types in the Sloan Digital Sky Survey Imaging Data*, AJ, vol. 122, 1861–1874, 2001.

Strauss, M. A., Weinberg, D. H., Lupton, R. H., Narayanan, V. K., Annis, J., Bernardi, M., Blanton, M., Burles, S., Connolly, A. J., Dalcanton, J., Doi, M., Eisenstein, D., Frieman, J. A., Fukugita, M., Gunn, J. E., Ivezić, Ž., Kent, S., Kim, R. S. J., Knapp, G. R., Kron, R. G., Munn, J. A., Newberg, H. J., Nichol, R. C., Okamura, S., Quinn, T. R., Richmond, M. W., Schlegel, D. J., Shimasaku, K., SubbaRao, M., Szalay, A. S., Vanden Berk, D., Vogeley, M. S., Yanny, B., Yasuda, N., York, D. G., Zehavi, I.: *Spectroscopic Target Selection in the Sloan Digital Sky Survey: The Main Galaxy Sample*, AJ, vol. 124, 1810–1824, 2002.

Sturm, E., Lutz, D., Tran, D., Feuchtgruber, H., Genzel, R., Kunze, D., Moorwood, A. F. M., Thornley, M. D.: *ISO-SWS spectra of galaxies: Continuum and features*, A&A, vol. 358, 481–493, 2000.

Sullivan, M., Mobasher, B., Chan, B., Cram, L., Ellis, R., Treyer, M., Hopkins, A.: *A Comparison of Independent Star Formation Diagnostics for an Ultraviolet-selected Sample of Nearby Galaxies*, ApJ, vol. 558, 72–80, 2001.

Tanaka, M., Matsumoto, T., Murakami, H., Kawada, M., Noda, M., Matsuura, S.: *IRTS Observation of the Unidentified 3.3-Micron Band in the Diffuse Galactic Emission*, PASJ, vol. 48, L53–L57, 1996.

Tielens, A. G. G. M.: *The Physics and Chemistry of the Interstellar Medium*, The Physics and Chemistry of the Interstellar Medium, by A. G. G. M. Tielens, pp. . ISBN 0521826349. Cambridge, UK: Cambridge University Press, 2005., 2005.

Tinsley, B. M.: *Evolutionary synthesis of the stellar population in elliptical galaxies. II - Late M giants and composition effects*, ApJ, vol. 222, 14–22, 1978.

Trumpler, R. J.: *Absorption of Light in the Galactic System*, PASP, vol. 42, 214–+, 1930.

Tuffs, R. J., Popescu, C. C., Völk, H. J., Kylafis, N. D., Dopita, M. A.: *Modelling the spectral energy distribution of galaxies. III. Attenuation of stellar light in spiral galaxies*, A&A, vol. 419, 821–835, 2004.

Turnrose, B. E.: *The stellar content of the nuclear regions of SC galaxies*, ApJ, vol. 210, 33–37, 1976.

Vassiliadis, E., Wood, P. R.: *Post-asymptotic giant branch evolution of low- to intermediate-mass stars*, ApJS, vol. 92, 125–144, 1994.

Vazdekis, A.: *Evolutionary Stellar Population Synthesis at 2 Å Spectral Resolution*, ApJ, vol. 513, 224–241, 1999.

Veilleux, S., Kim, D.-C., Sanders, D. B.: *Optical Spectroscopy of the IRAS 1 JY Sample of Ultraluminous Infrared Galaxies*, ApJ, vol. 522, 113–138, 1999.

Veilleux, S., Kim, D.-C., Sanders, D. B., Mazzarella, J. M., Soifer, B. T.: *Optical Spectroscopy of Luminous Infrared Galaxies. II. Analysis of the Nuclear and Long-Slit Data*, ApJS, vol. 98, 171–+, 1995.

Verstraete, L., Pech, C., Moutou, C., Sellgren, K., Wright, C. M., Giard, M., Léger, A., Timmermann, R., Drapatz, S.: *The Aromatic Infrared Bands as seen by ISO-SWS: Probing the PAH model*, A&A, vol. 372, 981–997, 2001.

Verstraete, L., Puget, J. L., Falgarone, E., Drapatz, S., Wright, C. M., Timmermann, R.: *SWS spectroscopy of small grain features across the M17-Southwest photodissociation front.*, A&A, vol. 315, L337–L340, 1996.

Wang, B., Heckman, T. M.: *Internal Absorption and the Luminosity of Disk Galaxies*, ApJ, vol. 457, 645–+, 1996.

Werner, M. W., Roellig, T. L., Low, F. J., Rieke, G. H., Rieke, M., Hoffmann, W. F., Young, E., Houck, J. R., et al.: *The Spitzer Space Telescope Mission*, ApJS, vol. 154, 1–9, 2004.

Westera, P., Lejeune, T., Buser, R., Cuisinier, F., Bruzual, G.: *A standard stellar library for evolutionary synthesis. III. Metallicity calibration*, A&A, vol. 381, 524–538, 2002.

Wild, V., Kauffmann, G., Heckman, T., Charlot, S., Lemson, G., Brinchmann, J., Reichard, T., Pasquali, A.: *Bursty stellar populations and obscured AGN in galaxy bulges*, ArXiv e-prints, vol. 706, 2007.

Wilson, R. W., Jefferts, K. B., Penzias, A. A.: *Carbon Monoxide in the Orion Nebula*, ApJ, vol. 161, L43+, 1970.

Witt, A. N., Thronson, H. A., Jr., Capuano, J. M., Jr.: *Dust and the transfer of stellar radiation within galaxies*, ApJ, vol. 393, 611–630, 1992.

Worthey, G.: *Comprehensive stellar population models and the disentanglement of age and metallicity effects*, ApJS, vol. 95, 107–149, 1994.

York, D. G.: *Highly ionized atoms observed with Copernicus*, ApJ, vol. 193, L127–L131, 1974.

Yun, M. S., Reddy, N. A., Condon, J. J.: *Radio Properties of Infrared-selected Galaxies in the IRAS 2 Jy Sample*, ApJ, vol. 554, 803–822, 2001.

Zheng, X. Z., Dole, H., Bell, E. F., Le Floc'h, E., Rieke, G. H., Rix, H.-W., Schiminovich, D.: *Infrared Spectral Energy Distributions of z˜0.7 Star-Forming Galaxies*, ArXiv e-prints, vol. 706, 2007.